

# **Nanostructuring of Zinc Oxide Based Functional Materials Directed by Tobacco Mosaic Viruses**

Von der Fakultät Chemie der Universität Stuttgart  
zur Erlangung der Würde eines Doktors der  
Naturwissenschaften (Dr. rer. nat.) genehmigte Abhandlung

Vorgelegt von  
**Nina Stitz**  
aus Stuttgart

Hauptberichter:	Prof. Dr. Joachim Bill
Mitberichter:	Prof. Dr. Bernhard Hauer
Prüfungsvorsitzender:	Prof. Dr. Thomas Schleid
Tag der mündlichen Prüfung:	25. Januar 2017

Institut für Materialwissenschaft  
Universität Stuttgart

2017







## **DECLARATION OF AUTHORSHIP**

I hereby certify that the dissertation entitled

**Nanostructuring of Zinc Oxide Based Functional Materials Directed by Tobacco Mosaic Viruses**

is entirely my own work except where otherwise indicated. Passages and ideas from other sources have been clearly indicated.

Name: \_\_\_\_\_

Signed: \_\_\_\_\_

Date: \_\_\_\_\_



The experimental work presented in this thesis was performed under supervision of Professor Dr. Joachim Bill and Dr. Petia Atanasova at the Institute for Materials Science of the University of Stuttgart between September 2011 and January 2015.

The present thesis has a non-cumulative structure. In the following, parts of the dissertation that have already been published in scientific journals or are designated for publication in scientific journals are listed. Other parts of the thesis were among contributions at scientific conferences either as oral presentations or poster contributions.

## SCIENTIFIC PUBLICATIONS

---

- (5) **Stitz, N.** *et al.*, in preparation  
Working title: “*Genetically Induced Enhancement of Mechanical Performance of Biohybrid ZnO Multilayer Systems*” found in **CHAPTER 4.6**
- (4) **Stitz, N.**, *et al.* 2016. *Sci. Rep.* **6**, 26518;  
“*Piezoelectric Templates – New Views on Biomineralization and Biomimetics*”  
found in **CHAPTER 4.4**
- (3) Atanasova, P., **Stitz, N.**, Sanctis, S., *et al.* 2015. *Langmuir* **31**, 3897–3903  
“*Genetically Improved Monolayer-Forming Tobacco Mosaic Viruses to Generate Nanostructured Semiconducting Bio/Inorganic Hybrids*” found in **CHAPTER 4.2**
- (2) Altintoprak, K., Seidenstücker, A., Welle, A., Eiben, S., Atanasova, P., **Stitz, N.**, *et al.* 2015. *Beilstein J. Nanotechnol.* **6**, 1399–1412.  
“*Peptide-Equipped Tobacco Mosaic Virus Templates for Selective and Controllable Biomineral Deposition*”
- (1) Eiben, S., **Stitz, N.**, Eber, F. *et al.* 2014. *Virus Res.* **180**, 92–96  
“*Tailoring the Surface Properties of Tobacco Mosaic Virions by the Integration of Bacterially Expressed Mutant Coat Protein*”

## CONFERENCE CONTRIBUTIONS

---

- 09/2014 **Invited Presentation and Award for DFG Start-Up Grant**  
Materials Science Engineering MSE, Darmstadt, Germany  
**N. Stitz**  
*Virus-Based Functional Materials*
- 12/2014 **Invited Presentation**  
Projekthaus NanoBioMater, Stuttgart, Germany  
**N. Stitz**  
*Virus-Based Functional Thin Films*
- 03/2013 **Presentation**  
Winter School, Forum on Advanced Materials, MIT Boston, USA  
**N. Stitz; P. Atanasova; S. Eiben; H. Jeske; J.J. Schneider and J. Bill**  
*Genetically Controlled Mineralization of Zinc Oxide on Tobacco Mosaic Virus*
- 08/2013 **Presentation and Poster**  
Summer School SPP 1569, Bad Herrenalb, Germany  
**N. Stitz; S. Eiben; P. Atanasova; S. Sanctis; R.C. Hoffmann; J. Bill et al.**  
*Fabrication of Virus-Templated Functional Composite Materials*
- 09/2012 **Presentation and Poster**  
Materials Science Engineering MSE, Darmstadt, Germany  
**N. Stitz; P. Atanasova; D. Rothenstein; J. Baier; J. Bill et al.**  
*Bio-Inspired Precipitation of Semiconducting Oxides on Genetically Modified Tobacco Mosaic Viruses*
- 03/2014 **Poster**  
Winter School SPP 1420 und SPP 1569, Potsdam, Germany  
**N. Stitz; S. Eiben; P. Atanasova; S. Sanctis; R.C. Hoffmann; J. Bill et al.**  
*Genetically Optimized Tobacco Mosaic Viruses as Scaffold for the in Vitro Generation of Semiconductor Bio/Metal-Oxide Nanostructured Architectures*
- 09/2012 **Poster**  
Ringberg Symposium, Ringberg, Germany  
**N. Stitz; S. Eiben; R.C. Hoffmann; P. Atanasova; J. Bill et al.**  
*Genetically Controlled Mineralization of Zinc Oxide on Tobacco Mosaic Viruses*



## TABLE OF CONTENTS

<b>1</b>	<b>INTRODUCTION.....</b>	<b>1</b>
<b>2</b>	<b>LITERATURE OVERVIEW .....</b>	<b>3</b>
<b>2.1</b>	<b>ZNO .....</b>	<b>3</b>
2.1.1	SYNTHESIS.....	3
2.1.2	STRUCTURE AND PROPERTIES.....	6
2.1.2.1	ELECTRICAL PROPERTIES.....	7
2.1.2.2	PIEZOELECTRIC PROPERTIES .....	10
2.1.2.3	PHOTOLUMINESCENCE.....	11
2.1.2.4	MECHANICAL PROPERTIES.....	12
<b>2.2</b>	<b>BIOMINERALIZATION .....</b>	<b>13</b>
2.2.1	NACRE.....	13
2.2.2	BONE .....	15
<b>2.3</b>	<b>BIO-INSPIRED SYNTHESIS.....</b>	<b>16</b>
<b>2.4</b>	<b>TOBACCO MOSAIC VIRUS .....</b>	<b>18</b>
<b>2.5</b>	<b>SELF-ASSEMBLY OF VIRAL PARTICLES.....</b>	<b>23</b>
<b>3</b>	<b>EXPERIMENTS.....</b>	<b>29</b>
<b>3.1</b>	<b>TOBACCO MOSAIC VIRUS ISOLATION, PURIFICATION AND DIALYSIS .....</b>	<b>29</b>
<b>3.2</b>	<b>REACTION SOLUTION FOR ZNO MINERALIZATION.....</b>	<b>29</b>
<b>3.3</b>	<b>TEMPLATE FORMATION.....</b>	<b>30</b>
3.3.1	SUBSTRATE PREPARATION .....	30
3.3.2	SELF-ASSEMBLED MONOLAYERS.....	30
3.3.3	SINGLE IMMOBILIZED VIRUSES .....	31
3.3.4	VIRUS MONOLAYERS VIA CONVECTIVE ASSEMBLY .....	31

---

<b>3.4</b>	<b>MINERALIZATION.....</b>	<b>32</b>
3.4.1	MINERALIZATION OF SINGLE VIRUS PARTICLES .....	32
3.4.2	MINERALIZATION OF THIN FILMS .....	32
<b>3.5</b>	<b>PIEZOACTIVE THIN FILMS.....</b>	<b>33</b>
<b>3.6</b>	<b>ZNO-BASED FIELD-EFFECT TRANSISTORS.....</b>	<b>34</b>
3.6.1	SUBSTRATE GEOMETRY.....	34
3.6.2	SUBSTRATE PREPARATION AND TEMPLATE FORMATION .....	34
3.6.3	ZNO MINERALIZATION ON FIELD-EFFECT TRANSISTORS.....	35
3.6.4	MEASUREMENT DETAILS.....	35
<b>3.7</b>	<b>NACRE-LIKE MULTILAYERS OF ZNO AND TMV .....</b>	<b>35</b>
3.7.1	TEMPLATE LAYERS FOR MULTILAYERED SAMPLES.....	36
3.7.2	PREPARATION OF MONOLITHIC SAMPLES WITH VARYING H <sub>2</sub> O CONTENT.....	36
3.7.3	PREPARATION OF MULTILAYERED SAMPLES .....	36
3.7.4	SAMPLE PREPARATION FOR SEM INVESTIGATIONS.....	38
3.7.5	SAMPLE PREPARATION FOR FRACTURE TOUGHNESS MEASUREMENTS .....	38
3.7.5.1	MASKING WITH PHOTOLITHOGRAPHY .....	39
3.7.5.2	PARTIAL ETCHING .....	39
<b>3.8</b>	<b>CHARACTERIZATION METHODS .....</b>	<b>39</b>
3.8.1	DYNAMIC LIGHT SCATTERING .....	39
3.8.2	ZETA POTENTIAL.....	40
3.8.3	ATOMIC FORCE MICROSCOPY .....	41
3.8.4	PIEZORESPONSE FORCE MICROSCOPY .....	41
3.8.5	SCANNING ELECTRON MICROSCOPY .....	42
3.8.6	X-RAY DIFFRACTION .....	43
3.8.7	PHOTOLUMINESCENCE.....	44
3.8.8	NANOINDENTATION .....	44

3.8.9	MICROINDENTATION AND DETERMINATION OF FRACTURE TOUGHNESS.....	45
<b>4</b>	<b>RESULTS AND DISCUSSION .....</b>	<b>47</b>
<b>4.1</b>	<b>REACTION SOLUTION FOR ZNO MINERALIZATION.....</b>	<b>47</b>
<b>4.2</b>	<b>VIRUS MONOLAYER FORMATION .....</b>	<b>52</b>
4.2.1	INFLUENCE OF TMV CONCENTRATION ON MONOLAYER FORMATION .....	56
4.2.2	INFLUENCE OF WITHDRAWAL VELOCITY .....	59
4.2.3	INFLUENCE OF VIRUS MONOLAYER QUALITY ON ZNO THIN FILM FORMATION.....	61
4.2.4	INFLUENCE OF VIRUS MONOLAYER QUALITY ON TRANSISTOR PROPERTIES .....	63
<b>4.3</b>	<b>MINERALIZATION WITH WATER-CONTAINING REACTION SOLUTION .....</b>	<b>68</b>
4.3.1	MINERALIZATION OF SINGLE TMV .....	69
4.3.2	MINERALIZATION OF THIN FILMS .....	74
4.3.2.1	FILM COMPOSITION AND TEXTURE .....	75
4.3.2.2	OPTICAL PROPERTIES.....	80
4.3.2.3	CORRELATION OF PARTICLE AND CRYSTALLITE SIZE .....	84
4.3.3	DEPOSITION MECHANISM .....	89
<b>4.4</b>	<b>PIEZOELECTRIC THIN FILMS .....</b>	<b>95</b>
4.4.1	REFERENCE MEASUREMENTS .....	95
4.4.2	TEXTURE INFLUENCE ON PIEZOELECTRIC PROPERTIES .....	96
4.4.3	TEMPLATE INFLUENCE .....	98
4.4.4	THICKNESS INFLUENCE .....	101
<b>4.5</b>	<b>ZNO-BASED FIELD-EFFECT TRANSISTORS.....</b>	<b>102</b>
4.5.1	FET PERFORMANCE IN DEPENDENCY OF H <sub>2</sub> O CONTENT ON NH <sub>2</sub> -SAMs .....	103
4.5.2	THICKNESS DEPENDENCY OF THE FET PERFORMANCE ON NH <sub>2</sub> -SAMs.....	106
4.5.3	VIRUS-BASED FETs DEPOSITED FROM WATER-CONTAINING SOLUTIONS.....	109
<b>4.6</b>	<b>MONOLITHIC ZNO FILMS AND MULTILAYERED FILMS OF TMV AND ZNO .....</b>	<b>113</b>
4.6.1	MONOLITHIC ZNO FILMS .....	113

## TABLE OF CONTENTS

---

4.6.1.1	MICROSTRUCTURE AND COMPOSITION OF MONOLITHIC ZNO FILMS .....	113
4.6.1.2	MECHANICAL PROPERTIES OF MONOLITHIC ZNO FILMS .....	114
4.6.2	MULTILAYERED FILMS OF TMV AND ZNO .....	118
4.6.2.1	MICROSTRUCTURE AND COMPOSITION OF MULTILAYERED SAMPLES.....	119
4.6.2.2	MECHANICAL PROPERTIES OF MULTILAYERED SAMPLES .....	124
<b>5</b>	<b>SUMMARY .....</b>	<b>135</b>
<b>6</b>	<b>ZUSAMMENFASSUNG .....</b>	<b>141</b>
<b>7</b>	<b>PUBLICATION BIBLIOGRAPHY.....</b>	<b>147</b>
<b>8</b>	<b>DANKSAGUNG.....</b>	<b>155</b>
<b>9</b>	<b>CURRICULUM VITAE.....</b>	<b>157</b>

**LIST OF ABBREVIATIONS**

30%TMV-His <sub>6</sub>	mixed assembly of tobacco mosaic virus and 30% of the histidine mutant
<i>a</i>	lattice parameter
<i>A</i>	anisotropy factor
<i>a</i>	measured crack length within coating
AFM	atomic force microscope
APTES	3-aminopropyltriethoxysilane
<i>b</i>	measured crack length on substrate
BSE	backscattered electrons
<i>c</i>	lattice parameter
<i>c</i>	concentration
CA	convective assembly
CBD	chemical bath deposition
COOH	carboxyl
<i>C<sub>ox</sub></i>	gate oxide capacitance
<i>D</i>	drain
<i>d<sub>33</sub></i>	piezoelectric constant
<i>d<sub>eff</sub></i>	effective piezoelectric constant
<i>D<sub>H</sub></i>	hydrodynamic diameter
DLS	dynamic light scattering
<i>D<sub>PL</sub></i>	crystallite size calculated from PL data
<i>D<sub>V</sub></i>	same as <i>D<sub>XRD</sub></i> , crystallite size calculated from XRD data
<i>D<sub>XRD</sub></i>	crystallite size calculated from XRD data
<i>E</i>	piezoelectric tensor
<i>E</i>	Young's modulus

LIST OF ABBREVIATIONS

---

$E^*$	measured UV emission
E50Q	tobacco mosaic virus mutant without RNA
$E_C$	Young's modulus coating
$E_G$	band gap
$e_{ij}$	piezoelectric stress coefficients
$E_S$	Young's modulus silicon substrate
FET	field-effect transistor
G	gate
$g_c$	growth per cycle
$g_{c,SEM}$	growth per cycle determined by SEM measurements
$h$	Planck's constant
$H$	hardness
ICDD	International Center for Diffraction Data
$I_D$	drain current
IEP, pI	isoelectric point
$I_{on/off}$	on/off ratio
ITO	indium tin oxide
$K_C$	fracture toughness coating
$K_S$	fracture toughness silicon substrate
$L$	channel length
$m_e$	effective electron mass
$m_h$	effective hole mass
MLS	multilayered sample
MOSFET	metal-oxide field-effect transistor
NH <sub>2</sub>	amino
$P$	polarization
PFM	piezoresponse force microscope

## LIST OF ABBREVIATIONS

---

$P_i$	polarization components
PL	photoluminescence
PPLN	periodically polarized lithium niobate
PVP	polyvinylpyrrolidone
$R$	radius
r.H.	relative humidity
S	source
$s$	distance of the placed indent to coating
SAM	self-assembled monolayer
SE	secondary electrons
SEM	scanning electron microscope
SPP buffer	sodium potassium phosphate buffer
$T$	texture coefficient
TEAOH	tetraethylammonium hydroxide
TFT	thin film field-effect transistor
TMV	tobacco mosaic virus
TMV-Cys	S3C, cysteine mutant of tobacco mosaic virus
TMV-Lys	T158K, lysine mutant of tobacco mosaic virus
$t_{Ox}$	thickness of the oxide
$u$	ratio of bond length to $c$ -axis ratio ( $c/a$ )
$V$	volume
$V_{AC}$	alternating current bias
$V_{DS}$	drain-source voltage
$V_{GS}$	gate-source voltage
$V_{Th}$	threshold voltage
$v_w$	withdrawal velocity
$W$	channel width

## LIST OF ABBREVIATIONS

---

wtTMV	tobacco mosaic virus wildtype
XRD	X-ray diffraction
$Z^*$	effective bond charge
$\Psi_c$	dimensionless factor
$\varepsilon$	dielectric constant
$\varepsilon_j$	strain
$\varepsilon_{Ox}$	dielectricity of the oxide
$\phi$	dimensionless factor calculated from the slope substrate crack length vs. crack length in coating
$\lambda$	dimensionless factor
$\mu$	field-effect mobility
$\nu_c$	Poisson ratio coating
$\nu_s$	Poisson ratio silicon substrate
$\sigma_r$	residual stress
$\zeta$	zeta potential



## 1 INTRODUCTION

Conventional synthesis of ceramic materials generally involves harsh reaction conditions, such as high temperatures, pressures and often hazardous reaction conditions, resulting in costly and energy-consuming synthesis. However, these materials often provide wide fields of application due to their outstanding properties. For example, zinc oxide (ZnO) is a semiconductor with promising electrical and optical properties allowing implementation in the fields of electronic, optoelectronic and sensor applications. A more detailed insight into the properties and possible applications of ZnO with the relevant literature references is given in Section 2.1.

Nature provides numerous examples of how to 'produce' materials with sophisticated properties. In the course of evolution, many organisms developed the ability to form highly complex, inorganic materials out of solution at ambient conditions, such as nacre and bone. These materials owe their extraordinary properties to their complex micro- and nanostructure. Nacre consists of a highly hierarchical nanostructure of a protein matrix and embedded calcium carbonate platelets. The hierarchical 'brick and mortar' combination of a soft and stiff phase allows the material to be harder and tougher than the pure mineral. Additional details on biomineralization and biominerals, as well as the relevant references are given in Section 2.2.

Great effort has been spent on gaining insights into the highly complex processes of biomineralization. The aim is to transfer these processes to a bio-inspired approach to technologically more important materials, which are not found as biominerals to pave the way for new fields of application. Bio-inspired synthesis approaches, such as chemical bath deposition, are low in cost and environmentally friendly. The low synthesis temperatures and ambient pressure allow the use of temperature-sensitive substrates (more details in Section 2.3). Attempts at understanding biomineralization revealed that more or less complex biomacromolecules trigger and/or direct the formation of inorganic materials. These biomolecules provide regularly arrayed chemical groups often with specific binding.

There are numerous biomolecules with a great potential for implementation in bio-inspired synthesis, but some provide specific advantages, such as the tobacco mosaic virus (TMV). The

rod-like virus particle has a high stability in various solvents over a broad temperature and pH range. Thus, TMV supports implementation many mineralization processes. The RNA sequence is well-known and allows various genetic modifications providing various possible functional groups located on the virus surface. More details on TMV and the relevant references are given in Section 2.4 and Section 2.5.

In the present work, TMV and genetically engineered mutants are combined with an optimized low-temperature approach for ZnO synthesis in order to generate functional thin films. The simple evaporative assembly method, convective assembly, is applied to generate homogeneous virus monolayers serving as a basis for further mineralization. The genetic modification is proven to have a big impact on the morphology of the template layers (Section 4.2) and consequently on the subsequent ZnO deposition [1]. Small amounts of water added to the methanolic reaction solution allow tuning of both crystallite size and texture of the deposited ZnO films (Section 4.3). For the first time, it is shown that the intrinsic piezoelectricity of the virus template strongly enhances the degree of texture of the deposited films [2].

The next step is to fabricate functional thin films. In doing so, three potential fields for future applications are chosen: (1) thin piezoelectric films (Section 4.4), (2) field-effect transistors (Section 4.5), and (3) multilayered structures (Section 4.6). The intrinsic piezoelectricity of TMV combined with the tunable texture of the deposited ZnO films leads to thin hybrid films with a more than two-fold increased piezoelectric response compared to films on non-piezoelectric templates. Genetic modification of TMV can result in denser and more homogeneous template monolayers. TMV/ZnO field-effect transistors fabricated with these mutants show an improved performance with higher mobility and faster switching. By repeatedly combining monolayers of genetically engineered TMV and ZnO to hierarchic multilayers, superior mechanical properties are achieved. The films show an improved toughness while not only maintaining their stiffness and hardness, but increasing it.

## 2 LITERATURE OVERVIEW

### 2.1 ZnO

The oxidic compound zinc oxide (ZnO) occurs naturally in the form of zincite, which can be found in the USA, Italy, Namibia, Poland, Spain, and Australia. It has a red or orange color due to manganese and iron impurities, respectively, whereas pure synthetic ZnO is colorless [3].

#### 2.1.1 SYNTHESIS

There are many synthesis routes resulting in a great diversity of ZnO samples ranging from powder over bulk material to nanostructures. However, in most cases it is difficult to synthesize smooth ZnO thin films due to the preferential growth in *c*-axis direction even at very low temperatures leading to columnar structures. Conventional synthesis methods, as well as growth of high quality ZnO, require harsh reaction conditions, such as high temperatures, pressure and extreme chemical conditions. Most powders synthesized for technical applications use either the so-called 'French' or 'American' processes which both involve the oxidation of metallic zinc vapor at elevated temperatures [4].

ZnO cannot be grown from a melt due to its high vapor pressure. However, there are several possibilities to synthesize high quality ZnO [5]. Vapor phase transport is commonly used to synthesize not only bulk ZnO substrates [6], but also thin films [7] and even nanorods [8]. In general, solvothermal growth [9] and several epitaxial growth techniques, such as metal organic chemical vapor deposition, molecular beam epitaxy and pulsed laser deposition are used [5].

Especially for piezoelectric applications, highly crystalline textured ZnO is mostly produced via radio-frequency magnetron sputtering [10], pulsed laser deposition methods [11,12], or chemical vapor deposition [13]. Piezoelectric polycrystalline ZnO films synthesized at more moderate conditions via sol-gel methods required additional heating and annealing steps [14]. If textured films with preferred *c*-axis orientation are obtained without epitaxial growth conditions (i.e. crystal orientation of the deposited layer does not follow the crystal orientation of the template), the preferred orientation is referred to as 'self-texture' [15].

Nanostructures of ZnO are accessible in various different shapes, such as nanorods, nanobelts, nanosprings and nanocombs using e.g. a solid-vapor phase thermal sublimation technique [16]. ZnO nanowires and nanobelts have been suggested for applications in piezoelectric nanogenerators [17].

However, all these synthesis methods, especially the physical ones, are very energy-intensive and expensive, and, additionally, the properties of the ZnO are highly dependent on microstructure and composition and, thus, on the synthesis route.

Chemical bath deposition (CBD) is a well-established process to synthesize ZnO by thermohydrolysis ('forced hydrolysis') of zinc-containing precursors at moderate reaction conditions below 100°C, and thus allows integration of temperature-sensitive organic templates [18–20]. Deposition is induced by a pH increase often coupled with slight temperature increases. CBD though mostly yields micrometer sized hexagonal needles due to the preferential growth in *c*-axis direction [20,21]. However, by addition of structure-directing agents, such as graft copolymers [22], homopolymers [23] or amino acids and peptides [24], these problems can be overcome. Control over crystallite formation and size is important for the materials' properties which are highly dependent on microstructure and crystallite size, for example. The solvent can be changed from water to alcohols, such as 2-propanol or methanol, since hydrolysis of zinc salts is decelerated in organic solvents allowing further control over crystallite size and growth [23,25]. For the formation of nanocrystalline ZnO films deposited onto self-assembled monolayers from a methanolic reaction solution containing a structure-directing polymer (polyvinylpyrrolidone, PVP), Lipowsky *et al.* suggest three stages of particle formation [26]. Therefore, various molar ratios of the zinc species and the polymer were investigated ranging from [PVP] : [Zn<sup>2+</sup>] of 0 to 1.6. Low polymer concentrations led to immediate ZnO particle formation, whereas high concentrations completely hindered the formation nanocrystalline ZnO. The optimum ratio was found to be [PVP] : [Zn<sup>2+</sup>] = 1. The initial stage occurs upon mixing the precursors (before heating) and contains no particles at [PVP] : [Zn<sup>2+</sup>] higher than 0.8 (Figure 2-1, top left). The intermediate stage starts directly after heating the solution to 60°C and is firstly characterized by the fast formation of amorphous needle-like zinc-containing particles within the first five minutes (Figure 2-1, top right). The needle-like particles then dissolve again freeing zinc ions that then crystallize to ZnO nanocrystallites leading to both film formation and aggregation in solution (Figure 2-1, bottom

left). After two to three hours, aggregation in solution is favored over film formation leading to growth of the aggregates (final stage, Figure 2-1, bottom right).

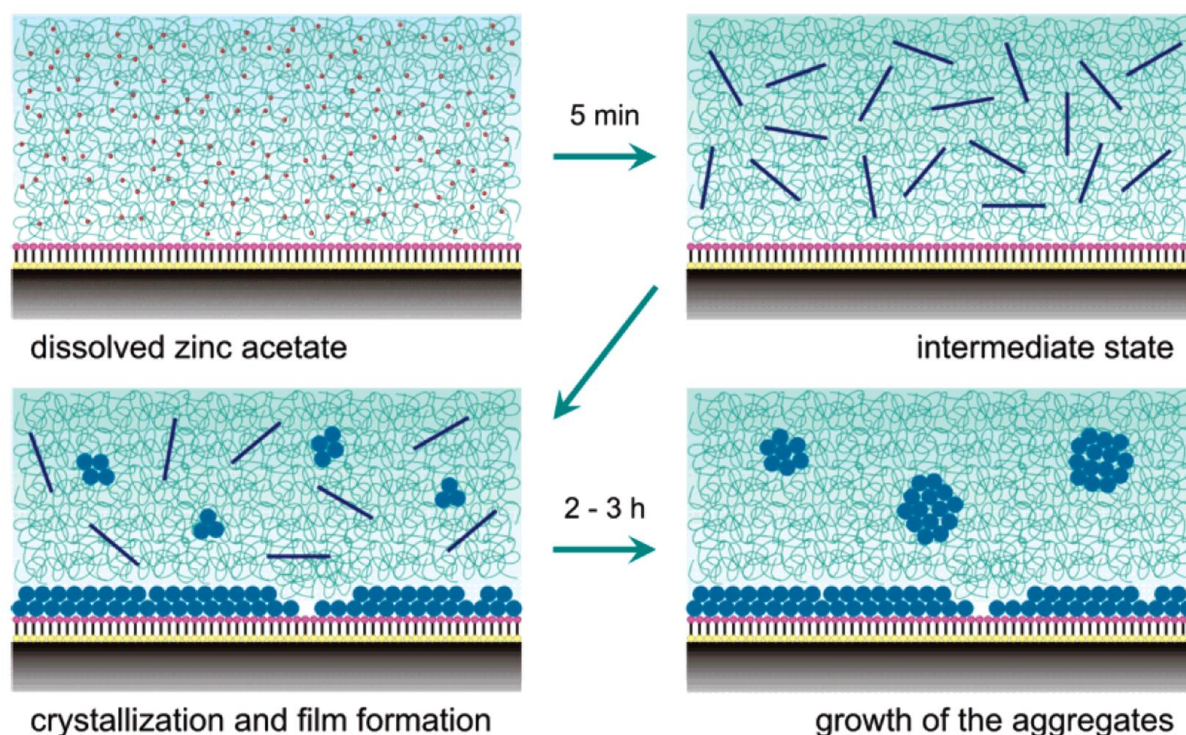


**Figure 2-1:** Schematic view taken from reference [26] of the processes in solution and at the substrate/template interface during ZnO film deposition as suggested by Lipowsky *et al.*. The formation and dissolution of the intermediate specular particles control the concentration of zinc species keeping the balance between deposition and precipitation in solution [26].

The intermediate stage is characterized by constant ZnO particle sizes in the range of 8 to 15 nm during mineralization depending on the molar ratio of  $[PVP] : [Zn^{2+}]$ . Whereas the final stage presents the long-term behavior with linear growth of the particles in solution by agglomeration processes [26].

The possibility to synthesize nanocrystalline ZnO under such mild reaction conditions allows its integration in bio-inspired material synthesis (cf. Section 2.3) approaches adapting principles from biomineralization (cf. Section 2.2) which are explained in detail in the indicated chapters.

### 2.1.2 STRUCTURE AND PROPERTIES

The thermodynamically stable modification of ZnO at ambient conditions is the hexagonal wurtzite structure (space group  $P6_3mc$ , lattice parameters:  $a = 3.2496 \text{ \AA}$  and  $c = 5.2042 \text{ \AA}$  [27]). The binding in ZnO is characterized by  $sp^3$  hybridization of the electron states. Thus, there are four equivalent orbitals directed in tetrahedral geometry. Each zinc ion has four neighboring oxygen ions in this tetrahedral configuration and vice versa (Figure 2-2 A). The distinct axis of ZnO ( $c$ -axis) follows one of the tetrahedral binding orbitals. According to the sign convention, the positive  $c$ -axis direction points from zinc to oxygen [5].

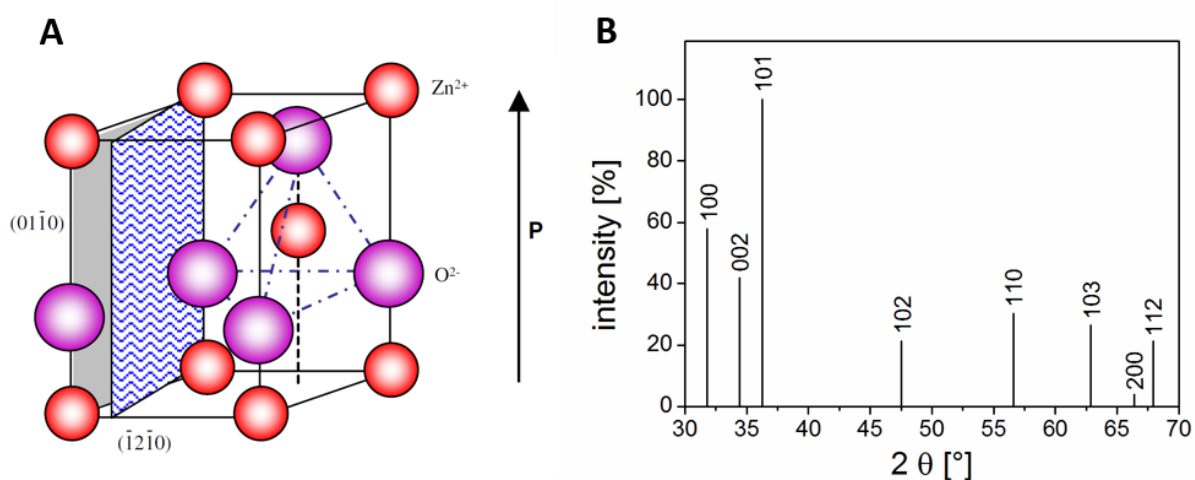


**Figure 2-2: A**, Model of the ZnO wurtzite structure taken from reference [16]. The tetrahedral coordination of the  $Zn^{2+}$  ion (red) with  $O^{2-}$  ions (purple) is indicated as well as the polar axis P. **B**, Stick pattern of the ZnO reflections with their relative intensities from powder diffractogram. Data for the plot was taken from the International Center for Diffraction Data (ICDD, 01-079-0206).

The structure consists of alternating planes of tetrahedrally coordinated  $O^{2-}$  and  $Zn^{2+}$  ions stacked along the  $c$ -axis leading to the polar  $\pm(0001)$  planes. The cohesive energy per bond is as high as 7.52 eV [28]. This leads to a very high thermal stability of ZnO with a melting point of 2242 K. Oxygen has a very high electronegativity (3.5), and zinc a considerably low one (0.91), leading to a bond polarity (cf. Figure 2-2 A) resulting in an effective bond charge  $Z^*$ . The electrostatic forces also cause a distortion of the tetrahedrons leading to a small deviation from the ideal wurtzite structure [29]. The relative intensities of the ZnO wurtzite reflections of a powder diffractogram are given in Figure 2-2 B in a stick pattern plotted from the International Center for Diffraction Data (ICDD, 01-079-0206). The three main reflections have usually the following relative intensities:  $I_{100}$  is 57,8%,  $I_{002}$  is 41,9%, and  $I_{101}$  is 100% (ICDD,

01-079-0206). If the relative intensities of the reflections of a XRD pattern of a thin film differ from these values, the film is textured and shows a preferential orientation.

### **2.1.2.1 ELECTRICAL PROPERTIES**

ZnO is a prominent II-VI compound semiconductor and has been investigated for more than 80 years [5]. At ambient conditions, ZnO has a large direct band gap of 3.37 eV which is in the same region as the one of GaN. This results in several advantages of the electric properties, such as higher breakdown voltages, toleration of larger electric fields and less electronic noise, as well as high-temperature and high-power applications [28].

Undoped ZnO is an intrinsic *n*-type semiconductor. There are two possible explanations for that which are (1) intrinsic defects (oxygen vacancies and interstitial zinc atoms) and (2) hydrogen, which is a donor in ZnO and always present during synthesis [5,28]. The electron density is as high as  $10^{21} \text{ cm}^{-3}$  [30]. The electron mobility of ZnO is temperature-dependent and exhibits a maximum of about  $2000 \text{ cm}^2 \text{ V}^{-1} \text{ s}^{-1}$  at 80 K [31].

Due to high electron mobility and sensitivity, transparency in the range of visible light, and low power consumption, ZnO-based field-effect transistors (FETs) are particularly interesting. Additionally, they have a high stability against water and oxygen and are not toxic. ZnO-based FETs can be synthesized at moderate reaction conditions by solution processing, e.g. via chemical bath deposition [32,33]. In general, each grain boundary is an obstacle for fast percolation pathways of electrons. Various additional parameters influence the performance of a FET device. Since only some tens of nanometers are available for the active space charge region in FETs, not only the thickness of the semiconducting layer [34], but also the interface roughness [35] strongly influence the FET properties.

There are various different FETs depending on both material combination and geometric setup, such as the metal-oxide semiconductor field-effect transistor (MOSFET) or the thin film field-effect transistor (TFT). In general, a FET is a three-terminal semiconductor device: gate (G), source (S) and drain (D). In this work, a unipolar FET with bottom-contact/bottom-gate geometry is used (Figure 2-3 A-C). The gate consists of a layer of highly *n*-doped silicon covered with a 90 nm thick dielectric layer of silicon dioxide. The gold electrodes (30 nm), drain and source, are attached by means of a 10 nm intermediate adhesive layer of indium tin

oxide (Figure 2-3 A). The electrodes possess an interdigital structure with a channel width of 10 nm and a channel length of 10  $\mu\text{m}$  (Figure 2-3 C).

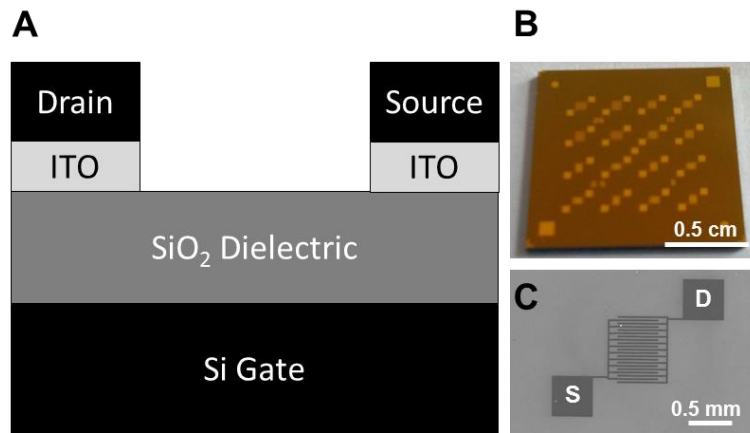


**Figure 2-3:** **A**, Schematic setup of a transistor with its three terminals gate (G), source (S) and drain (D). The gate is covered with a 90 nm thick dielectric layer (SiO<sub>2</sub>). The 30 nm thick gold electrodes, drain and source, are attached with a 10 nm intermediate adhesive layer of indium tin oxide (ITO). **B**, Image of a Fraunhofer substrate used in this work with 16 transistor units present. Always four units have the same channel length (e.g. four units with 10  $\mu\text{m}$ ). **C**, Zoom on a single transistor unit showing the interdigital structure including drain (D) and source (S).

The flow of charge carriers (either electrons or holes, drain current  $I_D$ ) in the FET is controlled by the voltage-induced (gate-source voltage  $V_{GS}$ ) creation – or variation – of a conductive channel between drain (D) and source (S). The gate-source voltage  $V_{GS}$  induces a charge accumulation in the semiconductor near the dielectric barrier layer (depletion layer). When this depletion layer reaches charge neutrality  $V_{GS}$  equals to the threshold voltage  $V_{Th}$ . Upon further increasing  $V_{GS}$  in combination with an applied voltage between drain and source (drain-source voltage  $V_{DS}$ ), the charge carriers move from drain to source parallel to the dielectric surface in the channel causing the drain current  $I_D$  (inversion layer).

The most important FET parameters that can be extracted from the output and transfer characteristics (cf. Figure 2-4) are the field-effect mobility  $\mu$ , the on/off ratio  $I_{on/off}$ , the threshold voltage  $V_{Th}$  and the hysteresis. The field-effect mobility  $\mu$  is a measure for the mobility of charge carriers in the semiconductor.

Since it is independent of the device geometry, it allows a comparison between FETs with different geometrical setups. The on/off ratio  $I_{on/off}$  is the ratio between the drain current in the operational 'ON' state (at maximum  $V_{GS}$ ) and the minimum drain current in the



nonoperational 'OFF' state. A high on/off ratio stands for a fast switching behavior between 'ON' (logic level '1') and 'OFF' (logic level '0') states.

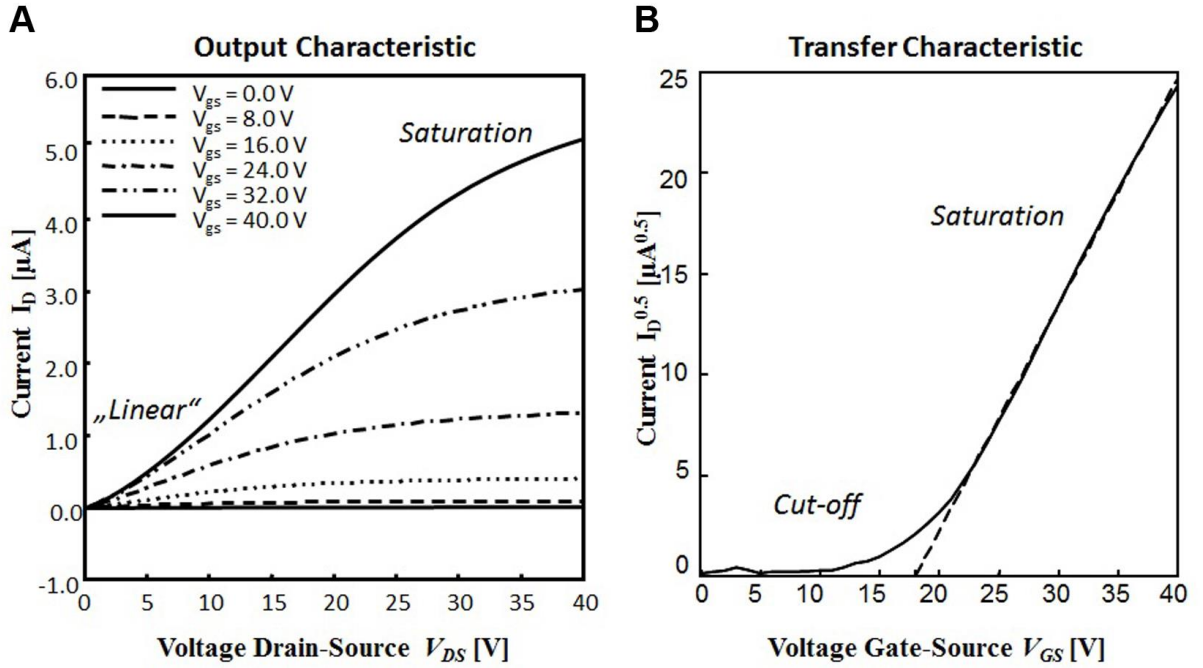


**Figure 2-4:** **A**, Output and **B**, transfer characteristics of a FET. **A**, Drain current  $I_D$  in dependency of the applied drain-source voltage  $V_{DS}$  for different gate-source voltages  $V_{GS}$ . The curves first show a linear regime until they reach the saturation drain current  $I_{D,sat}$ . **B**, Transfer characteristic by plotting the square root of the drain current  $I_D$  versus the gate-source voltage  $V_{GS}$  for a constant drain-source voltage  $V_{DS}$ . By linear fitting according to equation (2-2), the mobility  $\mu$  and the threshold voltage  $V_{Th}$  are determined from the slope and the intersection with the abscissa of the straight line. The channel is closed in the cut-off region ('OFF' state) and opened in the saturation region ('ON' state) [36].

The threshold voltage  $V_{Th}$  is the minimum gate-source voltage  $V_{GS}$  needed to create a conducting pathway between drain and source. The hysteresis is determined from the transfer characteristics and describes the difference between the drain current observed in forward and backward sweep.

Figure 2-4 shows exemplarily the output (Figure 2-4 A) and transfer (Figure 2-4 B) characteristics of a FET device for different applied  $V_{GS}$ . The output curves reveal two areas. The first area is the triode region in which  $I_D$  is approximately proportional to  $V_{GS}$ , which is described by equation (2-1).

$$I_D = \mu C_{ox} \frac{W}{L} [2(V_{GS} - V_{Th})V_{DS} - V_{DS}^2] \quad (2-1)$$

Equation (2-1) is valid for  $V_{DS} \ll V_{GS} - V_{Th}$ .  $W$  represents the channel width,  $L$  the channel length and  $\mu$  the mobility.  $C_{Ox}$  is the gate oxide capacitance per unit area and is determined by the dielectricity of the oxide  $\epsilon_{Ox}$  and its thickness  $t_{Ox}$  (cf. equation (2-3)).

The second area is the strong inversion in which the transistor should be used. It is characterized by equation (2-2), which is valid for  $V_{DS} > V_{GS} - V_{Th}$ .

$$I_{D,sat} = \mu C_{Ox} \frac{W (V_{GS} - V_{Th})^2}{L} \quad (2-2)$$

$$C_{Ox} = \epsilon_{Ox} t_{Ox} \quad (2-3)$$

The FET characteristics are obtained by fitting the measured data to equation (2-2). In such a way, the transfer characteristics, such as the mobility  $\mu$  and the threshold voltage  $V_{Th}$ , can be extracted. The on/off ratio  $I_{on/off}$  is the ratio of the drain current value at 0 V and the drain current at maximum voltage (30 V) [37].

### 2.1.2.2 PIEZOELECTRIC PROPERTIES

Piezoelectric materials have gained interest since they offer various applications as sensing, actuation or energy harvesting materials. Bond polarity, thus an intrinsic dipole moment, together with the non-centrosymmetric crystal structure leads to a pronounced piezoelectricity, i.e. an externally applied mechanical stress results in a polarization without external field and vice versa. The effect is distinctive in ZnO and the most pronounced one in all tetrahedrally coordinated semiconductors [5]. The piezoelectric tensor of ZnO has, due to its symmetry, three independent non-zero components  $e_{ij}$  (piezoelectric stress coefficients). They give the polarization components  $P_i$  as a result of the strain  $\epsilon_j$ . In Voigt notation the piezoelectric tensor  $E$  is then defined by the piezoelectric stress coefficients  $e_{33}$ ,  $e_{31}$  and  $e_{15}$  [5]:

$$E = \begin{pmatrix} 0 & 0 & 0 & 0 & e_{15} & 0 \\ 0 & 0 & 0 & e_{15} & 0 & 0 \\ e_{31} & e_{31} & e_{33} & 0 & 0 & 0 \end{pmatrix} \quad (2-4)$$

Two of the components ( $e_{33}$  and  $e_{31}$ ) represent the contribution of the polarization  $P_3$  in  $c$ -axis, and  $e_{15}$  describes the polarization  $P_1$  perpendicular to the  $c$ -axis by a shear strain  $\epsilon_5$ . The strain along the  $c$ -axis is described by  $\epsilon_3 = (c - c_0)/c_0$  and within one of the basal planes as  $e_{1,2} = (a - a_0)/a_0$ , respectively. Thus, the  $c$ -directed polarization  $P_3$  can be determined as:

$$P_3 = e_{33}\varepsilon_3 + e_{31}(\varepsilon_1 + \varepsilon_2) \quad (2-5)$$

The polarization  $P$  has two microscopic contributions that are superimposed [5]: (1)  $P^{(1)}$  caused by lattice deformation. This is the so-called ‘clamped-ion’ contribution. The parameter  $u$  is the ratio of bond length to  $c$ -axis ratio ( $c/a$ ). And (2), the additional contribution  $P^{(2)}$  which is attributed to internal relaxation, the so-called ‘internal-strain’ contribution. Not only the lattice constants  $a$  or  $c$  are changed by a strain  $\varepsilon$ , but there is also an internal displacement of the sublattices to each other, which results in a change of  $u$ . Since ZnO has a strong bond polarity, this internal displacement results in the additional polarization term  $P^{(2)}$ , which scales with the aforementioned effective bond charge  $Z^*$ . For most tetrahedrally coordinated compound semiconductors, the absolute values of  $P^{(1)}$  and  $P^{(2)}$  are equal and have opposite signs. Thus, those II-VI compounds have a very low piezoelectric effect [5]. However, calculations by Dal Corso *et al.* showed that in the case of ZnO the  $P^{(1)}$  contribution is very low. Thus, the internal strain-contribution  $P^{(2)}$  is less compensated by  $P^{(1)}$ . Therefore, ZnO has a very pronounced piezoelectric effect [38]. Instead of using the piezoelectric stress coefficients  $e_{ij}$ , the piezoelectric behavior can be described by the piezoelectric strain coefficients  $d_{ij}$  which are connected to  $e_{ij}$  through the elastic moduli. The piezoelectric strain coefficients describe the polarization in dependence of the externally applied stress  $d_{ij} = dP_i/dX_j$  [ $\text{C N}^{-1}$ ] ( $= [\text{mV}^{-1}]$ ) instead of the correlation of the polarization with the relative changes in the lattice constants, as in the case of  $e_{ij} = dP_j/d\varepsilon_j$  [ $\text{C m}^{-2}$ ] [5]. The piezoelectric strain coefficients of ZnO are  $d_{33} \approx 12 \times 10^{-12} \text{ C N}^{-1} \approx 12 \text{ pm V}^{-1}$ ,  $d_{31} \approx -5 \text{ pm V}^{-1}$  and  $d_{15} \approx -10 \text{ pm V}^{-1}$  [5,29].

### 2.1.2.3 PHOTOLUMINESCENCE

ZnO exhibits not only excellent luminescent properties, but also shows a number of intrinsic and extrinsic radiative defect levels, which emit light in a wide range within the visible region from violet over blue to red [39]. Thus, the room temperature photoluminescence spectrum of ZnO has an additional broad deep band emission ranging from 400 to 600 nm to the near band edge sharp UV peak around 370 nm. The broad emission band is usually attributed to intrinsic and/or extrinsic defects, such as oxygen vacancies at the surface which usually vanish upon annealing [40–42]. However, the near band edge emission is dependent on the crystallite size for nanocrystalline ZnO. Brus *et al.* [43] provide an analytical approximation for

the first excited electron state with which the crystallite size can be determined from the measured UV emission  $E^*$ :

$$E^* = E_g + \frac{h^2}{8R^2} \left( \frac{1}{m_e} + \frac{1}{m_h} \right) - \frac{1.8e^2}{\epsilon R} + \text{smaller terms} \quad (2-6)$$

where  $E_g$  is the band gap for bulk ZnO (3.377 eV),  $h$  is Planck's constant,  $R$  is the radius of the ZnO nanocrystallites. The effective electron mass  $m_e$  is given as  $0.24m_0$ , and the effective hole mass  $m_h$  is given as  $0.45m_0$ . The dielectric constant  $\epsilon$  of ZnO is 3.7 and the smaller terms can be neglected [43].

#### 2.1.2.4 MECHANICAL PROPERTIES

The mechanical properties highly depend on the synthesis methods and microstructure of the obtained ZnO. Micro and nanoindentation have been widely used to characterize the hardness  $H$  and Young's modulus  $E$  of ZnO. Bulk single crystalline ZnO shows hardness values of  $5.0 \pm 0.1$  GPa and a Young's modulus of  $111.2 \pm 4.7$  GPa [44]. However, it is important to note that these values depend on the crystal surface that is measured on. Coleman *et al.* report values for bulk crystals in  $a$ -axis direction of  $H_a = 2 \pm 0.2$  GPa and  $E_a = 163 \pm 6$  GPa, whereas in  $c$ -axis direction values of  $H_c = 4.8 \pm 0.2$  GPa and  $E_c = 143 \pm 6$  GPa are observed, which is attributed to the slipping process along the basal planes [45]. This behavior was found to be different for epitaxially grown thin  $a$ - and  $c$ -axis oriented ZnO films on sapphire. Here, the slipping process along the basal planes was hindered by dislocations created in the epilayer during the epitaxial growth conditions leading to increased values of hardness for the epitaxial films of  $H_{a,epitaxial} = 6.6 \pm 1.2$  GPa and  $H_{c,epitaxial} = 5.8 \pm 0.8$  GPa [45]. The increased hardness of the bulk crystals of a factor 2 in  $c$ -axis direction was confirmed by Basu and Barsoum [46]. For polycrystalline films values for hardness ranging from 1.5 to 12 GPa and Young's moduli from 40 to 120 GPa can be found [28], which highlights the strong dependency of the mechanical properties on both synthesis and microstructure.

## 2.2 BIOMINERALIZATION

Roughly 540 million years ago, many mostly multicellular organisms started to develop the ability to produce mineralized skeletal structures by making use of biomineralization processes. Nowadays, more than sixty minerals produced by living nature are known. Corals, algae, mollusk shells, and diatoms are organisms producing biominerals. Biominerals are compounds, which are made of an organic phase (often biomacromolecules, such as proteins) and an inorganic phase, such as calcium, magnesium, silicon, and iron oxides or carbonates. Most of them are calcium-based minerals due to its presence in the oceans and its importance in cells as a messenger [47]. The mineralization process is genetically determined and leads to complex-shaped minerals tailored to very specific functions, such as structural support (bones and shells), mechanical strength (teeth) and e.g. magnetic reception for navigation purposes, as in the case of magnetotactic bacteria [48].

Biomineralization processes are very complex, not fully understood and both amorphous and crystalline inorganic phases can occur. However, in all cases, more or less complex biomacromolecules initiate and/or direct the formation of inorganic material via specific interactions. This can, on the one hand, be a vesicle, which is an aqueous compartment surrounded by an impermeable lipid membrane. Within this compartment ion accumulation is realized via ion-pumps. On the other hand, protein or polysaccharide cages may also serve as accumulation places for ions, which lead to nucleation and growth of the biomineral. Such containers can then be inside the cell (ferritin) or outside (collagen) [48]. The extraordinary properties of such biominerals are a result of the sophisticated hierarchical structure of the organic and inorganic phase. Since the minerals are in general very stiff and brittle and the organic counterparts are tough but less stiff, the simple combination of both cannot lead to the superior toughness with reasonable stiffness that is realized in biominerals, e.g. in nacre or bone [49].

### 2.2.1 NACRE

Nacre is the iridescent layer coating the inner part of many mollusk shells. The iridescent effect is caused by interference patterns occurring when light passes through the multilayer structure. Nacre is a nanocomposite of 95 wt% of aragonite platelets and 5 wt% of thin intermediate biopolymer layers (Figure 2-5 A). The shell layer is formed by mantle cells that

first build up an extracellular organic matrix framework parallel to the shell surface. The organic phase consists of  $\beta$ -chitin-protein complex which is terminated on its surface by acidic macromolecules rich in aspartic acid. The inorganic phase nucleates at distinct places with calcium binding properties.

Crystals then preferentially grow in *c*-axis direction until they hit the next matrix layer. Since the preferential growth is limited in the confined space formed by the organic matrix, the crystals grow in *a*- and *b*-direction forming the aragonite platelets resulting in a 'brick and mortar' structure (Figure 2-5 A, inset) [47,52].

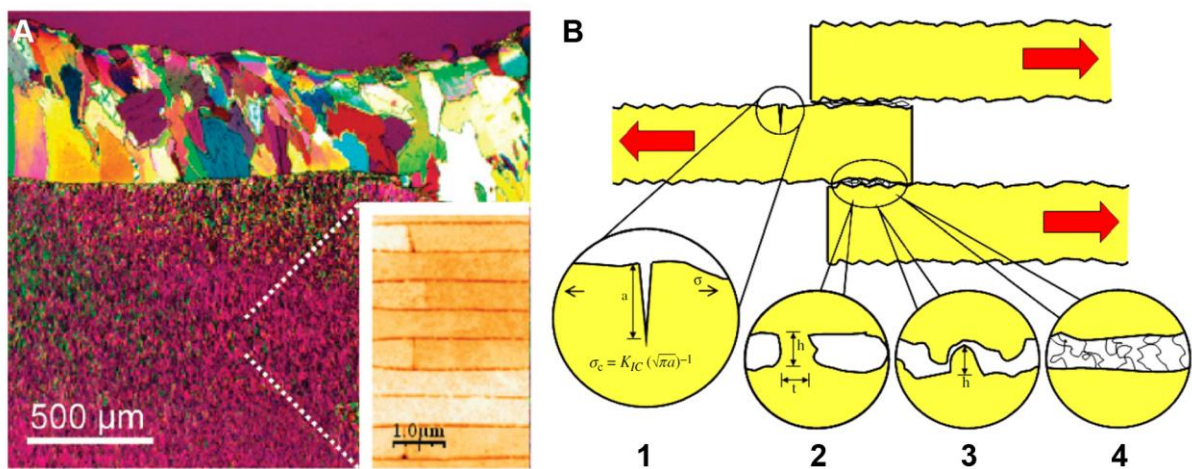


**Figure 2-5: A**, Polarized light microscope image of a cross-sectional sample of Red Abalone shell. The mosaic-like area in the upper part is a calcite layer and the bottom is the nacreous layer. The inset shows an AFM image acquired in the nacreous layer revealing the 'brick and mortar' structure of the aragonite platelets (thickness 400 – 500 nm) and the organic phase (thickness 40 – 50 nm). Image is taken from reference [50]. **B**, Scheme of four different failure mechanisms in nacre upon tensile stress along the tiles. (1) tensile fracture of the tile due to its small dimensions, (2) shear fracture of the mineral bridges between the platelets, (3) friction due to nanoasperities on the platelets, and (4) stretching of the organic chains between the platelets. Image is taken from reference [51].

The  $\mu\text{m}$ -sized platelets themselves consist of nanocrystallites in the range of 30 – 80 nm, stacked along the same crystallographic direction which provides high adhesion. On top of the platelets there are assemblies of nanoasperities. Within the organic matrix holes allowing the formation of mineral bridges between the platelets can be found. Both nanoasperities and mineral bridges are important for the outstanding mechanical properties of nacre (Figure 2-5 B). Each of the features in the architecture contributes to the toughening of the material, which has not only a doubled strength due to its layered structure [53], but also an

octuplicated fracture toughness compared to monolithic  $\text{CaCO}_3$  [54]. The layered structure leads to a modulation of the Young's modulus and forces a crack to take a convoluted path leading to energy dissipation. Furthermore, the platelets can slip which redistributes stress. The nanoparticles within the platelets rotate and deform upon external stress resulting in further energy dissipation. The toughening mechanism occurring due to the hierarchical structure can be summarized to crack blunting/branching, microcrack formation, plate pull-out, crack bridging, platelet sliding, stretching of the protein fibrils, protein fibrils causing crack bridging, as well as weakened stress concentration, stress redistribution, and strain hardening [52]. All these effects act in a synergetic way; however, the individual importance is not yet clarified [52,54].

The outstanding mechanical properties of nacre have led to great interest in mimicking its structure for the synthesis of novel nanocomposite materials. By combining polymers and clay platelets, the strength of nacre was combined with elastic moduli in the range of bone [55–57]. However, in these films the content of the organic component was larger, thus resembling nacre's structure even less. Several nacre-like structures were obtained with calcium carbonate [58–60], silicates [61] and inorganic oxides, such as  $\text{TiO}_2$  [50,62],  $\text{ZnO}$  [63,64],  $\text{Al}_2\text{O}_3$  [65],  $\text{ZrO}_2$  [66],  $\text{V}_2\text{O}_5$  [67], and magnetite [68].

### **2.2.2 BONE**

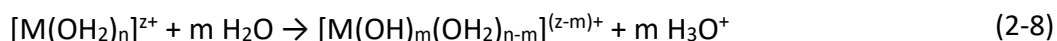
Bone is also a biomineral with a hierarchical microstructure and outstanding properties. The basic building blocks are collagen fibrils reinforced with mineralized particles of carbonated hydroxyapatite. Depending on the assembly of mineralized collagen fibrils, various structures can occur allowing the adaption of different bones to their mechanical functions. The bone forming cells, so-called osteoblasts, deposit the organic matrix of collagen units in bone packets, where the mineral precipitates. Bone material is constantly remodeled in the body by resorption of bone material by osteoclasts followed by deposition of new bone material formed by osteoblasts. A third cell type is also involved in this complex process of bone formation. Osteocytes are believed to serve as strain sensors [49]. Already in the late 19<sup>th</sup> century, Julius Wolff proposed that bone is deposited and reinforced in areas of greatest stress ('Wolff's Law'). Ever since the discovery of collagen's piezoelectricity in the 1960s, it has been proposed as a potential mechanism for osteoblasts to detect such areas of greater stress [69–72]. However, the mechanisms are more complex, since streaming potential and fluid-

generated shear stress contribute as well. Nonetheless, experiments with isolated collagen fibers in the absence of any cells such as osteoblasts, revealed that the charges occurring upon the bending of collagen fibers, due to their piezoelectric properties, induced preferential mineralization of hydroxyapatite [72,73]. This strongly hints that piezoelectric properties of templates have a huge impact on preferred mineralization of material which could be adapted to the formation of other materials besides hydroxyapatite.

## 2.3 BIO-INSPIRED SYNTHESIS

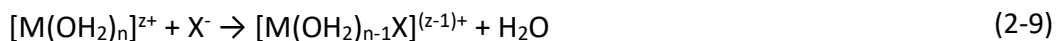
As already mentioned above in the context of nacre and bone formation, there is great interest in transferring and adapting the principles of biomineralization to the synthesis of functional materials, such as oxides, sulfides or other ceramics, at ambient conditions that are usually produced under harsh reaction conditions. In this so-called ‘bio-inspired’ approach two main characteristics are found: (1) precursors for the ceramic are dissolved in an aqueous or alcoholic solution, and, (2) functionalized surfaces act as templates promoting the nucleation and crystallization at the template/solution interface. The mild reaction conditions of the aforementioned CBD processes (cf. Section 2.1.1) allow the integration of such organic templates in the bio-inspired synthesis of functional materials.

Such solution-based synthesis of oxides involves the hydrolysis of metal ions and subsequent condensation of the hydroxylated complexes. Jolivet *et al.* divide the formation of colloidal particles up into the following steps [74]: Formation of a zero-charge precursor  $[M(OH)_z(OH_2)_{N-z}]^0$ ; nucleation; growth of nuclei and aging of the particles. Initially, the metal ion  $M^{z+}$  is hydrated by a hydration sphere of water molecules around the central metal ion, which is shown in equation (2-7). This is followed by the formation of the zero-charge precursor by deprotonation of the solvated metal ions.

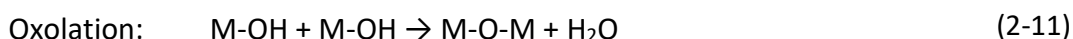
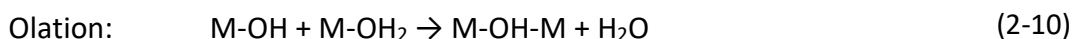


Reaction (2-8) depends on the solution’s acidity. Additionally, the complexation with the anionic species ( $X^-$ ) controls the precipitation from solution, as given in (2-9).





The hydrolyzed metal ions condensate further, first to nuclei, and then grow by both olation and oxolation. Olation describes the formation of a hydroxo bridge (2-10), and oxolation the formation of an oxo bridge (2-11).



During the last step, the aging of the solution, processes like Ostwald ripening and agglomeration, occur.

In general, there are two possible mechanisms for nucleation. Nucleation can be either homogeneous, i.e. nuclei form in solution due to the previously described hydrolysis and condensation and are subsequently attached to the functionalized surface. The other possibility is a heterogeneous nucleation, which is an ion-by-ion mechanism, i.e. the metal hydroxide complex present in solution adsorbs to the functional surface, and by splitting off of water molecules the metal oxide remains. It is often difficult to say that one of the two mechanisms occurs exclusively. Also, a mixed mechanism of both heterogeneous and homogeneous nucleation taking place at the same time is possible.

Various templates have been exploited for bio-inspired mineralization processes, such as organic systems, surfaces functionalized with Langmuir-Blodgett films, liquid crystals, polyelectrolytes, and self-assembled monolayers (SAM). The latter are mostly siloxane-terminated carbon chains with a functional head group. Activation of silicon substrates leaves behind a layer of hydroxylated amorphous silicon dioxide. In such a way, reactive sites for anchoring of the SAM's trichlorosilyl groups are given. Cross-linking of the trichlorosilyl groups and van der Waals interactions between the carbon chains lead to the formation of functional monolayers.

Various functional head groups, such as  $-NH_2$ ,  $-COOH$ ,  $-OH$ ,  $-CN$ ,  $-CH_3$ ,  $-Br$ ,  $-SH$ ,  $-SO_3H$ , are either directly accessible or the terminal group can be in-situ changed. Furthermore, SAMs offer the possibility to easily pattern the functionalized surface, e.g. by soft-patterning via PDMS stamps or photolithography with a mask [75].

Additionally, biomolecules are of great interest as templates, since they are of identical size, (complex) shape, and chemical groups. Various biomolecules have been employed in the bio-inspired synthesis of, e.g., ZnO, such as amino acids [24], peptides [24], proteins [76,77], and DNA [78].

## 2.4 TOBACCO MOSAIC VIRUS

The tobacco mosaic virus (TMV) was discovered at the end of the 19<sup>th</sup> century. Mayer [79] and Beijerinck [80] found that the infection of tobacco plants with mosaic structures on the leaves was caused by a non-bacterial pathogen resulting in the discovery of the first virus and establishing virology as an essential topic in biology. TMV is a plant virus infecting not only tobacco plants, but also plants belonging to the same family resulting in (1) yellowish mosaic patterns on the leaves and (2) hindered growth of the leaves [81]. However, it is not harmful for mammals and can easily be handled under laboratory conditions.

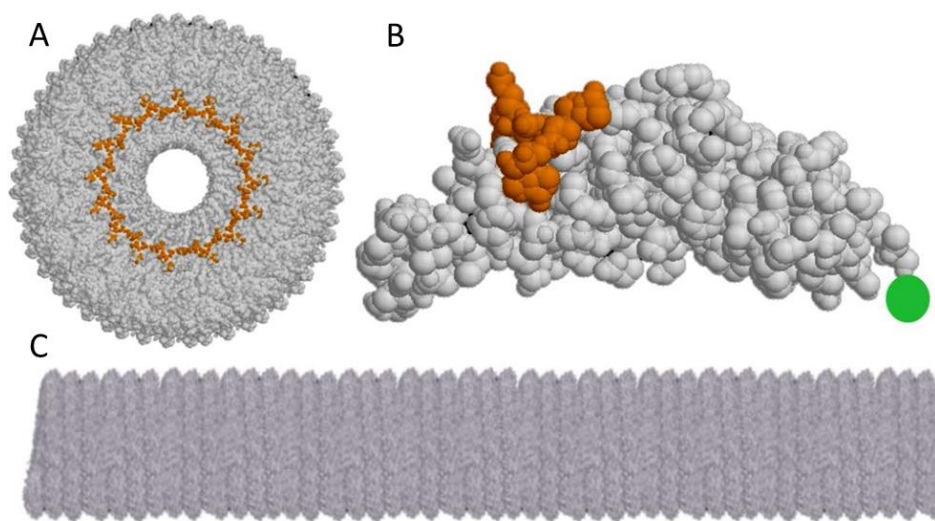


**Figure 2-6:** Models taken with MDL Chime from protein database (pdb) files of TMV (vulgare strain). **A**, Front view of the virus particle's cross-section with the inner channel of 4 nm. The embedded RNA is indicated by the orange-colored part. On single turn consists of  $16\frac{1}{2}$  coat proteins. **B**, single coat protein with the position of the RNA indicated in orange. The green circle marks the last four amino acids which are missing in the pdb file. **C**, modelled structure of part of TMV with ca. 45 loops (complete structure consists of 131 loops). Image taken from reference [85].

TMV is a rigid helical rod-like virus particle with a length of 300 nm and a diameter of 18 nm with an inner channel of 4 nm [82]. The most important structural discoveries were not

possible until the successful purification of TMV, for which Wendell Stanley was awarded the Nobel Prize in Chemistry in 1946. First structural analyses were performed by X-Ray diffraction [83]. Ever since then more detailed knowledge has been gained by advanced microscopy techniques. The RNA of TMV (vulgare strain) consists of 6,395 nucleotides. This results, in combination with the identical copies of 2,132 coat proteins, in 131 turns and  $16\frac{1}{2}$  proteins per turn, with a pitch of 2.3 nm per turn [84], which leads to a  $49_3$  screw axis. Each coat protein represents a sequence of 158 amino acids (Figure 2-6 B). 17 coat proteins form a disc and more than 50 discs assemble with the single stranded RNA to the rod-like virus particle [82] (Figure 2-6 A, C).

Amino acids on the outer surface of the TMV particle play an important role for the surface charges and surface functionalities which are of great interest for e.g. mineralization. Not all amino acids present in the coat protein are accessible, since many are deep inside the structure (e.g. lysine). The distribution of amino acids within each coat protein leads to an internal dipole moment within the coat protein and thus, the TMV structure.

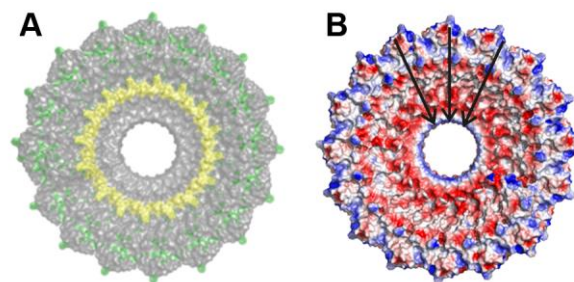


**Figure 2-7:** Models of TMV discs created by PyMol [86]. **A**, shows the coat protein structure and also the incorporated RNA (yellow). Aromatic amino acids are indicated in green **B**, calculated electrostatic potential (in vacuum and without the charges introduced by the RNA). Red areas indicate negative charges and blue areas indicate positive charges. The black arrows indicate the dipole moment of single coat proteins within the TMV structure. Obtained from pdb structure 3J06 manipulated with PyMol, the PyMOL Molecular Graphics System, Version 1.7.4 Schrödinger, LLC.

In Figure 2-7, the model of a TMV disc with incorporated RNA and a disc showing the electrostatic potential as it is calculated by PyMol are shown for one turn of the helix. The 17 individual coat protein dipoles form such a disc. The arrangement of the amino acids leads to a more positive electrostatic potential of the outer surface. Towards the center more negative charges are present. The PyMol software cannot calculate the potential with the strongly negatively charged RNA. In Figure 2-7 A, the TMV disc is shown with the RNA indicated in

yellow. Thus, the insertion of the very negative RNA will strongly increase the number of negative charges in the center and enhance the dipole moment pointing from the positive outer surface to the negative inner channel. In Figure 2-7 B, the intrinsic coat protein dipoles are indicated as arrows.

Only such amino acids present on the virus' outer surface contribute to electrostatic charges in solution e.g. arginine. The isoelectric point (IEP) of TMV particles (RNA + coat protein), where the net surface charge is zero, is around 3.5 [87,88]. The IEP of the pure coat protein (no RNA) is shifted to higher pH values due to the lack of negative charge contribution given by RNA [89]. Below the IEP, the net charge of the surface is positive. Above the IEP, the net surface charge is negative. The positive charges present on the outer surface are compensated by strong charge contribution of the RNA leading to the negative net charge. The surface charge in solution is called zeta potential ( $\zeta$ ) and strongly dependent on the ionic strength. In such a way, pronounced differences of the zeta potential  $\zeta$  were reported at constant pH 7.8 but varying ionic strength. High ionic strength reduces the zeta potential to zero [90,91], whereas values of -80 mV are obtained for a low ionic strength of  $10^{-6}$  [91]. Positive values of the zeta potential are possible at least down to pH 2.5 before degradation of TMV sets in [92].

Plant viruses like TMV have gained importance not only due to high control over monodispersity and surface chemistry, but also due to their chemical and thermal stability and access to multiple genetically engineered mutants. All this makes them versatile scaffolds. The enormous stability is owed to the aforementioned complex structure of TMV. The virus retains its infectivity for more than 50 years. Infected plant leaves can be frozen or freeze-dried [88] and the viruses within preserve infectivity. The virus particles can withstand temperature ranges from 4°C (long time storage) and heating up to 60°C. Over short time ranges of about 10 minutes, the virus is stable even at temperatures as high as 90°C [88]. At even higher temperatures, the virus protein structure is destroyed by denaturation.

TMV particles are stable in a broad pH range from slightly below 3 up to 9 [92] and surprisingly stable in polar solvents, such as ethanol, methanol and acetone. An overview of its stability in several solvents and buffers is provided by Alonso *et al.* [93]. The high chemical and thermal stability is only given for the intact virus structure. Experiments on the temperature stability of the pure coat protein reveal denaturation at temperatures as moderate as 35°C in buffer [94], highlighting the stability of TMV particles.

When TMV is implemented as a template in mineralization experiments or for the formation of functional virus-based thin films, the virus particles need to be immobilized on substrates. Oxidized silicon substrates are hydrophilic due to the formation of hydroxyl groups. TMV strongly interacts with the oxidized silicon via hydrogen bonds. The adhesion is so strong that the cross-section of the virus structure is deformed significantly. AFM investigations of Knez *et al.* and Lee *et al.* both confirmed a height decrease of TMV on silicon compared to hardly any height change when TMV was immobilized on weakly interacting substrates like graphite [95] or polystyrene films [96]. Since changes in width are not accessible via AFM due to a convolution of the measured signal with the tip shape and samples prepared on TEM grids show not the same interactions as a silicon wafer, Knez *et al.* could not demonstrate the width change due to deformation. However, by combining small-angle X-ray scattering and grazing incident small-angle X-ray scattering and fitting the data to a cylinder model, Lee *et al.* were able to determine the height/width aspect ratio of TMV on silicon to 0.57, which even indicates a collapsing of the inner cavity [96].

Even though it was expected that the sequencing of TMV's protein structure seemed to be challenging due to its high large molecular weight, the finding that it consisted of a large number of identical coat proteins accelerated the discovery [97]. The complete sequence of the 158 amino acids of the coat protein was the largest protein sequenced to that point and the third sequenced in total as early as 1960 [98]. The detailed knowledge and the outstanding stability make chemical modifications of the TMV surface, such as click chemistry [99], possible. Additionally, various genetic modifications are accessible by exchanging amino acids of the coat protein. Thus, the surface chemistry of the virus particle is changed and distinct functionalities can be introduced depending on the desired application, e.g. antigen presentation [100,101], metallization [102,103] or chemical coupling [104,105]. In such a way, cysteine (TMV-Cys) or lysine (TMV-Lys) groups, for example, are present on the virus's outer surface [104]. A different assembly approach was followed in order to incorporate histidine into the wildtype (wtTMV). In a mixed assembly, *in vitro*, coat protein with a hexahistidine tag and wtTMV coat protein were assembled to 30%TMV-His<sub>6</sub> mutant [106]. To investigate the processes of assembling and disassembling, the coat proteins in the wtTMV particle, the E50Q mutant was designed [107]. It assembles in very stable protein nanotubes without RNA. Thus, it is also not restricted in length and could be used for preparation of metal nanowires with lengths of more than 1  $\mu\text{m}$  [108].

These outstanding thermal and chemical properties of TMV and, additionally, the possible genetic engineering make TMV a versatile tool in nanotechnology as a nanoscale platform for various organic and inorganic structures. Deposition of those materials on the TMV scaffold is based on the chemical functionalities provided by the amino acids of the coat protein. Either electrostatic interactions or complex formation are the driving forces. Various materials have been produced via TMV-based material synthesis. It was shown that, e.g., CdS, PbS, and SiO<sub>2</sub> could successfully be deposited onto TMV [109]. Metal/virus hybrid materials have been synthesized by reduction of manifold metal ions such as Pd<sup>2+</sup>, Ag<sup>+</sup> and Au<sup>3+</sup> on the virus outer surface [110]. Zhou *et al.* deposited Au nanostructures site-selectively in the inner channel of TMV [111]. Knez *et al.* synthesized Ni, Co [112] and Cu [113] nanowires on the inner channel, but also on the outer surface [114] by adjusting the experimental conditions. Such metal coated TMV have possible applications in, for example, lithium ion batteries [115] and anode materials in methanol fuel cells [116]. Moreover, TMV has recently been used as a scaffold for metal-organic frameworks [117].

Different approaches have been taken to deposit semiconducting metal oxide clusters, such as ZnO, onto TMV. Processes like atomic layer deposition [118], electroless deposition [119], and chemical bath deposition [120] were applied to produce nanocrystalline ZnO/TMV hybrid materials. Atanasova *et al.* successfully implemented the wtTMV/ZnO hybrid in field-effect transistors (FETs). It was shown that those FETs only worked with the hybrid material (TMV + ZnO) and showed a low threshold voltage  $V_{Th}$ , high field-effect mobility  $\mu$  and, on/off ratio  $I_{on/off}$ .

In addition to its outstanding thermal and chemical stability, TMV itself shows piezoelectric properties. Electromechanical coupling often occurs in biopolymers due to their strong correlation with, e.g., polar bonds and optical activity [121]. The piezoelectric effect is the linear coupling between an electric field and strain. However, especially in nanoscale systems, such as TMV, the flexoelectric effect contributes, which is the linear coupling of the electric field and the *gradient of strain* [122]. Kalinin *et al.* investigated the electromechanical activity of TMV immobilized on mica with piezoresponse force microscopy [123]. They suggested two intrinsic mechanisms for the electromechanical response. Firstly, the inhomogeneous field beneath the tip can result in a piezoelectric response due to incomplete compensation. This could happen in a case of intrinsic piezoelectric properties of the proteins and also due to

surface piezoelectricity caused by negative charges on the outside and positive charges on the inside. The second possibility they state is flexoelectric coupling. Thus, a dipole moment proportional to the local curvature is induced by mechanical deformation of the protein shell. By fitting their data to both models, they found the flexoelectric contribution to be dominant in the case of TMV [123]. However, they did not take the mechanical deformation of TMV upon immobilization on strongly hydrophilic substrates, such as silicon and mica, into account. The mechanical deformation of the structure surely influences the measurement of the piezoelectric constant. Effects of 'substrate clamping' are described for thin piezoelectric films, reducing the measured piezoelectric constant due to mechanical deformation of the film on the substrate [124,125].

Genetically engineered M13 phages were already successfully integrated in a piezoelectric generator [126]. M13 phages have a similar structure as wtTMV. The coat proteins are arranged helically with a five-fold rotational axis and a two-fold screw symmetry, whereas wtTMV has a  $49_3$  screw axis. The intrinsic dipole moment is in the case of wtTMV caused by the arrangement of amino acids within the coat proteins. Lee *et al.* enhanced the intrinsic dipole moment by fusing negatively charged amino acids to the coat protein. In such a way, the piezoelectric response was enhanced. However, the piezoelectric behavior of such complex biomolecules cannot be explained with classic piezoelectric theories. Effects are more complex and could include space-dependent piezoelectric matrices and stress-gradient induced polarization. Thus, the origin of the piezoelectric effects remains unknown and the description is phenomenological up to now [126].

## **2.5 SELF-ASSEMBLY OF VIRAL PARTICLES**

Self-assembled nanostructures have gained in interest due to remarkable collective properties with potential applications in the field of nanoelectronics and sensing, for example. Additionally, homogeneous, dense, and especially monolayers with reproducible quality are a prerequisite for mineralization of thin functional films.

Natural bionanoparticles, such as TMV, have several advantages compared to synthetically produced nanoparticles. Synthetically produced nanoparticles lack both control over size and shape, but these two conditions determine the physical properties of nanoobjects. TMV and other bionanoparticles show monodispersity and controlled surface charge chemistry, since

the entire structure is coded in its RNA. Additionally, the surface chemistry can be genetically engineered by a controlled exchange or addition of amino acids in the coat protein without losing the ability to form stable particles.

There are several possibilities to self-assemble viruses in ordered structures from 1D to 3D. The already very high aspect ratio of TMV can be further increased by head-to-tail association of several particles to nanowires. It is known that such head-to-tail assemblies are formed in solution and favored in acidic conditions at pH below 4, since interface repulsions at the virus ends are reduced [127,128]. However, those structures disassemble easily. One way of maintaining such head-to-tail connections in a broad pH range is simultaneous polymerization with polyaniline and thus stabilizing the connection [129].

Different strategies are used to produce 2D assemblies. An easy method is the so-called 'Pickering Emulsion', where the assembly takes place at a liquid/liquid interface [130]. Densely packed, ordered TMV assemblies were investigated at water/oil interfaces [91]. The in-plane packing depends on the TMV concentration and the ionic strength of the water solution, since ions present in the solution shield TMV's surface charge. Ordering occurred parallel to the oil/water interface at low concentrations, and for high concentrations the orientation was perpendicular to the interface. The main disadvantage of such ordered self-assembled virus films is that the transfer of such films to a solid substrate is complicated.

Therefore, an easier way to obtain 2D oriented virus monolayers is to directly assemble them on a flat solid substrate, e.g. silicon or mica. Oxidized silicon substrates are known to strongly interact electrostatically with the charged virus particles [95,96]. Drop-and-Dry method, dip [131] and spin [132] coating are well established and studied methods to produce thin films of bionanoparticles. Apart from the surface interaction, other factors, such as concentration, ionic strength, pH value of solution, and substrate wettability govern film formation [133].

To achieve increased ordering for asymmetric particles, such as TMV, convective assembly (CA) and confined drying assembly lead to better results, since they further control the evaporation process. Convective assembly, in particular, has the advantage that only microliters of a colloidal solution are necessary to cover square centimeters of the substrate [134,135]. The method was first introduced by Denkov *et al.* [136,137]. They analyzed the dynamics of the 2D ordering of  $\mu\text{m}$ -sized polystyrene latex spheres. The main forces governing the ordering are attractive capillary forces due to the formed meniscus between particles



(nucleus formation) and the convective transport of particles towards the ordered region and evaporation front (crystal growth). Ordering of the film, and thus nucleus formation, start when the thickness of the spread film reaches roughly the size of the suspended particles [136,137].

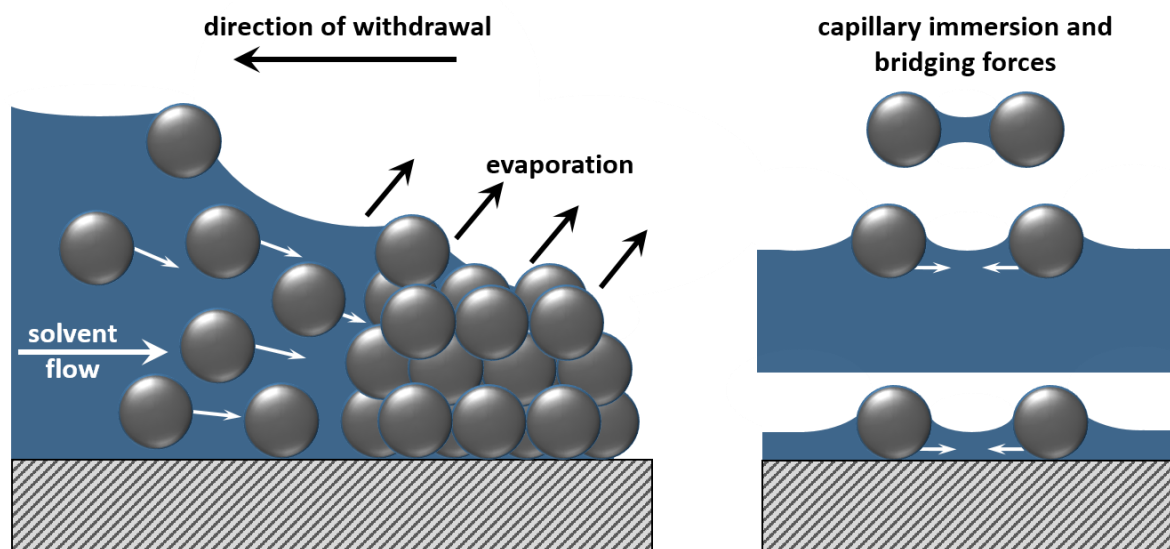


**Figure 2-8:** Combined phenomena involved with convective assembly and deposition during evaporation. Evaporation of the solvent causes liquid convection. Small menisci form between the particles. The solvent flowing towards these regions transports more particles towards the 2D particle crystal which leads to crystal growth. Image was adapted from reference [133].

The main driving force is the liquid convection which is directly caused by the evaporation of solvent (Figure 2-8 left). Between the particles, small, strongly curved menisci are formed leading to a capillary pressure drop (Figure 2-8 right). Thus, solvent from the surrounding areas flows towards these regions transporting more suspended particles to the surrounding region of the 2D particle crystal. This leads to a growth of the array of particles [133].

Prevo *et al.* further developed the method [138]. They dragged a very small volume (a few microliters) of the colloidal solution confined in a meniscus between two plates (cf. Figure 2-9). A triple contact line is formed between substrate, air, and solution. The particles flow through the liquid to this contact line, depending on particle-particle and particle-substrate interactions.

The evaporation of the solvent at the triple contact line drives the convection rate of the particles. Densification of the formed layer is generated by capillary forces between the

colloidal particles causing an additional in-plane shear on the assembly. Most work was performed on spherical particles, however, some work has been done on anisotropic particles, such as carbon nanotubes [139,140], and gold nanorods [141].

TMV was the first virus nanoparticle to be studied with convective assembly. Kuncicky *et al.* achieved hierarchically ordered arrays of virus bundles [134]. Contrary to experiments on spherical particles, the main influencing factors were the substrate wettability and the meniscus withdrawal speed instead of the evaporation rate. Both substrate wettability and meniscus withdrawal speed result in a dewetting at the triple contact line and a shear-induced alignment.

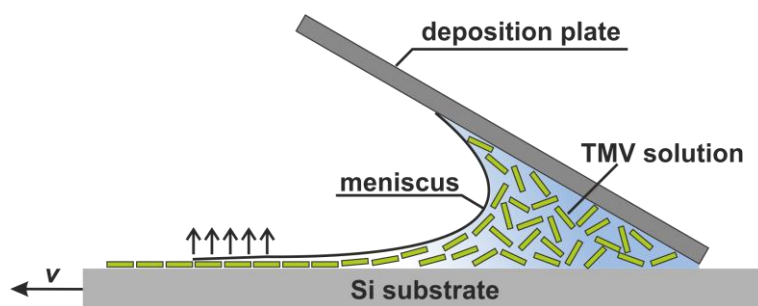


**Figure 2-9:** Schematic drawing of the convective assembly (CA) process of TMV particles taken from reference [106]. A droplet of the virus solution is trapped between the deposition plate and the silicon substrate forming a meniscus. As the substrate is pulled the meniscus is spread over the substrate causing the anisotropic TMV particles to align as the solvent evaporates.

Evaporation of the solvent induces a re-circulatory flow, and withdrawal of the meniscus imposes a viscous shear, both leading to orientation and elongation of particles (Figure 2-10). Wargacki *et al.* obtained more uniform films on hydrophilic substrates and used different surface functionalities provided by self-assembled monolayers [135]. With low concentrations and high withdrawal velocities, long 1D fibre structures were obtained. Monolayers with high order and also multi-layered ordered films were achieved by either increasing the concentration or reducing the withdrawal velocity. Depending on the chosen parameters, viruses were oriented perpendicular or parallel to the triple contact line (cf. Figure 2-10).

Virus orientation parallel to the triple contact occurs for high concentrations and low withdrawal velocities and might be attributed to the local liquid crystal transition from isotropic to nematic [142]. Additionally, it can be seen when less viscous virus solutions are evaporated very quickly (opposite conditions) [133].

However, it is important to note that both Kuncicky *et al.* and Wargacki *et al.* conducted their experiments with TMV solutions in a 10 mM phosphate buffer. Thus, positively charged ions present in the buffer ( $\text{Na}^+$ ,  $\text{K}^+$ ) shield TMV's negative surface charge, reducing the interparticle repulsion which does not allow comparison of the assembly behavior between either genetically or chemically modified TMV and the wildtype.

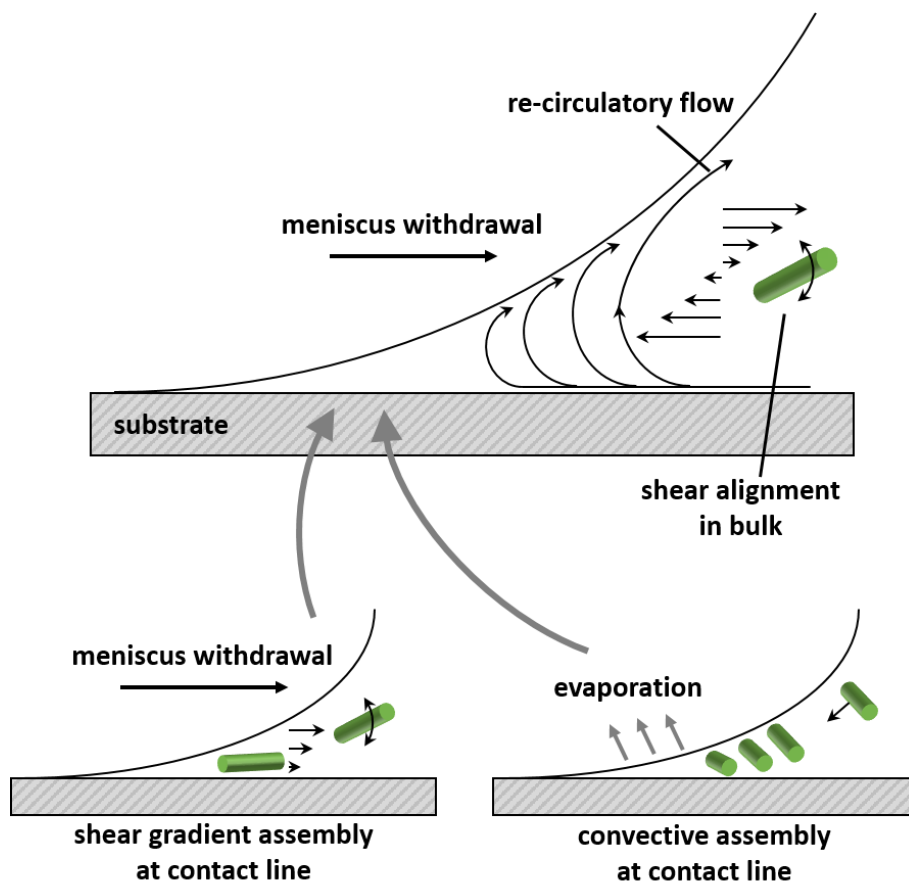


**Figure 2-10:** Proposed mechanism of assembly of anisotropic particles, such as TMV, on hydrophilic substrates. Already further away from the triple contact line some preordering occurs within the particle suspension due to velocity gradients in the re-circulatory flow. Close to the contact line either shear gradient assembly (bottom-left) or convective assembly (bottom-right) can occur. A shear gradient causes the particles to align in the direction of withdrawal, whereas predominant convective assembly (at high evaporation rates [133] or close to liquid crystal transition [142]) leads to particle alignment parallel to the contact line and orthogonal to direction of withdrawal. Image was adapted from reference [133].



### 3 EXPERIMENTS

In all cases when reference is made to H<sub>2</sub>O, it was nanopure, double deionized water purified from a Millipore<sup>TM</sup> with a resistivity  $\geq 18 \text{ M}\Omega \text{ cm}$ .

#### 3.1 TOBACCO MOSAIC VIRUS ISOLATION, PURIFICATION AND DIALYSIS

All TMV solutions, including wtTMV and the different mutants used in this work (TMV-Lys, TMV-Cys, E50Q, 30%TMV-His<sub>6</sub>), were provided by Dr. Sabine Eiben from the Institute of Biomaterials and Biomolecular Systems of the University of Stuttgart. All virus extraction from plant material or production within *E.coli*, purification and subsequent dialysis of the obtained solutions were performed there and kindly provided for this work. Thus, the procedures are not described and can be found elsewhere in detail [1,106].

#### 3.2 REACTION SOLUTION FOR ZNO MINERALIZATION

ZnO was precipitated from a methanol reaction solution containing a polymer as a structure-directing agent based on Lipowsky *et al.* [25]. Methanolic stock solutions of zinc acetate dihydrate  $\text{Zn}(\text{OOCCH}_3)_2 \cdot 2 \text{H}_2\text{O}$  (Sigma-Aldrich), polyvinylpyrrolidone (PVP, Sigma-Aldrich,  $M_w = 10000$ , Lot# BCBJ4889V) and tetraethylammonium hydroxide (TEAOH, Aldrich Chemistry) were prepared. The concentrations were 34 mM (zinc acetate), 21.7 mM (PVP) and 75 mM (TEAOH). Stock solutions were used for up to one week.

The reaction solution was prepared out of the three stock solutions in the following way. One volume unit each of the zinc acetate solution and the PVP stock solution were mixed. Then, the same volume unit of the TEAOH stock solution was added dropwise by using a peristaltic pump at a flow rate of  $1.04 \text{ mL min}^{-1}$  under continuous stirring. Thus, the resulting precursor reaction solution with a ratio of  $[\text{PVP}]:[\text{Zn}^{2+}]:[\text{TEAOH}] = 1:1.6:3.5$  and final concentrations of  $[\text{Zn}^{2+}] = 11.3 \text{ mM}$ ,  $[\text{PVP}] = 7.2 \text{ mM}$ , and  $[\text{TEAOH}] = 25 \text{ mM}$  were obtained. The reaction solution was always prepared freshly.

Small amounts of H<sub>2</sub>O were added to the reaction solution to enhance hydrolysis of the precursor and control particle size and texture. Varying volume fractions of H<sub>2</sub>O were mixed with the freshly prepared reaction solution directly before mineralization to a total volume of 1 ml. Thus, solutions with 1 vol% H<sub>2</sub>O were obtained by mixing 10 μL of H<sub>2</sub>O with 990 μL of reaction solution. Solutions with 0, 1, 2, 3, and 5 vol% H<sub>2</sub>O were prepared accordingly.

### **3.3 TEMPLATE FORMATION**

In this work, different template layers on silicon substrates were used for bio-inspired deposition of ZnO – on the one hand, self-assembled monolayers (SAMs) with differently charged functionalities and, on the other hand, wtTMV and several genetically engineered mutants.

#### **3.3.1 SUBSTRATE PREPARATION**

Silicon wafers (100, *p*-doped polished wafers, Silchem, Germany) used as substrates were thoroughly cleaned prior to use. For this purpose, repeated sonication in H<sub>2</sub>O, ethanol/acetone (1:1 V/V) for 10 minutes was performed. This was followed by a plasma cleaning step (10 min, 30 W) to hydrophilize the substrates and an additional 10 min ultrasonication in H<sub>2</sub>O water. After each sonication step, the substrates were washed 10 times with the corresponding solvent. Finally, the hydrophilized substrate surface was dried under a N<sub>2</sub> stream.

#### **3.3.2 SELF-ASSEMBLED MONOLAYERS**

Self-assembled monolayers (SAMs) with two different functionalities, amino (NH<sub>2</sub>) and carboxy (COOH), were prepared as described in detail in [102,143]. The procedures will be outlined shortly here.

3-aminopropyltriethoxysilane (APTES, 99 vol%, Acros organics) was deposited from a 2.0 vol% solution in ethanol/H<sub>2</sub>O (95:5 V/V) in order to functionalize the cleaned silicon substrates with a SAM film with NH<sub>2</sub>-terminal group. The mixture was left five minutes to hydrolyze prior to immersion of the cleaned silicon substrate for one hour at room temperature. Subsequently, the functionalized wafers were thoroughly washed several times with ethanol and dried under a N<sub>2</sub> stream.

3-(Triethoxysilyl)propylsuccinic anhydride (94 vol%, abcr) solution in toluene (10 vol%) was used for COOH-functionalizing of silicon substrates. Wafers were immersed for 16 hours and subsequently sonicated in a series of solvents (toluene, N,N-dimethylformamide (Aldrich: 99.9% HPLC grade) and H<sub>2</sub>O; 20 min for each step) leading to improved monolayer organization and removal of any physisorbed multilayers. All functionalized wafers were stored in the dark until mineralization and were mineralized on the same day.

### 3.3.3 SINGLE IMMOBILIZED VIRUSES

Silicon substrates (4 x 4 mm<sup>2</sup>) were cleaned as described in Section 3.3.1. A droplet (3 μL) of the corresponding virus solution in H<sub>2</sub>O (0.2 mg mL<sup>-1</sup>) was incubated on the cleaned wafer for 10 min. The droplet was removed and the wafer dried under a N<sub>2</sub> stream.

### 3.3.4 VIRUS MONOLAYERS VIA CONVECTIVE ASSEMBLY

Homogeneous virus monolayers of wtTMV and its mutants are a prerequisite for the formation of virus-based functional thin films and can be obtained by convective assembly (CA). Therefore, a customized setup was built within a glass chamber maintaining constant temperature and humidity. Cleaned silicon substrates (15 x 15 mm<sup>2</sup>) were mounted on a substrate holder connected to a linear motor (dip-coater, KSV Instruments, Espoo, Finland) outside the chamber. A droplet of the virus solution (5 μL) was trapped between a glass deposition plate (14 x 40 mm<sup>2</sup>, hydrophilized, cleaned as described in Section 3.3.1) under a certain fixed angle and the silicon substrate. The resulting meniscus trapped between deposition plate and silicon substrate leads to a triple interface between solution, substrate, and air. The linear motor pulled with a certain adjustable withdrawal velocity  $v_w$ , stretching out the meniscus over the substrate while capillarity holds the bulk of the droplet in the wedge. As the solvent evaporates, the viruses were aligned onto the silicon substrate.

All assemblies were conducted at  $23 \pm 2^\circ\text{C}$  and a humidity of  $35 \pm 2\%$  r.H, adjusted with saturated LiCl solution. The concentration  $c$  of wtTMV and its mutants (TMV-Lys, TMV-Cys, E50Q, and 30%TMV-His<sub>6</sub>), dispersed in H<sub>2</sub>O, was either 1.9 mg mL<sup>-1</sup> or 5 mg mL<sup>-1</sup> in H<sub>2</sub>O. The withdrawal speed  $v_w$  was varied between 0.6 mm min<sup>-1</sup> and 1.2 mm min<sup>-1</sup>. Experiments with each virus type applying a certain assembly condition were repeated until the trend was confirmed. When no specific orientation was observed, at least two substrates were analyzed,

and up to dozens of substrates were analyzed in case a specific orientation was achieved in order to ensure reproducibility of the monolayer formation via convective assembly.

### **3.4 MINERALIZATION**

Either single virus particles (cf. Section 3.3.3), virus monolayers (cf. Section 3.3.4) or SAMs (cf. Section 3.3.2) were prepared to investigate the mineralization processes with different reaction solutions (cf. Section 3.2). Solutions with immersed substrates were heated to 60°C in closed vessels in an oil bath for 90 min (= one mineralization cycle). After 90 min, the substrates were removed, cleaned thoroughly with methanol and dried under a N<sub>2</sub> stream. The next mineralization cycle was started with fresh reaction solution.

#### **3.4.1 MINERALIZATION OF SINGLE VIRUS PARTICLES**

Single virus particles were immobilized on silicon substrates (cf. Section 3.3.3) and subsequently mineralized with varying numbers of mineralization cycles in order to monitor the selectivity of the deposition process and the height increase after each mineralization step via atomic force microscopy (AFM, cf. Section 3.8.3). One to three mineralization cycles were performed (cf. Section 3.2 and 3.4) with the corresponding reaction solution and following each the virus height was determined via AFM (cf. Section 3.8.3).

Reference experiments of immobilized viruses were conducted in pure methanol at 60°C for different time spans in order to state the height increase during the mineralization process, since previous experiments showed that both methanol and the temperature treatment change the virus height [144]. As viruses completely degraded after 90 min in pure methanol, time was reduced to 5 to 15 min. Again, the height was determined by AFM (cf. Section 3.8.3).

#### **3.4.2 MINERALIZATION OF THIN FILMS**

For the fabrication of functional thin film materials, SAMs (cf. Section 3.3.2) or virus monolayers prepared by CA (cf. Section 3.3.4) are used as templates for the ZnO mineralization. The CA conditions where the viruses formed dense homogeneous monolayers were chosen. If not indicated otherwise, the conditions were the ones given in Table 3-1.

Such TMV monolayers and also SAMs were subsequently mineralized between 5 and 80 cycles depending on the demanded film thickness with different water contents. These films formed



the basis for all following functional thin films. Depending on the desired function, both film thickness and water content in the reaction solution were chosen.

**Table 3-1:** Convective assembly (CA) parameters ( $c$ ,  $v_w$ ,  $V$ ) for dense virus monolayers for different TMV.

Virus	CA conditions		
	$c$ [mg mL <sup>-1</sup> ]	$v_w$ [mm min <sup>-1</sup> ]	$V$ [μL]
wtTMV	5	1.2	5
TMV-Cys	1.9	0.6	5
E50Q	1.9	0.6	5

### 3.5 PIEZOACTIVE THIN FILMS

For the preparation of the piezo-active thin films, silicon substrates were cleaned (cf. Section 3.3.1) and functionalized with NH<sub>2</sub>- and COOH-SAMs (cf. Section 3.3.2). Additionally, the piezoelectric wtTMV was used as a template. Homogeneous virus monolayers were produced via CA (cf. Section 3.3.4) with the conditions given in Table 3-1 ( $c = 5$  mg mL<sup>-1</sup>;  $v_w = 1.2$  mm min<sup>-1</sup> and  $V = 5$  μL).

On the one hand, it was investigated whether different textures show differences in their piezoelectric behavior. Therefore, NH<sub>2</sub>-based samples were mineralized with different reaction solutions. The 100 textured sample was prepared by applying 15 mineralization cycles with a reaction solution with 3 vol% H<sub>2</sub>O. The 002 textured sample was obtained by mineralizing the SAM 20 times with the 2 vol% H<sub>2</sub>O reaction solution. The number of mineralization cycles was adjusted so that the films have the same thickness.

Additionally, template and thickness influence on the piezoelectric properties were investigated. Therefore, samples were prepared on wtTMV, NH<sub>2</sub>-, and COOH-SAMs with 2 vol% H<sub>2</sub>O in the reaction solution. The samples were mineralized 20 and 40 times, respectively.

## 3.6 ZNO-BASED FIELD-EFFECT TRANSISTORS

Field-effect transistors (FETs) based on different templates, deposited with varying water content in the reaction solution, as well as FETs with purely methanolic reaction solution, were prepared. The FET measurements, the extraction of mobility  $\mu$ , threshold voltage  $V_{Th}$  and on/off ratio  $I_{on/off}$  out of the measured output and transfer characteristics, were conducted by our project partners of TU Darmstadt (Shawn Sanctis (M.Sc.), Dr. Rudolf Hoffmann and Professor Dr. Jörg Schneider) within the scope of the priority program SPP1569 'Generation of Multifunctional Inorganic Materials by Molecular Bionics'.

### 3.6.1 SUBSTRATE GEOMETRY

FET substrates with bottom-gate/bottom-contact geometry were purchased from Fraunhofer Institute for Photonic Microsystems, Dresden, Germany. These substrates are composed of a highly  $n$ -doped ( $n \sim 3 \times 10^{17} \text{ cm}^{-3}$ ) silicon substrate covered by a thermally grown layer of  $\text{SiO}_2$  (90 nm). The prefabricated source-drain electrodes consist of gold (30 nm) and are connected via an intermediate adhesive layer of indium tin oxide (10 nm). The electrodes have an interdigital pattern, with a channel width of 10  $\mu\text{m}$  and a channel length of 10  $\mu\text{m}$  (cf. Figure 2-3).

### 3.6.2 SUBSTRATE PREPARATION AND TEMPLATE FORMATION

The substrate cleaning described in Section 3.3.1 was adjusted for the use of the prefabricated FET substrates. Substrates were subsequently sonicated for 5 min in different solvents (acetone, 2-propanol and  $\text{H}_2\text{O}$ ). This was followed by a shortened plasma treatment at higher power (1 min, 70 W) to protect the gold contacts and repeated sonication in  $\text{H}_2\text{O}$  (10 min). After each sonication step, the substrates were thoroughly washed with the corresponding solvent and dried under a  $\text{N}_2$  stream.

Prestructured FET substrates were either coated with  $\text{NH}_2$ -SAMs or virus monolayers.  $\text{NH}_2$ -SAMs were prepared as described in Section 3.3.2. Then, additional samples, deposited with optimum mineralization conditions were prepared on wtTMV and E50Q via CA with the parameters given in Table 3-1. The mineralization procedure is described in the following section.

### 3.6.3 ZNO MINERALIZATION ON FIELD-EFFECT TRANSISTORS

First, FETs were prepared with purely methanolic reaction solutions applying 10 mineralization cycles. As a next step, it was necessary to determine the optimum water content in the reaction solution for best FET performance (cf. Section 4.5). In doing so, samples with different water content (2, 3, and 5 vol% H<sub>2</sub>O) were prepared on NH<sub>2</sub>-SAMs. The number of cycles was varied in such a way that the thickness of the obtained ZnO layers was similar in all cases (8, 6, and 4 cycles, respectively).

The second step was to determine the optimum thickness on NH<sub>2</sub>-SAMs using the reaction solution with 2 vol% H<sub>2</sub>O. Thus, two samples each were prepared with 6, 8, 10, and 12 mineralization cycles.

The optimum conditions were transferred to both wtTMV- and E50Q-based FETs. These were prepared with 2 vol% H<sub>2</sub>O and 8 mineralization cycles. Three individual transistor substrates with four transistor units each were prepared for each virus-type.

### 3.6.4 MEASUREMENT DETAILS

Electrical characterizations were performed in a glove box with an HP 4155A Semiconductor Parameter Analyzer (Agilent) under argon atmosphere by Shawn Sanctis (M.Sc.), TU Darmstadt. Output characteristics of all FETs were obtained by varying the drain-source voltage  $V_{DS}$  from 0 to 30 V for gate-source voltages  $V_{GS}$  from 0 to 30 V in 10 V steps. Additionally, the transfer characteristics were measured for a constant drain-source voltage  $V_{DS}$  of 30 V and varying gate-source voltages  $V_{GS}$  from -5 to 30 V. Subsequently, the mobility values were extracted, performing a linear fit to the square root of drain current from the transfer characteristics. Further details of the extraction parameters can be found in reference [120].

## 3.7 NACRE-LIKE MULTILAYERS OF ZNO AND TMV

Multilayered TMV/ZnO samples were prepared to mimic the microstructure of nacre and enhance the mechanical properties. Since water in the reaction solution influences not only the crystallite size, but also the texture, first bulk reference samples were prepared to correlate the H<sub>2</sub>O content with the mechanical properties. With this knowledge, different virus monolayer morphologies were chosen to prepare multilayered samples.

### 3.7.1 TEMPLATE LAYERS FOR MULTILAYERED SAMPLES

Different template morphologies (cf. Figure 4-5 and Figure 4-7) resulting from the convective assembly (CA) investigations were chosen for the preparation of multilayered samples. Silicon substrates (15 x 15 mm<sup>2</sup>) were cleaned as described in Section 3.3.1. The first virus monolayer was deposited on these silicon substrates. The CA parameters were all the same ( $c = 1.9 \text{ mg mL}^{-1}$ ;  $v_w = 0.6 \text{ mm min}^{-1}$ ;  $V = 5 \text{ }\mu\text{L}$ ), but different mutants were chosen: wtTMV, E50Q, and TMV-Cys (cf. Section 2.4). The monolayers were prepared as described in Section 3.3.4 and later on the following virus layers were also deposited via CA with the same parameters, but on the mineralized ZnO.

### 3.7.2 PREPARATION OF MONOLITHIC SAMPLES WITH VARYING H<sub>2</sub>O CONTENT

Since the samples were investigated via nanoindentation, the film thickness had to be increased to avoid influence of the silicon substrate on the hardness  $H$  and Young's modulus  $E$ . This was achieved by increasing the number of mineralization cycles. Addition of H<sub>2</sub>O to the system increases the crystallite size; therefore, the number of mineralization cycles was adjusted for all water contents (Table 3-2).

**Table 3-2:** Number of mineralization cycles for the bulk reference samples for all water contents.

H <sub>2</sub> O [vol%]	0	2	3	5
number of cycles	100	80	60	30

All samples were mineralized as described in Section 3.4.2. The functionalized silicon substrates were immersed in the corresponding water-containing reaction solution and mineralized for 90 minutes at 60°C. The steps were repeated with fresh reaction solution until the desired number of mineralization cycles as given in Table 3-2 was achieved.

### 3.7.3 PREPARATION OF MULTILAYERED SAMPLES

The multilayered samples (MLS) were prepared by combining convective assembly (CA) with ZnO mineralization via chemical bath deposition (CBD). Figure 3-1 shows the mineralization procedure in detail. Silicon substrates were functionalized with wtTMV, E50Q, and TMV-Cys as described in Section 3.7.1.

Since the 3 vol% H<sub>2</sub>O monolithic reference sample showed the best mechanical properties, multilayered samples were prepared at these conditions (cf. Section 3.2). To achieve the optimum thickness ratio of 1:10 of the organic phase to the inorganic phase [50], the number of mineralization cycles was adjusted accordingly. Functionalized silicon substrates were mineralized 6 times, and then the CA was repeated with the silicon substrate rotated 90°. This process was repeated 10 times. Thus, 10 organic/inorganic bilayers were obtained.

For the samples used for fracture toughness analysis (cf. Section 3.7.5) only 5 bilayers were produced. In all cases, the resulting number of mineralization cycles of the multilayered samples was the same as for the bulk reference sample. The starting layer is always an organic layer and the final layer is an inorganic layer.

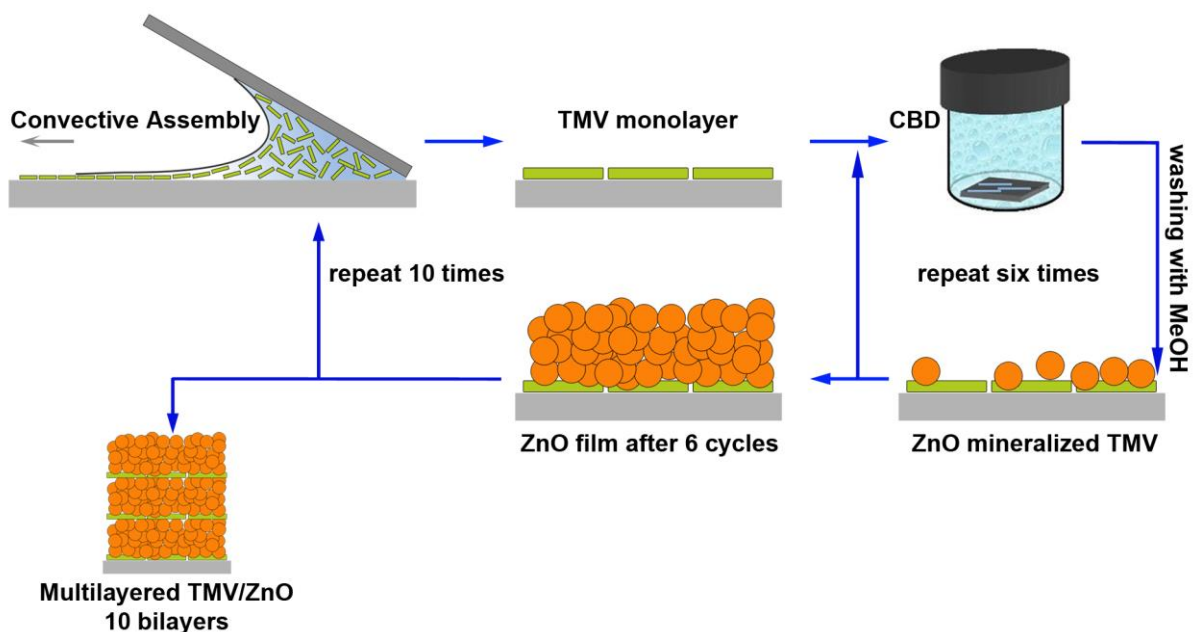


**Figure 3-1:** Scheme of the synthesis pathway of multilayered TMV/ZnO samples. Ordered TMV monolayers are prepared via convective assembly (CA). By applying 6 mineralization cycles of the chemical bath deposition with 3 vol% H<sub>2</sub>O in the methanolic reaction solution thin ZnO films are deposited on the TMV monolayer. Then the process is started again with CA on the deposited ZnO film and repeated until 10 organic/inorganic TMV/ZnO bilayers are obtained. For fracture toughness samples (cf. Section 3.7.5) only 5 bilayers were prepared.

For the following nanoindentation investigations, the sample size of the 15 x 15 mm<sup>2</sup> silicon substrates had to be reduced. Thus, the samples were given to the crystal preparation of the Max Planck Institute for Solid State Research, where the samples were cut according to Figure 3-2.

All edges were removed (black dotted lines) and most of the samples were cut in half (grey dotted line). The resulting sample size was either  $\approx 12 \times 12 \text{ mm}^2$  (1) or  $\approx 12 \times 6 \text{ mm}^2$  (1a). The edges (2) were used for fresh preparation of cross-section SEM samples.

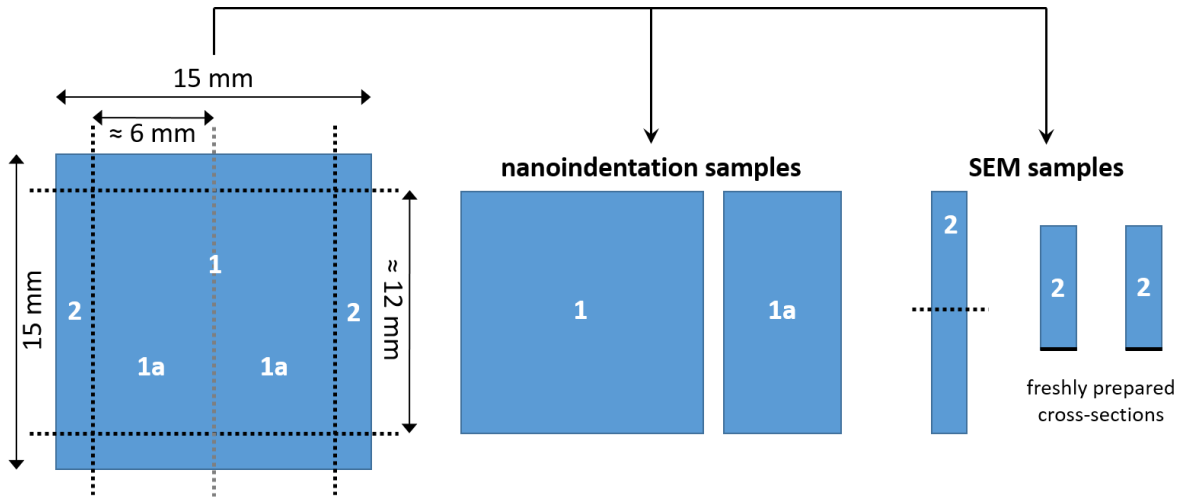


**Figure 3-2:** Scheme of the sample preparation process of nanoindentation and SEM samples. Substrates (left side) were cut along the black dotted lines resulting in the nanoindentation samples (1). Most of the nanoindentation samples were once again cut along the grey dotted line (1a). The remaining edges (2) were used for SEM sample preparation. Right before SEM analysis, they were broken in two pieces (right side) resulting in two fresh fracture surfaces.

### 3.7.4 SAMPLE PREPARATION FOR SEM INVESTIGATIONS

As mentioned above, the  $15 \times 15 \text{ mm}^2$  samples (monolithic and multilayered samples) were reduced in size for nanoindentation by cutting the edges. These edges were then used to prepare SEM specimen to determine the morphology of the layers as well as their thickness. Therefore, a fresh fracture surface was prepared by breaking the edges with a wire cutter. Such samples were glued onto cross-section SEM holders (PLANO GmbH, aluminum  $45^\circ/90^\circ$ ) with carbon conductive tabs. Additionally, the samples were sputtered with 0.5 nm platinum-palladium (80:20) alloy.

### 3.7.5 SAMPLE PREPARATION FOR FRACTURE TOUGHNESS MEASUREMENTS

For fracture toughness measurements, samples were necessary, where one part is the bare silicon substrate with a sharp edge to the film. Therefore, the film was partially covered with a photoresist by photolithography in order to protect part of the ZnO film, while the rest was etched to have the bare substrate left.

### 3.7.5.1 MASKING WITH PHOTOLITHOGRAPHY

The samples were covered with photoresist S1805 (Shipley Company) on a spin coater for 30 s at 4500 rpm. Subsequently, the samples were baked at 90°C on a hot plate for 2 min and exposed for 40 s with Maskligner MA6. The chrome mask was positioned in such a way that the larger part of the samples was covered. Afterwards, the samples were developed with developer AZ 726 MIF (AZ Electronic Materials GmbH) for 30 s, washed with a large amount of water and dried under a N<sub>2</sub> stream. The preparation was conducted by Marion Hagel of the Nanostructuring Lab of the Max Planck Institute for Solid State Research.

### 3.7.5.2 PARTIAL ETCHING

Masked samples were carefully dipped into 0.5 M HCl, until the unprotected part of the sample was wetted to remove the ZnO films (reference and multilayer) from the unprotected part of the substrate. Following that, samples were washed with H<sub>2</sub>O and dried with N<sub>2</sub>. In the next step, the samples were then completely immersed in acetone to remove the photoresist and dried with N<sub>2</sub>. In such a way, a sharp edge between the bare silicon substrate and the film was obtained.

## 3.8 CHARACTERIZATION METHODS

In the following, the characterization methods used in this work will be described shortly with a focus on the experimental setup, parameters and conditions chosen for measurements.

### 3.8.1 DYNAMIC LIGHT SCATTERING

In order to determine the particle size in solution, dynamic light scattering (DLS) experiments were performed by Alexander Greß [145] on a Malvern Zetasizer®3000HS equipped with a He-Ne laser with a wavelength of 633 nm and 90° detection. Measurements were carried out at 60°C. The viscosity  $\eta$  of the reaction solution at 60°C was determined with a RheoStress® 1 (Thermo Haake, rotor DG43 Ti, and beaker DG42) with constant shear rate  $\dot{\gamma}$  of 300 s<sup>-1</sup>. The measurement duration was 60 s and the viscosity was evaluated 10 times resulting in a value of  $\eta = 0.76$  mPa s. The refractive index of the reaction solution was measured with a refractometer to be  $n_{RS} = 1.328$ . Real and imaginary part of the refractive index of the formed ZnO were obtained from the manufacturer's manual ( $n_R = 2.0$  and  $n_I = 0.1$ ). Measurements were conducted for different periods of time and repeated at least three times to ensure

reproducibility. The reaction solutions were prepared as described in Section 3.2 with varying water contents. Measurements were performed without subruns collecting data points every 15 s. The data points were averaged over four individual measurements with fresh solution and the standard deviation was determined. For the generation of the plots of the hydrodynamic diameter in dependency of the time, three consecutive data points were averaged to smooth the plot.

### **3.8.2 ZETA POTENTIAL**

The zeta potentials of single virus particles, as well as of COOH- and NH<sub>2</sub>-SAMs, were determined. Measurements on single viruses were performed on a ZetaSizer Nano ZS in DTS 1070 Cells at 25°C by Dr. Sabine Eiben and Dipl.-NanoSc. Angela Schneider from the Institute of Biomaterials and Biomolecular Systems, University of Stuttgart.

Virus particles were precipitated by ultracentrifugation (Beckman Coulter Optima L-90 k, 45 Ti Rotor) at 34,000 rpm for 115 minutes at 4°C. The remaining pellet was resuspended overnight in the corresponding buffer solution. A first round of experiments was carried out in 10 mM sodium potassium phosphate (SPP) buffer in a pH range from 4.9 to 8.3 and a virus concentration of 0.8 mg mL<sup>-1</sup> for wtTMV, TMV-Lys, and TMV-Cys. A second round of experiments was conducted with wtTMV and TMV-Lys, respectively, diluted to a final concentration of 0.5 mg mL<sup>-1</sup> in both H<sub>2</sub>O and 1 mM NaCl solution at pH 5.5 and 8. The pH was adjusted with NaOH. Three individual measurements with automatic subruns were performed for each pH value. The zeta potential was evaluated according to the Smoluchowski equation. The given values are the average values of the three individual measurements and their standard deviations.

A SurPASS Electrokinetic Analyzer (Anton Paar GmbH) was used to determine the zeta potential of silicon substrates functionalized with either COOH- or NH<sub>2</sub>-SAMs (cf. Section 3.3.2). The measurements were performed by Dipl.-Ing. Nina Blumenstein from the Institute for Materials Science, University of Stuttgart. The functionalized silicon substrates (10 x 20 mm<sup>2</sup>) were attached to the stamps of the variable gap cell with double-sided tape. A gap height of 100 µm was adjusted. Prior to and during the measurements, a 1 mM KCl buffer solution was purged with N<sub>2</sub>. A 0.1 M HCl solution was utilized for automatic titration. Each data point was obtained by applying four pressure ramps from 0 to 400 mbar,



while measuring the streaming current. By using a Fairbrother-Mastin approach [146], the zeta potential was calculated.

### 3.8.3 ATOMIC FORCE MICROSCOPY

Atomic force microscope (AFM) measurements were conducted on a Digital Instruments MultiMode™ 8 from Bruker with a NanoScope V controller operated in tapping mode to measure the reduced virus height due to interaction with the hydrophilic oxidized silicon substrate, and also to monitor the mineralization processes in dependency of both water content and cycle number. Silicon cantilevers and PPP-NCHR-W (Nanosensors)  $n^+$  doped tips with resistivity 0.01 – 0.02  $\Omega$  cm were used. The height of the viruses and the roughness of films was evaluated with the manufacturer's software Nanoscope. According to the instructions of the manufacturer, the background in the images was flattened prior to height analysis. The height was averaged over the length of the viruses with the software.

### 3.8.4 PIEZORESPONSE FORCE MICROSCOPY

Piezoresponse force microscopy (PFM) was performed in contact mode on the same AFM. Stiff conductive tips were used (Bruker, MSP-RC). A standard sample of periodically poled lithium niobate (PPLN, Bruker) with a known piezoelectric constant  $d_{33}$  of 8 pm  $V^{-1}$  [147,148] was used as a reference. ZnO samples were deposited on different templates with varying thickness (cf. Section 3.5) and silicon references were also glued onto the holders via carbon conductive tabs (PLANO GmbH) and connected with silver paste. Varying AC biases ( $V_{AC}$ ) were applied with amplitudes from 2 to 10 V in 2 V steps and a frequency of 20 kHz to stay below the cantilever's resonance frequency [149]. The vertical piezoresponse signals (first and second harmonic) were collected on five different places of each sample along with the topography information.

The vertical amplitude was averaged over the area of each image with the Nanoscope software. Subsequently, all those values were averaged to obtain one average response for each sample for each applied bias. The deflection sensitivity of the cantilever was determined to convert the averaged recorded mV signal to a pm signal. Finally, the average pm signal was plotted over the applied bias for each sample. The slope of the linear response corresponded to the effective piezoelectric constant  $d_{eff}$  of each sample.

The  $d_{33}$  coefficient is generally defined considering that the piezoelectric response is measured using a capacitor-like structure in which the material is placed in a homogeneous electrical field (Figure 3-3 A). However, in the case of the PFM measurements, the field emerging from the tip is rather a point charge (Figure 3-3 B and C) than a planar field (cf. Figure 3-3 A) [149].

Determination of the  $d_{33}$  coefficient is not straight-forward, due to the non-uniform electric field emanating from the tip of the AFM during PFM measurements. In Figure 3-3 A, a homogeneous electric field within a sample is shown in a capacitor-like structure. Figure 3-3 B and C represent the electric fields emerging from the more point-like AFM tip during the PFM measurement for a thick sample (Figure 3-3 B) and a thin film (Figure 3-3 C).

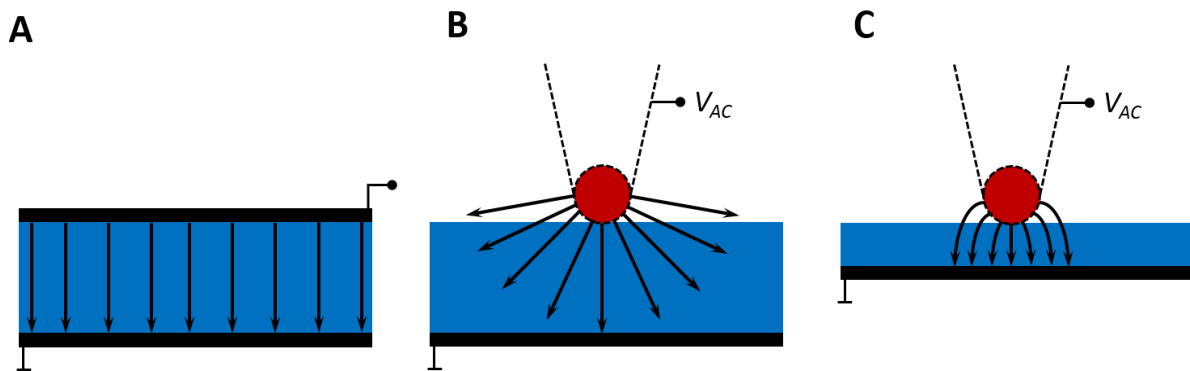


**Figure 3-3:** **A**, Homogeneous electric field in a capacitor-like structure; **B**, non-uniform electric field emerging from the AFM tip during the PFM measurement, and **C**, more uniform electric field emerging from the AFM tip in a thin sample.

For thicker films, the resulting electric field is non-uniform (Figure 3-3 B), whereas, a more uniform condition is reached for thin samples (Figure 3-3 C) during the PFM measurements. For the weak indentation regime, i.e. when both indentation load and contact area are small, the  $d_{33}$  value can be approximated by  $d_{33} = 2 \cdot d_{eff}$  [126,150], where  $d_{eff}$  is the obtained slope in the measurements. Moreover, the effective voltage sensed by the material will be smaller for a thicker sample due to the more radial electric field over the volume leading to a smaller effective  $d_{33}$  (cf. Section 4.4.4.)

### 3.8.5 SCANNING ELECTRON MICROSCOPY

Scanning electron microscopy (SEM) was carried out on a Field Emission SEM Zeiss DSM982 Gemini with a thermal Schottky Field Emitter at the Stuttgart Center for Electron Microscopy

(StEM) at the Max Planck Institute for Solid State Research. The secondary electrons were detected by an in-lens detector. The microscope was operated at an acceleration voltage of 3 kV with a working distance of 3 mm. Samples were glued onto SEM holders (PLANO GmbH, aluminum 12.5 mm) with carbon conductive tabs. For cross-section investigations, the samples were broken with a wire cutter prior to attaching them on cross-section SEM holders (PLANO GmbH, aluminum 45°/90°) with carbon conductive tabs. Samples were sputtered with 0.5 nm platinum-palladium (80:20) alloy.

### 3.8.6 X-RAY DIFFRACTION

X-ray diffraction (XRD) measurements were conducted on a Panalytical X'Pert MRD equipped with a Co tube and polycapillary optics, an Eulerian cradle, a diffracted beam monochromator, and a scintillation counter. Symmetrical  $\theta-2\theta$  scans were performed covering the reflections 100, 002, and 101. Thereby, in order to avoid detection of diffracted intensity from the silicon substrate crystal, the specimen was tilted to an angle of  $\chi = 10^\circ$  using the cradle. The measurements were kindly conducted by Maritta Dudek of the Max Planck Institute for Intelligent Systems, Department Mittemeijer. All following fitting and evaluation of the data was done in cooperation with Professor Dr. Andreas Leineweber of TU Freiberg (formerly Max Planck Institute for Intelligent Systems, Stuttgart).

The Scherrer analysis to determine the crystallite size was carried out in the following way: The instrumental resolution was obtained with a LaB<sub>6</sub> measurement. A Pawley fit was performed to the 100, 002, and 101 reflections of ZnO and convoluted with a Lorentz function. The full width at half maximum  $\beta(2\theta)$  of the Lorentz function was identified and used to calculate the 'volume weighted mean column height'  $D_V$  according to the Scherrer equation

$$D_V = \frac{180}{\pi} \cdot \frac{\lambda}{\cos \theta \cdot \beta(2\theta)}$$
 The crystallite size is later referred to as  $D_{XRD}$  to distinguish the crystallite sizes determined by different methods. In order to determine the anisotropy of the crystallites, the crystallite size was also evaluated in different crystallographic directions ([100] and [001]) by fitting  $\beta(2\theta)$  and a 2<sup>nd</sup> order spherical harmonic description of the crystallite size. The anisotropy factor  $A$  is given as  $A = \frac{D_{[100]}}{D_{[001]}}$ .

Additionally, the diffraction scans were evaluated by fitting a pseudo-Voigt function, considering the presence of the  $\alpha_1$ - $\alpha_2$  doublet with a 2:1 intensity ratio, to each of the three recorded diffraction peaks, as well as a background function. The ratio of the integrated

intensity of the 002 and 100 reflections is taken as a measure for the preferred orientation of the ZnO crystallites. The texture coefficient is given as  $T = \frac{I_{002}}{I_{100}}$ . For a random powder, this ratio would be 0.7. Thereby the tilting away from  $\chi = 0^\circ$  is ignored in the discussion.

### 3.8.7 PHOTOLUMINESCENCE

Room temperature photoluminescence measurements are performed on a spectrofluorometer (Horiba Jobin YVON Fluorolog-3) equipped with a Xe lamp. An excitation wavelength  $\lambda_E$  of 310 nm was used to excite the films prepared with different water content in the reaction solution (cf. Section 3.4.2). Scans were performed from 330 to 550 nm with an integration time of 1 s and an increment of 1 nm to collect both near band edge emission and deep band emission. To calculate the crystallite size according to equation (2-6), more accurate scans of the near band edge emission were conducted from 330 to 400 nm with an integration time of 2.5 s and an increment of 0.5 nm. The 'smaller terms' mentioned in equation (2-6) were neglected for the calculation. Maxima were determined with the system's software for several samples of each reaction condition. Calculations were then performed with the averaged maxima and their standard deviation.

### 3.8.8 NANOINDENTATION

Nanoindentation measurements were performed in the continuous stiffness measurement mode. Thus, the indenter tip was constantly driven into the sample and, additionally, a harmonic load was applied. A sharp cube corner indenter (tip radius  $\approx 40$  nm) was used instead of the normally used Berkovich indenter due to its reduced sensitivity against the films' surface roughness. Furthermore, it allows creating plastic deformation within small indentation depths. Thus, the field of deformation (combination of elastic and plastic deformation) stays within the film, minimizing the substrate influence. This is crucial for the investigation of thin films. The film's surface roughness has to be well below the tip radius. Thus, a roughness of less than 30 nm is necessary.

In general, nanoindentation data obtained at shallow penetration depth are affected by the sample's surface roughness, and there is a noticeable substrate influence for indentation depths larger than 20% of the total film thickness [151]. Thus, in order to take these limitations into account, the nanoindentation data were evaluated in the contact depth range between

10% and 20% of the total film thickness. The obtained data were evaluated using the method described by Oliver and Pharr [152].

To obtain good statistics and to characterize the samples over a large area on every sample at three different places, 25 indents were performed with a distance of 10  $\mu\text{m}$ . The mean values from all these curves were evaluated and averaged in one graph.

### 3.8.9 MICROINDENTATION AND DETERMINATION OF FRACTURE TOUGHNESS

Microindentation was used to determine the fracture toughness  $K_{Ic}$  of the multilayered samples and their monolithic references (cf. Section 3.7) by a recently described method which uses partially coated substrates [153]. It involves the formation of radial cracks upon indentation in the uncoated substrate region in close proximity to the coating and subsequent detection of the crack length with varying load. Fracture toughness is then estimated by comparing the lengths of the cracks that propagate into and away from the film. A major advantage of this method is that it largely avoids the risk of substrate/film delamination and allows including residual stress effects [153].

A Leica VMHT MOT hardness tester was used. The applied loads for the indents were 0.3 and 0.5 kg. Indents were placed in the silicon substrate in such a way that one of the four cracks propagates into the ZnO film. The crack length was measured via light microscope.

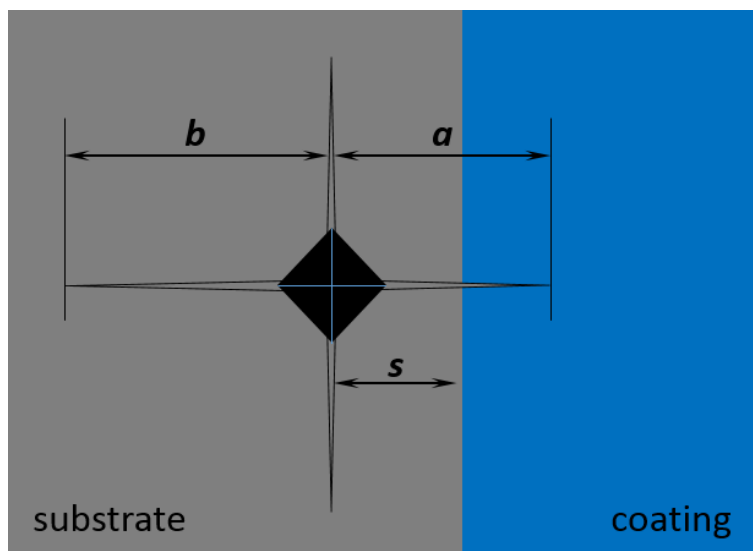


**Figure 3-4:** Scheme of the indentation geometry for the determination of the fracture toughness  $K_{Ic}$  of the sample. The indent is placed on the bare silicon substrate in the distance  $s$  to the coating and one of the radial cracks propagates into the coating ( $a$ ), whereas crack  $b$  propagates in silicon.

Specifically, the fracture toughness  $K_c$  of the film can be estimated from the measured crack length on the substrate ( $b$ ) and within the coating ( $a$ ) (Figure 3-4), according to equation (3-1) [153]

$$K_c = \left\{ K_s^2 \left[ 1 + \lambda \frac{(\phi \cdot b - a)}{t} \sqrt{\frac{E_c(1 - \nu_s^2)}{E_s(1 - \nu_c^2)}} \right]^2 \pm \left[ 2\psi_c \sigma_r \sqrt{t} \sqrt{\frac{E_c(1 - \nu_s^2)}{E_s(1 - \nu_c^2)}} \right]^2 \right\}^{1/2} \quad (3-1)$$

where the dimensionless factors  $\lambda$  and  $\psi_c$  are 0.45 and 0.95 respectively, and  $t$  is the film thickness, which was determined via cross-section SEM images. The formula was derived for the condition that the crack in the coating ( $a$ ) is always shorter than the crack in silicon ( $b$ ). Thus, the equation is not valid for  $a > b$  [153]. If  $a > b$ , the fracture toughness cannot be determined exactly, but is not bigger than the fracture toughness of the silicon substrate  $K_s$ .

For the fracture toughness  $K_s$ , Young's modulus  $E_s$ , and Poisson ratio  $\nu_s$  of the silicon substrate, respective values of 0.83 MPa m<sup>1/2</sup>, 163 GPa, and 0.22 were used [153]. For the Young's modulus of the films  $E_c$ , values obtained by nanoindentation were used, while a Poisson ratio  $\nu_c$  of 0.25 was assumed. The dimensionless factor  $\phi$  was calculated from the slope of the dependence of the substrate crack length vs. the crack length in the film. The residual stress in the film  $\sigma_r$  was neglected in this case. The standard deviation of the fracture toughness  $\Delta K_c$  was estimated by applying the law of error propagation, which leads to the following equation

$$\Delta K_c = \sqrt{\left(\frac{\partial K_c}{\partial E_c} \Delta E_c\right)^2 + \left(\frac{\partial K_c}{\partial a} \Delta a\right)^2 + \left(\frac{\partial K_c}{\partial b} \Delta b\right)^2 + \left(\frac{\partial K_c}{\partial t} \Delta t\right)^2} \quad (3-2)$$

equation (3-1) is partially derived for each measured variable. The  $\Delta$  values are the standard deviations obtained when determining each of the error-prone variables ( $E_c$ ,  $t$ ,  $a$ , and  $b$ ).

## 4 RESULTS AND DISCUSSION

### 4.1 REACTION SOLUTION FOR ZNO MINERALIZATION

In aqueous solutions, ZnO particles grow fast to large particles, especially elongated in *c*-axis direction due to enhanced growth in this direction (cf. Section 2.1.1). The change to nonaqueous solvents, such as alcohols, allows much more control over the synthesis leading to nanocrystalline thin films [23,25]. Additionally, formation of the corresponding oxide is favored in alcoholic solvents due to the dehydrating effect of the solvent. The formation of nanocrystalline ZnO deposited from a methanolic reaction solution containing a polymer as structure-directing agent onto sulfonate-terminated SAMs was confirmed [154]. Thus, in this work, a methanolic reaction solution based on the recipe of Lipowsky *et al.* [25] was modified and used. Small amounts of water were added to the reaction solution to trigger the hydrolysis rate resulting in ZnO nanocrystals with a varying, defined crystallite size and also affecting the texture of the obtained films (cf. Section 4.3.2). In order to monitor the development of the particle size over the reaction time via dynamic light scattering (DLS) measurements, the necessary parameters for the measurement were determined. Whereas the determined refractive index of the reaction solution ( $n_{RS} = 1.328$ ) hardly differed from pure methanol ( $n_{MeOH} = 1.313$ ), the viscosity of the reaction solution is higher ( $\eta = 0.76$  mPa s) compared to pure methanol ( $\eta_{MeOH} = 0.35$  mPa s). This is caused by the addition of the polymeric structure-directing agent polyvinylpyrrolidone. The polymer chains present in the solution lead to an enhanced shear resistance of the solution.

DLS measurements were then conducted with the obtained measured parameters (cf. Section 3.8.1) to determine the hydrodynamic diameter  $D_H$  of the formed species in solution for varying water contents. It is important to note that the hydrodynamic diameter is calculated assuming a spherical particle with hydration sphere [155]. All solutions were prepared freshly at room temperature and were placed in the preheated DLS apparatus directly after mixing with the corresponding water amount.

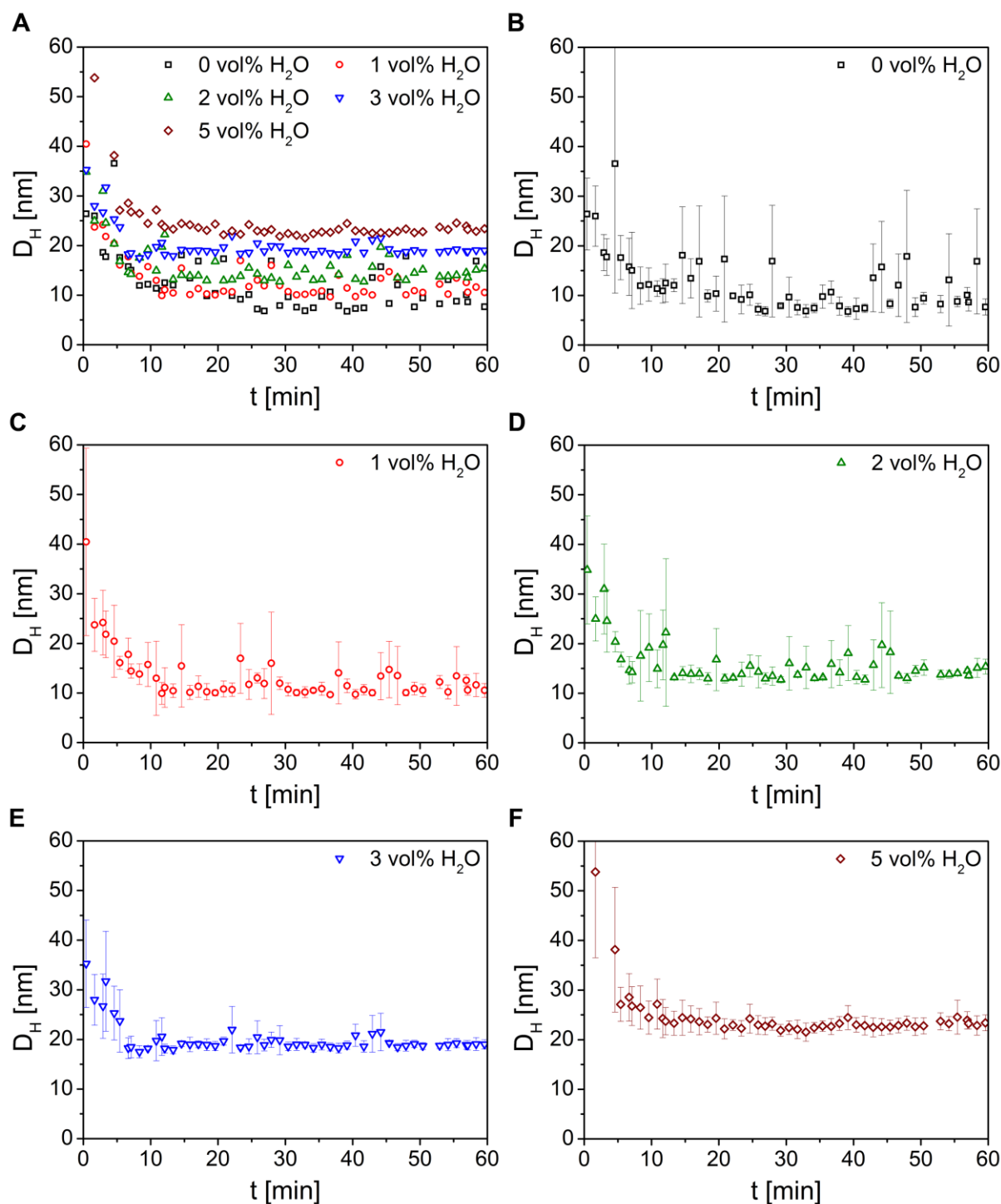


**Figure 4-1:** Dynamic light scattering (DLS) experiments of reaction solutions containing different amounts of H<sub>2</sub>O. **A**, shows all analyzed solutions in one plot. The determined hydrodynamic diameter  $D_H$  is given in dependency of the measurement time  $t$ . Each data point corresponds to a mean value of four measurements with individually prepared reaction solutions. Three consecutive averaged data points were averaged to smooth the plot. **B-F**, show the same curves individually with the corresponding standard deviations.



Figure 4-1 A shows the measured hydrodynamic diameter  $D_H$  as a function of reaction time for different water content in the reaction solution (0, 1, 2, 3, and 5 vol% H<sub>2</sub>O) averaged from four individual measurements. After small fluctuations during the first 10 minutes, the measured signal is constant for all water contents in the course of the measured time frame.

Figure 4-1 B-F show the same curves given in Figure 4-1 A individually for each water content. Here also the standard deviations obtained from the four individual measurements are given. The smallest particles are obtained without water in the reaction solution (Figure 4-1 B). However, the measured signal jumps and is less constant. Additionally, the standard deviations are rather high, indicating larger deviations between individual measurements. With increasing water content the measured  $D_H$  increases, the signal is more stable and the standard deviations are smaller (Figure 4-1 C-F).  $D_H$  was then evaluated in the regime without heating effects (20-60 min) by averaging the individual data points. The measured  $D_H$  increases from 11 nm (0 vol% H<sub>2</sub>O) to 23 nm (5 vol% H<sub>2</sub>O) by addition of H<sub>2</sub>O to the methanolic reaction solution. The individual values of  $D_H$  for each water content in the reaction solution are given in Table 4-1.

**Table 4-1:** Obtained hydrodynamic diameter  $D_H$  in dependence of the water content. The values were obtained from the smoothed curves given in Figure 4-1. To calculate the mean  $D_H$  value and its standard deviation, the first ten values were left out due to thermal fluctuations while heating the solution.

H <sub>2</sub> O [vol%]	0	1	2	3	5
$D_H$ [nm]	11 ± 3	12 ± 2	15 ± 2	19 ± 1	23 ± 1

An additional experiment was carried out to analyze the particle size and stability over a longer time span. Longer mineralization times lead to a linear increase of the particle size to a nearly tripled value of the measured hydrodynamic diameter  $D_H$  after 400 minutes (Figure 4-2 A). Additionally, the long-term measurements revealed stable particle sizes without further agglomeration for 90 minutes, which corresponds to the mineralization time of one mineralization cycle (Figure 4-2 B).

This correlates well with the constant particle size observations of Lipowsky *et al.* during their so-called intermediate stage of particle formation with followed linear increase after a reaction time of 2 hours during the final stage (cf. Section 2.1.1) [26].

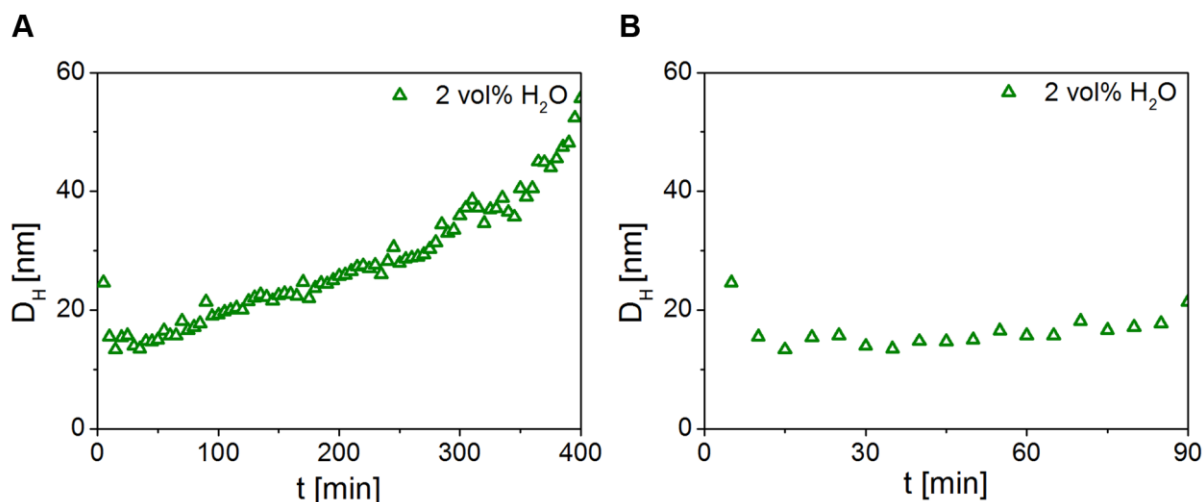


**Figure 4-2: A**, DLS long-term measurement with a reaction solution with 2 vol%  $H_2O$ . **B**, Insight of the first 90 minutes of the measurements representing one mineralization cycle. The particle size is constant during one mineralization cycle and agglomeration/particle growth occurs thereafter. The particle size was measured every 5 minutes.

Thus, in order to monitor the influence of the increasing water content in the reaction solution, measurements for varying water contents (0, 1, 2, 3, and 5 vol%  $H_2O$ ) were conducted for only 60 minutes in the methanolic reaction solutions, since the preliminary long-term measurements revealed no changes in the last 30 minutes of the reaction time applied for one deposition cycle of 90 minutes. Measurements with different hydrolysis times (0, 1, and 5 minutes) prior to mineralization revealed no differences in the obtained particle sizes.

The controlled addition of water to the methanolic reaction solution has two major effects, as can be seen from the plots in Figure 4-1 A-F. (1) The hydrodynamic diameter  $D_H$  rises with increasing water content in the reaction solution, allowing easy control over the particle size by controlling the added amount of water. (2) The detected signal remains more constant with less scattering of the values with increasing water content.

The results are well reproducible, which can be seen from the small standard deviation of the data points representing four individual measurements with individually prepared reaction solutions. The first collected data points of each measurement deviate a lot due to heating of the solution from room temperature up to  $60^\circ C$  during the measurement. This causes convection currents in the solution disturbing the measured signal by superposition of the different contributions to diffusion. These contributions to diffusion are (1) different sizes of the scattering centers and (2) Brownian motion due to thermal fluctuations.

A possible explanation for the stabilization of the measured signal with increased water content in the reaction solution could be the following. The reaction is conducted at 60°C, which is close to the boiling point  $T_b = 65^\circ\text{C}$  [156] of the solvent methanol. Methanol is 100% soluble in water [156] with a non-azeotropic boiling point diagram, i.e. without a minimum or maximum [157]. Thus, the addition of water to the purely methanolic system increases the boiling point of the mixture. Heating a solution leads to thermal convections and turbulences, which increase the closer the solution gets to its boiling point. The herein reported measurements were performed close to the boiling point, which causes problems for the DLS measurements. The thermal convection and the turbulences lead to the aforementioned superposition of size and thermal effects of the detected diffusion.

Thus, even the small amounts of water added to the system might decrease these effects by increasing the boiling point of the mixture. The effect is most pronounced for the addition of 3 and 5 vol% (Figure 4-1 E and F). These curves show hardly any fluctuations in the detected signal compared to the purely methanolic system, which shows large fluctuations and standard deviations (Figure 4-1 B).

The detected particles are instantly formed in the solution, also without any addition of a template, which strongly hints towards a homogeneous nucleation. It is well-known that alcoholic solutions decelerate the hydrolysis rate of zinc precursors, allowing more control over the size of nanocrystallites [23]. Thus, small amounts of added water increase the hydrolysis rate of the precursor and also increase the possibility to form hydroxylated species necessary for olation and oxolation processes (cf. Section 2.3). This process can clearly be seen in the larger measured particle size upon increasing the water content in the reaction solution. Possibly, the added water leads to a larger number of homogeneously distributed nucleation sites in the solution. However, the increasing number of scattering centers cannot be determined, since the count rate is dependent on the particle size as well. The obtained mean values for the hydrodynamic diameter  $D_H$  are given in Table 4-1.

In DLS measurements, only scattering centers are detected. It is not possible to conclude from these measurements, (1) whether agglomerates or single particles are detected, (2) what the particle form is (known tendency of ZnO to grow anisotropically), and (3) the actual particle/crystallite size. Since it is a solution-based method, the hydrated particles/crystallites are detected leading to a higher measured value than the actual diameter (cf. Figure 4-19 A).

Thus, the results need to be correlated with different methods, such as AFM, SEM, and also crystallite sizes calculated from both XRD and PL data (see below Sections 4.3.1 and 4.3.2.3).

## 4.2 VIRUS MONOLAYER FORMATION

The precondition necessary for any further synthesis of virus-based thin functional films is the reproducible generation of homogeneous monolayers. Especially the implementation of genetically engineered TMVs requires thorough adjusting and knowledge of the morphology of the monolayers. Otherwise it is impossible to distinguish whether the changed properties are caused by genetic modification or just packing differences. The mutants used in this thesis were chosen to cover a broad range of surface chemistry. Various parameters of the convective assembly process influence the organization behavior of the virus particles. Thus, controlling these parameters is essential for the experiments. Such parameters are e.g. virus concentration, withdrawal velocity, temperature, humidity, and wettability of the substrate [133].

All experiments were performed with oxidized hydrophilic silicon substrates (cf. Section 3.3.1). Thus, the wettability was kept constant throughout all measurements. Additionally, both humidity and temperature were not altered within the self-made convective assembly setup (cf. Section 3.3.4). Only virus concentration  $c$  and withdrawal velocity  $v_w$  were changed to distinguish the different assembly behaviors caused by genetic modification of the viruses [1].

Virus solutions are generally stored in sodium potassium phosphate buffers. Usually, the buffer supports the formation of denser and more ordered monolayers [135,158]. The increased electrolyte concentration results in a higher number of counter ions close to the TMV particle. Therefore, the Debye length is decreased, since the potential decrease is stronger in shorter distance to the surface [159]. Thus, ionic strength has a strong impact on the interaction between the particles and on the monolayer formation. Shielding of the surface charges of the viruses by counter-ions reduces the particle-particle repulsion promoting densification of the layer.

However, herein the counter-ions would additionally shield the differences arising due to genetic modification. In such a way, no direct investigation of the mutation's effect on

assembly properties is accessible. To be sure that all differences in alignment occur due to genetic modification at any given experimental condition, only buffer-free solutions obtained by dialysis were used.

Additionally, it is known that alkali metal ions, such as  $\text{Na}^+$  and  $\text{K}^+$ , have a negative influence on later applications of e.g. TMV/ZnO hybrids in field-effect transistors. Sodium ions introduce trap states into semiconductors possibly reducing the FETs performance [160].

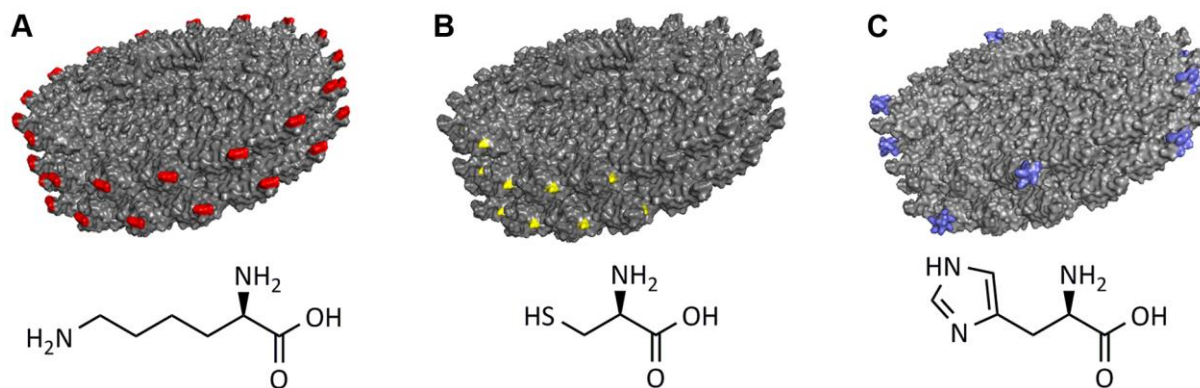


**Figure 4-3:** Visualization of the genetic modification of TMV mutants. Above: Disc models generated with PyMol (pdb structure 3J06) [86]. Below: Chemical structure of the corresponding amino acid generated with ChemBioDraw, PerkinElmer, CambridgeSoft. **A**, TMV-Lys mutant (T158K) and chemical structure of amino acid lysine with the position of the genetic modification indicated in red. **B**, TMV-Cys mutant (S3C) and chemical structure of amino acid cysteine with the position of the genetic modification indicated in yellow. The cysteine modification is not that easily accessible at the surface and thus not always visible in the model. **C**, 30%TMV-His<sub>6</sub> mutant and chemical structure of amino acid histidine with the position of the His<sub>6</sub> tags indicated in purple. Here, only 30% of the coat proteins carry the modification.

Moreover, residual buffer on a TMV monolayer could subsequently influence mineralization (1) by shielding charged functional groups and (2) by possible interaction of the ions with the reaction solution. This again makes it impossible to attribute occurring differences to genetic modifications. All these obstacles were sidestepped by using only buffer-free virus stock solutions for the CA experiments and further dilution to the desired concentrations with  $\text{H}_2\text{O}$ .

To access various possibilities to influence monolayer formation, a broad range of mutants was chosen. The changes in the functional groups present on the surface compared to the wildtype, the resulting changes in the electrostatic potential and the changed calculated pI are given in Figure 4-3 and Figure 4-4, respectively. In order to reduce the negative net surface charge of wtTMV (Figure 4-4 A, cf. Section 2.4), the neutral threonine at the C-terminus was

exchanged by the positively charged lysine resulting in the Lys mutant (T158K, Figure 4-3 A and Figure 4-4 B). In such a way, the interparticle repulsion between the identically charged virus particles in solution should be reduced, resulting in higher packing densities at the same experimental conditions.

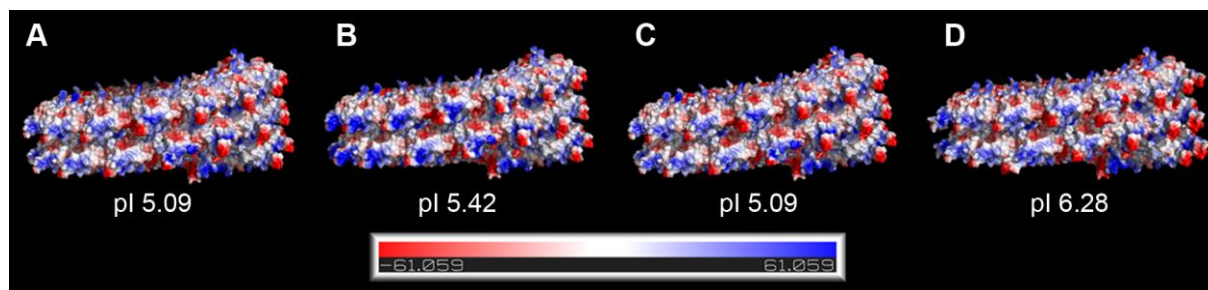


**Figure 4-4:** Calculated electrostatic potential of the outer surface (in vacuum and without the charges introduced by the RNA) of wtTMV/E50Q (**A**), TMV-Lys (**B**), TMV-Cys (**C**) and 30%TMV-His<sub>6</sub> (**D**) in side view [86]. Positive electrostatic potentials are indicated in blue and negative potentials in red. Additionally, the calculated pIs (taking all amino acids into account, not only surface exposed ones) are given below the models. Models are obtained from pdb structure 3J06 manipulated with PyMol, the PyMOL Molecular Graphics System, Version 1.7.4 Schrödinger, LLC.

To analyze stronger interparticle interactions, a Cys mutant (S3C) was used. The thiol groups of the cysteine (Figure 4-3 B) can form disulfide bridges [161] leading to strong connections between particles and, thus, changes in the self-organization behavior. Additionally, it is known that the functional groups introduced in TMV-Cys, and also 30%TMV-His<sub>6</sub> (Figure 4-3 C and Figure 4-4 D), have an affinity towards ZnO, which might influence mineralization in a later step [162,163]. The E50Q mutant offers various possibilities. It has the same surface charges as wtTMV (Figure 4-4 A), but lacks RNA. Thus, it has a higher flexibility influencing the organization on the surface, but not changing the surface chemistry [1].

All the indicated surface charges and pIs in Figure 4-4 are only calculated values. Yet, zeta potential ( $\zeta$ ) measurements (cf. Section 3.8.2) confirmed the influence of the genetic modification on the net surface charge. All zeta potential  $\zeta$  values for wtTMV and mutants in dependency of the buffer concentration are summed up in Table 4-2.

The negative charges are reduced in the case of TMV-Lys compared to wtTMV over the measured pH range. At pH 8.3 the value dropped from  $\approx -33$  mV for wtTMV to  $\approx -17$  mV for TMV-Lys (in 10 mM sodium potassium phosphate (SPP) buffer, cf. Table 4-2). The inserted

lysine functionality on the outer surface introduced more positive charges to the overall negative net charge, thus reducing the absolute value of charge. Consequently, the TMV-Lys mutant has a lower negative net surface charge.

**Table 4-2:** Measured values of the zeta potential  $\zeta$  for wtTMV, TMV-Lys and TMV-Cys at pH 8.3 in 10 mM SPP buffer. The zeta potential  $\zeta$  of wtTMV and TMV-Lys is listed additionally in 1 mM NaCl. Moreover,  $\zeta$  of TMV-Lys in H<sub>2</sub>O without any buffer, thus, at pH 5.5 is given [164].

medium	$\zeta$ [mV]		
	wtTMV	TMV-Lys	TMV-Cys
10 mM SPP (pH 8.3)	-33	-17	-37
1 mM NaCl (pH 8.3)	-53	-35	-
H <sub>2</sub> O (pH 5.5)	-	-55 <sup>[164]</sup>	-

TMV-Cys, on the other hand, showed slightly enhanced negative  $\zeta$  values compared to wtTMV. At pH 8.3, the negative charge was  $\approx -37$  mV (in 10 mM SPP buffer). This increase of the negative net surface charge indicates that the cysteine functionality was also deprotonated.

These experiments to determine the net surface charge at pH 8.3 were conducted in 10 mM SPP buffer, since the virus stock solutions are generally stored in this buffer. For convective assembly, only buffer-free solutions were used to rule out influences of the buffer during the assembly process. Thus, the actual surface potentials during the convective assembly process are different. Yet, the tendency of the differences between the mutants and the comparison between them should still be valid. In order to experimentally prove this assumption, measurements of wtTMV and TMV-Lys in H<sub>2</sub>O with strongly reduced buffer concentration (1 mM NaCl) were performed. The resulting zeta potential  $\zeta$  for wtTMV was  $\approx -53$  mV for 1 mM NaCl compared to  $\approx -33$  mV for 10 mM SPP buffer. In the case of TMV-Lys, this led to a value for the zeta potential  $\zeta$  as high as  $\approx -35$  mV for TMV-Lys in 1 mM NaCl compared to  $\approx -17$  mV for TMV-Lys in 10 mM SPP buffer (cf. Table 4-2).

In pure H<sub>2</sub>O, the zeta potential of TMV-Lys drops down to  $\approx -55$  mV [164] confirming the trend of higher absolute net charges with reduced counter ion concentration. The measurements conducted in buffer-free dialyzed virus solutions were only conducted for TMV-Lys, since the detected signal is very low, noisy and deviates a lot, resulting in very challenging experiments.

The manufacturer of the measurement equipment recommends to perform the measurements with at least 1 mM NaCl.

However, the zeta potential measurements clearly lead to the conclusion that the net surface charges are strongly increased with reduced buffer concentration, since the zeta potential values measured in H<sub>2</sub>O are closer to the Stern potential (electric surface potential) in the absence of counter ions [159].

#### 4.2.1 INFLUENCE OF TMV CONCENTRATION ON MONOLAYER FORMATION

The influence of concentration was investigated at two different concentrations (5 and 1.9 mg mL<sup>-1</sup>) for wtTMV and all mutants [1]. However, due to the different preparation method (cf. Section 3.1), the highest concentration available for 30%TMV-His<sub>6</sub> was limited to 1.9 mg mL<sup>-1</sup> [106].

For that reason, this mutant was excluded for the first round of experiments with a concentration  $c = 5 \text{ mg mL}^{-1}$  and the withdrawal velocity  $v_w = 1.2 \text{ mm min}^{-1}$  performed at constant temperature and humidity. For high concentration and withdrawal velocity ( $c = 5 \text{ mg mL}^{-1}$  and  $v_w = 1.2 \text{ mm min}^{-1}$ ), the morphology of the formed monolayer is similar (Figure 4-5 A-D) for all investigated viruses (wtTMV, TMV-Lys, TMV-Cys, and E50Q).

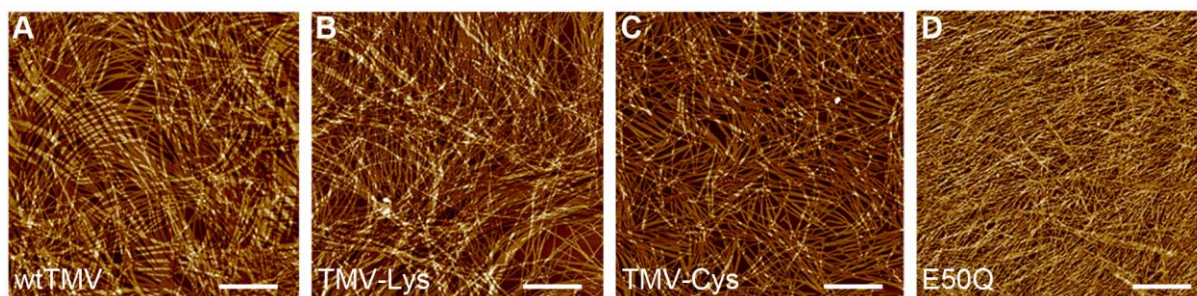


**Figure 4-5:** AFM height images of wtTMV (A), TMV-Lys (B), TMV-Cys (C), and E50Q (D) layers obtained via CA ( $c = 5 \text{ mg mL}^{-1}$ ,  $v_w = 1.2 \text{ mm min}^{-1}$ , humidity: 35% r.H). The withdrawal direction is from right to left. All scale bars represent 2  $\mu\text{m}$  [1].

Since all experiments were conducted with buffer-free virus solutions, the enhanced interparticle repulsion led to the preferred formation of head-to-tail associations (e.g. Figure 4-5 A) with a low degree of interparticle connections (bundles). This is well-known to happen in more acidic environments (cf. Section 2.5) [127,128]. Since the virus solutions are



dialyzed and dispersed in H<sub>2</sub>O, the pH is reduced to 5.5 [165] compared to buffered solutions (pH 7.4) - favoring these conditions with predominant head-to-tail association.

In all cases, this resulted in fibers with a length of several micrometers, which were bound tightly to the substrate without losing their head-to-tail association, even without supported aniline polymerization as reported by Niu *et al.* In most cases, the formed TMV wires were virus bundles connected via head-to-tail association (Figure 4-5 A-C).

Only the E50Q mutant formed head-to-tail virus assemblies to long wires of single particles (Figure 4-5 D). All virus types assembled to structures without preferred orientation at these conditions. However, all virus particles were homogeneously distributed in wavy structures over large surface areas.

At these given conditions, most of the viruses have sufficient space to align parallel to the contact line (perpendicular to the direction of withdrawal) forming head-to-tail associations. However,  $v_w$  was too high to give the particles enough time to align parallel to the withdrawal direction. Such effects have been reported in the literature for wtTMV at high evaporation rates by Prevo and Velev [133]. Russell *et al.* reported such conditions for assemblies from diluted suspensions of carbon nanotubes [166] and Vonna *et al.* for actine filaments [167].

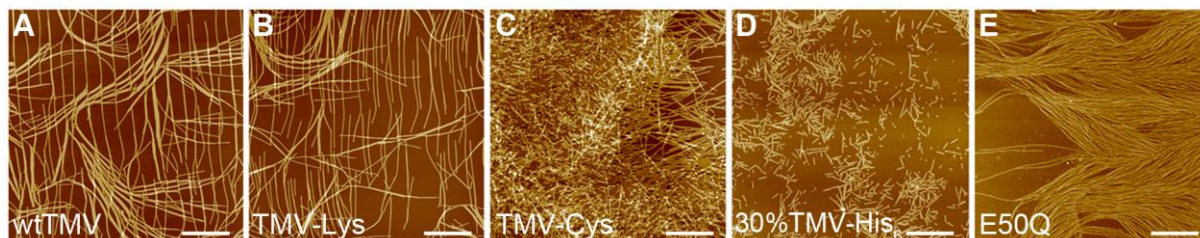


**Figure 4-6:** AFM height images of wtTMV (A), TMV-Lys (B), TMV-Cys (C), 30%TMV-His<sub>6</sub> (D), and E50Q (E) layers obtained via CA ( $c = 1.9 \text{ mg mL}^{-1}$ ,  $v_w = 1.2 \text{ mm min}^{-1}$ , humidity: 35% r.H). The withdrawal direction is from right to left. All scale bars represent 2  $\mu\text{m}$  [1].

The next step was to reduce the virus concentration, but to maintain the same withdrawal velocity ( $c = 1.9 \text{ mg mL}^{-1}$  and  $v_w = 1.2 \text{ mm min}^{-1}$ ) [1]. For these experiments, the 30%TMV-His<sub>6</sub> mutant could be included. The lower concentration of  $c = 1.9 \text{ mg mL}^{-1}$  led to more pronounced differences between the mutants.

Both wtTMV and TMV-Lys (Figure 4-6 A, B) formed single micrometer-sized virus wires perpendicular to the withdrawal direction, i.e. parallel to the triple contact line. In such cases,

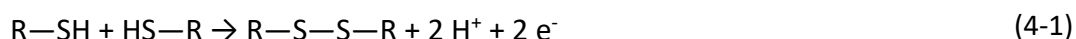
the virus assembly of the anisotropic particles is not driven by the shear-gradient in solution, but by solvent evaporation due to low viscosity and high evaporation.

This is in good accordance with the general findings of Prevo and Velev for anisotropic particles [133]. They state that solutions with anisotropic particles at low concentration have a low viscosity, so that the shear-gradient is not the predominant assembly step. In contrast, the convective assembly mechanism driven by evaporation leads to structures parallel to the triple contact line (cf. Figure 2-10).

The reduced surface charge of the TMV-Lys mutant due to genetic modification compared to wtTMV does not affect the assembly behavior, indicating that the interparticle repulsion is not a dominant factor in assembly under these conditions.

The assembly behavior of the TMV-Cys mutant shows drastic differences compared to both wtTMV and TMV-Lys. As can be seen in Figure 4-6 C, the TMV-Cys mutant forms dense disordered films covering the entire substrate. The single virus particles are strongly intertwined. A possible explanation can be derived from its genetic modification. In the absence of buffer ions, the thiol groups introduced upon genetic modification possibly oxidize, forming disulfide bridges which connect the virus particles and reduce their mobility.

The disulfide bond formed between two cysteine groups forming a covalent linkage, as shown in (4-1), is often used in nature, resulting in stable protein nanostructures and switch protein functions [168–170].



The 30%TMV-His<sub>6</sub> mutant showed a behavior different from all other used mutants and wtTMV. Neither head-to-tail association nor densely packed viruses were observed (Figure 4-6 D). The absence of buffer led to a strong particle-particle repulsion resulting in an organization of isolated islands with short virus bundles spaced far apart from each other.

Even though the surface chemistry of the E50Q mutant is identical to that of wtTMV, their assembly behavior under these conditions is very different (Figure 4-6 E). E50Q forms aligned, hole-containing monolayers consisting of long fibers that are oriented in the direction of withdrawal. The resulting layer is similar to what Prevo and Velev [133] refer to as

'submonolayers'. They occur when evaporation ruptures the film, followed by dewetting and densification of particles by retracting film edges [131].

The only difference between wtTMV and E50Q is the absence of RNA within the virus tube, resulting in a more flexible structure. This can especially be seen from AFM investigations of the virus height upon adhesion to an oxidized silicon substrate. WtTMV strongly interacts with the silicon substrate via hydrogen bonds (cf. Section 2.4), leading to a reduced height, which was measured to be around 14 nm, which is in good accordance with reported literature values [95,96].

However, the measured values for the E50Q mutant reveal an increased height reduction to values as low as 9 to 10 nm. The absence of RNA leads to a higher flexibility of the rod and favors an easier deformation of the rod upon adhesion. Thus, E50Q interacts with a higher surface area of the silicon substrate compared to wtTMV.

The enhanced flexibility leads to enhanced adhesion of the virus particles towards the silicon substrate and also favors ordered alignment. Opposed to wtTMV, the E50Q particles were not able to flip parallel to the contact line, even though the concentration was as low as in the case of wtTMV. Consequently, the virus particles oriented themselves parallel to the withdrawal direction (Figure 4-6 E). These facts and the trend to form longer particle associations in the case of E50Q (cf. Section 2.4, [108]), leads to a shear-gradient induced alignment in the direction of withdrawal, orthogonal to the contact line.

#### **4.2.2 INFLUENCE OF WITHDRAWAL VELOCITY**

Since the differences occurring between wtTMV and the mutants due to genetic modification were most pronounced in the case of the low virus concentration ( $c = 1.9 \text{ mg mL}^{-1}$ ), this concentration was chosen to investigate the influence of withdrawal velocity reduction to  $v_w = 0.6 \text{ mm min}^{-1}$ , which is the smallest velocity possible with the applied setup (cf. Section 3.3.4) [1].

Upon these conditions, wtTMV and TMV-Lys mutants assembled in similar structures (Figure 4-7 A, B). However, by reducing  $v_w$  to  $0.6 \text{ mm min}^{-1}$ , the assembly is no longer solely driven by convective evaporation, but also by shear-gradient induced alignment (cf. Section 2.5). Speed reduction reduced the evaporation speed as well, since the solvent

film is spread slower over the surface. This allowed shear-gradients to become more dominant, resulting in the formation of virus bundles as well.

Even though particles had more time to orient, no alignment in withdrawal direction was observed and the virus particles also did not flip in the direction of the contact line. The obtained effect was rather corresponding to an intermediate situation. The reduced  $v_w$  of  $0.6 \text{ mm min}^{-1}$  led to the formation of long virus bundles that arranged to holey monolayers with some short range ordering, however, without preferred orientation (Figure 4-7 A, B).

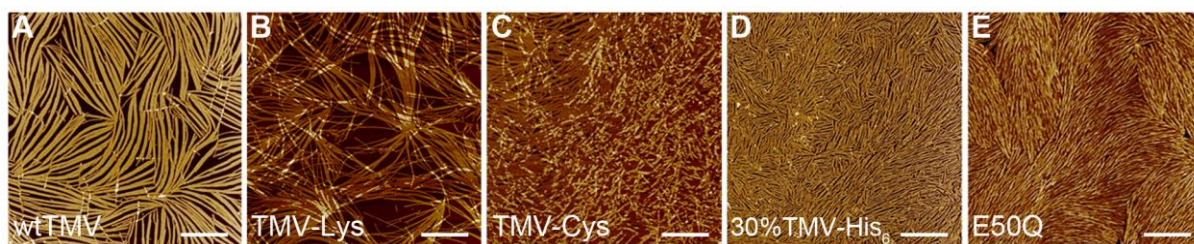


**Figure 4-7:** AFM height images of wtTMV (A), TMV-Lys (B), TMV-Cys (C), 30%TMV-His<sub>6</sub> (D), and E50Q (E) monolayers obtained via CA ( $c = 1.9 \text{ mg mL}^{-1}$ ,  $v_w = 0.6 \text{ mm min}^{-1}$ , humidity: 35% r.H.) without buffer. The withdrawal direction is from right to left. All scale bars represent  $2 \mu\text{m}$  [1].

Even though there was an increased time span for viruses to orient in the still very small shear-gradient (concentration still low), this was not sufficient to align them in the direction of withdrawal. Contrary to the behavior of both wtTMV and TMV-Lys, the assembly behavior of TMV-Cys mutant did not change by reducing  $v_w$ . The morphology of the virus layer was again completely disordered, but closely packed (Figure 4-7 C). As explained before, the strong connection between the virus particles upon formation of disulfide bridges is favored in the absence of buffer. Thus, the assembly of this particular mutant is independent from the withdrawal velocity within the analyzed conditions.

Furthermore, the reduced  $v_w$  of  $0.6 \text{ mm min}^{-1}$  led to an increased size of the virus islands formed in the case of 30%TMV-His<sub>6</sub>. Additionally, larger scans revealed wide stripe patterns (Figure 4-8 A and B) of the short unordered, but homogeneous, virus bundles parallel to the contact line (Figure 4-7 D). However, there were always large virus-free areas of bare silicon (cf. dark areas in Figure 4-8 B) substrate present showing insufficient monolayer formation even at the maximum concentration available for this mutant.

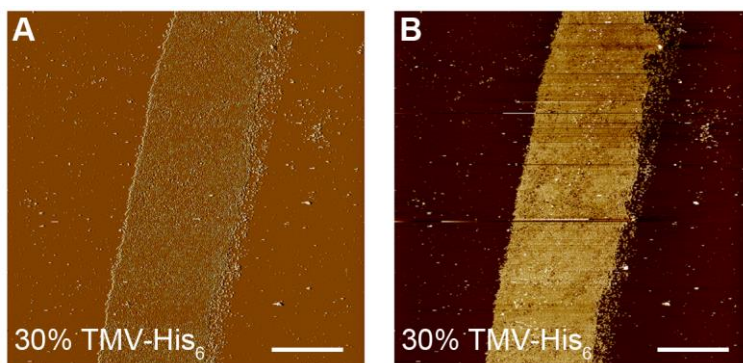


**Figure 4-8:** **A**, AFM amplitude image and **B**, AFM height image of 30%TMV-His<sub>6</sub> monolayers obtained via CA ( $c = 1.9 \text{ mg mL}^{-1}$ ,  $v_w = 0.6 \text{ mm min}^{-1}$ , humidity: 35% r.H.) without buffer. The virus monolayers (bright areas in B) form a stripe pattern on the silicon substrate revealing large uncovered areas (dark areas in B) of the bare silicon substrate. The withdrawal direction is from right to left. All scale bars represent  $10 \mu\text{m}$ .

The reduction of  $v_w$  to  $0.6 \text{ mm min}^{-1}$  was beneficial for the E50Q mutant which already showed the best behavior at higher  $v_w$  (Figure 4-6 E). Very densely packed, defect-free monolayers were found by reducing  $v_w$  (Figure 4-7 E). The particles had sufficient time to fill the previously reported holes forming smooth monolayers consisting of dense wavy bundles with short range ordering. The strong initial interaction of the flexible virus particles with the silicon substrate hinders perfect orientation along the withdrawal direction, since irregularities in the array cannot be corrected during the assembly process [171].

#### 4.2.3 INFLUENCE OF VIRUS MONOLAYER QUALITY ON ZnO THIN FILM FORMATION

In order to demonstrate the effect of genetic modification on TMV/ZnO hybrid materials, samples prepared under the same CA conditions ( $c = 1.9 \text{ mg mL}^{-1}$  and  $v_w = 0.6 \text{ mm min}^{-1}$ ) were mineralized as described in Section 3.2. The advantage of this synthesis is the highly selective mineralization of ZnO nanocrystals on the virus structure only and not on the bare silicon substrate (cf. Section 4.3.1). After two deposition cycles, the virus structures were completely covered with nanocrystalline ZnO (Figure 4-9). However, the quality of the virus monolayer directly influences the quality of the ZnO film [1].

The virus structures obtained via convective assembly were still visible after mineralization in the case of the hole-containing virus layers of wtTMV and TMV-Lys (Figure 4-9 A and B). The denser the morphology of the virus film, the less of its previous structure could be seen after mineralization (Figure 4-9 C-E), since the smooth and dense structure of the virus film is transferred to the deposited ZnO film.

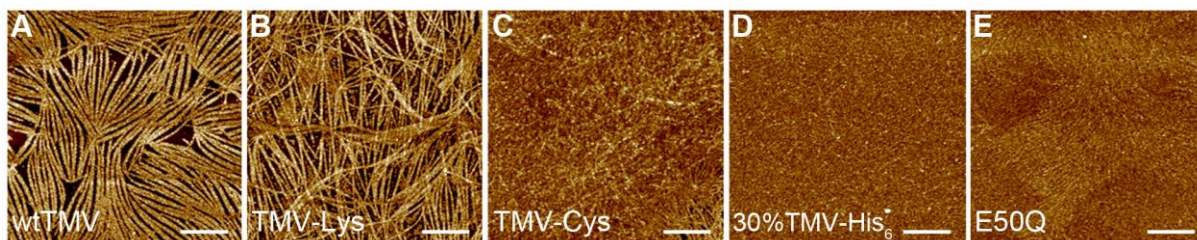


**Figure 4-9:** AFM height images of ZnO mineralized wtTMV (A), TMV-Lys (B), TMV-Cys (C), 30%TMV-His<sub>6</sub> (D), and E50Q (E) monolayers obtained via CA ( $c = 1.9 \text{ mg mL}^{-1}$ ,  $v_w = 0.6 \text{ mm min}^{-1}$ , humidity: 35% r.H) without buffer with two deposition cycles. The withdrawal direction is from right to left. All scale bars represent 2  $\mu\text{m}$  [1].

Notably, in the case of E50Q, where the smoothest and densest virus layers were obtained, the formed ZnO is also very smooth and completely hides the wavy virus structures, even after only two deposition cycles (Figure 4-9 E). To monitor this quantitatively, the roughness ( $R_{ms}$ ) of the obtained structures was determined via AFM from  $10 \times 10 \mu\text{m}^2$  scans. The resulting values are visualized in Figure 4-10. The differences in the organization behavior due to genetic modification subsequently influenced the quality of the formed ZnO films. The E50Q mutant generated the smoothest hybrid films with  $R_{ms}(\text{E50Q}) = 4.8 \pm 0.3 \text{ nm}$  compared to  $R_{ms}(\text{wtTMV}) = 11.0 \pm 1.5 \text{ nm}$ ,  $R_{ms}(\text{TMV-Lys}) = 10.5 \pm 1.3 \text{ nm}$ ,  $R_{ms}(\text{TMV-Cys}) = 6.3 \pm 0.1 \text{ nm}$ , and  $R_{ms}(30\%\text{TMV-His}_6) = 5.4 \pm 0.7 \text{ nm}$  [1].

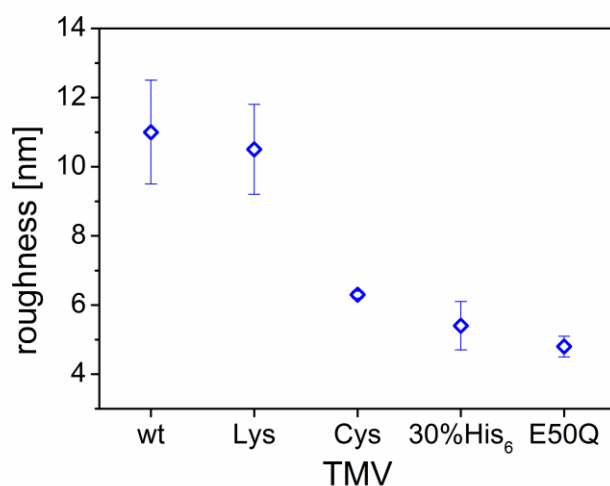


**Figure 4-10:** Surface roughness ( $R_{ms}$ , obtained from  $10 \times 10 \mu\text{m}^2$  AFM images, cf. Figure 4-9) of wtTMV/ZnO, TMV-Lys/ZnO, TMV-Cys/ZnO, 30%TMV-His<sub>6</sub>/ZnO, and E50Q/ZnO hybrid films after 2 deposition cycles [1].

#### 4.2.4 INFLUENCE OF VIRUS MONOLAYER QUALITY ON TRANSISTOR PROPERTIES

To monitor the influence of virus alignment, in view of genetic engineering, on the functional properties of TMV/ZnO hybrids, their electrical properties were analyzed. Both wtTMV and E50Q mutant were selected, since they only differ in their assembly behavior and not in the surface chemistry (cf. Section 2.4). In such a way, additional influences that varied functional groups of other mutants could have on (1) ZnO deposition and (2) the semiconducting properties, could be neglected. For these measurements, a field-effect transistor (FET) with a bottom-gate/bottom contact geometry was chosen.

First of all, the convective assembly behavior of both wtTMV and E50Q had to be analyzed on the prestructured FET substrates. For both mutants, the conditions with the best assembly behavior, i.e. the densest and most homogeneous monolayers obtained, on bare silicon were chosen. Thus, for wtTMV the conditions were  $c = 5 \text{ mg mL}^{-1}$  and  $v_w = 1.2 \text{ mm min}^{-1}$  and for E50Q  $c = 1.9 \text{ mg mL}^{-1}$  and  $v_w = 0.6 \text{ mm min}^{-1}$ .

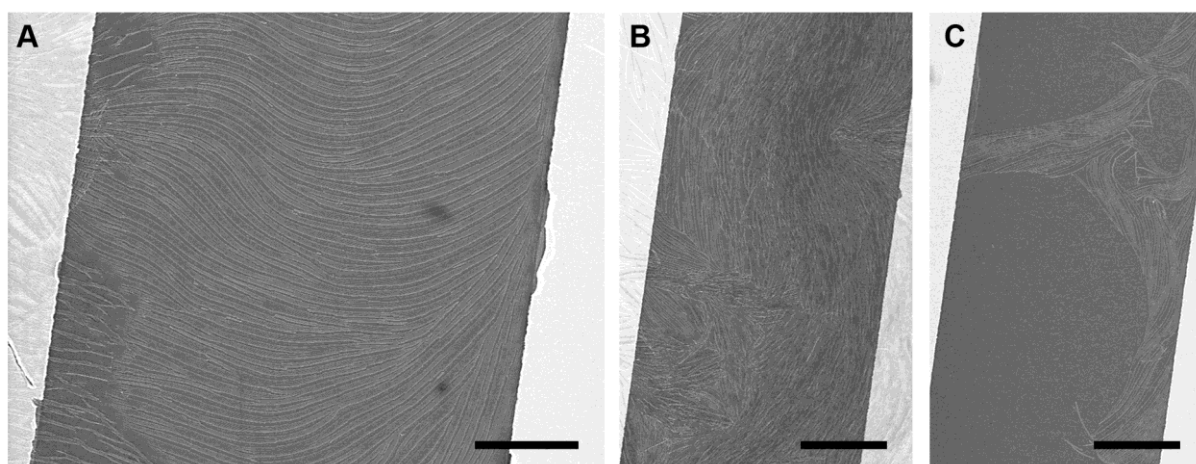


**Figure 4-11: A-C**, SEM images of wtTMV monolayers immobilized via CA ( $c = 5 \text{ mg mL}^{-1}$  and  $v_w = 1.2 \text{ mm min}^{-1}$ ) on prestructured FET substrates in different magnifications showing the different monolayer morphologies on different spots of the substrate (**B**, **C**). All scale bars are  $2 \mu\text{m}$ . Samples were sputtered with  $0.5 \text{ nm Pt:Pd (80:20)}$ .

Prestructured FET substrates possess gold electrodes forming the interdigital circuit with a height difference towards the  $\text{SiO}_2$  layer of  $30 \text{ nm}$  (cf. Figure 2-3). Thus, differences in the assembly process on FET substrates compared to silicon substrates were expected: (1) due to the height differences causing an obstacle in the assembly pathway and (2) the affinity of TMV towards gold which was known from previous experiments [120]. This is valid for both wtTMV and E50Q, since they have the same surface chemistry (cf. Section 2.4).

Detailed SEM investigations over the entire substrate area (Figure 4-11 and Figure 4-12) revealed the formation of reproducible virus monolayers in both cases. Figure 4-11 clearly shows the difference occurring in the case of wtTMV, when changing from the bare silicon (cf. Figure 4-5 A) substrate to the prestructured FET substrate.

As described above, wtTMV formed homogeneous but disordered template layers under these conditions (cf. Figure 4-5 A). On the FET substrates, monolayers with many holes with varying density between the electrodes were formed (Figure 4-11 B, C). This is probably attributed to the larger rigidity of wtTMV virus particles compared to E50Q which does not allow the viruses to assemble as smoothly and densely.

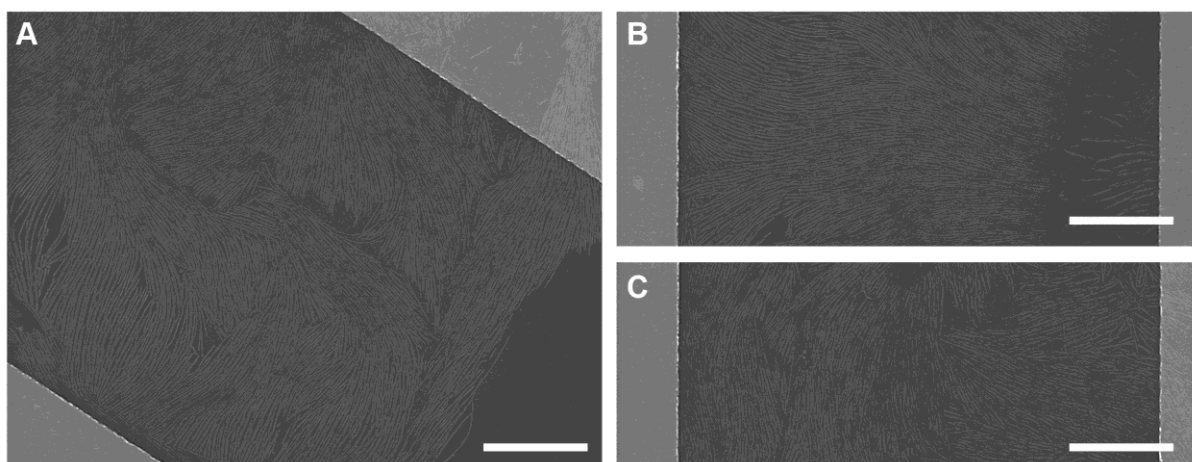


**Figure 4-12: A-C**, SEM images of E50Q immobilized via CA on prestructured FET substrates ( $c = 1.9 \text{ mg mL}^{-1}$  and  $v_w = 0.6 \text{ mm min}^{-1}$ ) in different magnifications showing the different monolayer morphologies on different spots of the substrate (**B**, **C**). All scale bars are  $2 \mu\text{m}$ . Samples were sputtered with  $0.5 \text{ nm Pt:Pd (80:20)}$ .

The flexible RNA-free E50Q mutant showed similar organization behavior on both bare silicon (cf. Figure 4-7 E) and prestructured substrates. Homogeneous, dense monolayers with few defects were formed (Figure 4-12) that strongly resemble the structures obtained on bare silicon (cf. Figure 4-7 E). Even though there were also small uncovered areas (Figure 4-12 A), the overall surface coverage was high (Figure 4-12 A-C) and by far more homogeneous compared to wtTMV, where in some spots voids dominated (Figure 4-11 C). It is well-known that not only the thickness of the semiconducting layer, but also its homogeneity are crucial for FET performance. If the deposited layers of semiconducting material get too thick, the performance is affected by resistivity effects caused by bulk material [34]. If the layers are too thin, the surface morphology is not homogeneous leading to a decrease of the performance.



In order to take the aforementioned general importance of film thickness and homogeneity on performance into account, the film thickness and homogeneity after 10 mineralization cycles of the resulting ZnO film were analyzed via SEM in top view and cross-sections (Figure 4-13).

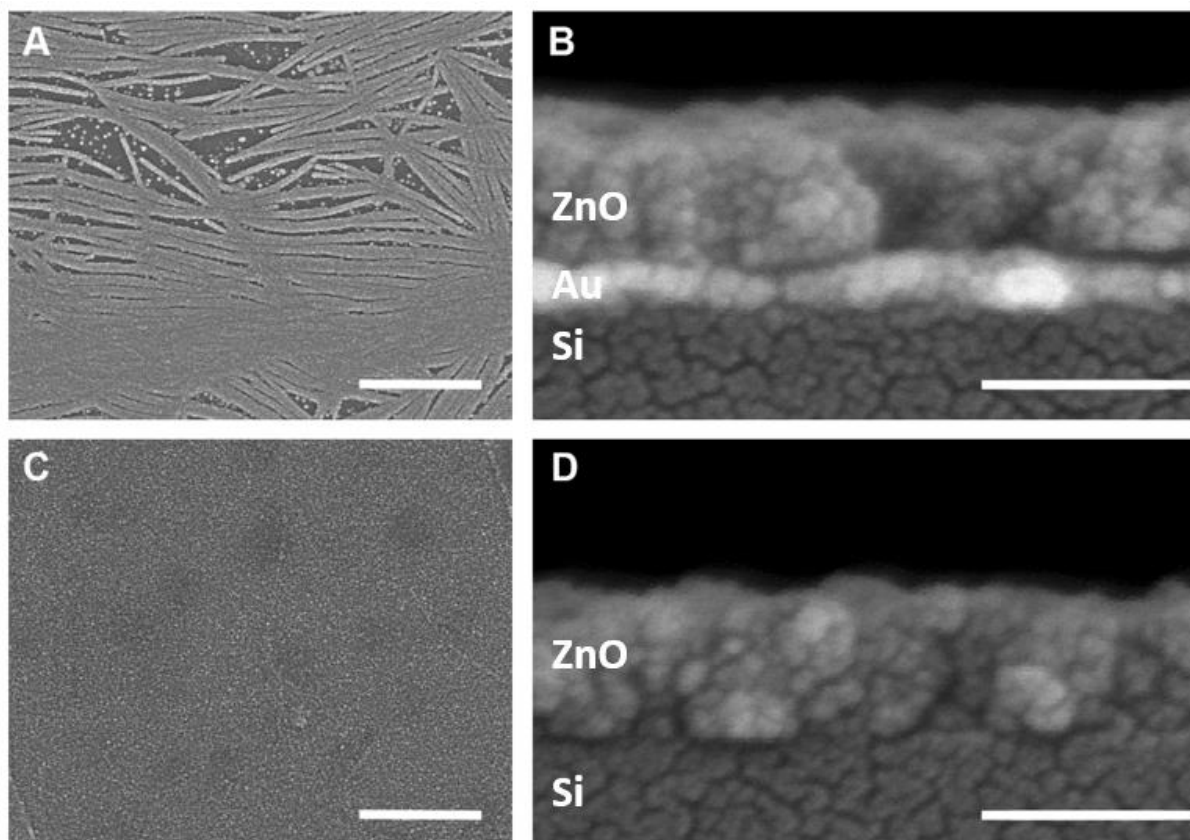


**Figure 4-13:** SEM images of wtTMV-based (A, B) and E50Q-based (C, D) FETs mineralized with ZnO in top view (A, C) and cross-section (B, D). Viruses were immobilized on prestructured FET substrates via CA with the conditions indicated in Figure 4-11 and Figure 4-12. The top view indicate the distribution of the bio/inorganic film between the gold electrodes for wtTMV-based ZnO FET (A) and E50Q-based ZnO FETs (C). The cross-section SEM images show the ZnO layers after 10 deposition cycles on wtTMV (B) and E50Q (D). Scale bars in top view are 2  $\mu\text{m}$  and 100 nm for the cross-sections. All samples were sputtered with 0.5 nm Pt:Pd (80:20).

The SEM analyses of mineralized FET substrates in top view clearly show a discontinuous ZnO film with inhomogeneous ZnO coverage between the gold electrodes in the case of wtTMV-based FETs (Figure 4-13 A). Single mineralized virus bundles are visible. The voids that were already observed after wtTMV immobilization via CA (cf. Figure 4-11 C) were not closed due to the highly selective mineralization of ZnO.

In contrast, mineralized E50Q-based FET substrates show a completely dense and homogeneous ZnO coverage (Figure 4-13 C). No single virus bundles are visible. The increased virus density achieved by using the genetically engineered E50Q mutant during the CA process (cf. Figure 4-12), resulting in a homogeneous and dense template layer, leads to a continuous and homogeneous ZnO film.

The cross-sectional SEM images (Figure 4-13 B, D) revealed in both cases the formation of ZnO layers with a thickness  $84 \pm 2$  nm and  $83 \pm 2$  nm on wtTMV and E50Q templates, respectively. In the case of the wtTMV-based FET, the thin gold layer of the interdigital structure can be seen underneath the ZnO layer (Figure 4-13 B).

This is probably the cause for the determined homogeneous thickness in the case of wtTMV. The virus particles are attracted to the gold electrodes [120] and the template layer is thus more homogeneous on the interdigital gold structure than between the electrodes. The top view images (Figure 4-13 A) clearly pointed out the presence of inhomogeneity in the ZnO film of wtTMV-based ZnO FETs.

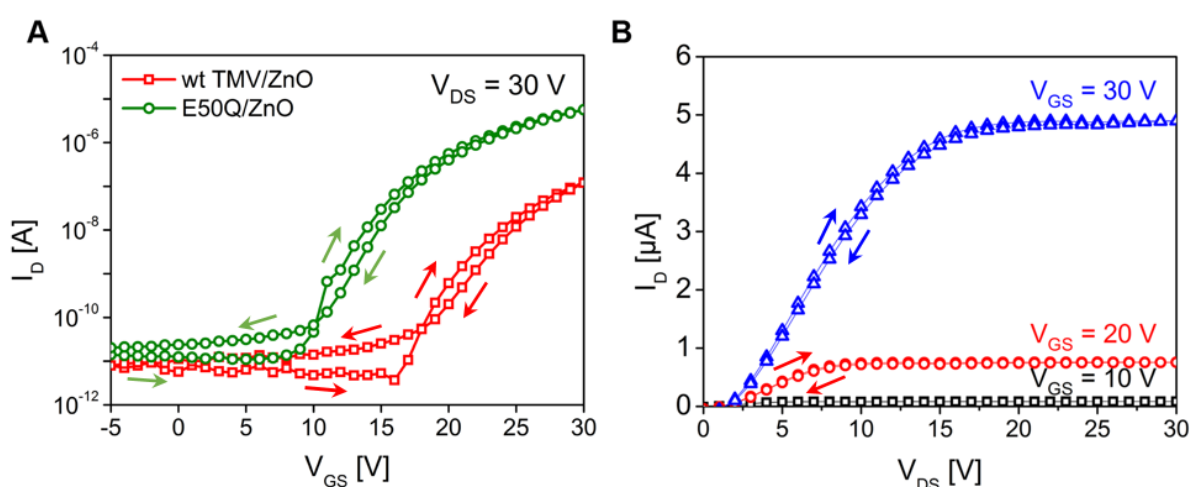


**Figure 4-14:** Performance of a FET produced by convective assembled wtTMV- and E50Q-based ZnO hybrid materials deposited from purely methanolic reaction solutions applying 10 deposition cycles. **A**, Transfer characteristics for constant drain-source voltage at 30 V. **B**, Output characteristics of E50Q/ZnO obtained at drain-source voltages of 30 V, for gate-source voltage varied from 0 – 30 V in 10 V steps [1].

The individual FET properties of 12 transistor units (preparation cf. Section 3.6.3) were measured and the crucial parameters, such as mobility  $\mu$ , threshold voltage  $V_{Th}$ , and on/off ratio  $I_{on/off}$ , were extracted from the output and transfer characteristics. It is noteworthy that all fabricated FET devices with corresponding TMV/ZnO hybrid material combinations

(wtTMV and E50Q) showed typical electronic transistor behavior at ambient conditions without any post-treatment (Figure 4-14).

The essential FET parameters are the on/off ratio  $I_{on/off}$ , threshold voltage  $V_{Th}$ , and the charge carrier mobility  $\mu$ .  $I_{on/off}$  gives a measure for the device's switching capability from the operational 'ON' state to the non-operational 'OFF' state (cf. Section 2.1.2.1). The threshold voltage  $V_{Th}$  is the minimum gate-source voltage  $V_{GS}$  needed to create a conducting pathway between drain and source. Considering these parameters, a clear difference is observable between wtTMV-based and E50Q-based FETs due to the virus monolayer density and homogeneity.

A distinct overall improvement of the FET performance was observed in the case of E50Q/ZnO hybrid material. The average  $\mu$  of all 12 individual E50Q-based transistors was  $2.3 \times 10^{-3} \text{ cm}^2 \text{ V}^{-1} \text{ s}^{-1}$ , in comparison to a value of  $5.9 \times 10^{-4} \text{ cm}^2 \text{ V}^{-1} \text{ s}^{-1}$  for wtTMV/ZnO-based hybrid material (Figure 4-14 and Figure 4-15).

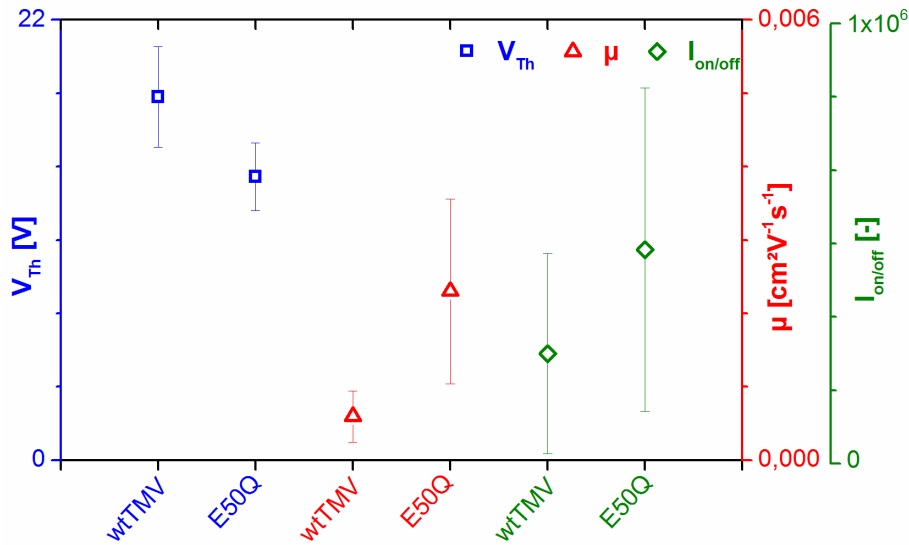


**Figure 4-15:** Averaged field-effect mobility ( $\mu$ ), threshold voltage ( $V_{Th}$ ) and on/off ratio ( $I_{on/off}$ ) of wtTMV/ZnO and E50Q/ZnO FETs, respectively, deposited from purely methanolic reaction solutions applying 10 deposition cycles. The data points represent the mean value of 12 transistor units with the standard deviation given as error bars [1].

This overall improvement of the E50Q-based transistors is accompanied by a higher  $I_{on/off}$  of  $4.8 \times 10^5$  and the smaller  $V_{Th}$  of 14.2 V, which indicates a faster and earlier switching of the device. The values for wtTMV-based FETs are an  $I_{on/off}$  of  $2.4 \times 10^5$  and  $V_{Th}$  increased to

18.1 V. This is further supported by the reduced hysteresis seen in the transfer characteristics of the E50Q/ZnO hybrid (Figure 4-14 A).

The surface coverage and density of the virus monolayer templating the mineralization have a direct influence on the amount of ZnO deposited within the active semiconductor channel region, since ZnO mineralizes selectively on the viruses (cf. Section 4.3.1). From Meulenkamp's work on ZnO nanoparticles dispersed in an electrolyte between drain and source, it is known that both film discontinuity and heterogeneity strongly influence the electron transport between the particles (interparticle) within a semiconducting ZnO thin film consisting of nanocrystals [172].

In our case, a clear change in the FET performance is observable upon the changed morphology and microstructure of the virus monolayer templating the mineralization, since E50Q leads to more homogeneous template layers compared to wtTMV. In accordance with Meulenkamp's work, a more discontinuous ZnO film results in a hindered formation of an optimum percolation pathway between drain and source, transporting the charges through the nanocrystalline film. Opposite to that, a dense ZnO film providing more interparticle connections between the nanocrystallites offers a superior pathway for the charge transfer between drain and source [173]. The robustness and defined reproducibility is highlighted in Figure 4-15, where the averaged values for  $\mu$ ,  $V_{Th}$ , and  $I_{on/off}$  of 12 transistor devices and the standard deviations are plotted [1].

### **4.3 MINERALIZATION WITH WATER-CONTAINING REACTION SOLUTION**

Prior to synthesizing thin ZnO films on virus monolayers (cf. Section 4.3.2), single immobilized wtTMV were mineralized with different water contents in the reaction solution. (cf. Section 4.3.1). In doing so, the DLS data obtained from the reaction solution (cf. Section 4.1) and thus, the differences introduced by the addition of water to the methanolic reaction solution, could be correlated with the deposition on a template. In Section 4.3.3, the results from the analysis of the reaction solution, the mineralization of single wtTMV, as well as the deposition of thin films are correlated and a deposition mechanism is suggested.

### 4.3.1 MINERALIZATION OF SINGLE TMV

Single wtTMV were immobilized (cf. Section 3.4.1) on a freshly cleaned silicon wafer and mineralized with a varying number of mineralization cycles (1 to 3) with 0, 1, 2, 3, and 5 vol% water in the methanolic reaction solution (cf. Section 3.2).

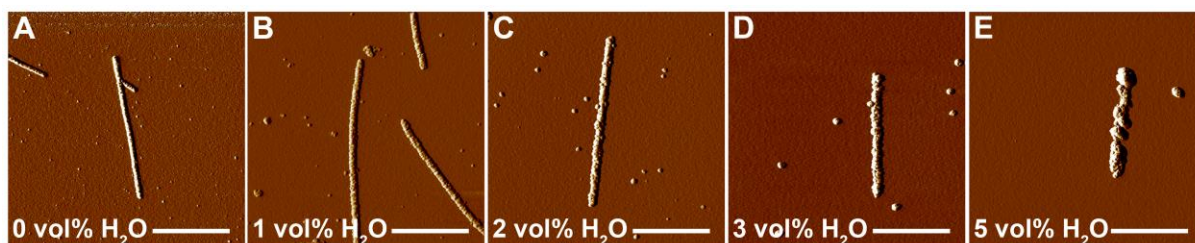


**Figure 4-16:** AFM amplitude images of wtTMV particles immobilized on silicon after one mineralization cycle with **A**, 0 vol%; **B**, 1 vol%; **C**, 2 vol%; **D**, 3 vol%, and **E**, 5 vol% water in the methanolic reaction solution. All scale bars are 500 nm.

After each mineralization step, AFM images of at least 10 individual mineralized virus particles were recorded and the average height was determined with the NanoScope Analysis software (cf. Section 3.8.3).

Since it is known from previous experiments [144] that the virus cross-section is deformed not only due to adhesion on the surface (cf. Section 2.4), but also upon treatment with temperature and methanol, reference experiments of immobilized wtTMV in pure methanol at 60°C were also conducted to determine a starting height for mineralization.

**Table 4-3:** Averaged height  $h$  of the TMV particles after different numbers of mineralization cycles (1 – 3) mineralized with varying water content in the reaction solution (0, 1, 2, 3, and 5 vol% H<sub>2</sub>O). For the average height  $h$  least 10 virus particles were measured on two different substrates for each condition (cycle number and water content) and the standard deviations were calculated. It was not possible to determine the height after the 3<sup>rd</sup> deposition cycle in the case of mineralization with 5 vol% H<sub>2</sub>O due to progressed parasitic mineralization.

	0 vol% H <sub>2</sub> O	1 vol% H <sub>2</sub> O	2 vol% H <sub>2</sub> O	3 vol% H <sub>2</sub> O	5 vol% H <sub>2</sub> O
$h$ [nm] 1 <sup>st</sup> cycle	18.9 ± 0.4	23.2 ± 0.2	32.9 ± 1.6	36.6 ± 1.3	50.6 ± 6.4
$h$ [nm] 2 <sup>nd</sup> cycle	30.7 ± 1.0	46.6 ± 2.2	46.0 ± 1.4	53.4 ± 1.2	84.2 ± 7.3
$h$ [nm] 3 <sup>rd</sup> cycle	40.1 ± 1.2	59.9 ± 1.6	71.7 ± 3.5	85.6 ± 3.1	-

Even after only one mineralization cycle with the differing water amounts, drastic differences in mineralization behavior are visible in the AFM amplitude images (Figure 4-16 A-E). In all cases, the viruses are densely and smoothly covered with nanoparticles.

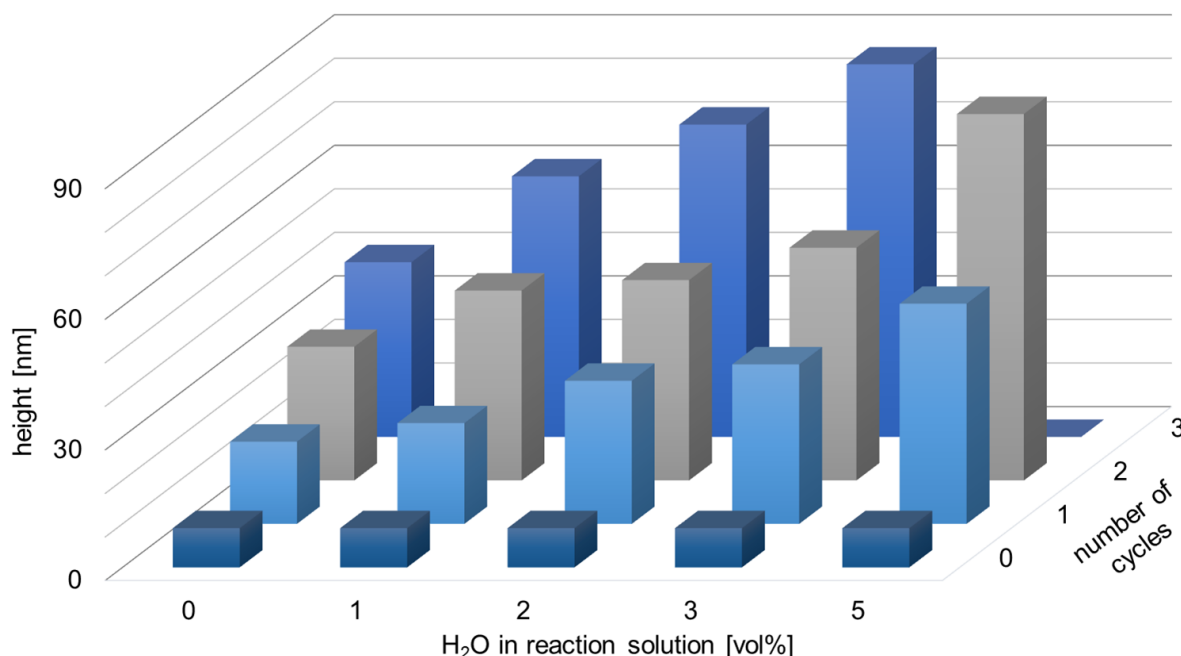


**Figure 4-17:** Evolution of the virus height determined via AFM in dependency on both the water content (0, 1, 2, 3, and 5 vol% H<sub>2</sub>O) and the number of mineralization cycles (0 – 3) as a 3D plot (lacking standard deviation, given in 2D plot in Figure 4-18). The reference height (0 mineralization cycles, c0) is always the height determined after 5 min in pure methanol at 60°C. The value of the height after 3 mineralization cycles with 5 vol% H<sub>2</sub>O could not be determined via AFM since also the parasitic particles increase in size and grow. In this case, no bare wafer area was available to measure the relative height of mineralized wtTMV to bare silicon substrate. The plotted average height was determined from at least 10 individual virus particles and 2 individual samples per condition (water content, number of cycles).

The mineralization is in all cases highly selective, i.e. mineralization occurs preferentially on the template compared to the substrate. The ZnO particles that form homogeneously in solution (cf. Section 4.1) interact with the virus template and are thus preferentially attached on the virus template, irrespective of the water content in the reaction solution. However, the roughness of the covered wtTMV templates, as well as the size of the parasitic particles on the substrate, increase with increasing water content.

This is also reflected in the quantitative evaluation of the average height of the mineralized wtTMV particles, obtained from AFM height images. The values are listed in Table 4-3 and given in two different plots of the same data in Figure 4-17 and Figure 4-18.

On the one hand,  $h$  increases linearly with the number of mineralization cycles, e.g. for 0 vol% H<sub>2</sub>O the height increases from  $18.9 \pm 0.4$  nm after the 1<sup>st</sup> cycle over  $30.7 \pm 1.0$  nm (2<sup>nd</sup> cycle) to  $40.1 \pm 1.2$  nm after the 3<sup>rd</sup> cycle (cf. Table 4-3).

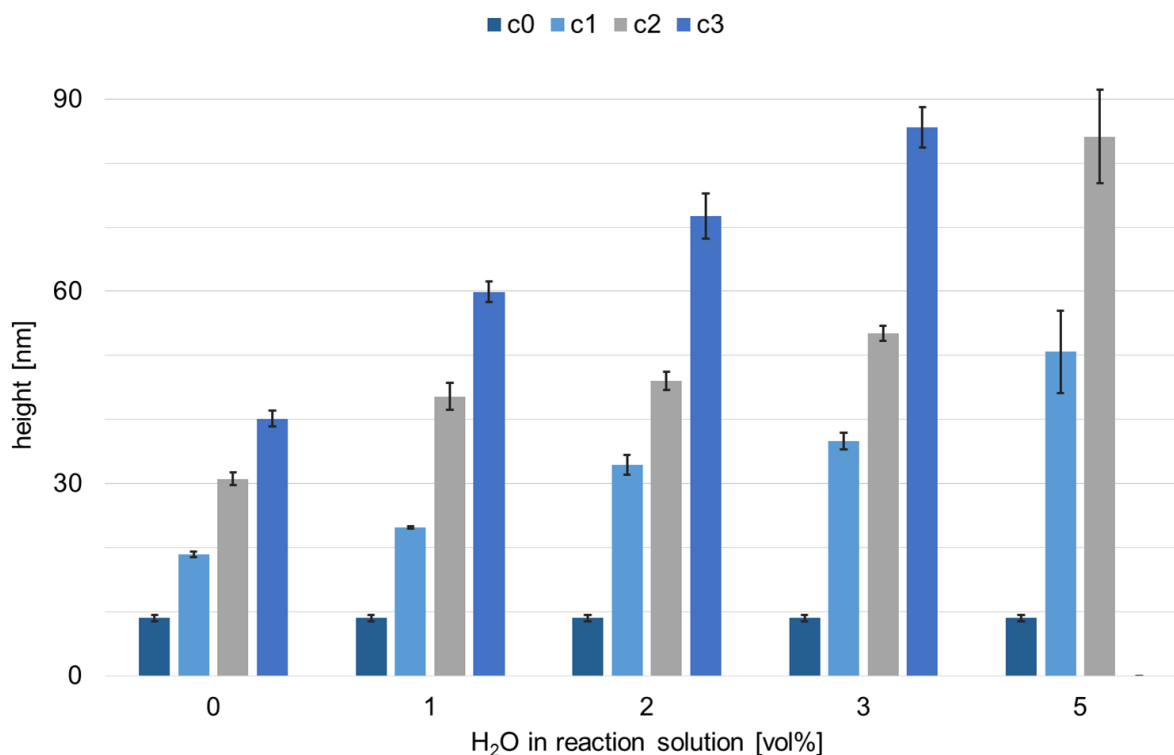


**Figure 4-18:** 2D visualization of the height evolution of mineralized wtTMV particles in dependency on both the number of mineralization cycles (c0 – c3) and the water content in the reaction solution. The same data as in Figure 4-17 are plotted, but additionally the standard deviations are given indicating the high degree of reproducibility. The averaged values plotted here were obtained from at least 10 individual virus particles and 2 individual samples per condition.

After each mineralization cycle, the solution is exchanged and new ZnO particles are formed freshly in the solution (cf. Section 4.1). These attach to the already deposited ZnO particles from the previous mineralization cycle resulting in a linear height increase with increasing number of mineralization cycles. The growth rates with 0 vol% H<sub>2</sub>O obtained here, are similar to the ones obtained with a slightly different mineralization solution without water on wtTMV [120] or on other templates, such as DNA [78].

On the other hand, the height gain per cycle rises linearly with increasing water content. This indicates that by adding water to the reaction solution, the particle size is increased due to enhanced hydrolysis of the precursors. The height values presented are the mean values of at least 10 individual virus particles on two individual substrates for each condition (Table 4-3).

The low standard deviation from the mean value (only plotted in Figure 4-18) confirms the high reproducibility. The obtained linear increase of the average height  $h$  with increasing water content at a constant number of mineralization cycles (Figure 4-17) supports the results of the hydrodynamic diameter  $D_H$  obtained by DLS experiments (cf. Table 4-1), where such a linearity was obtained as well. To compare this in more detail, a linear fit was conducted for each of the water contents, in order to determine the average growth per cycle.

**Table 4-4:** Growth per cycle  $g_c$  determined by linear fit of the measured height from c0 to c3 for each water content used. The slope then gives  $g_c$ .

H <sub>2</sub> O [vol%]	0	1	2	3	5
$g_c$ [nm cycle <sup>-1</sup> ]	11	17	20	26	38

Therefore, it was assumed that there is no difference in the deposition on wtTMV (c1) and the subsequent mineralization on ZnO (c2, c3). As a starting point for mineralization (c0), the height of wtTMV after five minutes in methanol at 60°C is used in all cases. In such a way, the average thickness increase of the deposited material with each cycle can be determined for all water contents, which is referred to as growth per cycle  $g_c$  (Table 4-4). The obtained growth per cycle  $g_c$  is then compared to the hydrodynamic diameter  $D_H$ .

The values measured for the hydrodynamic diameter  $D_H$  (cf. Table 4-1) in solution via DLS correspond to the particle size assuming a spherical particle plus the hydration sphere [155] around the particles (Figure 4-19 A, B). The growth per cycle  $g_c$  indicates the increase in ZnO layer thickness per mineralization cycle (Figure 4-19 C-E). This does not necessarily mean that only one particle monolayer is deposited, but also more particles may be attached filling voids between the first deposited layer (Figure 4-19 D).

The herein measured values of  $D_H$  are in all cases (except for 0 vol% H<sub>2</sub>O) smaller than the determined growth per cycle  $g_c$  by AFM. Since the  $D_H$  values are measured in solution via DLS, the values are obtained with the assumption of spherical particles, which have a hydration



sphere [155], one can draw several conclusions. The actual particle size is smaller than  $D_H$  in solution due to the also measured hydration sphere (visualized in Figure 4-19 A, B).

The growth per cycle  $g_c$  is always bigger than the value for  $D_H$  measured in solution. This indicates that not a single monolayer of the formed species is deposited on the virus template (Figure 4-19 C), but possibly interstitials are filled as given in Figure 4-19 D. Especially in the case of 5 vol% H<sub>2</sub>O, the effect is pronounced and indicates nearly a double layer deposited.

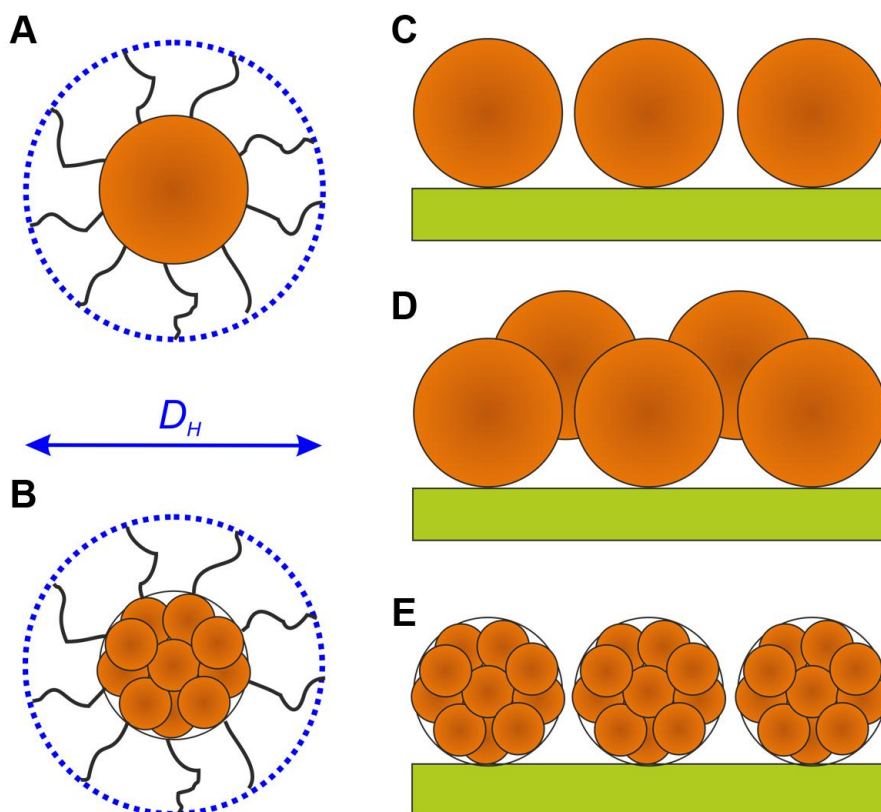


**Figure 4-19:** Visualization of the hydrodynamic diameter  $D_H$  for a ZnO nanocrystallite (A) and an agglomerate of the same size consisting of smaller crystallites (B). Three different possibilities for growth per cycle  $g_c$  on TMV particles (green). Either a monolayer of ZnO nanocrystallites can be deposited (C), or free interstitial space can be filled with a second layer (D) or a monolayer of agglomerates consisting of smaller crystallites can be deposited (E). Additionally, interstitial space can also be filled in the case of agglomerates (not depicted).

However, from the DLS and AFM measurements, it is still not possible to conclude, whether the formed species in solution that are subsequently deposited on the TMV consist of smaller crystallites forming stable agglomerates of constant size (Figure 4-19 E), or whether the measured size corresponds to the crystal size (Figure 4-19 D). To answer this question, the values obtained from solution and the mineralization of single virus templates will be correlated with the calculated data from thin films (cf. Section 4.3.2.3).

Additionally, it is difficult to tell exactly how much material is deposited during the crucial first mineralization cycle, when the template influence is the most pronounced from the AFM measurements, since only a combination of the height of both virus and deposited material is measured. From the reference measurements in pure methanol at 60°C it is known that the virus structure contracts fast within the first 5 minutes due to heat and solvent treatments resulting in a decreased height of only 9 nm. After longer exposure to pure methanol (15 minutes), the height is not further changed [144]. However, it is not detectable, whether the TMV structure shrinks before the first deposition of ZnO particles or whether the deposition of ZnO occurs simultaneously with the shrinking.

### 4.3.2 MINERALIZATION OF THIN FILMS

In order to synthesize functional thin ZnO films, film formation in dependency of the water content and the template needs to be investigated. For this purpose, thin films were prepared with the same number of cycles (20 mineralization cycles), but varying water content (0 – 3 vol% H<sub>2</sub>O) on wtTMV. Virus monolayers were obtained with the optimized convective assembly (CA) conditions ( $c = 5 \text{ mg mL}^{-1}$  and  $v_w = 1.2 \text{ mm min}^{-1}$ ) of Section 4.2.

The overall film thickness increases by raising the water content in the reaction solution and leaving the mineralization cycles constant, as can be seen from the SEM cross-section images (Figure 4-20 A-D) and the quantitative evaluation in Table 4-5. The thickness of the films increased from  $124 \pm 4 \text{ nm}$  in the absence of water to  $306 \pm 6 \text{ nm}$  with 3 vol% H<sub>2</sub>O in the reaction solution.

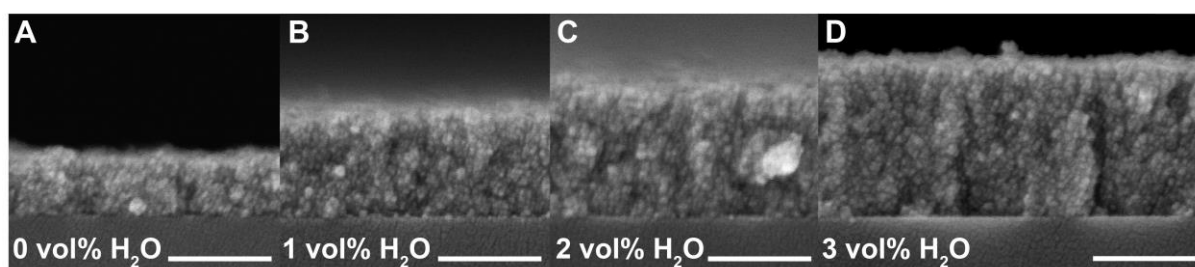


**Figure 4-20:** SEM cross-sections of thin ZnO films on wtTMV monolayers produced via convective assembly (CA,  $c = 5 \text{ mg mL}^{-1}$  and  $v_w = 1.2 \text{ mm min}^{-1}$ ) after 20 mineralization cycles with **A**, 0 vol%; **B**, 1 vol%; **C**, 2 vol%, and **D**, 3 vol% H<sub>2</sub>O in the methanolic reaction solution. All scale bars represent 200 nm. Samples were sputtered with 0.5 nm Pt:Pd (80:20).

The increase in film thickness indicates that the water added to the methanolic reaction solution accelerates the hydrolysis of the precursor, leading to an increase in particle size, and might also affect the number of nuclei formed in solution. Thus, the deposited films possibly increase in thickness due to the larger particles being deposited (cf. DLS results in Section 4.1). The SEM cross-section images (Figure 4-20 A-D) show that all films were nanoporous, smooth, exhibited a homogeneous thickness over the entire sample and showed very good adhesion on the substrate. The nanopores result from the homogeneous nucleation process in solution and subsequent attachment of the formed particles, leaving behind some voids. Since the samples are not further temperature-treated, these pores are not closed by diffusion and sintering.

**Table 4-5:** Resulting film thickness  $t$  of ZnO films after 20 mineralization cycles with varying water content in the reaction solution (0 – 3 vol% H<sub>2</sub>O). The growth per cycle  $g_{c,SEM}$  was determined by subtraction of the virus height after methanol treatment (9 nm) and dividing by the number of cycles assuming linear growth behavior.

H <sub>2</sub> O [vol%]	0	1	2	3
$t$ [nm]	124 ± 4	198 ± 3	248 ± 3	306 ± 6
$g_{c,SEM}$ [nm cycle <sup>-1</sup> ]	6	10	12	15

The growth per cycle  $g_{c,SEM}$  was calculated from the measured thicknesses (Table 4-5) of the cross-section SEM images (Figure 4-20 A-D) by subtraction of the thickness of the TMV monolayer and division by the number of mineralization cycles. The obtained values correlate well with the results of both DLS (cf. Table 4-1) and AFM (cf. Table 4-4) investigations.

#### 4.3.2.1 FILM COMPOSITION AND TEXTURE

X-ray diffraction (XRD) investigations were performed on the films deposited from reaction solutions with varying water content to ensure the formation of ZnO.

XRD investigations revealed the formation of nanocrystalline ZnO (Figure 4-21). The typical three reflections (100; 002; 101) of the hexagonal wurtzite structure of ZnO are observed. The broadening of the reflections indicated the formation of nanometer-sized crystallites. A Scherrer analysis was performed in order to determine the crystallite size of the obtained films. The resulting crystallite sizes are given in Table 4-6, revealing an increase of the obtained

crystallite size  $D_{XRD}$  with increasing water content indicating the enhanced hydrolysis of the precursors in the reaction solution favoring crystallite growth.

This is in good accordance with the results for water-dependent development of the particle size obtained from DLS (cf. Table 4-1), AFM (cf. Table 4-4), and SEM cross-sections (cf. Table 4-5). However, the accuracy of the data, especially in the case of the sample prepared without water in the reaction solution, is low, due to the low signal-to-noise ratio and the overall very low intensity of the reflections and their broadness due to the nanocrystalline character of the samples.

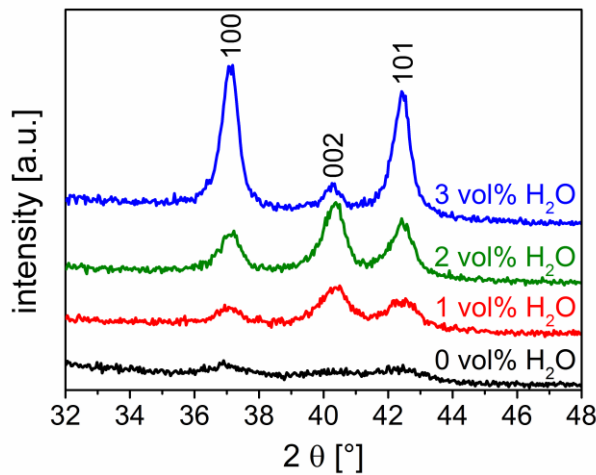


**Figure 4-21:** XRD patterns of the films obtained after 20 mineralization cycles with different water content. In all cases, ZnO is formed in the wurtzite structure. However, for 1 and 2 vol% H<sub>2</sub>O, the intensity of the 002 reflection is increased, compared to the ones of 100 and 101 indicating a 002 texture of these samples. Whereas, the relative intensity ratio indicates a 100 texture of the sample prepared with 3 vol% H<sub>2</sub>O in the reaction solution.

The XRD patterns in Figure 4-21 reveal not only the formation of ZnO in wurtzite structure, but also the striking fact that the texture of the formed films changes with increased water content. In a randomly oriented ZnO powder the ratio of the relative intensities of the 002 and 001 reflections is approximately 0.7 (cf. Section 2.1.2 and Figure 2-2 B).

**Table 4-6:** Resulting crystallite sizes  $D_{XRD}$  of the Scherrer analysis of the ZnO films prepared with different water content in the reaction solution.

H <sub>2</sub> O [vol%]	0	1	2	3
$D_{XRD}$ [nm]	3 ± 1	7 ± 1	10 ± 1	15 ± 1

The reflections of the film prepared without water can hardly be seen, whereas the samples prepared with 1 and 2 vol% water in the reaction solution show an enhanced relative intensity of the 002 reflection, compared to the ones of 100 and 101, clearly indicating a preferential attachment of the crystallites in *c*-axis direction leading to a 002 texture.

By addition of 3 vol% H<sub>2</sub>O, the texture is changed to a 100 texture. This effect of texture-tuning by variation of the water content was not only observed on wtTMV, but also on NH<sub>2</sub>- and COOH-SAMs. This indicates that the tuning is mostly induced by the reaction solution. However, the degree of texture differs on the various templates which will be dealt with below (cf. Section 4.3.3).

In general, the growth kinetics of different crystal planes vary in a crystal. This leads after nucleation and incubation to a distinct macroscopic shape with well-defined low index crystallographic faces. ZnO has three types of fast growth directions:  $\langle 2\bar{1}0 \rangle$ ,  $\langle 010 \rangle$  and  $\langle 001 \rangle$  [16]. It is well-known that ZnO precipitated from aqueous solutions forms crystals elongated in *c*-axis, since the crystals tend to maximize the areas of the nonpolar  $\{2\bar{1}0\}$  and  $\{010\}$  facets that have a lower energy than the  $\{001\}$  facets [16].

Thus, textured ZnO films are rather easily obtained due to the preferential growth in *c*-axis, i.e.  $\langle 001 \rangle$  direction. The tendency of ZnO to form textured layers without epitaxial growth conditions is referred to as 'self-texture'. Such films are, for instance, obtained by sol-gel synthesis [174] on seeded substrates by combining successive ion layer absorption reaction (SILAR) and chemical bath deposition (CBD) [175], and also via metalorganic chemical vapor deposition (MOCVD) [176–179]. Especially in the case of the MOCVD process, the deposition parameters can be varied in such a way that the *c*-axis texture flips to an *a*-axis texture. This is usually realized by variation of the ratio of H<sub>2</sub>O and diethylzinc [179]. The same changes of texture by variation of experimental parameters can be found for sputtered thin ZnO films. Kajikawa summarizes these findings and reports that parameter changes like, amongst others, the negative bias voltage, the distance between target and substrate, and the pressure can change the texture, in most cases from *c*-axis to *a*-axis [180]. However, these reactions are CVD processes, thus, the reactive species are gases and the reaction takes place at reduced pressures and elevated temperatures, whereas the herein reported texture changes occur in a solution-based process. Therefore, a direct comparison is not possible.

PVP was added to the methanolic reaction solution to control crystal growth which resulted in nanometer-sized crystallites (cf. Table 4-6). This was also reported by others using similar reaction systems [154,181]. Jia *et al.* assumed that PVP slows down particle growth, but maintains the same growth rates of the individual planes. Thus, the building units for the films still have distinct crystalline facets [181].

In order to gain further information on the causes of texture changes induced by water in this work, it was attempted to obtain information about the shape of the formed crystallites: It is possible to determine the crystallite size along different crystallographic axis (cf. Section 3.8.6).

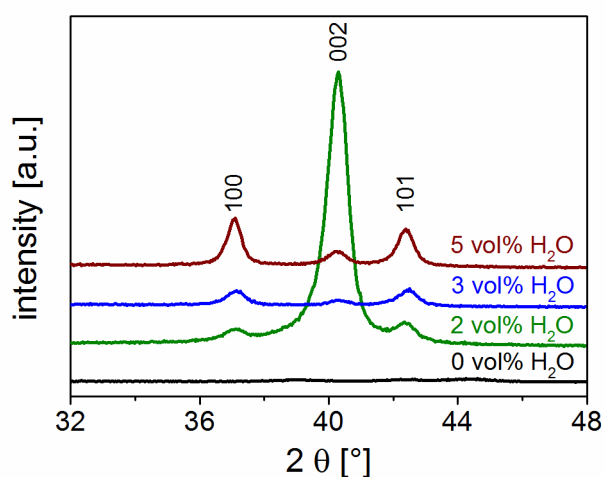


**Figure 4-22:** XRD patterns of thick ZnO films prepared with varying water content in the reaction solution. The thickness was adjusted by variation of the number of mineralization cycles (100 deposition cycles for 0 vol%; 80 for 2 vol% H<sub>2</sub>O, 60 for 3 vol%, and 15 for 5 vol% H<sub>2</sub>O) to reach thicknesses in the range of 1 μm.

However, these analyses require sharp reflections and a low signal-to-noise ratio in order to get accurate results. Thus, only XRD data of thick samples leading to high signal intensities could be analyzed (Figure 4-22). Applying 100 mineralization cycles with 0 vol% H<sub>2</sub>O led to films with a thickness of around 500 nm with still insufficient intensity of the reflections for crystallite anisotropy determination. Consequently, no information on the shape of the crystallites is available for 0 vol% H<sub>2</sub>O.

When adding water, less mineralization cycles are necessary to achieve ZnO film thicknesses above 1 μm due to the enlarged crystallite size upon addition of water to the reaction solution.

Therefore, the analysis was performed for 2 vol% H<sub>2</sub>O applying 80 cycles, for 3 vol% H<sub>2</sub>O applying 60 cycles and 5 vol% H<sub>2</sub>O applying 15 cycles (Figure 4-22).

Only the film deposited with 2 vol% H<sub>2</sub>O exhibited a 002 texture (*c*-axis), whereas a 100 texture is observed for 3 and 5 vol% H<sub>2</sub>O by comparing the relative intensities of the reflections. The direction-dependent crystallite size analyses show an increase of the anisotropy with increasing water content. The anisotropy factor *A*, which is given by the ratio of the crystallite size in [100] direction to the crystallite size in [002] direction, increases from  $A_{2\text{ vol}\%} = 1.3$ ,  $A_{3\text{ vol}\%} = 1.4$  to  $A_{5\text{ vol}\%} = 1.6$ .

The ideal anisotropy ratio of ZnO is 0.6 resulting in a crystal shape as given in Figure 4-23 A. The indicated anisotropy, measured for the herein used system, shows that with increasing water content the structure moves further away from the ideal shape more to flatter shape of the crystallites (Figure 4-23 C, D).

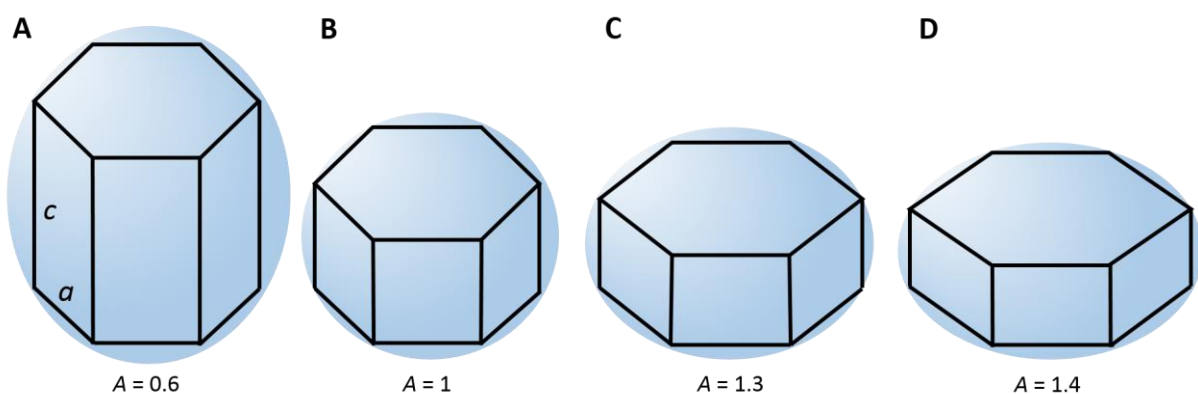


**Figure 4-23:** Schematic drawing of hexagonal ZnO crystallites with varying anisotropy factors. **A**, the ideal ratio of 0.6 resulting of the wurtzite structure. **B**, anisotropy ratio of 1 if  $a = c$ . **C**, anisotropy factor of 1.3 as it is determined for 2 vol% H<sub>2</sub>O leading to a 002 texture of the film and **D**, representing an anisotropy factor of 1.4 as it is determined for 3 vol% H<sub>2</sub>O resulting in a 100 texture of the film.

When increasing the water content further, the crystallites grow in [100] direction, which is in contrast to the expected preferential growth in *c*-axis direction. There are many reports that structure-directing additives in the solution can attach to the polar surface and thus hinder the preferential crystal growth, e.g. citrate ions [182] or gelatin [183].

Moreover, it is reported by Wang *et al.* that the addition of water to a purely methanolic reaction solution strongly influences the shape of the formed ZnO crystallites [184]. They state

(1) that the polar H<sub>2</sub>O molecules are attracted to ZnO's polar facets hindering further growth in the [001] direction, and (2) that the growth in [100] direction is accelerated leading to platelet-like structures [184].

However, in this work the situation is more complex by the combined influences of PVP and water. It might be the case that the PVP present in this system and as well the addition of water act as such a structure-directing additives and hinder the growth in *c*-axis leading to an elongation of the particles in [100] direction.

With low water content, especially for 2 vol% H<sub>2</sub>O, the particles are less anisotropic which seems to favor the attachment of the polar plane perpendicular to the *c*-axis, leading to the typical 'self-texture' of ZnO as can be seen from the XRD patterns (cf. Figure 4-22).

Yet, for higher water contents, the particles get a bit flatter resulting in a slightly bigger polar plane as it is also reported by Wang *et al.* [184]. Paradoxically, the crystallites formed in solution attach preferentially with their nonpolar plane, even though the contact area with the polar plane is bigger. This leads to a 100 texture of the films with a water content higher than 2 vol%. The cause of this paradox attachment cannot be answered within the scope of this work.

However, it has to be taken into account that with increased texture, the intensities of the other reflections decrease. In the case of the 002 texture, this means that the crystallite size determination works well along the *c*-axis due to the high intensity of the 002 reflection and is less accurate in [100] direction due to the low intensity of the 100 reflection.

#### **4.3.2.2 OPTICAL PROPERTIES**

The measured room temperature photoluminescence of the films, prepared from the water-containing methanolic reaction solution confirmed the formation of nanocrystalline ZnO as well as the previously performed XRD measurements (cf. Section 4.3.2.1). Upon excitation at  $\lambda_E = 310$  nm, the near band edge UV emission, as well as the broad emission in the visible light were observed (Figure 4-24 A). The deep band emission in the visible regime is attributed to defects (cf. Section 2.1.2.3).



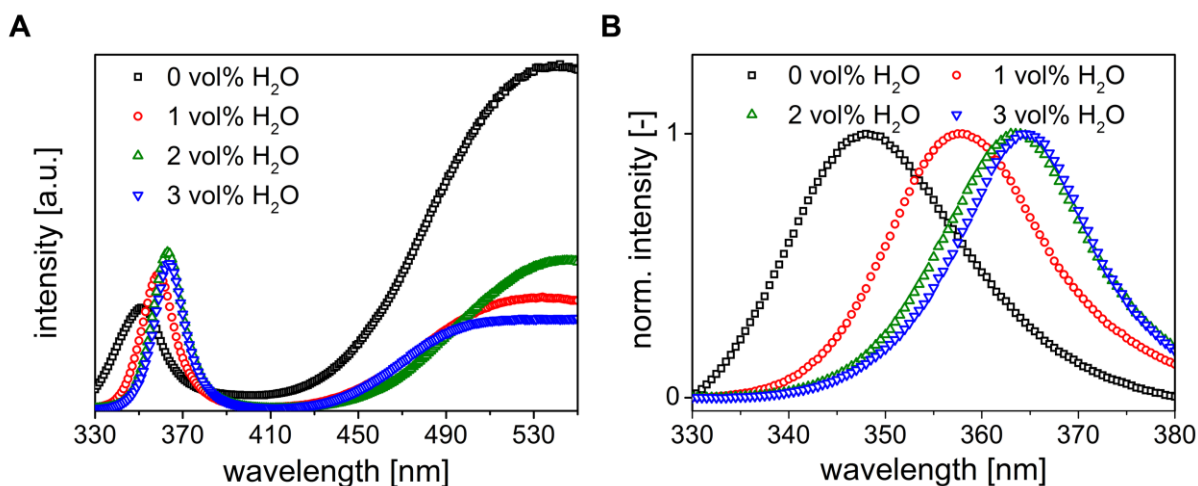


**Figure 4-24:** **A**, Photoluminescence ( $\lambda_E = 310$  nm) of ZnO films prepared with varying water content (0 – 3 vol% H<sub>2</sub>O, 20 deposition cycles), without post-treatment. **B**, Photoluminescence ( $\lambda_E = 310$  nm) of the UV emission maximum of ZnO films prepared with 0 – 3 vol% H<sub>2</sub>O (20 deposition cycles), without post-treatment. The intensities of the UV emission maxima were normalized to 1 to clearly show the red-shift due to increased crystallite size in more detail.

Especially in nanocrystalline films, there are a large number of interfaces leading to a high number of defects and intensive emission in the visible regime. To prove the contribution of defects to deep level emission one set of samples, prepared with 1 vol% H<sub>2</sub>O in the reaction solution, was annealed in air at 150°C and 400°C.

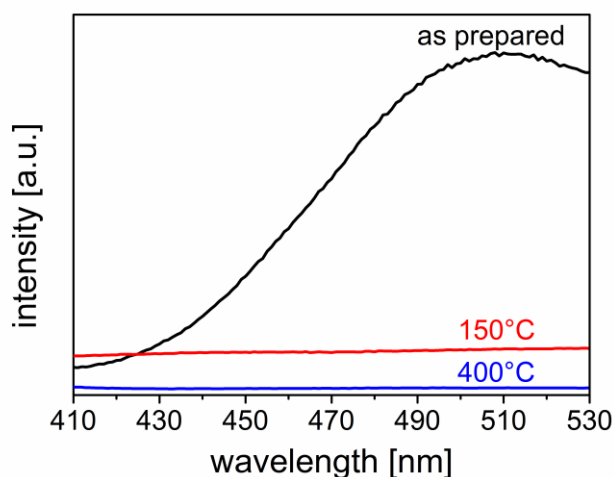


**Figure 4-25:** Photoluminescence ( $\lambda_E = 310$  nm) of a ZnO film as prepared and after four hours annealing in air at 150°C and 400°C, respectively. Samples were prepared with 1 vol% H<sub>2</sub>O in the reaction solution and 30 deposition cycles.

Upon annealing, the broad emission in the visible region vanishes (Figure 4-25). Since these deep band emissions are attributed to singly ionized oxygen vacancies [41,42], annealing in air leads to a filling of the vacancies and, thus, eliminates the defect states causing the deep band emission.

The strong UV luminescence of the films synthesized in the presence of water (Figure 4-24) in particular provides evidence of a good crystal quality of the nm-sized ZnO crystals. The addition of water to the reaction solution causes not only an increased intensity of the UV emission compared to the deep band emission, but also a red-shift of the position of the UV emission, indicating bigger crystallite sizes with increased water addition.

**Table 4-7:** Resulting crystallite sizes  $D_{PL}$  by calculation from the position of the UV emission maxima  $E^*$  according to equation (2-6). The corresponding ZnO films were prepared with different water content in reaction solution on wtTMV monolayers obtained via convective assembly. Maxima were determined with the systems software for several samples of each reaction condition in order to obtain the averaged maxima and their standard deviation.

H <sub>2</sub> O [vol%]	0	1	2	3
$E^*$ [nm]	354.9 ± 5.0	358.3 ± 2.1	361.3 ± 1.6	363.4 ± 1.3
$D_{PL}$ [nm]	10 ± 2	11 ± 1	14 ± 2	17 ± 3

Additional scans of the UV emission with smaller increments and higher integration times (cf. Section 3.8.7) were collected (Figure 4-24 B) to determine the red-shift of the UV maxima more accurately. With the help of equation (2-6), the crystallite size can be calculated dependent on the position of the UV emission maximum [43]. The calculated crystallite sizes  $D_{PL}$  of the corresponding UV maxima  $E^*$  are given in Table 4-7.

The calculated crystallite size  $D_{PL}$  of the photoluminescence data confirms the enlarged crystallites obtained by addition of water to the reaction solution. The determination of the position of the UV maximum was the least accurate for the sample without water. The standard deviations were highest in this case (Table 4-7).

The determination of the UV maxima gets more accurate with increasing water content, indicating better reproducibility. However, the increased accuracy of the UV maxima (lower standard deviations) is not reflected in more accurately calculated crystallite sizes  $D_{PL}$  (no reduction of the standard deviations, Table 4-7).

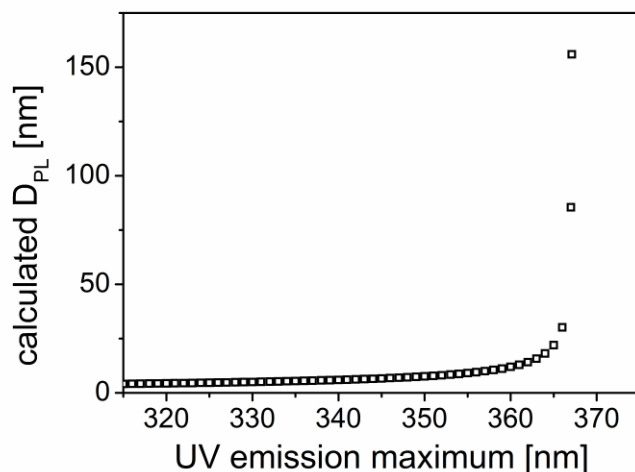


**Figure 4-26:** Visualization of equation (2-6) showing the obtained calculated crystallite size  $D_{PL}$  in dependency of the determined UV emission maximum, revealing a strong non-linearity towards higher values of the UV emission maximum.

This can be explained when taking a closer look at the equation (2-6) (cf. Section 2.1.2.3) used to determine the crystallite size. The equation (2-6) was solved for the diameter  $D_{PL}$ , plotted and visualized in Figure 4-26 revealing non-linear behavior for higher values of the UV maxima leading to a discontinuity of the equation above 367.2 nm.

Thus, for increasing values of the UV maximum, the changes of the calculated  $D_{PL}$  are more pronounced. Whereas a shift of the UV maximum from 349 to 350 nm changes the  $D_{PL}$  from 7.4 to 7.6 nm, the shift from 361 to 362 nm already increases the  $D_{PL}$  from 12.9 to 14 nm. This effect is even more pronounced for higher values of the UV maximum. Shifting the maximum from 365 to 366 nm changes the  $D_{PL}$  from 22.0 to 30.2 nm. For values above 367.2 nm, the formula is not valid any more due to discontinuity of the equation.

Even though the determined maxima are more accurate for higher water contents (the deviation is reduced from 5 nm to 1.3 nm, cf. Table 4-7), the standard deviation of the calculated crystallite size gets bigger. Since the values for the maxima differ not only on different spots of one sample, but also from sample to sample by roughly 0.5 to 1 nm (prepared under the same conditions), the absolute values obtained by this method are not as precise as e.g. the AFM measurements of the height increase (cf. Table 4-3). Thus, this inaccuracy of the calculated data from PL experiments has to be taken into account when comparing the data with values obtained by other measurement techniques.

The overall trend of larger particles/crystallites cannot only confirmed by PL data, but also in the case of DLS measurements of the reaction solution (cf. Section 4.1), AFM on single mineralized TMV (cf. Section 4.3.1), SEM of layers, and values calculated by Scherrer analysis from XRD data (cf. Section 4.3.2.1). In the following, the obtained data will be correlated in order to determine the growth mechanism in dependency of the water content.

#### 4.3.2.3 CORRELATION OF PARTICLE AND CRYSTALLITE SIZE

Various complementary techniques, such as DLS, AFM, SEM, XRD, and PL, were used to analyze the species formed in the reaction solution and on the template. The mineralization procedure used in this work was adapted from the procedure developed by Lipowsky *et al.* [25,26]. As mentioned in Section 2.1.1, Lipowsky *et al.* suggested three stages of particle formation (cf. Figure 2-1). The herein obtained results are in good accordance with the findings of Lipowsky *et al.* [26].

**Table 4-8:** Particle and crystallite sizes determined by DLS ( $D_H$ ), AFM ( $g_c$ ), SEM ( $g_{c,SEM}$ ), XRD ( $g_{c,SEM}$ ) and PL ( $D_{PL}$ ) in dependency of the water content in the reaction solution.

H <sub>2</sub> O [vol%]	0	1	2	3
$D_H$ [nm]	11 ± 3	12 ± 2	15 ± 2	19 ± 1
$g_c$ [nm cycle <sup>-1</sup> ]	11	17	20	26
$g_{c,SEM}$ [nm cycle <sup>-1</sup> ]	6	10	12	15
$D_{XRD}$ [nm]	3 ± 1	7 ± 1	10 ± 1	15 ± 1
$D_{PL}$ [nm]	10 ± 2	11 ± 1	14 ± 2	17 ± 3

Due to the fluctuations in the beginning of the DLS measurements (Figure 4-1), the formation of amorphous transient ZnO needles could not be proven in these experiments. However, the intermediate and the final states (cf. Figure 4-1) mentioned by Lipowsky *et al.* were clearly reproducible, for water-containing reaction solutions as well. Moreover, all measurement techniques confirmed the trend of increased particle/crystallite sizes with increasing water content in the reaction solution (Table 4-8). Prior to comparing the results of the different techniques, several differences have to be taken into account which are all mentioned individually above. (1) DLS measurements detect the hydrodynamic diameter  $D_H$ , thus, the crystallite or agglomerate with its hydration sphere (cf. Figure 4-19). (2) The growth per cycle  $g_c$  determined via AFM is averaged linearly over the first 3 cycles and has no clear starting

point due to the height decrease upon immersion into the reaction solution from 15 nm to 9 nm [144]. However, it is very accurate in determining the height in the early mineralization cycles. (3) The calculated growth per cycle  $g_{c,SEM}$  determined from the thicknesses of the SEM cross-sections assumes linear growth, thus, it was not differentiated between early template-controlled stages and later ZnO on ZnO deposition. (4) Calculated crystallite size  $D_{XRD}$  via Scherrer analysis is less accurate for thin films due to low signal-to-noise ratio and the overall small crystallite size. (5) For larger crystallite sizes  $D_{PL}$ , equation (2-6) loses its linear character and slight differences in the UV emission maximum lead to pronounced differences in crystallite size.

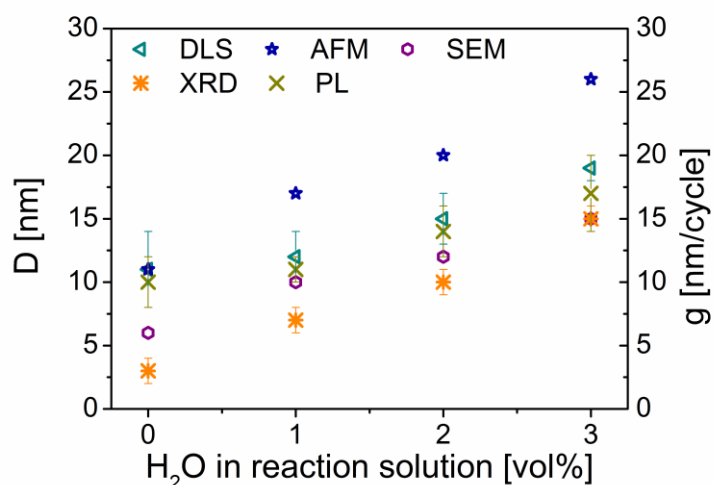


**Figure 4-27:** Plot of the particle/crystallite size and growth per cycle determined with various measurement techniques (DLS, AFM, SEM, XRD and PL) in dependency on the water content in the reaction solution. DLS data were obtained from the reaction solution (cf. Section 3.8.1). AFM was carried out on single mineralized wtTMV particles (cf. Section 3.4.1). SEM, XRD, and PL data were collected from ZnO films deposited on wtTMV monolayers obtained via convective assembly (cf. Section 3.4.2).

All measurement techniques confirm a linear growth of the obtained particle/crystallite size with increasing water content (Figure 4-27). Since the crystallite sizes calculated from both XRD and PL do not differ much and are always only slightly smaller than the hydrodynamic diameter obtained by DLS, one can conclude that no agglomerates are measured by DLS in the reaction solution, but single crystalline particles. This is in contrast to the findings of Lipowsky *et al.*, who detected agglomerates ( $\approx 20$  nm) of their ZnO species in both DLS and TEM investigations [26].

However, the ZnO species obtained by Lipowsky's approach were smaller (in a range of  $\approx 5$  nm) [25] than the herein reported particles. Thus, the smaller particles have a higher tendency to agglomerate in order to minimize surface energy. Apparently, the increased particle size obtained upon modifying the mineralization procedure led to a stabilization of the particles against agglomeration in solution during the reaction time of 90 minutes.

It is striking, that the AFM investigations differ from this behavior. Here, the growth per cycle is larger than the measured crystallite size. This effect is more pronounced for higher water contents, especially if the 5 vol% samples are taken into account (cf. Figure 4-1 and Figure 4-17). These findings of the AFM investigations suggest that during the early mineralization cycles, which are template-dominated, more than one crystallite layer is deposited. However, there are difficulties in gaining further information on the template control of the ZnO deposition. (1) AFM height investigations cannot be further extended to more cycles, since parasitic mineralization on the silicon wafer increases with the cycle number. Thus, relative height measurements between mineralized wtTMV particles and bare silicon wafer are impossible. (2) Since, template control is not clearly seen in the data obtained from SEM cross-sections after 20 mineralization cycles (cf. Figure 4-20 C) as well, more data is necessary. Thus, additional cross-section samples were prepared with 2 vol% water in the reaction solution.

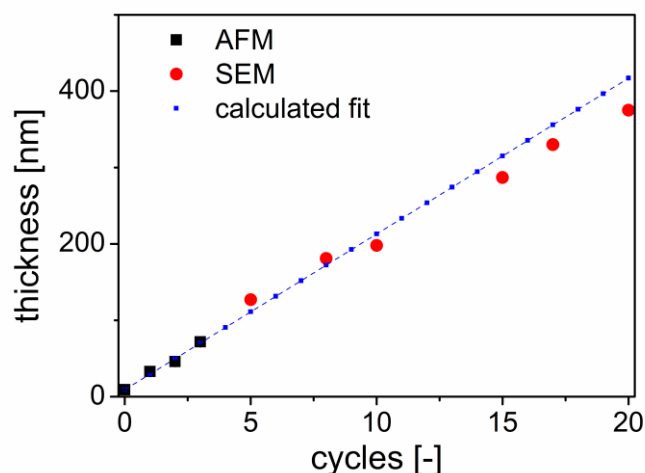


**Figure 4-28:** Comparison of the thickness of the mineralized layers obtained by AFM and SEM analyses for varying mineralization cycles. Additionally, the calculated linear fit to the height determined by AFM of the first three mineralization cycles is plotted. All samples were deposited with 2 vol% H<sub>2</sub>O in the reaction solution.

Figure 4-28 shows that the correlation of the AFM and SEM data works well. The linear slope fitted to the AFM data matches well to the thicknesses determined from additional SEM cross-sections after 5, 8, and, 10 mineralization cycles, respectively. For thicker films (15, 17 and, 20 mineralization cycles), the measured data from SEM cross-sections is lower than the predicted thickness from the linear fit. This correlates well with the fact that for thick films the template effect is not observable and only ZnO is deposited on ZnO with lower growth rates.

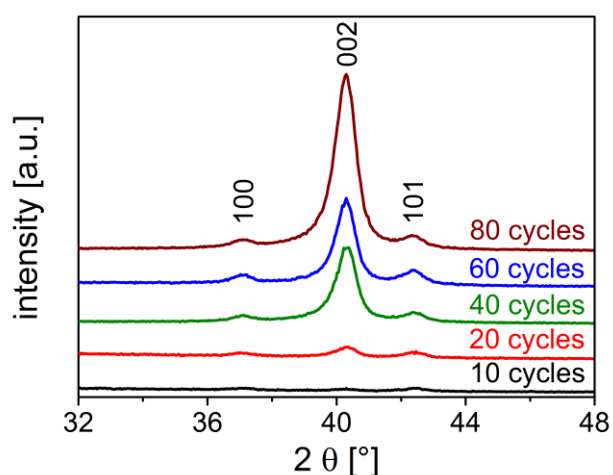


**Figure 4-29:** XRD patterns of ZnO films deposited on wtTMV from reaction solutions with 2 vol% H<sub>2</sub>O applying various deposition cycles (10 – 80 cycles) to obtain films with increasing thickness. With increasing film thickness, the 002 reflection's relative intensity increases compared to the intensities of the 100 and 101 reflections, indicating an increased texture with increasing film thickness.

XRD analyses of this series of films prepared with 2 vol% H<sub>2</sub>O in the reaction solution and varying film thickness, revealed a thickness dependency of the texture. The number of mineralization cycles was increased from 10 over 20, 40, and 60 to 80 (Figure 4-29). The XRD patterns reveal an increase of the 002 reflection's relative intensity with increasing film thickness compared to the intensities of both 100 and 101 reflections. In order to have a measure for the preferred *c*-axis orientation of the ZnO crystallites, the ratio of the integrated intensity of the 002 and 100 reflection is determined as described in Section 3.8.6. For a random powder with no preferred orientation, this ratio would be close to 0.7 (cf. Section 2.1.2 and Figure 2-2 B). In the following this ratio will be referred to as *T*, the texture coefficient.

In Table 4-9, the texture coefficients  $T$ , determined from the diffraction patterns given in Figure 4-29, are listed. For the thinnest film, the signal-to-noise ratio is the weakest, thus the fitted data is not very accurate. Therefore, for the thin film, only a small degree of  $c$ -axis orientation can be assigned from this data. However, with increasing film thickness, the texture coefficient increases strongly confirming quantitatively the trend visible in Figure 4-29.

Since X-rays penetrate into the film, also the initially formed less oriented areas (as can be seen after 10 cycles) contribute to the measured signal. The signal is thus a combination of areas with smaller degree of orientation in the substrate-near region and areas with increasing texture with increasing film thickness. In order to clarify whether it is possible to collect only signals from the very well oriented surface area by more surface sensitive grazing incidence measurements, the average information depth of a ZnO film measured under the smallest possible grazing incidence angle was estimated with the equations given in [185] and was found to be larger than the film thickness even for samples thicker than 1  $\mu\text{m}$ . Thus, the XRD patterns of the most textured surface-near area are not accessible, which possibly show a higher degree of texture. However, already the convoluted signal of areas close to the surface and those closer to the template show the thickness-dependency of the texture (cf. Figure 4-29).

**Table 4-9:** Texture coefficients  $T$  obtained from fitted XRD data of the films deposited from reaction solutions containing 2 vol%  $\text{H}_2\text{O}$  with varying film thickness.

Deposition cycles	10	20	40	60	80
$T$	1.0	6.1	12.7	11.1	17.8

The results from the thickness-dependent XRD analyses suggest that under the given experimental conditions (2 vol%  $\text{H}_2\text{O}$  in the reaction solution) the formed crystallites orient themselves preferentially to the template in such a way that a preferred  $c$ -axis orientation occurs. The orientation is not perfect in the early stages of the deposition (or at least not detectable with XRD due to low intensities), but with increasing thickness an ordering effect occurs, resulting in a more pronounced texture of the following deposited layers.



### 4.3.3 DEPOSITION MECHANISM

Applying the same number of deposition cycles, pronounced differences were observed when mineralizing SAMs and wtTMV monolayers. The XRD patterns of these ZnO films prepared on  $\text{NH}_2$ - and  $\text{COOH}$ -SAMs, as well as on wtTMV monolayers, exhibit differences in the degree of texture (Figure 4-30), i.e. the texture coefficient  $T$ .  $T$  is determined as the ratio of the integrated intensity of the 002 reflection divided by the integrated intensity of the 100 reflection. The texture coefficient  $T$  is strongly increased in the case of wtTMV ( $T_{wtTMV} = 12.7$ ), whereas the values for the SAMs ( $T_{\text{NH}_2} = 9$  and  $T_{\text{COOH}} = 5.9$ ) are lower [2].

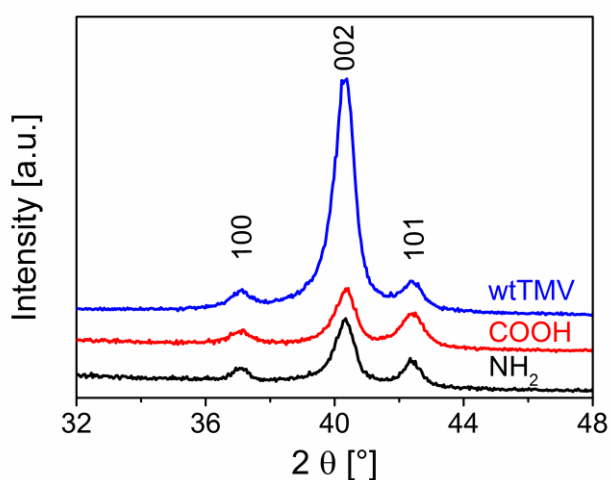


**Figure 4-30:** XRD patterns of films deposited from reaction solutions with 2 vol%  $\text{H}_2\text{O}$  on three different templates:  $\text{NH}_2$ -SAM,  $\text{COOH}$ -SAM, and wtTMV monolayer immobilized via CA. All samples were synthesized applying 40 deposition cycles.

In order to explain these differences in the degree of texture, the methanolic reaction solution has to be taken into account. At early stages of mineralization, in general, the interaction of the formed species in solution with the template controls the deposition. The processes in alcoholic PVP-containing reaction solutions and the deposition on SAMs have been analyzed by Jia [181] and Lipowsky [154]. The main findings are that the polymeric interpenetrating network yields a confined space during thermohydrolysis of the zinc-containing precursors upon heating of the reaction solution. This and the reduced hydrolysis rate in alcoholic solutions lead to formation of nanocrystalline hexagonal ZnO close to a spherical shape (cf. Figure 2-1, Figure 4-23, and Section 4.3.2.3) [26].

ZnO is polar and crystallites can have a  $\text{Zn}^{2+}$ -terminated (positive) and an  $\text{O}^{2-}$ -terminated (negative) side (cf. Section 2.1.2), resulting in an intrinsic dipole moment. Zeta potential

measurements of ZnO in both aqueous and 2-propanol solutions indicated a strong influence of the solvent on the overall surface charge [181].

Whereas in aqueous solution the ZnO particles were charged negatively with a value of  $\approx -20$  mV at pH 9 [181], the zeta potential was slightly positive in 2-propanol at the same pH, but close to zero with a value of  $\approx +5$  mV and below [181]. Measurements of the electrophoretic mobility of ZnO crystallites formed in a basic methanolic PVP-containing reaction solution by Lipowsky *et al.* revealed very small values close to zero that scattered strongly [26]. Therefore, it was concluded that the ZnO nanocrystals do not possess a substantial surface charge in the methanolic conditions.

Jia [181] states that ZnO film formation is mainly driven by electrostatic interactions between the SAM template and the ZnO nanocrystals formed homogeneously in solution and only to a smaller degree driven by van der Waals interactions. Calculations to determine the electrostatic interactions of the ZnO particles with SAMs were performed solely in an aqueous polymer-containing system at pH 6.4 due to a lack of knowledge of the parameters in alcoholic solutions [181]. For negatively charged SAMs (SO<sub>3</sub>H-SAM: -90 mV, OH-SAM: -70 mV) no film formation was observed in the experiments with the, under these conditions, slightly negatively charged ZnO (-10 mV) particles due to electrostatic repulsion and only weak van der Waals attraction which were also calculated. Whereas for positively charged SAMs (NH<sub>2</sub>-SAM: +38 mV), as well as only weakly charged SAMs (SH-SAM: -32 mV, SCOCH<sub>3</sub>-SAM: -12 mV), ZnO film formation was observed. In the case of the positively charged SAMs, the formation was concluded to be controlled by electrostatic and van der Waals attraction. In the case of the weakly charged SAMs, the attractive van der Waals interaction overruled the low electrostatic repulsion [181].

The zeta potential of single wtTMV particles, as well as the COOH- and NH<sub>2</sub>-SAMs (cf. Section 3.8.2), were determined at both pH 5.5 and 8 in aqueous solution. The value of 5.5 was chosen, since it is the pH of pure MilliQ water [165] and pH 8 is close to the pH of the deposition solution. The results are given in Figure 4-31. COOH-SAMs revealed the highest absolute zeta potential at both pH conditions with  $-87 \pm 4$  mV and  $-99 \pm 1$  mV, respectively. For wtTMV values of  $-48 \pm 1$  mV and  $-53 \pm 1$  mV were obtained. In both cases the zeta potential gets more negative with increasing pH values. However, the effect is more pronounced for COOH-SAMs indicating a stronger pH dependency. The behavior of NH<sub>2</sub>-SAMs

is different. The zeta potential is slightly positive at pH 5.5 with a value of  $+10 \pm 1$  mV. The zeta potential at pH 8 is then negative with a value of  $-24 \pm 3$  mV indicating that the isoelectric point (point of zero charge) lies within this pH range.

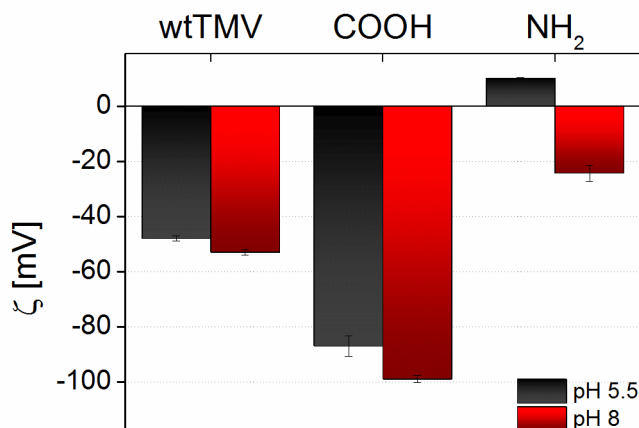


**Figure 4-31:** Zeta potential ( $\zeta$ ) of single wtTMV particles and silicon substrates functionalized with COOH- and NH<sub>2</sub>-SAMs, respectively. Values are given for pH 5.5 and pH 8 [2].

The film formation is described by the interaction of the ZnO nanocrystals, formed homogeneously in solution, with the template (cf. Section 2.1.1). If the deposition was mainly driven by electrostatic interactions, one would expect the highest degree of texture for the template with the highest zeta potential due to the biggest possible electrostatic interaction with the very weakly charged ZnO with the charge fluctuating around zero [26]. This does not fit with the experimental findings. The highest degree of texture was found on wtTMV followed by NH<sub>2</sub>-SAMs, and the lowest degree of texture on COOH-SAMs (cf. Figure 4-30). Since the template with the highest zeta potential showed the lowest degree of texture, electrostatic contributions could be ruled out.

Already Lipowsky *et al.* doubted that the simple explanation of an electrostatic interaction could explain the deposition mechanism in methanolic conditions [26]. They named the following facts that pointed in direction of oriented attachment of the polar ZnO crystals instead of simple electrostatically driven deposition. (1) The already mentioned very low surface charge of ZnO crystals they measured, (2) the high ionic strength of the system reducing the Debye length of the zeta potential, and (3) the fact that deposition was possible on both positively and negatively charged SAMs.

However, Lipowsky *et al.* did not take the effect of methanol on the SAMs into account. In solvents with low dielectric constants, such as methanol ( $\epsilon = 33.6$ ) [156], the capability of a solvent to electrolytically dissociate functional groups is strongly reduced according to the Nernst-Thomson rule [157]. This is reflected by higher  $pK_a$  values in methanol compared to water [186,187]. Rived *et al.* put together a large number of dissociation constants in methanol resulting in overview tables for  $pK_a$  values of different neutral and charged acids in methanol [187]. The  $pK_a$  of carboxylic species comparable to the COOH-SAMs used herein, such as butanoic acid is increased from 4.82 in water to 9.69 in methanol [187]. The  $pK_a$  value of protonated 1-butanamine (comparable to the herein used  $\text{NH}_2$ -SAM) is increased from 10.61 in water to 11.48 in methanol. It is important to keep in mind that this is a logarithmic scale. Thus, in both cases the equilibrium is shifted to the undissociated, uncharged species in methanol which strongly supports the fact that electrostatic contributions are insignificant in methanolic reaction conditions.

Additionally, the low dielectric constant of methanol leads to a smaller Debye length of the zeta potential resulting in a faster potential drop of the charges in solution. Measurements of the direct influence of organic solvents, such as methanol on the electroosmotic velocity and, thus, the zeta potential, were performed in water-solvent mixtures [186,188–191]. The general message is that an increasing percentage of organic solvent in organic/ $\text{H}_2\text{O}$  mixtures decreases the electroosmotic velocity and the zeta potential.

Firstly, the results of Schwer and Kenndler [186], who investigated the influence of several organic solvents on electrokinetic properties of fused silica, showed that the addition of 50% methanol reduced the zeta potential by a factor of 2 to 4 [186]. These results directly reflect the reduced surface charge due to (1) strongly decreased dissociation and (2) the faster drop of the potential due to the reduced Debye length. Secondly, Woan *et al.* reported that attractive van der Waals interactions between steel and silica surfaces were maximized in methanol [192] revealing the low impact of electrostatic contributions.

Thus, one can conclude for the herein used system that neither the template nor the ZnO crystallites [26] in solution are substantially charged and the deposition is not driven by electrostatic interactions.

The consideration of the  $pK_a$  values of the carboxylic and amine species might explain the small differences in texture between the SAMs (cf. Figure 4-30). The increase of the

dissociation constant is much higher for carboxylic species compared to amine species. Thus, the solvent effect is more pronounced leading to the smallest texture.

However, the question remains why the texture is strongly enhanced on TMV. These differences might be attributed to the piezoelectric properties of wtTMV allowing dipole/dipole interactions between TMV and polar ZnO leading to a strong enhancement in the texture of the deposited ZnO film. The virus particles are deformed strongly in their cross-section due to strong hydrogen bonds [95,96] with the oxidized silicon substrate (Figure 4-32 A, B). The strong interaction leads to a reduction of the height to 14 nm which was confirmed by AFM height analyses (Figure 4-32 C, D). This is in good accordance with literature values [95,96] that also state a change of the height/width ratio of 0.57 [96].

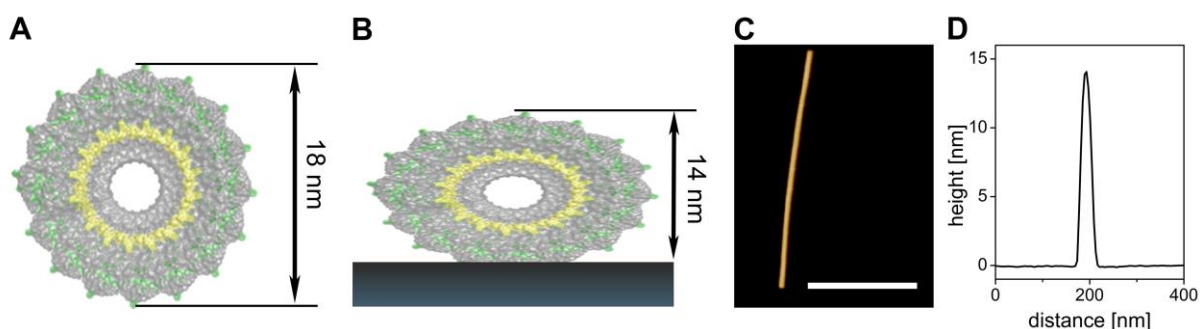


**Figure 4-32:** Scheme of the ongoing processes upon immobilization of wtTMV onto a silicon substrate. **A**, Cross-section of wtTMV in solution displaying the undeformed diameter of 18 nm. **B**, Deformed cross-section of wtTMV due to strong adhesion on the silicon substrate with reduced height of 14 nm. **C**, AFM height image of wtTMV immobilized on Si. The scale bar is 400 nm. **D**, Corresponding height profile determined from the AFM height image proofing the reduced height due to deformation [2].

Since wtTMV has piezoelectric properties due to its helical structure with intrinsic dipole moment (cf. Section 2.4) as in the case of M13 phages [126], such a mechanical deformation caused by adhesion leads to an enhanced dipole owing to the piezoelectric effect. The suggested rearrangement of the intrinsic dipoles within the structure of wtTMV because of mechanical deformation causing an increased dipole moment is shown in Figure 4-33 A. However, such surface charges caused by piezoelectric properties undergo relaxation processes and do not remain on the surface after deformation. But, in the case of the herein used methanolic reaction solution at 60°C, an additional effect occurs. Upon immersion of the immobilized and already deformed wtTMV into the reaction solution, an additional deformation of the cross-section occurs due to heat and solvent treatment, further reducing

the height of the virus particles to 9 nm. This was confirmed by control measurements in pure methanol at 60°C followed by AFM analyses (cf. Section 3.4.1) [144]. Additionally, the deformation of the cross-section leads to a flattened virus surface with increased contact area for the ZnO crystallites (Figure 4-33 C) [2].

Since the dissociation of surface groups is strongly reduced in the methanolic conditions, as mentioned above, the resulting increased texture on wtTMV-based ZnO films suggests that the main driving force for the enhanced oriented attachment is the dipole/dipole interaction between the piezoelectric wtTMV and polar ZnO nanocrystals. In the case of the SAMs, the additional contribution of dipole/dipole interactions is missing. Consequently, the deposition of ZnO crystallites during the early stages is less ordered resulting in a decreased texture.

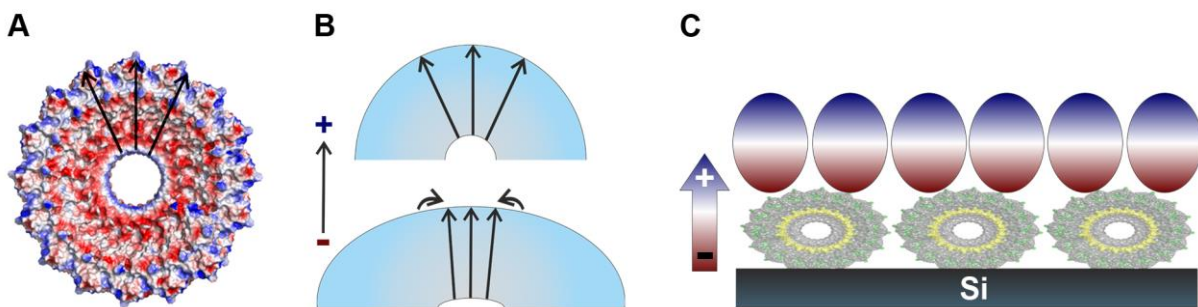


**Figure 4-33: A**, Intrinsic dipole moment of TMV's coat protein in the cross-section created with PyMol. The RNA was not taken into account in this visualization. Negative charges are indicated in red and positive charges in blue. The intrinsic dipole will further be enhanced under consideration of the negatively charged RNA. **B**, Visualization of the suggested rearrangement of the intrinsic dipoles due to mechanical deformation and the resulting parallel orientation of the dipoles when immobilized on a silicon substrate. **C**, Condition for mineralization of deformed wtTMV on a silicon substrate. The polar ZnO crystallites are indicated by the red and blue ovals. The piezoelectric effect occurring due to the mechanical deformation leads to an increased dipole moment and also a flattened virus structure. Thus, only in this condition an optimum 002 texture can be obtained by dipole/dipole interactions between wtTMV and polar ZnO crystallites [2].

At later stages of the ZnO deposition, the template is completely covered by ZnO (already after the first mineralization cycle in the case of wtTMV, cf. Figure 4-16) and any further deposition leads to ZnO film growth on predeposited ZnO. Subsequently, the template only has an indirect influence. The quality and degree of texture of further deposited ZnO is dependent on the first formed layers. In the case of the wtTMV, the dipole interactions lead to better oriented first crystallite layers which result in a better orientation and thus a higher texture of the subsequent ZnO layers.

In general, film growth competes with agglomeration in solution. ZnO crystallites can either contribute to film formation by attaching to the already formed layers or surface energy can be reduced by agglomeration in solution. (1) In early stages, the number of possible neighbors is higher when the particle is attached to the film leading to minimum three contacts. In these early stages agglomeration of single particles leads only to one contact. Thus, the reduction of surface energy is higher in the case of film formation and particles are preferentially incorporated in the growing film rather than agglomerating in solution. (2) At later stages, the number of particles has increased leading to higher probability of particle collisions leading to agglomeration nuclei, which will then grow at the expense of film formation, since the total surface is higher. The DLS measurements shown in Figure 4-2 A revealed this growing of the agglomerates with longer reaction times.

## 4.4 PIEZOELECTRIC THIN FILMS

The possibility to tune the texture of the deposited ZnO films by adjusting the water content together with the aforementioned texture enhancement on wtTMV opens up the possibility to synthesize piezoelectric films at close-to ambient conditions and to tune the piezoelectric properties of the films [2]. Usually harsh reaction conditions, such as high temperatures or ultrahigh vacuum conditions, are necessary to synthesize piezoelectric ZnO films, e.g. via radio-frequency magnetron sputtering [10] or pulsed laser deposition [11].

Piezoresponse force microscopy (PFM) allows local piezoelectric characterization directly on the piezoelectric sample, which makes it possible to measure the magnitude of the piezoelectric constant  $d_{33}$  locally and to visualize the single piezoelectric domains.

Firstly, reference measurements were performed on a standard sample (PPLN) and also on the always present bare silicon substrate. Secondly, the texture influence on the piezoelectric properties was monitored on NH<sub>2</sub>-SAMs by variation of the preparation process. Thirdly, films prepared under the same conditions with different templates were investigated, and, finally the influence of the film thickness was analyzed.

### 4.4.1 REFERENCE MEASUREMENTS

A commercially available PPLN standard sample (Bruker) was used to determine the deflection sensitivity of the used tip and to calibrate the system. The measured  $d_{33}$  was in good

accordance with the literature value of  $8 \text{ pm V}^{-1}$  [147,148]. Since all template monolayers are synthesized on oxidized silicon substrates, a bare silicon substrate was measured to determine the substrate contribution.

The resulting piezoresponse amplitude images of the bare silicon wafer are given in Figure 4-34. No image contrast is obtained at all applied biases (Figure 4-34 A-C) and the values are close to the system-inherent noise level.

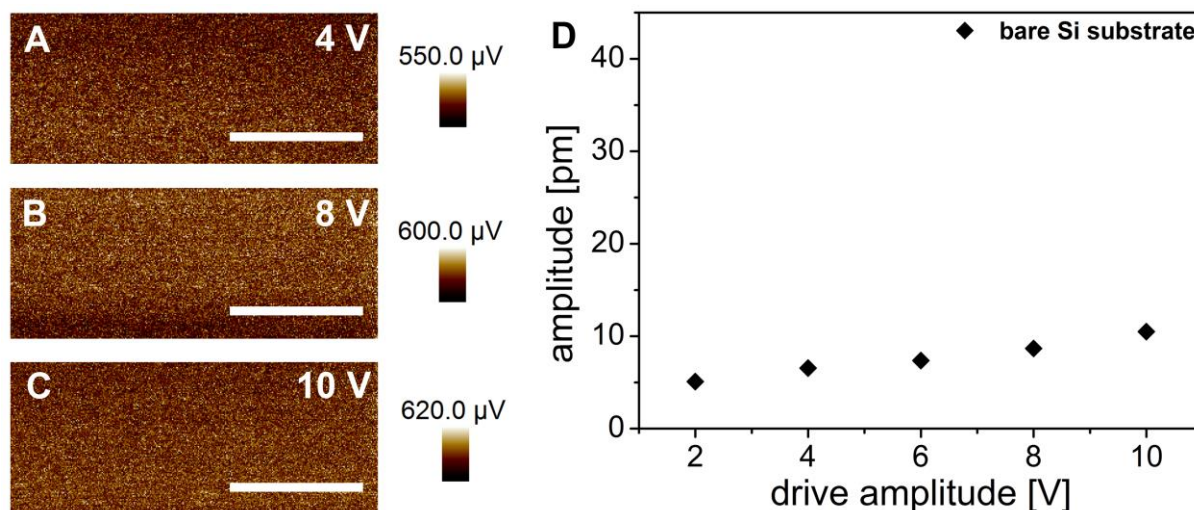


**Figure 4-34:** A-C, PFM amplitude images at 4, 8, and 10 V of a bare silicon substrate with native  $\text{SiO}_2$  top layer. All scale bars are 200 nm. D, Piezoresponse amplitude plotted over the applied bias ranging from 2 to 10 V. The plotted data points represent the averaged amplitude values (averaged over image area) of five individual measurements. The error bars are too small to be seen in the plot with typical values of below 1 pm. The resulting  $d_{eff}$  is  $0.6 \text{ pm V}^{-1}$ .

A quantitative evaluation of the amplitude values was performed by averaging the measured amplitude signal over the image area and repeating the measurements at five individual spots on the sample (Figure 4-34 D). The mean value of the amplitude of these five individual measurements is then plotted over the applied bias (= drive amplitude). The slope of the obtained line represents the piezoelectric constant  $d_{eff}$ , which is in this case as low as  $0.6 \text{ pm V}^{-1}$  [2].

#### 4.4.2 TEXTURE INFLUENCE ON PIEZOELECTRIC PROPERTIES

A 002 texture is mandatory in order to have a ZnO film with piezoelectric properties (cf. Section 2.1.2.2). Two differently textured thin ZnO films were prepared on  $\text{NH}_2$ -SAMs. By variation of the water content, either a 002 textured film (2 vol%  $\text{H}_2\text{O}$ , Figure 4-35 A, C) or a



100 textured film is deposited (3 vol% H<sub>2</sub>O, Figure 4-35 B, C), which is confirmed by XRD. SEM cross-sections reveal a similar film thickness, morphology, smoothness and porosity (Figure 4-35 A and B).

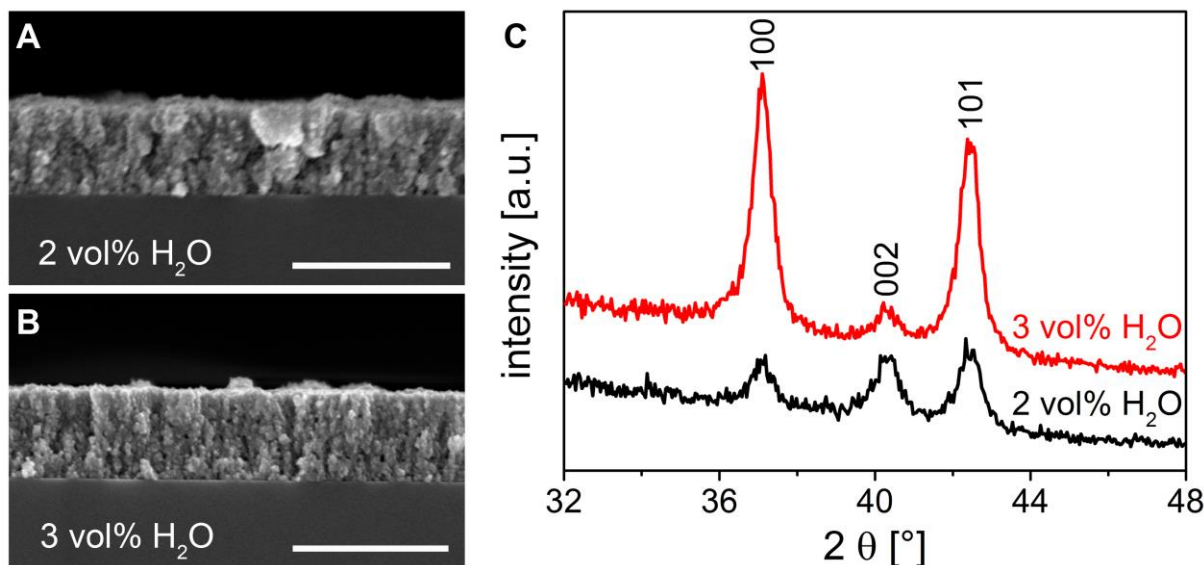


**Figure 4-35: A, B**, SEM cross-section images of ZnO films on NH<sub>2</sub>-SAMs prepared with 2 vol% H<sub>2</sub>O and 20 deposition cycles (**A**) and 3 vol% H<sub>2</sub>O and 15 deposition cycles (**B**). The scale bars represent 500 nm. **C**, XRD patterns of the corresponding films. Taking the relative intensities of the 100 and 002 reflections into account, a very small 002 texture is obtained with 2 vol% H<sub>2</sub>O and a 100 texture by adding 3 vol% H<sub>2</sub>O.

However, the behavior during the piezoelectric measurements is different, as expected. The slightly 002 textured sample shows increasing amplitude contrast when enhancing the applied bias from 4 V to 8 V (Figure 4-36 A, B), i.e. the contrast between dark and bright areas becomes larger. Bright areas get brighter with increased bias, since those domains are further deformed upon increasing the bias. Additionally, the signal is less noisy and the domains have sharper edges.

In the case of the 100 textured film, the measured piezoresponse amplitude does not change upon variation of the applied bias (Figure 4-36 C, D). Some diffuse contrast of grains is visible. However, the contrast remains the same upon increasing the voltage. These findings are supported by the quantitative analysis of several images of each sample for biases from 2 to 10 V. Only the sample with the slight 002 texture shows a linear increase of the deformation with increasing bias leading to a  $d_{eff}$  of 1.6 pm V<sup>-1</sup> (Figure 4-36 E).

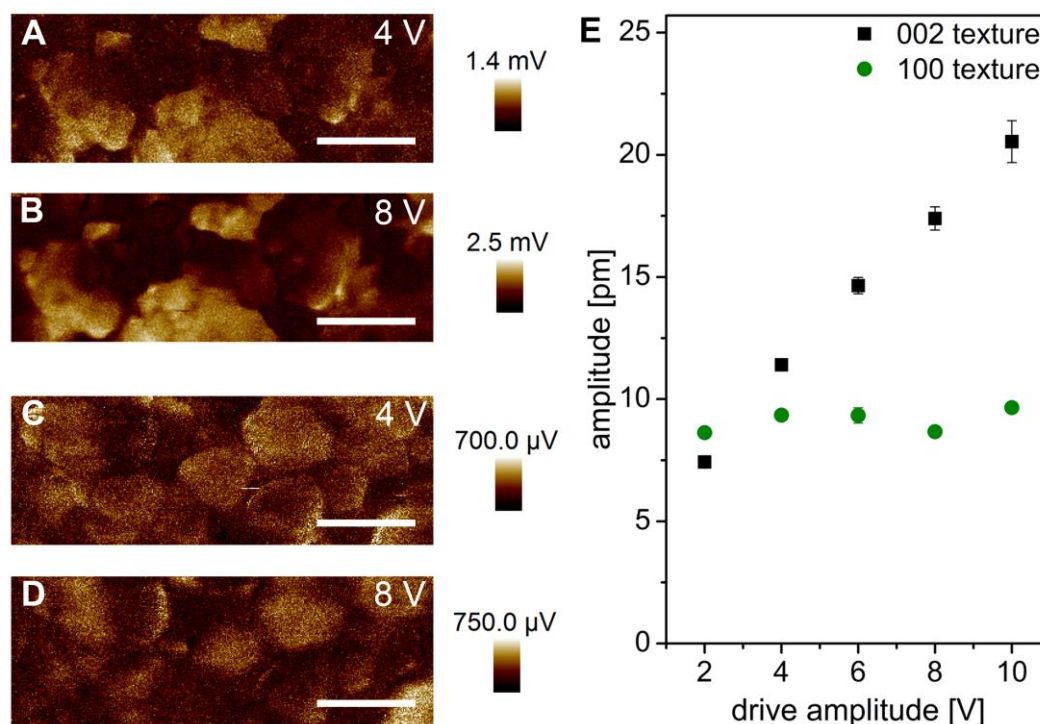


**Figure 4-36: A-D**, PFM amplitude images at 4 and 8V for ZnO films on NH<sub>2</sub>-SAMs with small 002 texture (**A, B**) and 100 texture (**C, D**). 002 textured films are deposited from solutions containing 2 vol% H<sub>2</sub>O (20 deposition cycles **A, B**) and 100 textured films are synthesized by addition of 3 vol% H<sub>2</sub>O. All scale bars are 100 nm. **E**, Vertical response plotted in dependency of the applied drive amplitude. Data points represent five individual experiments. Error bars show the corresponding standard deviation of the mean value.

The 100 textured sample only shows a constant signal below 10 pm, which is in good accordance with the inherent noise of the system. Several conclusions can be drawn from this proof of principle. (1) The 002 texture is mandatory for piezoelectric behavior. (2) Even such low degrees of texture, as obtained on the NH<sub>2</sub>-SAM, lead to piezoelectric behavior even though the  $d_{eff}$  is low. (3) There is no contribution from the silicon substrate, since no linear slope, as is the case with the bare silicon substrate (Figure 4-34), was observed for the 100 textured sample [2].

#### 4.4.3 TEMPLATE INFLUENCE

The effect of the more strongly interacting template wtTMV on the texture was already explained above in Section 4.3.3. Since the samples on different templates differ in their texture coefficient, the piezoelectric properties should also be affected. The amplitude images at 10 V for all templates of these piezoelectric measurements are shown in Figure 4-37 A

(above: NH<sub>2</sub>-based ZnO films, middle: COOH-based, and bottom: wtTMV-based) prepared as described in Section 3.5 with 2 vol% H<sub>2</sub>O in the reaction solution.

Both SAM-based ZnO films show pronounced dark/bright contrast. The dark areas indicate domains with low absolute values of amplitude. In the case of wtTMV-based ZnO films, more bright areas can be seen and, instead of dark areas, an intermediate brown contrast. This indicates that there are fewer areas with only small amplitude and that the overall mechanical deformation is larger [2].

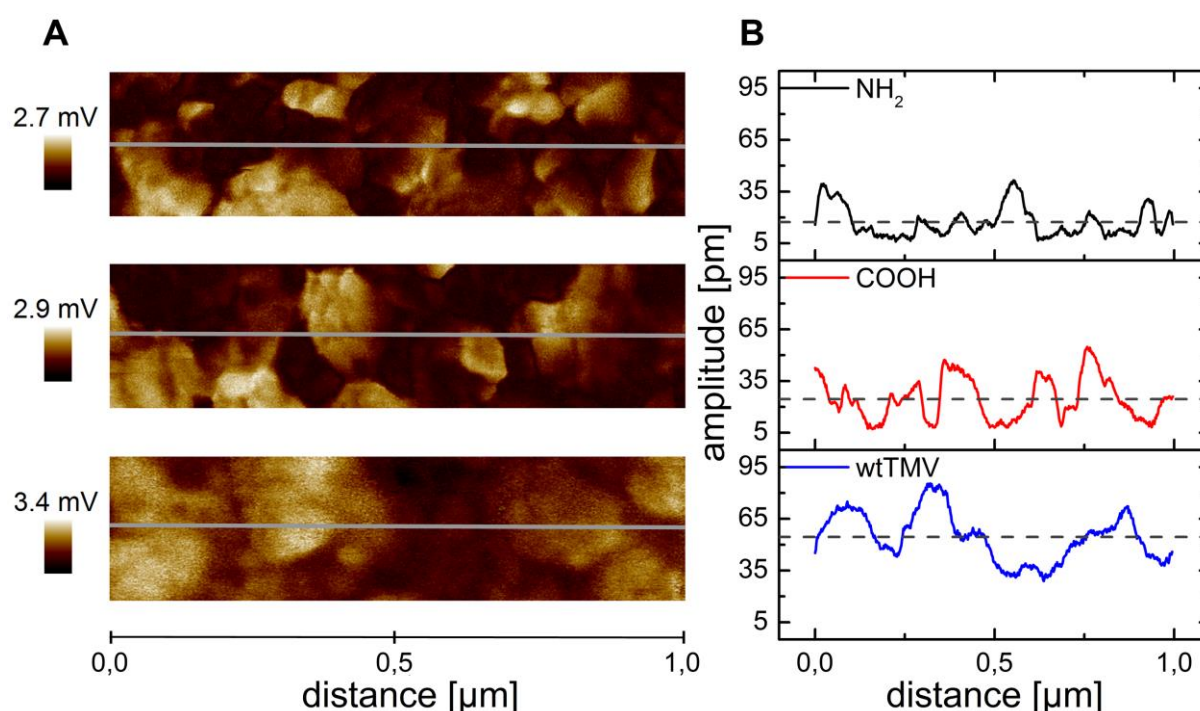


**Figure 4-37: A**, Amplitude images of the PFM measurements performed at 10 V for NH<sub>2</sub>-based films (top), COOH-based films (middle) and wtTMV-based films (bottom). **B**, Corresponding amplitude profiles taken along the grey lines (A) are shown for each template [2].

This is highlighted by the amplitude profiles (Figure 4-37 B) which were taken along the grey lines in Figure 4-37 A. The response of the NH<sub>2</sub>-based ZnO film deviates around a mean value of about  $17 \pm 9$  pm. The COOH-based film shows a slightly higher mean response of  $25 \pm 12$  pm (dashed line). In both cases, the maximum amplitude is in a range of 35 to 40 pm. The highest mean value of  $55 \pm 14$  pm is reached with the wtTMV-based films. Here, areas with increased amplitudes of up to 86 pm are reached. The strong deviations from the mean value is seen for all templates and are caused by different facts. (1) In general, a sample's roughness and topography strongly influence the electromechanical coupling between sample and AFM tip and, thus, also influence the piezoresponse. (2) The granular structure of

the films may influence and affect, on the one hand, the homogeneity of the electric field in the  $z$ -direction (cf. Figure 3-3), and, on the other hand, produce incoherent coupling between electromechanical response among different grains in the  $z$ -axis. Hence, the global effective signal would be affected. In order to take all these effects into account, the amplitude signal was averaged over the entire image area and measured on five different positions for each applied bias.

The piezoresponse is doubled in the case of wtTMV-based films due to the enhanced texture. To evaluate this quantitatively, the amplitude signal was averaged over the entire image area and measured at five different positions for each applied bias. The resulting curves are given in Figure 4-38. For all samples, a linear slope of the amplitude with increasing applied bias can be observed, which indicates piezoelectric behavior in all cases as expected, since all samples exhibit a 002 texture. Since the field under the AFM tip is not homogeneous, the values obtained from the slope are not the  $d_{33}$ , but an effective  $d_{eff}$ , which is smaller than the real  $d_{33}$  [193].

As already indicated by the amplitude profiles in Figure 4-37, the piezoelectric response is doubled in the case of wtTMV, resulting in a  $d_{eff,wtTMV} = 3.8 \text{ pm V}^{-1}$  compared to  $d_{eff,NH_2} = 1.6 \text{ pm V}^{-1}$  and  $d_{eff,COOH} = 2.0 \text{ pm V}^{-1}$ .

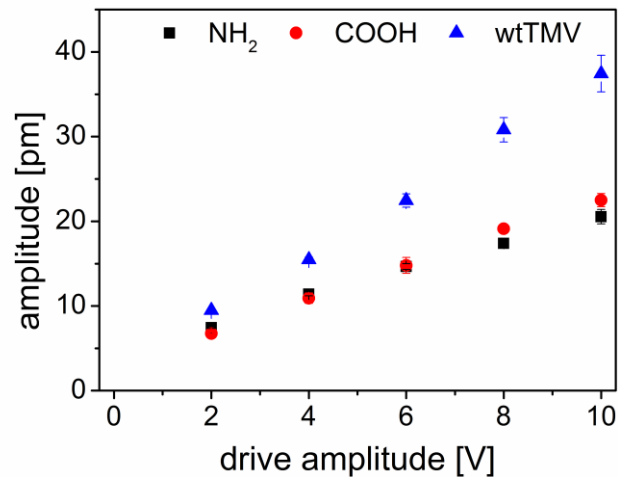


**Figure 4-38:** Linear dependency of the vertical amplitude signal on the drive amplitude for textured ZnO films deposited from reaction solutions with 2 vol% H<sub>2</sub>O in the reaction solution and applying 20 deposition cycles. Data points correspond to mean values of five individual measurements. Error bars show the standard deviation from those mean values.

The piezoelectric virus template strongly enhances the piezoelectric constant due to a strongly enhanced texture caused by dipole/dipole interactions during the mineralization process. Taking the inhomogeneous electric field under the tip into account and the weak indentation regime of the tip into the sample compared to the tip radius [126,150],  $d_{33}$  can be estimated from  $d_{eff} = 0.5 \times d_{33}$  [150]. Thus, the resulting  $d_{33,wtTMV}$  is determined to be  $7.6 \text{ pm V}^{-1}$ .

Bulk ZnO has a  $d_{33}$  of  $12 \text{ pm V}^{-1}$  [29] and polycrystalline ZnO films produced under harsh reaction conditions, such as radio-frequency-plasma-assisted pulsed-laser deposition method, result in a  $d_{33}$  of  $12 \text{ pm V}^{-1}$  [11].

The herein obtained  $d_{33,wtTMV}$  is higher than the  $6 \text{ pm V}^{-1}$  obtained at more moderate reaction conditions for thin polycrystalline ZnO films prepared using a sol-gel method [14]. However, their synthesis included several heating steps and annealing at  $500^\circ\text{C}$  after each cycle, whereas the herein prepared films were synthesized environmentally friendly at low temperatures without post-treatment.

#### 4.4.4 THICKNESS INFLUENCE

As mentioned in Section 4.3.2.3, the texture is more pronounced in thicker films. Thus, PFM measurements were also performed on samples with a doubled number on mineralization cycles on wtTMV. The thicker sample with a thickness of roughly 860 nm shows a pronounced amplitude contrast comparable to the thin sample with a thickness of about 300 nm with large bright areas indicating the piezoelectric deformation (Figure 4-39 A-C).

Increasing the applied bias leads to a larger amplitude signal. However, the quantitative analysis of the results reveals that the obtained slope is lower compared to the 20 mineralization cycle sample (Figure 4-39 D), even though the texture is more pronounced (cf. Figure 4-29). The effective value is decreased from  $3.8$  to  $3.4 \text{ pm V}^{-1}$ .

This can be explained by the measurement setup. The  $d_{33}$  coefficient is defined considering that the piezoelectric response is measured using a capacitor-like structure, which would imply immersion of the material in a homogeneous electrical field. However, in the case of the PFM measurements, the field emerging from the tip is rather a point charge than a planar field [149].

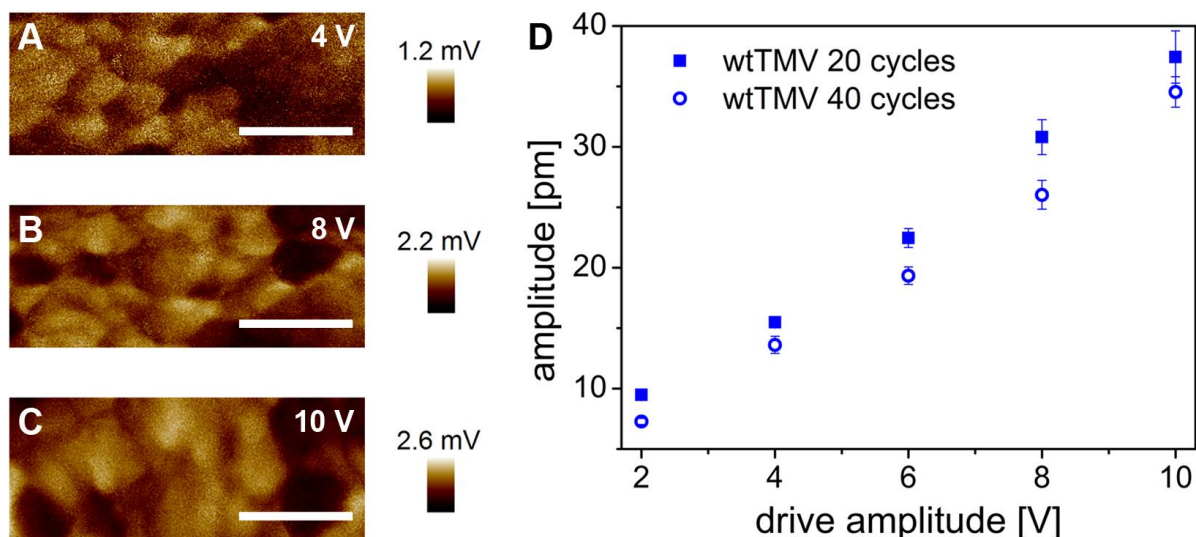


**Figure 4-39:** A-C, PFM amplitude images at 4, 8 and 10 V of a 002 textured, thick ZnO layer (40 mineralization cycles) deposited on a wtTMV monolayer obtained via CA. All scale bars are 200 nm. D, Vertical amplitude signal plotted over the drive amplitude for textured ZnO films on wtTMV deposited from reaction solutions with 2 vol% H<sub>2</sub>O in the reaction solution and applying 20 and 40 deposition cycles, respectively. Data points correspond to mean values of five individual measurements. Error bars show the standard deviation from those mean values.

Therefore, the effective voltage sensed by the material will be smaller for a thicker sample due to the more radial electric field over the volume, leading to a smaller effective  $d_{eff}$ . Thus, a smaller effective  $d_{eff}$  is measured due to the measurement technique, even though the thicker wtTMV-based sample is better oriented than the thinner one (cf. Figure 3-3) [2].

## 4.5 ZNO-BASED FIELD-EFFECT TRANSISTORS

Since crystallite size [172,194], interface roughness [35], active layer thickness [194,195] and crystallite orientation [179] all have an influence on electrical performance and are all affected upon addition of water to the methanolic reaction solution, first experiments on NH<sub>2</sub>-SAMs were carried out to find (1) the optimum water content (Section 4.5.1) and (2) the optimum ZnO thickness (Section 4.5.2) for the best and most reproducible FET performance. The findings from the NH<sub>2</sub>-SAMs were then again transferred to virus-based transistors and compared to the already discussed FETs prepared without water (Section 4.2.4).

#### 4.5.1 FET PERFORMANCE IN DEPENDENCY OF H<sub>2</sub>O CONTENT ON NH<sub>2</sub>-SAMs

Several FETs were synthesized on NH<sub>2</sub>-SAMs with varying water content in the reaction solution (2, 3, and 5 vol% H<sub>2</sub>O, cf. Section 3.6) in order to find the optimum water content for good, robust, and reproducible FET results.

Reproducibility is a crucial point for FETs, as it is e.g. pointed out in the IEEE standards for organic FETs [196]. Thus, not only a good FET performance is crucial, but also only small deviations in the measured values in between reproduced samples. To ensure reproducibility, two individual substrates were prepared and measured for each experimental condition.

As shown in Figure 2-3 B, the herein used Fraunhofer FET substrates always possess four identical transistor units with the same channel length. This resulted in eight individual transistor units that were evaluated for each experimental setup. In Figure 4-40 the FET characteristics ( $V_{Th}$ ,  $\mu$ , and  $I_{on/off}$ ) are presented as a function of the water content in the reaction solution.

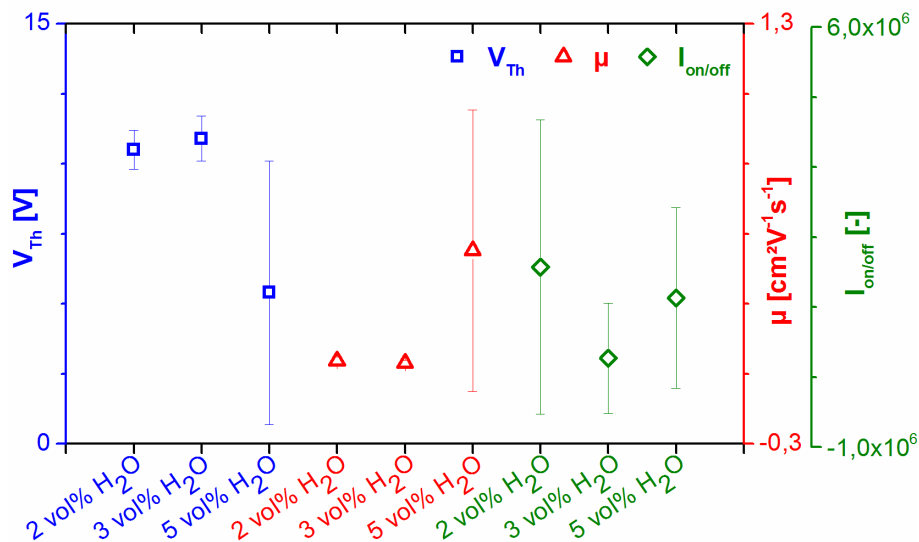


**Figure 4-40:** Visualization of the FET characteristics ( $V_{Th}$ ,  $\mu$ , and  $I_{on/off}$ ) extracted from output and transfer characteristics for ZnO films deposited from reaction solutions with varying water content in the reaction solution (2, 3, and 5 vol% H<sub>2</sub>O) onto NH<sub>2</sub>-SAMs. The number of deposition cycles was adjusted to obtain similar thickness (8, 6, and 4 cycles). Each data point plotted is the mean value of eight individually measured transistor units of two substrates and the standard deviations are indicated. The data values are also given in Table 4-10.

Each data point is the mean value of the measurements of eight individual transistors and the standard deviation is given. Since the values stretch over a large range, the obtained values

and the corresponding standard deviations are provided in numbers in Table 4-10. The number of cycles was reduced with increasing water content to get an approximate film thickness between 150 and 170 nm on the basis of the determined growth per cycle (cf. Section 4.3).

On first sight, the FET performance of the 5 vol% H<sub>2</sub>O sample seems to be the best with the lowest threshold voltage  $V_{Th}$ , highest mobility  $\mu$  and a good on/off ratio  $I_{on/off}$  (Figure 4-40). However, the results show a poor reproducibility, since large deviations for all three FET characteristics are obtained for 5 vol% H<sub>2</sub>O. The threshold voltage  $V_{Th}$  and mobility  $\mu$  show large deviations (Figure 4-40).

The values given in Table 4-10 confirm that the standard deviation of the samples prepared with 5 vol% H<sub>2</sub>O is close to 100%. These samples were thus not further considered for the optimum water content due to the poor reproducibility of the data even though at first sight the highest mobility was reached.

**Table 4-10:** FET characteristics  $V_{Th}$ ,  $\mu$ , and  $I_{on/off}$  extracted from the measured output and transfer characteristics for ZnO films with varying water content (2, 3, and 5 vol% H<sub>2</sub>O) deposited on NH<sub>2</sub>-SAMs. The number of cycles was adjusted to 8, 6, and 4 cycles accordingly to obtain a similar film thickness. For each condition two individual transistor substrates were prepared and eight individual transistor units were analyzed in total. The values given are averaged over all units and the standard deviations are given.

H <sub>2</sub> O [vol%]	$V_{Th}$ [V]	$\mu$ [cm <sup>2</sup> V <sup>-1</sup> s <sup>-1</sup> ]	$I_{on/off}$ [-]
2	10.5 ± 0.7	(1.6 ± 1.6)·10 <sup>-2</sup>	(2.0 ± 2.5)·10 <sup>6</sup>
3	10.9 ± 0.8	(7.7 ± 10)·10 <sup>-3</sup>	(4.8 ± 9.2)·10 <sup>5</sup>
5	5.4 ± 4.7	(4.4 ± 5.4)·10 <sup>-1</sup>	(1.5 ± 1.5)·10 <sup>6</sup>

The on/off ratio  $I_{on/off}$  showed poor reproducibility independent of the water content. Thus, the focus was laid on both threshold voltage and mobility to choose the optimum water content. For 2 and 3 vol% H<sub>2</sub>O, the threshold voltage  $V_{Th}$  is more constant with values around 10.5 ± 0.7 V and 10.9 ± 0.8 V, respectively. Additionally, for 2 and 3 vol% H<sub>2</sub>O, the reached values of the mobility  $\mu$  were by far more constant compared to the 5 vol% H<sub>2</sub>O sample. Between the 2 and 3 vol% H<sub>2</sub>O sample, the most reproducible and lowest threshold voltage  $V_{Th}$  as well as the highest mobility  $\mu$  ((1.6 ± 1.6)·10<sup>-2</sup> cm<sup>2</sup> V<sup>-1</sup> s<sup>-1</sup>) were reached with 2 vol% H<sub>2</sub>O



in the reaction solution, the thickness of the semiconductor layer was optimized for this water content (cf. Section 4.5.2).

A possible explanation of the varying reproducibility of the FET performance for different water contents is the increasing crystallite size with higher water content in the reaction solution (cf. Section 4.3.2.3). Increasing the crystallite size reduces the number of grain boundaries and thus creates a better percolation pathway for the electrons. However, increasing the crystallite size increases the interface roughness between the ZnO nanocrystallites and the SiO<sub>2</sub> dielectric where the channel of the FET is formed, as well. Larger crystallites have a lower contact area with the dielectric (Figure 4-41 A-C). Okamura *et al.* showed that the field-effect mobility  $\mu$  increases by a factor of 50, when the roughness is reduced by 1.7 nm [35].

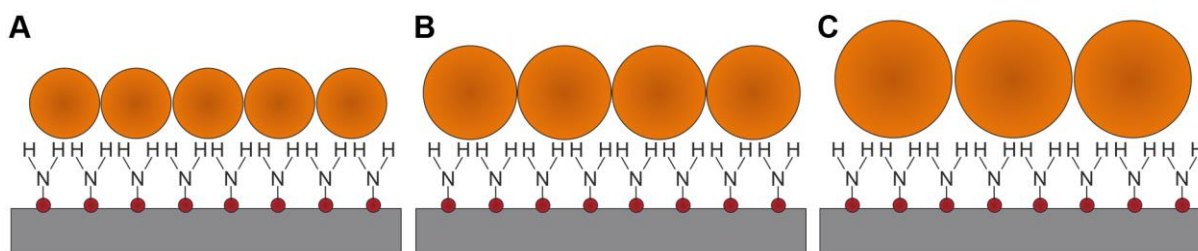


**Figure 4-41:** Scheme of the FET channel region with the SiO<sub>2</sub> dielectric (grey) functionalized with NH<sub>2</sub>-SAMs and mineralized with ZnO. The water content for mineralization is varied from 2 vol% H<sub>2</sub>O (A), over 3 vol% H<sub>2</sub>O (B) to 5 vol% H<sub>2</sub>O (C) leading to increasing crystallite sizes with increasing water content. The interface roughness increases with the water content due to the reduced contact area of larger crystallites with the SiO<sub>2</sub> dielectric layer where the percolation pathway of the electrons is formed.

The increased interface roughness by increased crystallite size reduces the performance. Hence, an optimum between increased crystallites and moderate interface roughness needs to be found. Herein, the biggest crystallites are obtained for 5 vol% H<sub>2</sub>O, which also result in the largest interface roughness due to the reduced contact area with the dielectric (Figure 4-41 C). Therefore, the large values for the mobility of the 5 vol% H<sub>2</sub>O sample are obtained due to the reduction of grain boundaries, which is in accordance with the findings of Oh *et al.* [194]. The results indicate that the increased interface roughness leads to a large deviation of the values and poor reproducibility of the results.

Reducing the crystallite size by decreasing the water content to 2 and 3 vol% H<sub>2</sub>O, increases the contact area between the ZnO nanocrystallites and the SiO<sub>2</sub> dielectric (Figure 4-41 A, B).

This has two effects. (1) The threshold voltage  $V_{Th}$  is increased, but the standard deviation is drastically decreased and (2) the mobility  $\mu$  is decreased, but also with reduced standard deviation. Thus, the FET performance is more reproducible in these cases and the best performance is seen for the 2 vol% H<sub>2</sub>O samples.

The effects on the on/off ratio  $I_{on/off}$  are not that pronounced. The enhanced performance of the FETs prepared with 2 vol% H<sub>2</sub>O might also be affected by the 002 texture obtained under these conditions (cf. Section 4.3.2.1). The oriented attachment of the crystallites might lead to a better percolation pathway for the electrons and thus increase the mobility  $\mu$ .

So far, there have been no investigations reported drawing a connection between the texture of a ZnO film and the FET performance. This is probably attributed to the fact that usually the synthesis method determines the texture and a variation of the texture can only be achieved by a complete change of the synthesis method.

Since the FET performance depends strongly on the above mentioned factors like e.g. crystallite size [172,194] and interface roughness [35] it is very difficult to attribute a changed performance to the change in texture if the complete synthesis method was varied. However, the findings of Fanni *et al.* hint towards a contribution of the texture of the film on electronic properties [179]. They were able to tune the texture of their ZnO film by adjusting the diethylzinc to water vapor ratio in the low-pressure metalorganic chemical vapor deposition. They did not fabricate FETs, but they report that both the carrier mobility and the carrier concentration are increased when tuning the texture from *a*-texture to *c*-texture leading to a lower resistivity even though the grain size is reduced. However, a direct comparison of the results of Fanni *et al.* and the herein obtained results is challenging due to the different synthesis method and thus, the different microstructure which strongly influences the properties.

#### **4.5.2 THICKNESS DEPENDENCY OF THE FET PERFORMANCE ON NH<sub>2</sub>-SAMs**

It was successfully shown that with the optimized water content of 2 vol% H<sub>2</sub>O, FETs with the most reproducible and best performance were synthesized (cf. Section 4.5.1). As a next step, the thickness of the semiconducting ZnO layer was adjusted to enhance the FET performance further. It is reported in literature that the performance of ZnO-based FETs is dependent on the thickness of the active semiconducting layer [194,195]. The number of cycles was adjusted

in such a way that ZnO active layers with a thickness of  $\approx 100$  nm ( $\pm 6$  cycles),  $\approx 140$  nm ( $\pm 8$  cycles),  $\approx 170$  nm ( $\pm 10$  cycles) and  $\approx 200$  nm ( $\pm 12$  cycles) were prepared. This was possible, since the determined growth per cycle from several SEM cross-section samples revealed an increment of growth of  $\approx 17.5$  nm cycle<sup>-1</sup>. Two sets of substrates were prepared for each experimental condition (6, 8, 10, and 12 deposition cycles with 2 vol% H<sub>2</sub>O on NH<sub>2</sub>-SAMs) resulting in eight individually measured transistor units per condition.

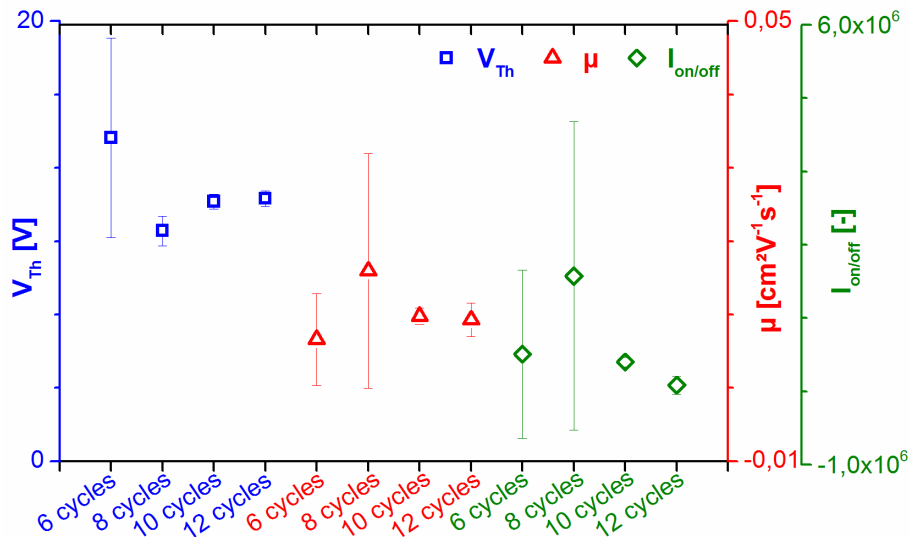


**Figure 4-42:** Visualization of the FET characteristics ( $V_{Th}$ ,  $\mu$ , and  $I_{on/off}$ ) extracted from output and transfer characteristics for ZnO films deposited from reaction solutions with 2 vol% H<sub>2</sub>O onto NH<sub>2</sub>-SAMs with varying cycle number (6, 8, 10, and 12 deposition cycles). Each data point plotted is the mean value of 8 individually measured transistors and the standard deviations are indicated. The data values are also given in Table 4-11.

In Figure 4-42 the resulting FET characteristics ( $V_{Th}$ ,  $\mu$ , and  $I_{on/off}$ ) are plotted versus the number of applied mineralization cycles. The absolute values of the plotted data points and their corresponding standard deviations are given in Table 4-11. The deviations in the FET characteristics are the highest for the thinnest films. With increasing film thickness the resulting values are more reproducible resulting in significantly smaller standard deviations. The effect is most pronounced for films with 10 and 12 deposition cycles, i.e. a thickness between 170 and 200 nm. Under both conditions the obtained threshold voltage  $V_{Th}$  is around 11.8 – 11.9 V, the mobility  $\mu$  is slightly below  $10^{-2}$   $\text{cm}^2 \text{V}^{-1} \text{s}^{-1}$ , and the on/off ratio  $I_{on/off}$  is between  $2.7 \cdot 10^5$  and  $6.3 \cdot 10^5$ . The results are well reproducible with only small standard deviations. Thus, the aimed thickness of the virus-based FETs in the next step was between 170 and 200 nm.

The dependency of the FET performance on the thickness of the active layer is reported by Chung *et al.* [195] and Oh *et al.* [194]. The former reported the best performance of their ZnO-based FETs prepared by radio-frequency sputtering at film thickness of around 55 nm [195]. Whereas the latter found the optimum film thickness to be 80 nm of their ZnO films prepared by magnetron sputtering [194]. The optimum film thickness is apparently dependent on the synthesis method and additional parameters, such as e.g. interface roughness [35] and porosity [172,197].

**Table 4-11:** FET characteristics  $V_{Th}$ ,  $\mu$ , and  $I_{on/off}$  extracted from the measured output and transfer characteristics for ZnO films with varying mineralization cycles (6, 8, 10, and 12) deposited on NH<sub>2</sub>-SAMs from reaction solutions containing 2 vol% H<sub>2</sub>O. For each condition two sets of transistors were prepared and in total eight individual transistor units were analyzed. The values given are averaged over all units and the standard deviations are given.

cycles	$V_{Th}$ [V]	$\mu$ [cm <sup>2</sup> V <sup>-1</sup> s <sup>-1</sup> ]	$I_{on/off}$ [-]
6	14.7 ± 4.5	(6.6 ± 6.3)·10 <sup>-3</sup>	(7.6 ± 13)·10 <sup>5</sup>
8	10.5 ± 0.7	(1.6 ± 1.6)·10 <sup>-2</sup>	(2.0 ± 2.5)·10 <sup>6</sup>
10	11.8 ± 0.3	(9.8 ± 1.1)·10 <sup>-3</sup>	(6.3 ± 0.7)·10 <sup>5</sup>
12	11.9 ± 0.3	(9.3 ± 2.3)·10 <sup>-3</sup>	(2.7 ± 1.5)·10 <sup>5</sup>

Both Chung *et al.* [195] and Oh *et al.* [194] reached threshold voltages  $V_{Th}$  in the range of 10 V which is in good accordance with the herein obtained 12 V without post-treatment. The reported on/off ratio  $I_{on/off}$  by Oh *et al.* of 10<sup>5</sup> is also in the same range as the herein obtained values. However, the mobility  $\mu$  obtained here is with  $\approx 10^{-2}$  cm<sup>2</sup> V<sup>-1</sup> s<sup>-1</sup> one magnitude smaller than in the case of the sputtered ZnO. This could be attributed (1) to the grain size and the resulting number of grain boundaries or (2) to porosity of the active ZnO semiconducting layer. The consideration of the grain size does not lead to clear conclusions since the grain size is as small as 1.2 – 3.8 nm in the case of Oh *et al.* [194] and 90 – 140 nm in the case of Chung *et al.* [195]. This indicates that the higher mobility values were obtained with both smaller and larger grains than the herein obtained grain size of about 10 nm.

The reduced mobility might be attributed to the higher porosity resulting from the solution-processed low-temperature synthesis (cf. Figure 4-48). Meulenkamp described a porous film as a resistor network and reports a strong decrease in mobility caused by the combined effect

of percolation and smaller contact area between the crystallites [172]. Thus, the herein reached lower mobility could be caused by the porosity of the film.

None of the aforementioned works indicate the reproducibility of their values or standard deviations of the obtained results, thus the reproducibility cannot be compared.

All herein prepared transistors work without post-treatment. The optimum conditions were found to be 2 vol% H<sub>2</sub>O in the methanolic reaction solution and a thickness of the active semiconducting layer of 170 – 200 nm allowing to tune the FET performance by variation of water content and layer thickness.

### 4.5.3 VIRUS-BASED FETs DEPOSITED FROM WATER-CONTAINING SOLUTIONS

The knowledge gained from the preliminary experiments on NH<sub>2</sub>-SAMs was then transferred to virus-based FETs in order to evaluate the influence of water in the reaction solution on the properties and compare them to FETs synthesized without water (cf. Section 4.2.4).

As described in the aforementioned section, wtTMV and E50Q virus monolayers were prepared via convective assembly with optimized conditions (cf. Section 3.6.2) for prestructured FET substrates. The number of mineralization cycles with the water-containing reaction solution was adjusted to reach a film thickness of 180 nm (cf. Figure 4-28) laying within the optimum film thickness range of 170 – 200 nm as determined in Section 4.5.2.

Figure 4-43 shows the output (A, B) and transfer (C) characteristics for wtTMV- and E50Q-based ZnO FETs deposited with 2 vol% H<sub>2</sub>O. In both cases typical electronic transistor behavior without any postprocessing is demonstrated. The E50Q-based ZnO transistor shows an improved FET performance compared to wtTMV. The output characteristics of E50Q-based ZnO FET (Figure 4-43 B) show a stronger current saturation compared to wtTMV-based ZnO FET (Figure 4-43 A). Additionally, the transfer characteristics (Figure 4-43 C) reveal a smaller hysteresis in the case of E50Q-based ZnO FET. The improved performance of the E50Q-based ZnO FET is evident from the extracted characteristics ( $V_{Th}$ ,  $\mu$ , and  $I_{on/off}$ ), which are listed in Table 4-12 and visualized in Figure 4-44.

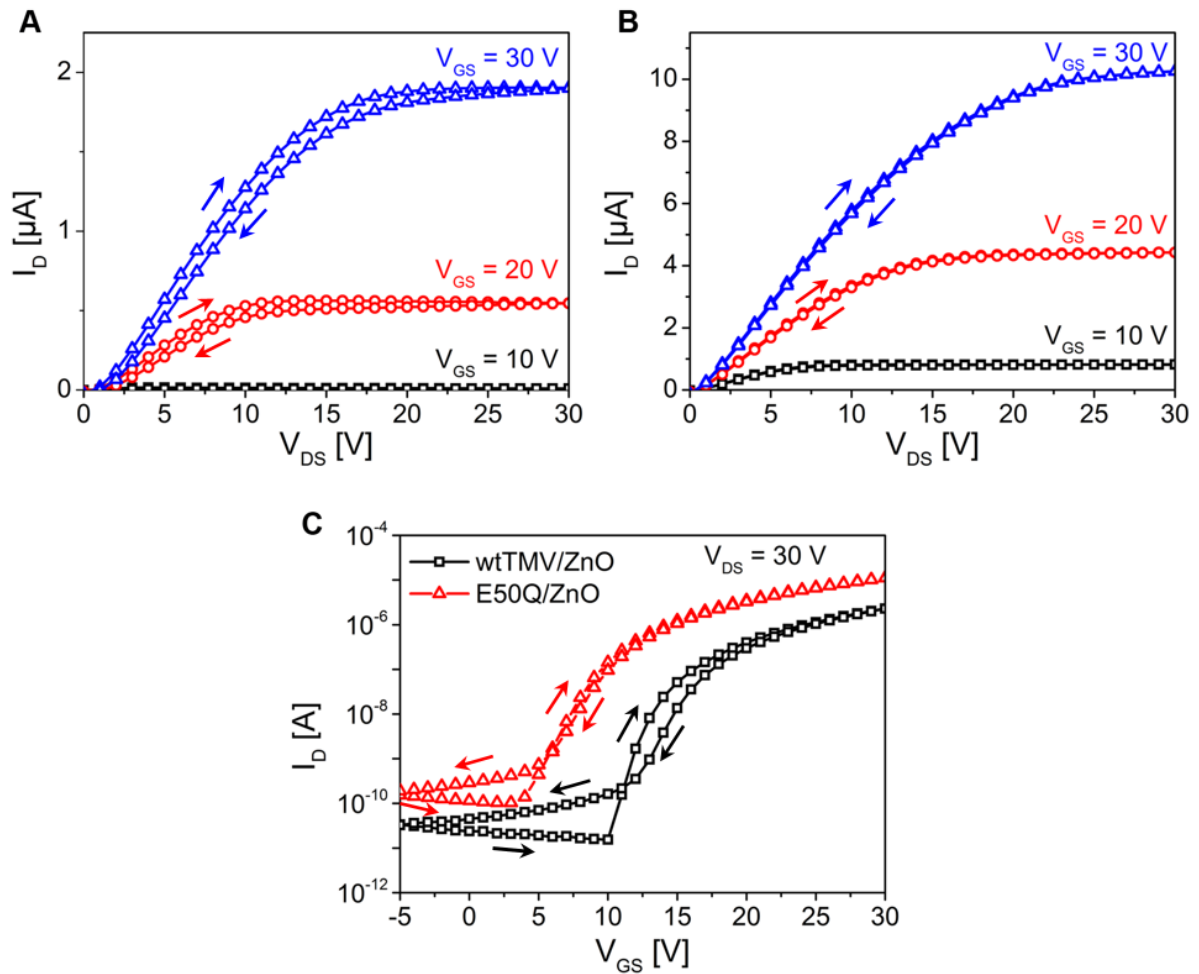


**Figure 4-43:** Output characteristics obtained from variation of the drain-source voltages  $V_{DS}$  from 0 to 30 V, for gate-source voltage  $V_{GS}$  varied from 0 – 30 V in 10 V steps of wtTMV-based (A) and E50Q-based (B) ZnO FETs deposited with 2 vol%  $H_2O$  in the reaction solution and 8 applied deposition cycles. Transfer characteristics (C) for constant drain-source voltage  $V_{DS}$  at 30 V.

The mobility  $\mu$  is increased by one order of magnitude to  $(2.7 \pm 0.1) \cdot 10^{-3} \text{ cm}^2 \text{ V}^{-1} \text{ s}^{-1}$ , whereas  $I_{on/off}$  is in the same order of magnitude. The results are well reproducible which can be seen from the small standard deviations (Figure 4-44). Thus, the performance improvement due to optimized virus packing density was reproduced with a varied deposition solution highlighting the contribution of monolayer quality to the performance.

As already discussed for FETs obtained without addition of water to the deposition solution (cf. Section 4.2.4) the increased virus packing density and resulting homogeneity of the E50Q/ZnO hybrid material lead to a better overall FET performance compared to wtTMV-based ZnO FETs. This is confirmed with the addition of water to the reaction solution, as well. The average threshold voltage  $V_{Th}$  of eight individual transistor units drops from  $12.1 \pm 1.3$  V

for the wtTMV-based ZnO FETs to  $8.9 \pm 0.6$  V for the E50Q-based ZnO FETs (cf. Table 4-12 and Figure 4-44).

**Table 4-12:** FET characteristics  $V_{Th}$ ,  $\mu$ , and  $I_{on/off}$  extracted from the measured output and transfer characteristics (cf. Figure 4-43) for ZnO films deposited on wtTMV and E50Q with 2 vol% H<sub>2</sub>O in the reaction solution applying eight mineralization cycles. For each condition two sets of transistors were prepared and in total eight individual transistor units were analyzed. The values given are averaged over all units and the standard deviations are given.

TMV	$V_{Th}$ [V]	$\mu$ [cm <sup>2</sup> V <sup>-1</sup> s <sup>-1</sup> ]	$I_{on/off}$ [-]
wtTMV	$12.1 \pm 1.3$	$(7.7 \pm 2.6) \cdot 10^{-4}$	$(1.1 \pm 0.6) \cdot 10^5$
E50Q	$8.9 \pm 0.6$	$(2.7 \pm 0.1) \cdot 10^{-3}$	$(2.2 \pm 1.7) \cdot 10^5$

The threshold voltage  $V_{Th}$  of the E50Q-based ZnO FET is further decreased to  $8.9 \pm 0.6$  V compared to the threshold voltage  $V_{Th}$  of  $11.8 \pm 0.3$  V obtained for NH<sub>2</sub>-based samples. This improved behavior might be attributed to the enhanced texture obtained on viruses compared to SAMs (cf. Figure 4-30). However, then the same effect would be expected for wtTMV. Probably the film discontinuity and increased interface roughness in the case of wtTMV cancel out the improvement of enhanced texture and better percolation pathway.

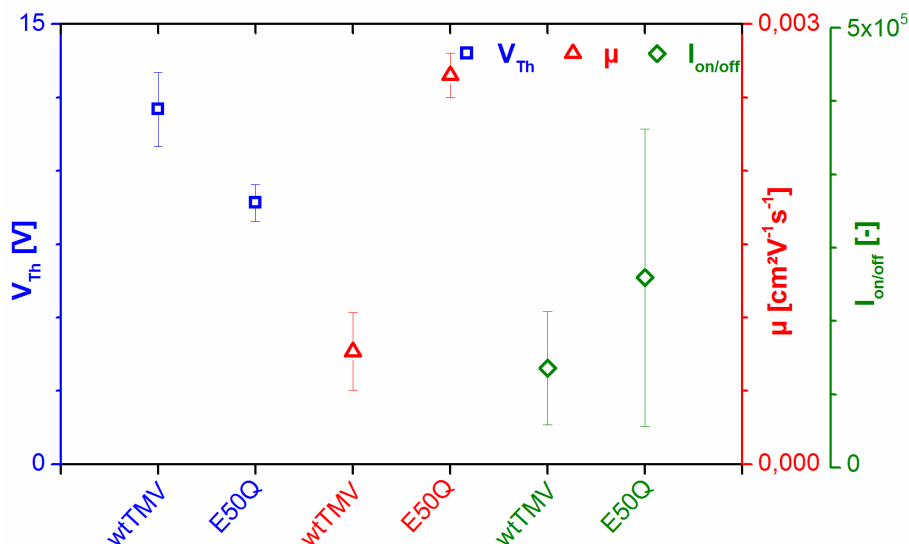


**Figure 4-44:** Visualization of the FET characteristics ( $V_{Th}$ ,  $\mu$ , and  $I_{on/off}$ ) extracted from output and transfer characteristics for ZnO films deposited on wtTMV and E50Q with 2 vol% H<sub>2</sub>O in the reaction solution applying eight mineralization cycles. Each data point plotted is the mean value of eight individually measured transistors and the standard deviations are indicated. The data values are also given in Table 4-12.

The next step was to compare the performance of virus-based FETs prepared without and with water present in the reaction solution. The comparison of the output characteristics (cf. Figure 4-14 and Figure 4-43) reveal a doubled saturation current for FETs prepared with 2 vol% H<sub>2</sub>O compared to the ones synthesized without water.

In Figure 4-45 the transfer characteristics of wtTMV-based (Figure 4-45 A) and E50Q-based (Figure 4-45 B) FETs prepared without and with water are shown. FETs prepared with water in the reaction solution switch at lower voltages. The addition of water to the reaction solution leads to a reduction of the threshold voltage  $V_{Th}$  from  $18.1 \pm 2.5$  V to  $12.1 \pm 1.3$  V in the case of wtTMV-based ZnO FETs and from  $14.1 \pm 1.7$  V to  $8.9 \pm 0.6$  V in the case of E50Q-based FETs (cf. Section 4.2.4 and Table 4-11). The changes of the values are less pronounced in the case of mobility  $\mu$  and on/off ratio  $I_{on/off}$ , but the overall reproducibility of the values is greatly enhanced, which is obvious from the reduced standard deviations. For the E50Q-based FETs the addition of water leads to a smaller hysteresis.

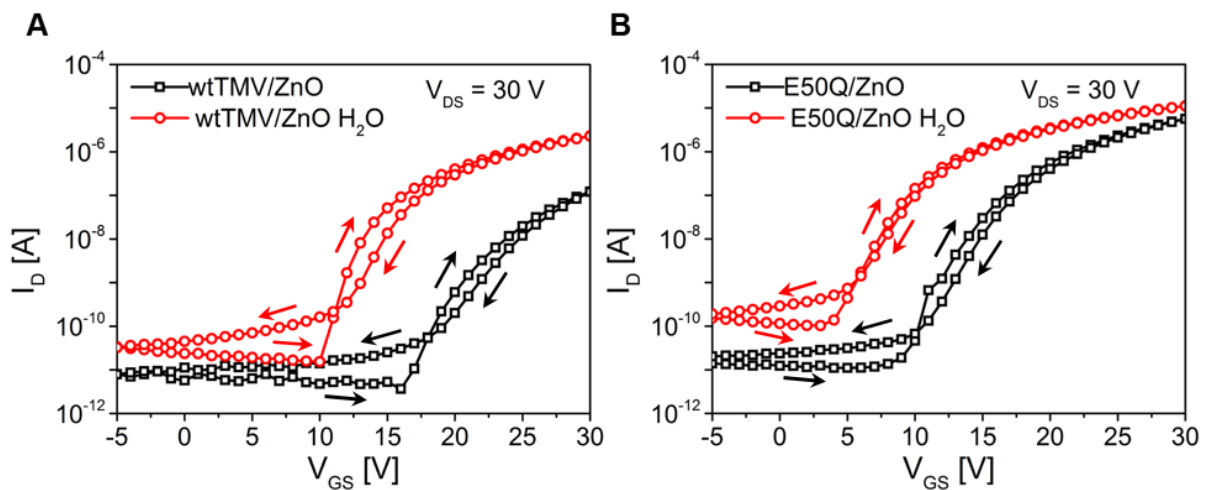


**Figure 4-45:** Transfer characteristics for constant drain-source voltage  $V_{DS}$  at 30 V. Comparison of wtTMV-based (A) and E50Q-based (B) ZnO FETs prepared without water (wtTMV/ZnO and E50Q/ZnO) and with 2 vol% H<sub>2</sub>O present in the reaction solution (wtTMV/ZnO H<sub>2</sub>O and E50Q/ZnO H<sub>2</sub>O).



## 4.6 MONOLITHIC ZnO FILMS AND MULTILAYERED FILMS OF TMV AND ZnO

The outstanding mechanical properties of the hierarchically assembled structure of nacre (cf. Section 2.2.1) have led to increased efforts to use its microstructure as a guideline for the design of new composite materials in order to improve the mechanical properties of functional materials. The challenging point is to combine hardness and toughness in a material. In the following, such an attempt to mimic a multilayered structuring by combination of convective assembly of virus monolayers and controlled ZnO mineralization resulting in a multilayered structure of repeating TMV/ZnO interlayers is reported.

### 4.6.1 MONOLITHIC ZnO FILMS

Monolithic reference samples on wtTMV were necessary in order to quantify the improvement of the mechanical properties due to the microstructure design of multilayered samples. Additionally, the influence of the addition of water to the reaction solution on the mechanical properties of the resulting monolithic ZnO films with 0, 2, 3, and 5 vol% H<sub>2</sub>O, respectively, was analyzed.

#### 4.6.1.1 MICROSTRUCTURE AND COMPOSITION OF MONOLITHIC ZnO FILMS

Since the hardness of films strongly depends on several parameters, such as crystallite size and also the crystallographic orientation (cf. Section 2.1.2.4), monolithic samples with varying water contents were prepared to find the optimum water concentration resulting in the best mechanical performance. The choice for the optimum water content for the preparation of the multilayered samples was made according to the obtained the XRD data (Figure 4-46 A), the morphology of the SEM cross-sections (Figure 4-46 B-E), and hardness  $H$  and Young's modulus  $E$  values (Figure 4-47 A, B).

Films prepared without water in the reaction solution showed poor crystallinity and a thickness of only  $460 \pm 20$  nm determined from SEM cross-sections after 100 deposition cycles (Figure 4-46 A, B). Increasing the water content to 2 vol% H<sub>2</sub>O, leads to a pronounced  $c$ -axis texture of the monolithic films and a thickness of  $1360 \pm 10$  nm after 80 deposition cycles (Figure 4-46 A, C).

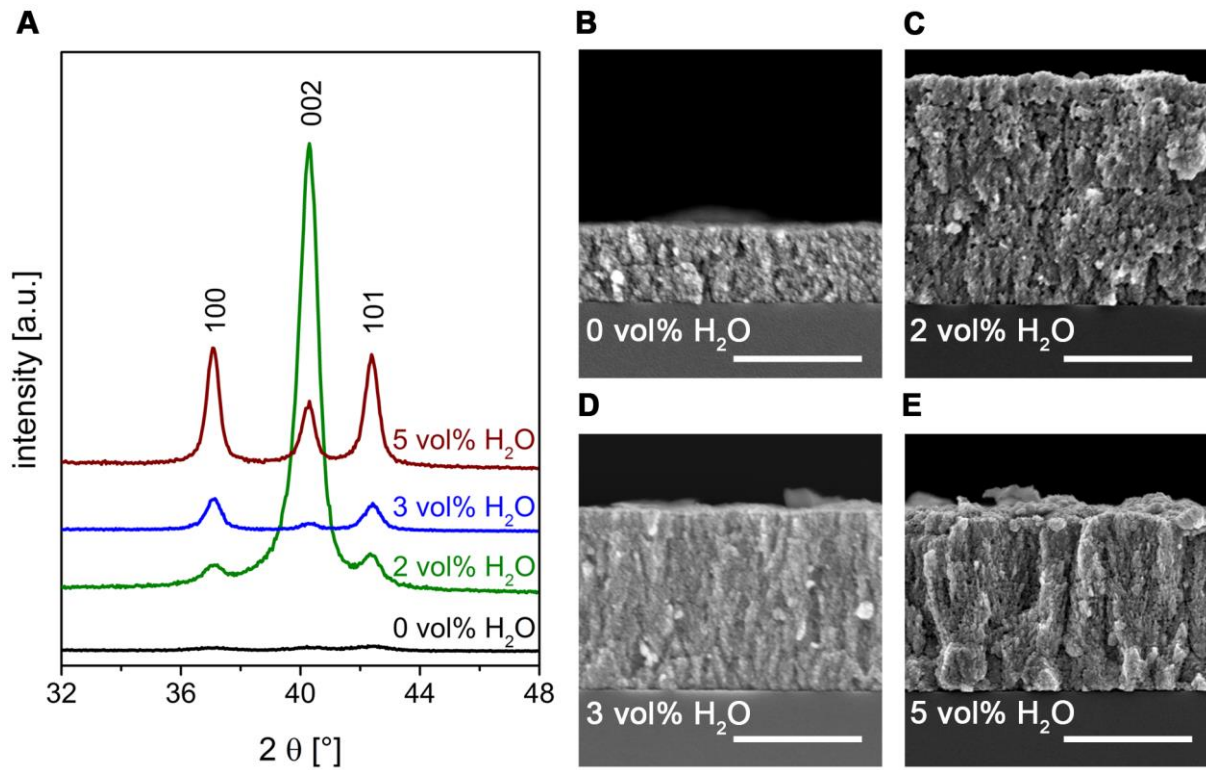


**Figure 4-46:** **A**, XRD patterns of ZnO films prepared with varying water content in the reaction solution on wtTMV monolayers. **B-E**, SEM cross-sections of ZnO films deposited with different water content in reaction solution and adjusted number of cycles. **B**, 0 vol% H<sub>2</sub>O, 100 deposition cycles, **C**, 2 vol% H<sub>2</sub>O, 80 deposition cycles, **D**, 3 vol% H<sub>2</sub>O, 60 deposition cycles and **E**, 5 vol% H<sub>2</sub>O, 30 deposition cycles. All samples were sputtered with 0.5 nm Pt:Pd (80:20). Scale bars represent 800 nm.

The effects of water in the reaction solution, such as (1) changed crystallite size and (2) texture have been discussed in Section 4.3.2.3 (cf. Figure 2-2 B for intensities reflexes of untextured ZnO). With 3 and 5 vol% H<sub>2</sub>O in the reaction solution, 100 textured films (Figure 4-46 A) are obtained with a thickness of around 1140 nm in both cases. However, the morphology of the films' cross-sections differs. Whereas, a smooth and dense film with homogeneous thickness was obtained by addition of 3 vol% H<sub>2</sub>O (Figure 4-46 D), a less uniform film was obtained with 5 vol% H<sub>2</sub>O (Figure 4-46 E). The increased crystallite size (cf. Section 4.3.2.3) caused a higher surface roughness and an increased inhomogeneity of the formed film. This can both be seen in Figure 4-46 E from the cross-section of the ZnO film and the visible part of the film's surface.

#### 4.6.1.2 MECHANICAL PROPERTIES OF MONOLITHIC ZNO FILMS

The monolithic ZnO films deposited from solutions with varying water content were used for nanoindentation experiments. The hardness  $H$  (Figure 4-47 A) and Young's modulus  $E$

(Figure 4-47 B) of the films were estimated as a function of the penetration depth and determined from the measured load-contact depth curves following the procedure of Oliver and Pharr [152], which is described in detail in Section 3.8.8. From the extracted  $H$  values (Figure 4-47 A) it is observable that the hardness rises with increasing water content until a maximum is reached for 3 vol% and then the hardness decreases again for further water addition (5 vol% H<sub>2</sub>O).

The same effect is observable for the Young's modulus, but less pronounced (Figure 4-47 B). The Young's modulus depends stronger on the contact depth than the hardness (especially seen for the thin sample with 0 vol% H<sub>2</sub>O in the reaction solution), because the elastic deformation field under the indenter tip penetrates deeper into the film than the plastic deformation field [198].

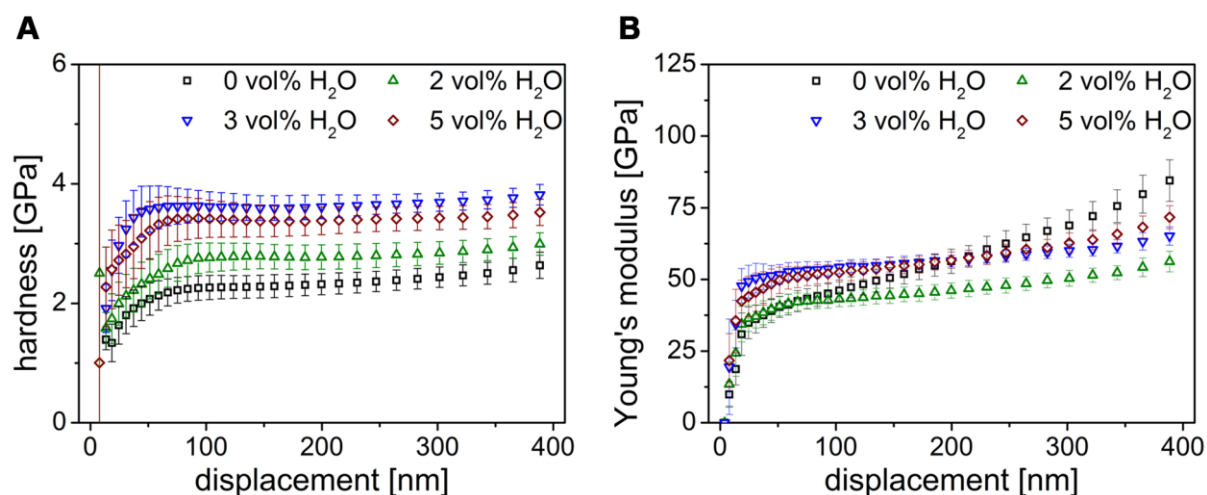


**Figure 4-47: A,** Hardness and **B,** Young's modulus as a function of the penetration depth measured by nanoindentation. All monolithic ZnO films were deposited on a wtTMV monolayer immobilized via CA, but with varying water content (0, 2, 3, and 5 vol% H<sub>2</sub>O) in the methanolic reaction solution. XRD and SEM results of the corresponding films are given in Figure 4-46.

Thus, the elastic deformation field is influenced by the substrate at lower penetration depth. When the penetration depth is in the same magnitude as the films surface roughness, the measured values are falsified by the roughness and should not be taken into account for evaluation. Additionally, it has to be taken into account for the evaluation of data, that for recorded penetration depths larger than 20% of the film thickness, the underlying silicon substrate influences the data [151]. Thus, hardness values were evaluated in the plateau region for penetration depths between 100 and 200 nm, and the Young's modulus also in the

plateau region below 100 nm. The values for hardness and Young's modulus extracted in such way are given in Table 4-13.

**Table 4-13:** Evaluated hardness  $H$  and Young's modulus  $E$  of the monolithic ZnO films in dependency of the water content in the reaction solution (0, 2, 3, and 5 vol% H<sub>2</sub>O) compared to the results of the monolithic ZnO films obtained by Lipowsky *et al.* on polyelectrolytes [63].

	0 vol% H <sub>2</sub> O	2 vol% H <sub>2</sub> O	3 vol% H <sub>2</sub> O	5 vol% H <sub>2</sub> O	[63]
$H$ [GPa]	$2.3 \pm 0.2$	$2.8 \pm 0.2$	$3.6 \pm 0.2$	$3.4 \pm 0.3$	1.7
$E$ [GPa]	$44 \pm 4$	$43 \pm 3$	$53 \pm 3$	$52 \pm 3$	35

As mentioned above, the hardness  $H$  of the monolithic layers increases from roughly  $2.3 \pm 0.2$  GPa for 0 vol% H<sub>2</sub>O up to a maximum of  $3.6 \pm 0.2$  GPa for 3 vol% H<sub>2</sub>O and decreases then down to  $3.4 \pm 0.3$  GPa for 5 vol% H<sub>2</sub>O. The values obtained under purely methanolic conditions (0 vol% H<sub>2</sub>O) can be compared with the results of Lipowsky *et al.* of ZnO films prepared on polyelectrolyte template layers. Both hardness  $H$  and Young's modulus  $E$  of the herein prepared water-free monolithic ZnO films on wtTMV are increased compared to the ZnO films prepared by Lipowsky *et al.* [63]. The reasons for these enhancements are not obvious, since the films differ in their texture, as well as their grain size.

In general, for materials with grain sizes in the micrometer range, the Hall-Petch relation  $\sigma = \sigma_0 + kd^{-0.5}$  is valid.  $\sigma_0$  and  $k$  are materials constants and  $\sigma$  is the yield stress, whereas  $d$  is the grain diameter. From this relation it is expected that the mechanical performance of a material increase with decreasing grain size, since grain boundaries hinder the movement of dislocations. However, there have been manifold reports [199–201] for several nanocrystalline materials, e.g. copper [202], that claim a decrease of the mechanical performance below a critical grain size (typically around 10 – 30 nm). This effect is referred to as 'inverse Hall-Petch effect'. This inverse Hall-Petch effect was not only reported in nanocrystalline metals, but also in nanocrystalline gallium-doped ZnO [203] and nanolaminates of ZnO and Al<sub>2</sub>O<sub>3</sub> [204]. As grains get smaller pile-ups contain less dislocations, the stress at the top of the pile-up is reduced. To generate dislocations in the neighboring grain a higher stress is needs to be applied. However, in very small grains, there is no pile-up of dislocations possible and the mechanism breaks down [205]. Thus, several explanations for the behavior have been suggested, e.g. grain rotation and grain boundary sliding being the dominant deformation mechanism [205,206].

Grain boundary sliding is the main deformation mode for nanocrystalline ceramics. The combination of Hall-Petch (enhanced mechanical properties with decreasing grain size, mm to  $\mu\text{m}$  regime) and inverse Hall-Petch effect (enhanced mechanical properties with increasing particle size, nm regime) leads to an optimum crystallite/grain size for mechanical properties which fits well with the herein obtained experimental results of nanocrystalline ZnO. Below 3 vol%  $\text{H}_2\text{O}$ , corresponding to a crystallite size below 15 nm (cf. Table 4-6), the inverse Hall-Petch seems to dominate, which is in good accordance with the critical crystallite size around 10 to 30 nm indicating that grain rotation and grain boundary sliding are the dominant deformation modes.

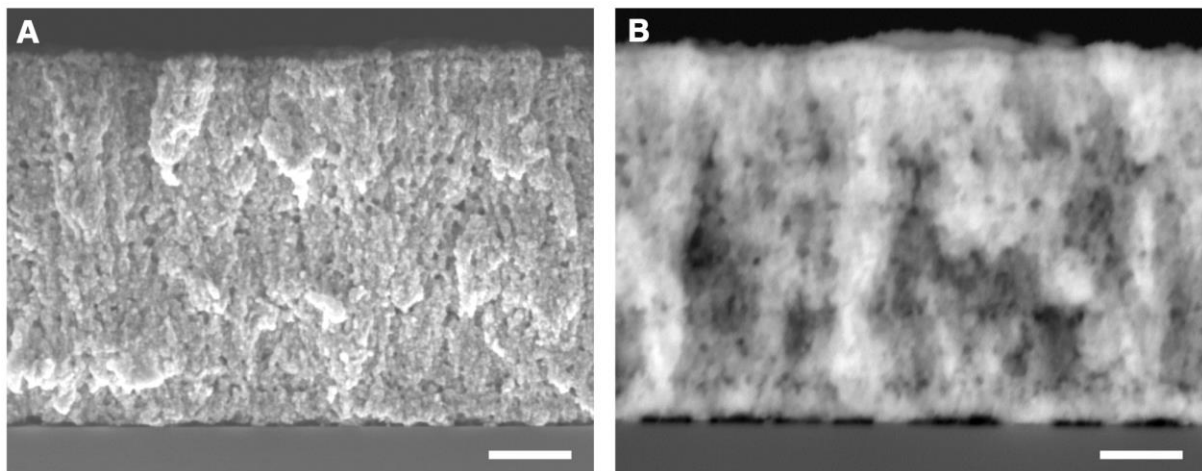


**Figure 4-48:** SEM cross-sections of an unspattered ZnO film deposited from a reaction solution containing 2 vol%  $\text{H}_2\text{O}$  (60 mineralization cycles) imaged with an SE in-lense detector (**A**) and a BSE detector revealing the film's porosity (**B**). The scale bars represent 200 nm.

Above the 3 vol%  $\text{H}_2\text{O}$ , the Hall-Petch effect might be valid, which is indicated by the reduced hardness for 5 vol%  $\text{H}_2\text{O}$ . However, this cannot be proven with the herein obtained results and is just an assumption. Nonetheless, the 3 vol%  $\text{H}_2\text{O}$  in the reaction solution, resulting in ZnO crystallites of 15 nm, seem to be the optimum water content in the reaction solution for the best mechanical performance of ZnO films. Thus, these conditions (3 vol%  $\text{H}_2\text{O}$  in the methanol reaction solution) were chosen for the preparation of the multilayered samples with wtTMV and the mutants.

The obtained hardness and Young's modulus values for the films deposited from the water-containing methanolic reaction solution at moderate reaction conditions are lower than the ones of single crystalline bulk ZnO (cf. Section 2.1.2.4), which might be attributed to the porosity of the prepared films. SEM cross-section analyses with unspattered ZnO films

deposited from reaction solutions with 2 vol% H<sub>2</sub>O indicated nanoporosity within the film (Figure 4-48 A). Imaging with a BSE detector confirmed the porosity of the film (Figure 4-48 B). Calculations by Martin *et al.* [207], where they evaluated the elastic properties of ZnO samples sintered to different densities as a function of the porosity, show a dramatic decrease of the mechanical properties with increasing porosity. For ZnO samples with a porosity of 20%, they reported a decrease in Young's modulus by 50% and for samples with 35% porosity the value of  $E$  decreased 70%.

The results of this work could not support the finding that a preferential  $c$ -axis orientation of the crystallites within the ZnO films leads to better mechanical properties compared to  $a$ -axis texture as reported by Coleman *et al.* [45] and Basu and Barsoum [46]. However, since in their works single crystalline ZnO and epitaxial ZnO were used, these discrepancies might result from the aforementioned crystallite size and porosity effects, which dominate for the nanocrystalline thin films used here.

#### **4.6.2 MULTILAYERED FILMS OF TMV AND ZNO**

Based on the known mechanisms that lead to the enhanced mechanical properties of nacre (cf. Section 2.2.1), such as the interface between organic and inorganic phase, mineral bridges, and nanoasperities, different virus monolayer morphologies were chosen for the multilayer samples. It is important to note, that the conditions were chosen based on the morphology obtained on bare silicon (cf. Section 4.2), however, the second virus layer has to be immobilized on the predeposited ZnO, thus the morphology might be affected, which had to be analyzed. (1) wtTMV was always used as a reference. (2) E50Q mutant was chosen, since it has a different assembly behavior as wtTMV, but provides the same surface chemistry. Therefore, it is possible to determine the influence of the monolayer morphology on the mechanical properties. (3) TMV-Cys was chosen due to the known affinity of cysteine towards ZnO [162,163] which should lead to an enhanced interaction between the organic and inorganic layers.

The CA conditions chosen for the first TMV monolayer on silicon are given in Section 3.7.1. Since analyses with both AFM and SEM showed a similar trend for virus assembly also on the roughened ZnO surface, for all following TMV layers, the same CA conditions were used on ZnO films deposited with 3 vol% H<sub>2</sub>O in the methanolic reaction solution. wtTMV maintained

the structures with voids, leaving space for mineral bridges (cf. Figure 4-6 A). E50Q homogeneously covered the ZnO with defect-free dense virus structures (cf. Figure 4-6 E). TMV-Cys again showed the tendency to form intermingling, dense, disordered virus layers due to formation of disulfide bridges (cf. Figure 4-6 C).

#### 4.6.2.1 MICROSTRUCTURE AND COMPOSITION OF MULTILAYERED SAMPLES

The multilayered samples (MLS) and their corresponding references were prepared as described in Section 3.7.3. For the analyses of the microstructure of the cross-sections, the cut-off edges (cf. Section 3.7.4) of the samples for the nanoindentation experiments were used and a fresh fracture surface was prepared.

In Figure 4-49, the corresponding SEM cross-section images for the MLS are shown. In all cases (wtTMV, E50Q, and TMV-Cys) the ‘brick and mortar’ structure of nacre (cf. Figure 2-5) was successfully mimicked (Figure 4-49 A, C, E). The organic interface between the individual ZnO layers can be seen as dark lines separating the ZnO. The first two ZnO layers seem to be a bit thinner in all cases compared to the following ones. However, the ZnO layer thickness is homogeneous throughout the layers. Some delamination between the layers can be seen (Figure 4-49 A, E), which is owed to the preparation of the fracture surface by simply breaking the samples with the help of a wire cutter (cf. Section 3.7.4). However, neither the MLS nor the monolithic references show any delamination of the entire film from the silicon substrate proving the strong adhesion of the first virus layer to the substrate and the ZnO layer. The reference samples show for each mutant a very similar monolithic structure (Figure 4-49 B, D, F) indicating no big influence of the different template morphology on the monolithic films. The film thicknesses  $t_{MLS}$  and  $t_{Ref}$  were determined from 10 individual SEM cross-section images and are given in Table 4-14.

The thickness of the monolithic samples is lower than the one of the MLS, since there are no organic interlayers in the monolithic films. The thickness difference between  $t_{MLS}$  and  $t_{Ref}$  fits well to the calculated height of all organic layers assuming a height of 9 nm for the viruses (as measured via AFM after methanol treatment, cf. Section 4.3.1). The increased thickness of the TMV-Cys MLS and the large standard deviation were caused by delamination between the layers due to preparation of the fracture surface, thus not allowing accurate thickness determination.

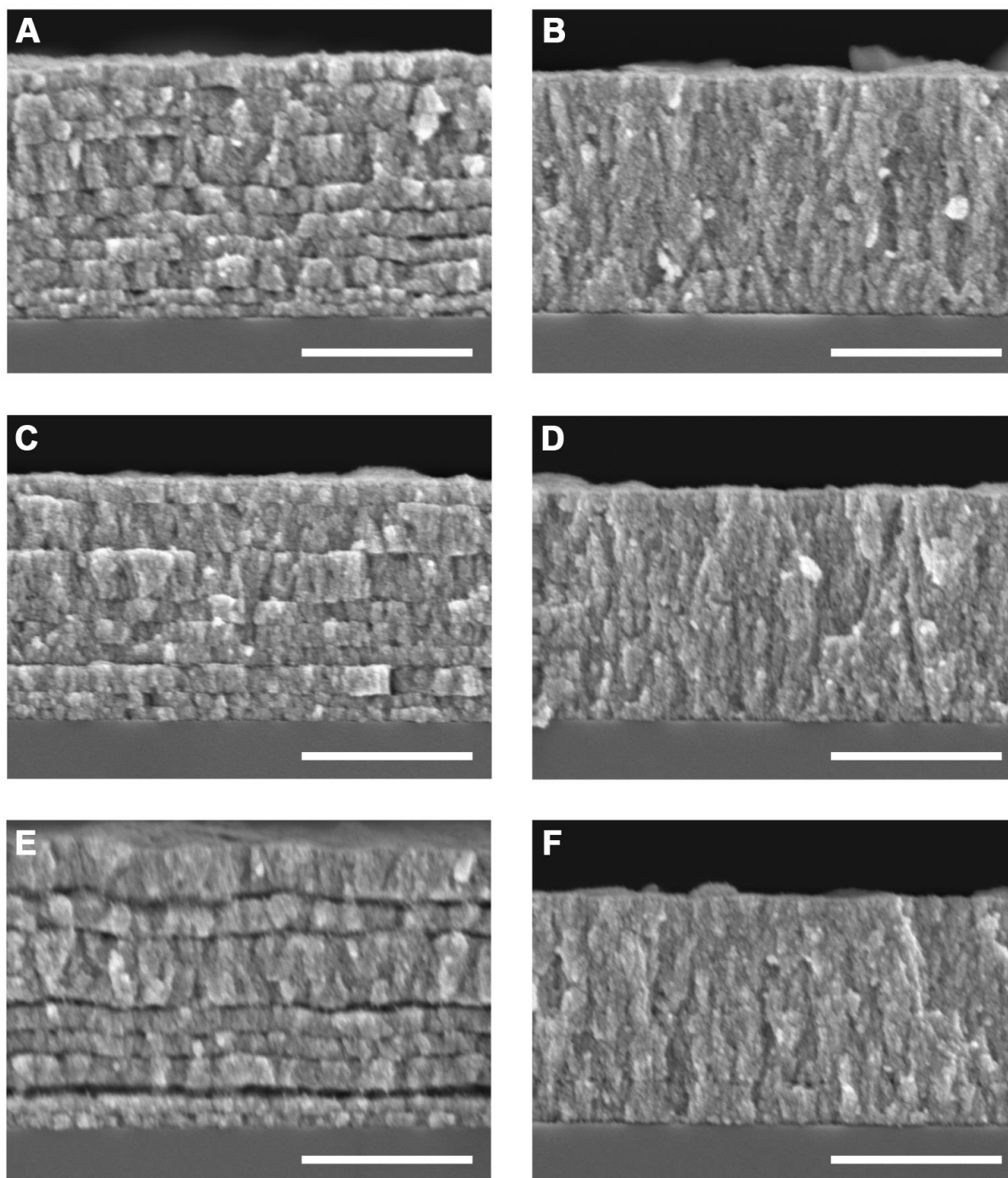


**Figure 4-49:** SEM cross-sections of the multilayered samples (MLS, left) and the corresponding reference sample (right). Films are deposited onto wtTMV (A, B), E50Q (C, D), and TMV-Cys (E, F). MLS were prepared by CA and ZnO deposition which was repeated until 10 organic/inorganic bilayers were obtained. CA conditions were  $c = 1.9 \text{ mg mL}^{-1}$ ;  $v_w = 0.6 \text{ mm min}^{-1}$ ;  $V = 5 \text{ } \mu\text{L}$ . Films were deposited from reaction solutions with 3 vol%  $\text{H}_2\text{O}$  applying six deposition cycles for the MLS. The corresponding references have one template layer and are subsequently mineralized as often as the MLS resulting in 60 deposition cycles. The scale bars represent 800 nm and all samples were sputtered with 0.5 nm Pt:Pd (80:20).



Evaluation of the thickness of individual ZnO layers revealed a thickness around 105 nm which is in good range of the optimum thickness ratio of about 1:10 between organic and inorganic material, as it is found in nacre (cf. Section 2.2.1), which was here obtained by choosing six mineralization cycles.

Not all 10 organic layers can be seen over the entire cross-section which is caused by the sample preparation. The cross-sections were prepared from the cut-off edges of the wafers. Due to the CA process, the virus monolayer did not always reach the end of the wafer perfectly, leaving such small areas virus-free. This only happened in the edge regions; therefore, nanoindentation (cf. Sections 3.8.8 and 4.6.2.2) was performed in the center of the samples and not the edge regions.

**Table 4-14:** Film thicknesses  $t$  of the MLS and corresponding monolithic references as obtained from 10 individual SEM cross-section images per sample.

	wtTMV	E50Q	TMV-Cys
$t_{MLS}$ [nm]	$1218 \pm 21$	$1151 \pm 23$	$1344 \pm 52$
$t_{Ref}$ [nm]	$1131 \pm 15$	$1094 \pm 10$	$1078 \pm 10$

The samples' surface roughnesses were obtained via AFM height images. In Figure 4-50 such AFM height images are shown exemplarily for the wtTMV-based MLS and monolithic reference sample. The roughness  $R_{ms}$  is  $20 \pm 3$  nm for  $5 \times 5 \mu\text{m}^2$  scans and  $11 \pm 2$  nm for  $1 \times 1 \mu\text{m}^2$  for both MLS and reference samples. There were no significant differences between wtTMV, E50Q, and TMV-Cys. The values confirm the samples' homogeneity which was already indicated by the cross-sections.

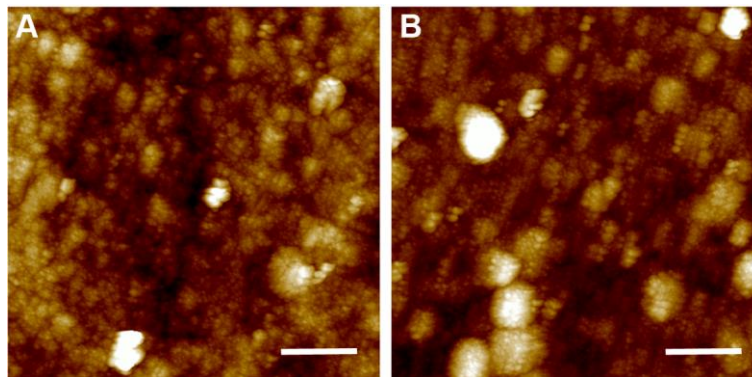


**Figure 4-50:** AFM height images of a multilayered sample with wtTMV as a template (A) and the corresponding monolithic reference on wtTMV (B). The scale bars represent 1  $\mu\text{m}$ .

For neither MLS nor monolithic reference samples cracks were found within the films or on top. The roughness is well below the required 30 nm (cf. Section 3.8.8), which is important for nanoindentation, since the roughness of the film should be below the indenter diameter of roughly 40 nm. On all samples some islands with increased height were found (very bright spots in Figure 4-50) which were avoided during nanoindentation (cf. Sections 3.8.8 and 4.6.2.2).

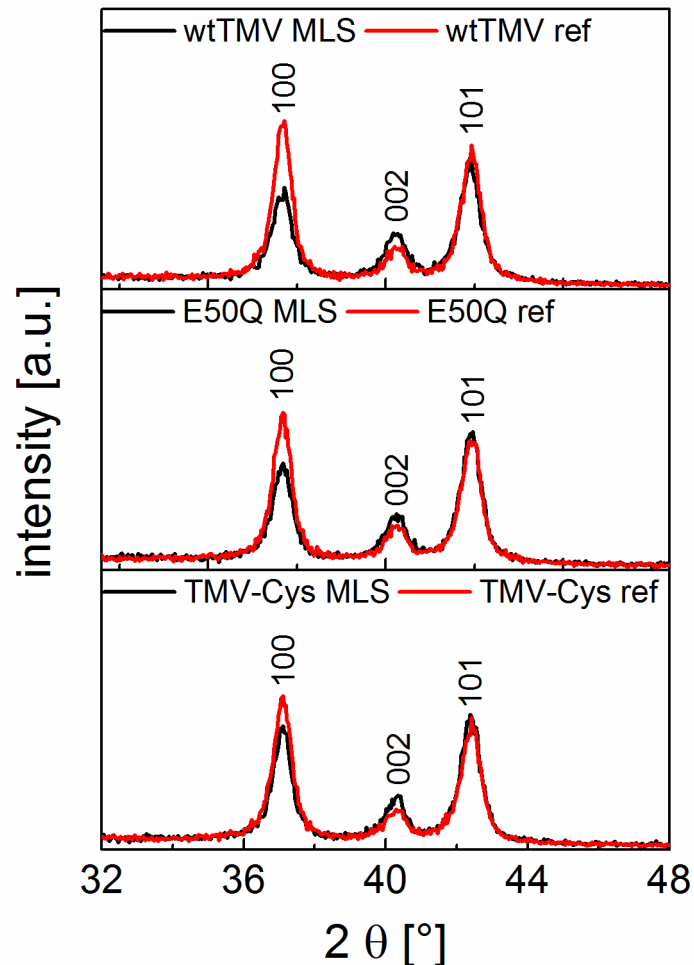


**Figure 4-51:** XRD patterns of the multilayered samples (MLS) and the corresponding references (ref) for all used TMV (wtTMV, E50Q, TMV-Cys) deposited from reaction solutions with 3 vol% H<sub>2</sub>O.

The XRD analyses of the MLS and their corresponding monolithic references revealed the formation of 100 textured ZnO for all virus templates for both the MLS and the references, respectively (Figure 4-51). This is in good accordance with the results for thin films deposited from reaction solutions containing 3 vol% H<sub>2</sub>O described in Section 4.3.2.1 (cf. Figure 4-21). However, differences in the relative intensities of the 100 and 002 reflections can be seen in

Figure 4-51 between MLS and references. The area under those reflections was fitted, as described in Section 3.8.6, and the texture ratio  $T_{100}$  of the integrated relative intensities of the 100 and the 002 reflections was used to quantify the differences in the crystallite orientations (Table 4-15).

The XRD patterns (Figure 4-51) revealed in general a higher degree of 100 texture of the reference samples compared to the MLS, which was confirmed by the quantitative evaluation (Table 4-15). This is in good accordance with the previously reported enhancement of the 002 texture with increasing film thickness in Section 4.3.2.3. The texture of the ZnO films is enhanced with increasing film thickness due to better ordering of the later deposited ZnO crystallites on already partially oriented ZnO layers (more details in Section 4.3.2.3).

**Table 4-15:** Texture coefficients  $T_{100}$  obtained from fitted XRD data of the MLS and corresponding reference (ref) films deposited from reaction solutions containing 3 vol% H<sub>2</sub>O.

TMV	$T_{100,MLS}$	$T_{100,ref}$
wtTMV	1.5	3.6
E50Q	1.6	3.0
TMV-Cys	2.1	3.3

In the case of the multilayered samples, this ordering is interrupted each time when a new virus layer is deposited via CA and the process of ordering needs to start again. However, in the case of TMV-Cys, this effect is less pronounced. Whereas the degree of texture drops by 58% from the reference to MLS in the case of wtTMV and by 47% for E50Q, the drop is only 36% in the case of TMV-Cys. This is also qualitatively visible in the XRD patterns (Figure 4-51), where the signals for MLS and reference of TMV-Cys show the smallest deviations from each other. This might be attributed to the enhanced affinity of ZnO crystallites towards cysteine. The affinity of cysteine towards zinc ions [162] and surfaces [163] has been reported: (1) Passerini *et al.* investigated the participation of amino acids, such as cysteine and histidine, in binding transition metals, e.g. zinc ions. With the help of protein function prediction with support vector machines they proved a strong interaction of cysteine and histidine with zinc ions [162]. (2) Rothenstein *et al.* investigated the interaction of 12mer peptides with single crystalline  $\pm 001$  ZnO surfaces in aqueous solutions. By the combination of phage display and NMR investigations they revealed a strong interaction of both histidine and cysteine with the single crystalline ZnO surfaces [163]. However, these finding cannot be directly compared with

the herein used system, since the binding situation is more complex for the large TMV-Cys molecule. Additionally, the herein used methanolic reaction solution makes a comparison challenging. Nonetheless, in the herein reported case, the stronger interaction between the cysteine functionalities present on genetically engineered TMV-Cys on the outer virus surface (cf. Figure 4-3) and the ZnO crystallites could facilitate the oriented attachment leading to increased texture already for a thinner film thickness.

#### **4.6.2.2 MECHANICAL PROPERTIES OF MULTILAYERED SAMPLES**

For the determination of the mechanical properties of the MLS and their monolithic references, both nanoindentation and microindentation experiments were performed, respectively. Nanoindentation (cf. Section 3.8.8) gave access to the samples hardness  $H$  and Young's modulus  $E$  as a function of the penetration depth. By microindentation (cf. Section 3.8.9) on partially coated silicon substrates, the fracture toughness  $K_c$  of the samples was determined.

##### ***HARDNESS AND YOUNG'S MODULUS***

Nanoindentation experiments were performed as described in Section 3.8.8 in order to investigate the effect of (1) the multilayering and (2) the genetic modification on the mechanical properties.

The obtained hardness and Young's moduli as a function of the indentation depth for the MLS and their monolithic references prepared with wtTMV, E50Q, and TMV-Cys are all given in Figure 4-52. For all samples, the hardness reaches a constant plateau after a penetration depth of 100 nm. Young's modulus does not reach that plateau and slightly increases, which can be observed in Figure 4-52 B, D, and F. This occurs due to the larger penetration of the elastic field and resulting substrate contribution to the signal (the causes for this behavior were explained in detail in Section 4.6.1.1 for the monolithic films).

For the wtTMV-based samples, the measurements revealed for both hardness and Young's modulus lower values for the MLS compared to the monolithic reference (Figure 4-52 A, B). The hardness decreases nearly by  $\approx 40\%$  for the MLS and Young's modulus by  $\approx 30\%$ . Changing the template to E50Q, which forms more homogeneous monolayers on both silicon and ZnO (cf. Figure 4-7 D and Section 4.6.2.2), reduces the decrease in hardness to  $\approx 17\%$ , and the decrease for Young's modulus to  $\approx 20\%$  (Figure 4-52 C, D). However, the situation is changed

for TMV-Cys. The hardness is increased by multilayering by a factor of  $\approx 27\%$  and Young's modulus is also enhanced by 10% upon multilayering (Figure 4-52 E, F).

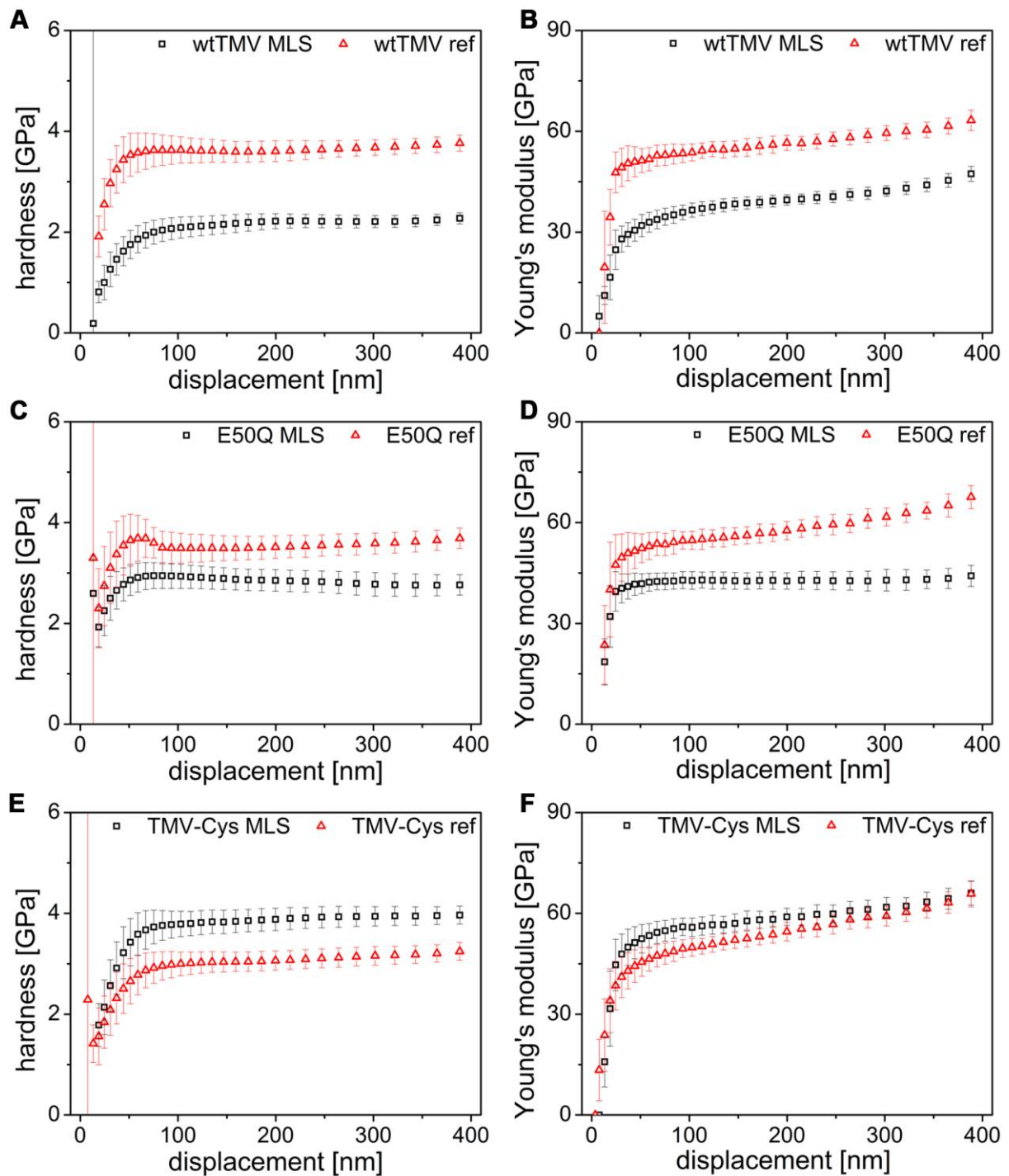


**Figure 4-52:** Hardness  $H$  (A, C, E) and Young's modulus  $E$  (B, D, F) as a function of indenter displacement measured by nanoindentation for MLS and their references prepared with wtTMV (A, B), E50Q (C, D), and TMV-Cys (E, F).

These differences in hardness and Young's modulus upon multilayering in dependency on the templates are visualized in Figure 4-53. Whereas the hardness of the MLS increases from

wtTMV over E50Q to TMV-Cys, the hardness of the references stays constant for wtTMV and E50Q and decreases for TMV-Cys (Figure 4-53 A). The same effect is observed for the Young's modulus: The value increases for the MLS from wtTMV over E50Q to TMV-Cys and for the references wtTMV and E50Q do not differ, while it is slightly decreased for TMV-Cys (Figure 4-53 B).

The combination of a stiff inorganic (here: ZnO) and a soft organic (here: TMV) to a layered structure should lead, according to the rule of mixture, to a lower Young's modulus of the layered composite compared to the pure inorganic [208]. In nanoindentation, the applied load is perpendicular to the layered structure, thus the Reuss model can be used to predict Young's modulus of the composite  $E_R$  as given in equation (4-2)

$$\frac{1}{E_R} = \frac{f_o}{E_o} + \frac{f_i}{E_i} \quad (4-2)$$

Here,  $f_o$  is the volume fraction of the organic phase and  $f_i$  the volume fraction of the inorganic phase, which were estimated from the obtained SEM cross-sections (Figure 4-49) by comparing the thicknesses  $t_{MLS}$  and  $t_{Ref}$  given in Table 4-14 in order to obtain the total thickness of the organic phase and dividing by the number of organic layers. The values are only obtained from cross-section images, i.e. the height of the organic layer. Therefore, differences in packing density cannot be considered. Since E50Q has a lower thickness than wtTMV (cf. Section 4.2.1),  $f_o$  is smaller for E50Q (cf. Table 4-16).  $E_{o/i}$  are Young's moduli of the organic and inorganic phases.

Additionally, the phenomenologically determined model for Young's modulus of Braem *et al.* given in equation (4-3) was used [209]. This was originally derived from experimental data of various dental composites and can be interpreted as a generalized Voigt model, where the resulting modulus  $E_B$  is a linear mixing of the logarithms of the moduli of organic and inorganic phase

$$E_B = E_o^{f_o} \cdot E_i^{f_i} \quad (4-3)$$

For the Young's modulus of wtTMV and E50Q, the literature value of 1 GPa of wtTMV determined by Zhao *et al.* [210] was used and, for the ZnO, the measured moduli of the reference samples were used (Figure 4-53 B).

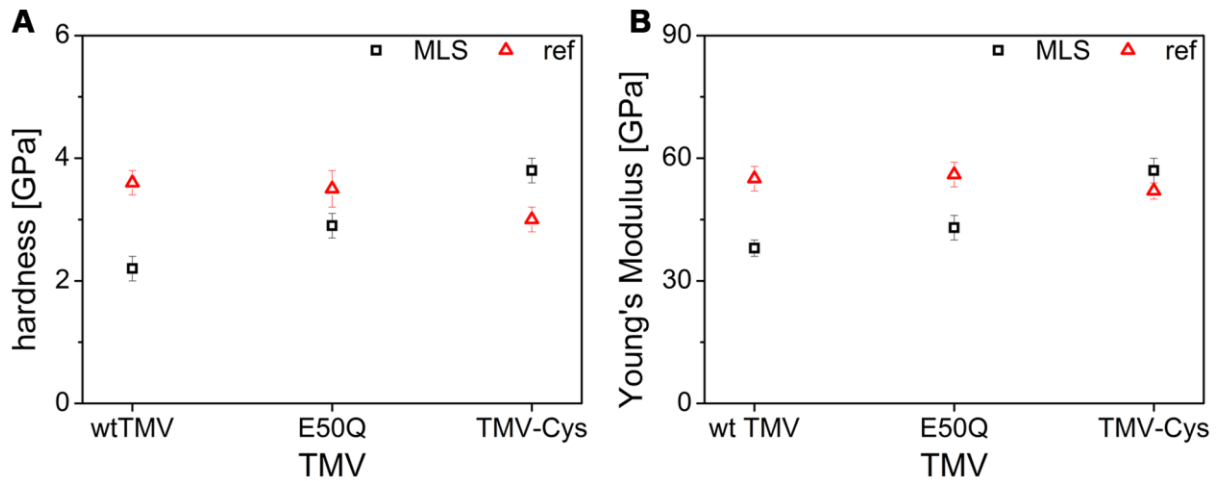


**Figure 4-53:** Hardness  $H$  (A) and Young's modulus  $E$  (B) of the MLS and monolithic references (ref) as a function of the template. The values were determined from the plateau regions of Figure 4-52 as described in detail in Section 3.8.8.

In such way, the measured values can roughly be compared with the theory. However, the values for E50Q are only an approximation, since Young's modulus is lower, due to the lack of RNA. Unfortunately, there is no knowledge of the Young's modulus of E50Q to this point. Thus, Young's modulus of wtTMV was used as an estimation. TMV-Cys is excluded from this evaluation, since the observed increase of the Young's modulus contradicts the theory. The values used for the calculation and the resulting  $E_R$  and  $E_B$ , as well as the measured  $E$  are given in Table 4-16. It can clearly be seen that both models correctly predict the slightly higher Young's modulus of E50Q-based samples, which is attributed to the lower volume fraction of the organic phase. However, to correctly predict the values, the Young's modulus of E50Q would be necessary.

The Young's moduli predicted from the Reuss model are by far too low compared to the experimentally obtained ones. It has been reported that Reuss models are less accurate for high ceramic contents [211]. Simulations of the system of multi-layered samples with varying polyelectrolyte and  $\text{TiO}_2$  layers indicated a strong influence of the mineral bridges on Young's modulus indicating a by far more complex situation than just applying the rule of mixture [212]. However, the phenomenological model of Braem *et al.* is in very good accordance with the herein measured Young's moduli leading to deviations in the range of only 7%. Thus, the decrease in Young's modulus can be at least partially attributed to mixing of a hard and soft material in these cases.

**Table 4-16:** Values used for calculation of Young's modulus of the composite applying the Reuss model ( $E_R$ ) and the phenomenological model by Braem *et al.* [209] ( $E_B$ ) for comparison with the measured values  $E$  for the wtTMV-based and E50Q-based MLS.

TMV	$f_o$ [-]	$f_i$ [-]	$E_o$ [GPa]	$E_i$ [GPa]	$E_R$ [GPa]	$E_B$ [GPa]	$E$ [GPa]
wtTMV	0.07	0.93	1	55	11	41	38
E50Q	0.05	0.95	1	56	15	46	43

In contrast to the rules of mixing, the Young's modulus of the TMV-Cys MLS is increased compared to the reference. A similar behaviour was observed for multi-layered systems of polyelectrolytes and ZnO [63], as well as TiO<sub>2</sub> [50]. Lipowsky *et al.* reported almost the same Young's modulus for the MLS sample (polyelectrolyte/ZnO, 40 GPa) and the monolithic reference (35 GPa), which they attributed to interactions between ZnO and the polyelectrolyte [63].

The increased determined Young's modulus suggests an enhanced organic/inorganic interaction, which is in accordance with the reported affinity of cysteine towards ZnO [162,163] which was explained more in detail above (cf. Section 4.6.2.1). This is supported by the aforementioned XRD results (cf. Figure 4-51), where the TMV-Cys based samples showed the smallest deviations between MLS and references.

As mentioned above, the hardness of the references, prepared on the different virus templates, is not the same (cf. Figure 4-53 A) for all templates even though the morphology of the cross-sections (cf. Figure 4-49, right column) did not differ. Whereas, wtTMV- and E50Q-based monolithic references have approximately the same hardness value taking the deviations into account, the monolithic samples prepared on TMV-Cys have a lower value. Since the morphology is the same, this could be caused by a structural difference. However, the XRD data revealed that the degree of texture in the case of the TMV-Cys/ZnO sample is between the ones of wtTMV/ZnO and E50Q/ZnO (cf. Table 4-15). The cause of the reduced hardness of the TMV-Cys/ZnO reference remains unclear so far, but was well reproduced. These findings highlight the importance of reference samples for each different template type, since manifold factors seem to govern the ongoing processes. Thus, the increases or decreases in hardness are always given in relation to the corresponding reference prepared on the same template.



Both wtTMV and E50Q interlayers between the inorganic ZnO layers cause a decrease in hardness as mentioned above, even though there are differences in the virus monolayer morphology. The morphology of the wtTMV layers contains large voids leaving space for large mineral bridges between the layers. E50Q in contrast forms very dense monolayers leaving no space for bridges between the inorganic layers. Thus, there seems to be no influence of the mineral bridges in the herein described cases.

The E50Q mutant possesses the same functional groups on the surface as the wildtype, thus the same organic/inorganic interaction is expected. Due to the lack of RNA, the E50Q mutant has a higher flexibility [1] and deforms even more when in contact with a substrate. This is also indicated by the assessed volume fraction of the organic phase in the case of E50Q (cf. Table 4-16). The higher degree of homogeneity on E50Q monolayers enhances the hardness of the E50Q MLS compared to wtTMV MLS. However, it is still decreased compared to the monolithic ZnO sample. This hints towards a poor interaction between the viruses and the ZnO. In such way, the ZnO layers slide on the virus layers upon deformation and the energy is not dissipated in the organic layer hindering one of the factors causing hardening in nacre.

Additionally, there are neither covalent bonds between the individual wtTMV and E50Q virus particles nor do they intermingle as in the case of TMV-Cys. Thus, the inter-virus interactions are the lowest in the case of wtTMV, since E50Q's monolayers are denser due to the enhanced flexibility [1]. Poor connections and interactions in between the virus particles leads to poor load transmission during deformation hindering an improved hardness. This would also explain the lower decrease of hardness in the case of E50Q caused by denser virus packing.

In contrast to the other virus templates TMV-Cys leads to an enhancement of the multilayer's hardness by  $\approx 27\%$  compared to the monolithic reference. The increase in hardness is in the same range as reported by Lipowsky *et al.* for multilayers consisting of polyelectrolytes and ZnO [63], and higher than in the case of TiO<sub>2</sub> multilayers [62].

Combination of a hard (ZnO) and a soft material (TMV) in alternating fashion leads to a periodical variation of Young's modulus (values given in Table 4-16). Koehler proposed that such variation of materials with high and low elastic constants results in an increased external stress necessary to drive the deformation field from one material to another [213]. Calculations by Fratzl *et al.* showed in general that layered systems consisting of two materials with different elastic moduli exhibit local differences in crack driving forces [214]. They even

report that crack propagation is suppressed in the soft layer, when the ratio of moduli is larger than 5, independent of the thickness of the organic layer. However, the periodical variation of moduli cannot be the only cause for the increased hardness of TMV-Cys/ZnO multilayers, since also in the case of wtTMV and E50Q the moduli are varied, but the hardness is decreased.

Thus, the hardness increase has to be attributed to the genetic modification of the viruses. Cysteine has not only an affinity towards ZnO enhancing the organic/inorganic interaction, the cysteine in TMV-Cys also leads to formation of disulfide bridges [1] and thus intermingled, well-connected virus particles strengthening the virus-virus connections (cf. Figure 4-7 D). Such a high anchoring of the organic adhesive phase contributes to the enhanced mechanical properties [54]. Thus, more force is necessary to drive the deformation field through the multilayered sample due to both the interactions between TMV-Cys/ZnO and TMV-Cys/TMV-Cys leading to an increased hardness.

#### **FRACTURE TOUGHNESS**

Nacre is well-known for its manifold possibilities to dissipate energy due to its extraordinary hierarchical microstructure leading to a very high fracture toughness  $K_c$ , while the high values for hardness and Young's modulus are preserved. The combination of stiffness, hardness and toughness is desirable for many materials. Thus, not only Young's modulus and the hardness of the herein synthesized TMV/ZnO multilayers are of great interest, but also the fracture toughness  $K_c$ .

Xia *et al.* developed a method to determine the fracture toughness of thin films by indentation [153], which is explained in detail in Section 3.8.9. It is necessary to have an uncoated area of bare silicon substrate with a sharp edge to the coating (cf. Figure 3-4). This is rather challenging for solution-processed samples, especially in organic solvents like methanol. In this case, simple masking with adhesive Teflon tape during mineralization, as it was done for aqueous TiO<sub>2</sub> mineralization solutions [50], was not possible due to dissolution of the glue at the given mineralization conditions. Replacing the tape with photoresist to mask part of the wafer during mineralization also failed, since methanol and the used base (tetraethylammonium hydroxide) are commonly used as strippers for photoresists. Thus, the half-coated substrates were prepared by partially removing the coating after the mineralization process. Therefore, the ZnO films (MLS and references) were masked and partially coated with a protective photoresist (cf. Section 3.7.5.1). Subsequently, the

unprotected part of the ZnO film was removed by etching. Finally, the protective photoresist layer was removed with acetone leaving behind a partially coated silicon substrate with a clear edge between coated and uncoated silicon (cf. Section 3.7.5.2).

Indents were placed on such partially coated samples in the bare silicon substrate in order to generate cracks around the indent with one crack propagating into the coating (cf. Figure 3-4). The derived formula (3-1) is independent of the distance of the indent to the coated area ( $s$ ) [153], however, it was attempted to keep the distance in similar ranges.

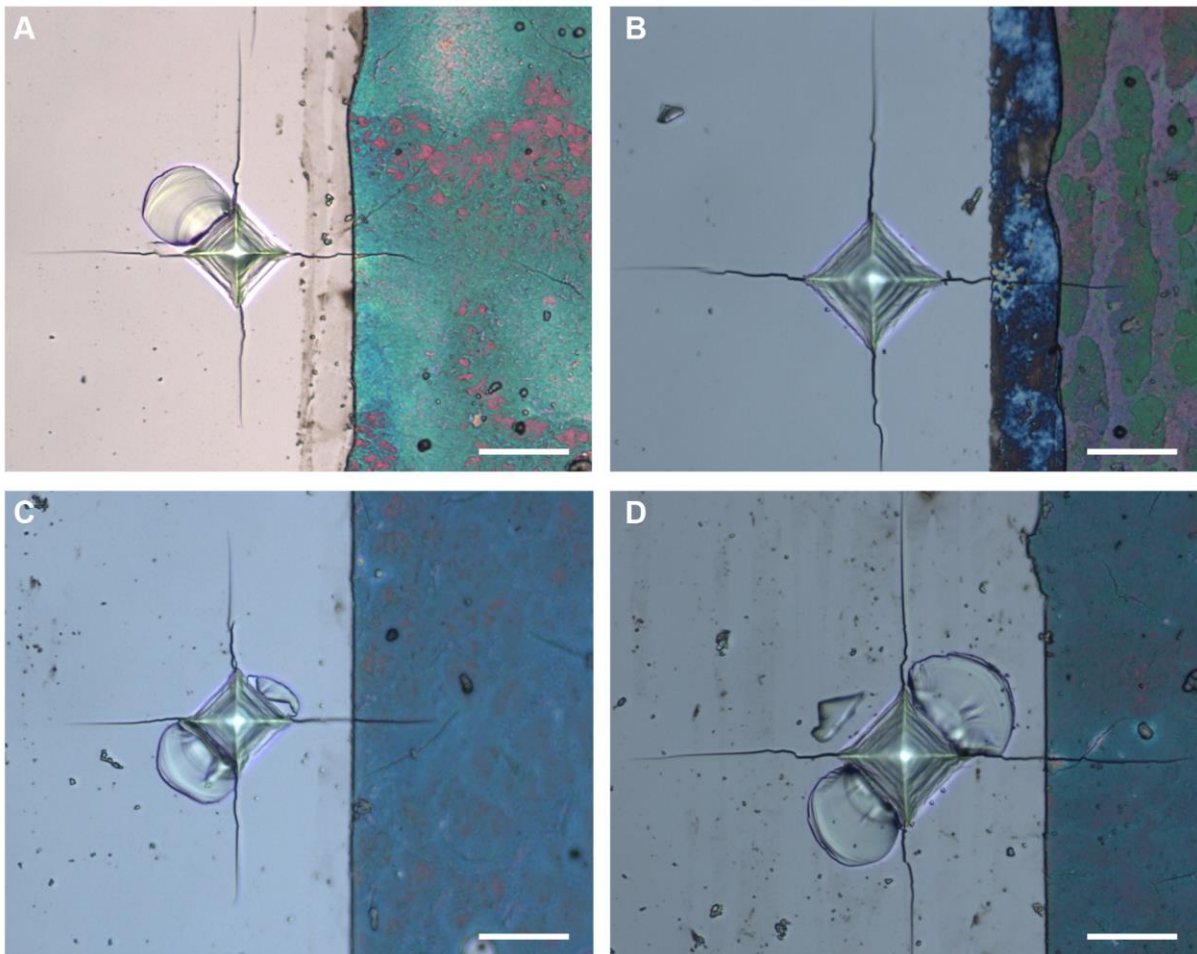


**Figure 4-54:** Light microscope images of indents placed in the silicon part of partially coated substrates with MLS samples (**A, B**) and reference samples (**C, D**) based on wtTMV (**A, C**) and TMV-Cys (**B, D**). Indents were obtained with 0.3 kg (**A, C**) and 0.5 kg (**B, D**). All scale bars are 20  $\mu\text{m}$ .

The obtained cracks were evaluated with the light microscope for multilayered samples (wtTMV, TMV-Cys) and the corresponding references prepared with 3 vol%  $\text{H}_2\text{O}$  as described in Section 3.7.3. Only five organic/inorganic bilayers were produced, since thicker films lead to delamination during the indentation and crack deflection. E50Q-based samples were not

included in the investigations since their mechanical properties were similar to wtTMV and did not lead to enhanced mechanical properties by multilayering.

The resulting indents are shown in Figure 4-54. The edges between uncoated silicon and coating obtained via the aforementioned partial etching of the ZnO layers resulted in very sharp edges, especially in the case of the references (Figure 4-54 C, D). For the MLS only very thin residuals of the first organic/inorganic bilayer were left behind and are visible between the indent and the coating (Figure 4-54 A, B). Some surface cracks were introduced in the layers due to the baking of the photoresist during the masking process in order to get partially coated samples for the fracture toughness evaluation (cf. Section 3.7.5.1).

The crack lengths  $a$  (crack propagating into the coating) and  $b$  (crack propagating into substrate) were evaluated for at least five and up to ten nice indents for each sample (cf. Figure 3-4 for the naming of the variables). The main finding is that cracks  $a$  in the reference samples are always longer than cracks  $b$ . Whereas cracks  $a$  in the MLS are always shorter than the cracks  $b$ . More energy is dissipated in the MLS than in the references, which proves an enhancement of the fracture toughness  $K_c$  in the case of the MLS compared to the references for both wtTMV and TMV-Cys.

The fracture toughness  $K_c$  was calculated according to equation (3-1) and (3-2) as described in detail in Section 3.8.9 and in reference [153]. This was only done for the multilayered samples, since the references did not fulfil the requirement of  $b > a$  [153], thus the formula is not valid for the references. However, it is possible to state that the fracture toughness of the references does not exceed the value of the silicon substrate. Thus, the fracture toughness of the references is maximally  $K_{c,Ref} = 0.83 \text{ MPa m}^{1/2}$  [153].

The obtained fracture toughness values of the MLS are  $K_{c,wtTMV} = 1.8 \pm 0.4 \text{ MPa m}^{1/2}$  and  $K_{c,cys} = 1.3 \pm 0.4 \text{ MPa m}^{1/2}$ . Even though no absolute values could be calculated for the references, the enhancement of the fracture toughness by mimicking nacre's hierarchical structure is at least +54% for wtTMV and +36% for TMV-Cys.

Several factors cause such enhancement of energy dissipation, among which the crack deflection along the organic/inorganic interface is of major importance. The SEM cross-section images shown in Figure 4-55 clearly illustrate the crack deflection in the MLS (Figure 4-55 A, C) compared to brittle fracture of the monolithic reference (Figure 4-55 B, D).

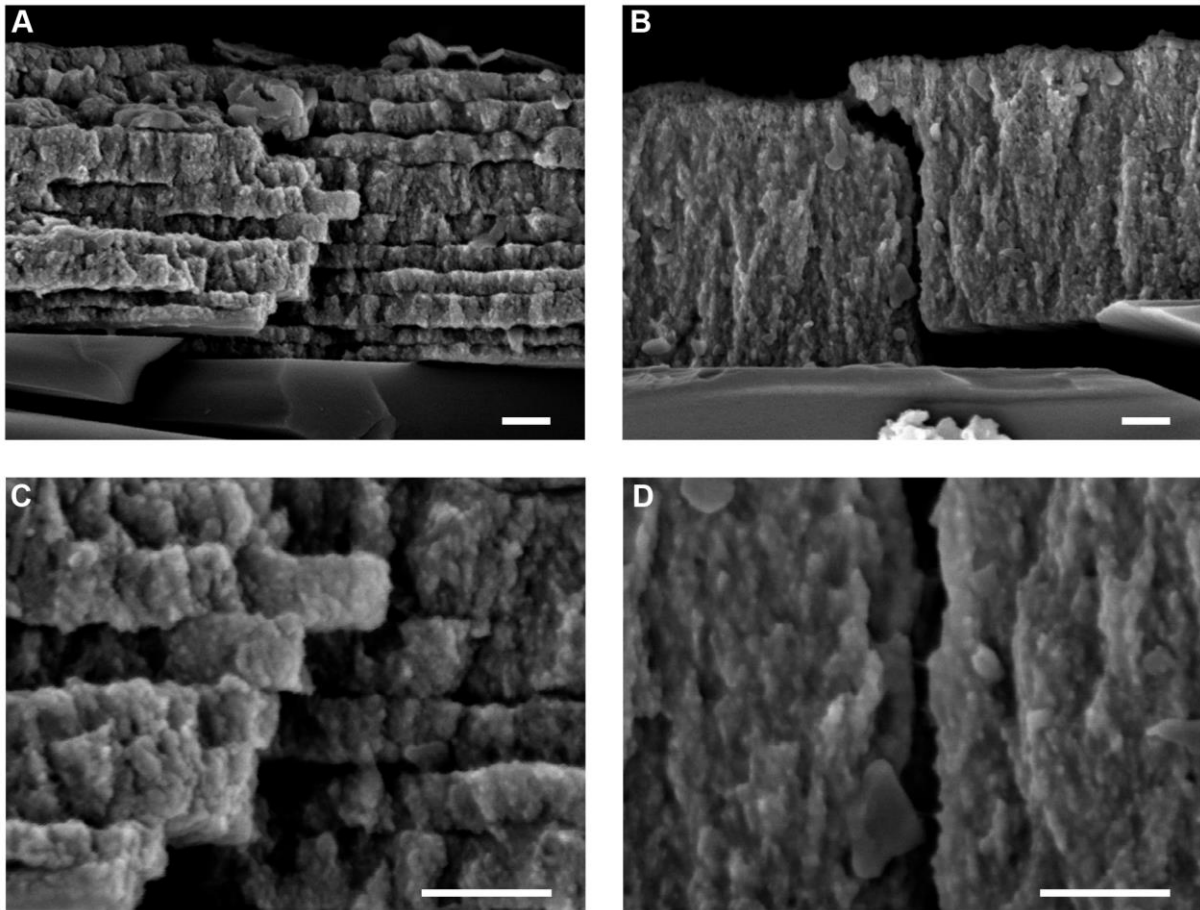


**Figure 4-55:** SEM cross-section images of wtTMV-based MLS (**A, B**) and monolithic reference (**C, D**) revealing crack propagation through the films. All scale bars are 200 nm. Samples were sputtered with 0.5 nm Pt:Pd (80:20).

The organic interlayers cause the crack to deflect, blunt and branch enhancing the energy dissipation. Additionally, a pull-out of cracked ZnO layers is observable, which is comparable to the platelet pull-out in nacre. The inherent surface roughness of the nanocrystalline ZnO layers resembles the nanoasperities of nacre (cf. Figure 2-5 B) inducing friction upon pull-out. The morphology of the individual ZnO layers consisting of nanocrystallites is similar to the nanostructured setup of the individual aragonite platelets in nacre. Thus, it can be expected that rotation and deformation of such nanocrystallites contributes to energy dissipation as described for nacre [55].

Usually, Young's modulus  $E$  and hardness  $H$  are reduced in composites with enhanced toughness  $K_c$ . In Table 4-17, the mechanical performance of both the wtTMV-based and the TMV-Cys-based MLS are given. In the case of wtTMV/ZnO composite both hardness and Young's modulus are reduced compared to the reference resulting in an enhanced fracture

toughness  $K_c$ . The fracture toughness  $K_c$  of the TMV-Cys/ZnO composite is also increased compared to the references (comparison crack lengths).

**Table 4-17:** Mechanical performance ( $E, H, K_c$ ) of MLS based on wtTMV and TMV-Cys and the corresponding references.

	MLS <sub>wtTMV</sub>	Ref <sub>wtTMV</sub>	MLS <sub>TMV-Cys</sub>	Ref <sub>TMV-Cys</sub>
$E$ [GPa]	$38 \pm 2$	$55 \pm 3$	$57 \pm 2$	$52 \pm 3$
$H$ [GPa]	$2.2 \pm 0.2$	$3.6 \pm 0.2$	$3.8 \pm 0.2$	$3.0 \pm 0.2$
$K_c$ [MPa m <sup>1/2</sup> ]	$1.8 \pm 0.4$	$0.83^{[153]}$	$1.3 \pm 0.4$	$0.83^{[153]}$

However, the absolute calculated value of  $K_c$ , as given in Table 4-17, is smaller than in the case of wtTMV. This is in good accordance with the previously discussed (cf. Section 4.6.2.2) enhanced hardness and constant Young's modulus of TMV-Cys/ZnO composites compared to the reference. The enhanced interaction of the cysteine groups with ZnO leads to a stiffer connection between the organic and the inorganic phase, allowing less energy dissipation highlighting the importance of the interaction of organic and inorganic phase.

In summary, the multilayering of viruses and ZnO led to an enhancement of the fracture toughness of the composite samples compared to their monolithic references. However, only the genetically engineered TMV-Cys mutant additionally showed improved hardness and constant Young's modulus.

## 5 SUMMARY

### REACTION SOLUTION FOR ZNO MINERALIZATION

A methanolic reaction solution with a structure-directing agent was used to synthesize nanocrystalline ZnO. Small amounts of water were added to the system in order to tune the crystallite size by triggering the hydrolysis rate. The water content was varied from 0 to 5 vol% and the reaction solution was investigated *in-situ* with dynamic light scattering. The measurements revealed that the size ( $\approx 16$  nm) of the formed particles was constant for 100 minutes followed by strong increases in particle size with longer reaction times (up to  $\approx 55$  nm). Thus, deposition cycles for later mineralization were chosen to be 90 minutes. The addition of water to the methanolic system led to a linear increase of the determined hydrodynamic diameter from  $11 \pm 3$  nm without addition of water, over  $15 \pm 2$  nm for 2 vol% H<sub>2</sub>O to  $23 \pm 1$  nm for 5 vol% H<sub>2</sub>O.

### VIRUS MONOLAYER FORMATION

Synthesizing functional thin films on viruses, such as TMV and the genetically modified mutants, requires homogeneous and reproducible template monolayers. Otherwise the inhomogeneity of the template layers leaves it impossible to assign changed properties to genetic modification. Mutants were chosen to cover a broad area of different surface functionalities: (1) For TMV-Lys mutant the neutral amino acid threonine was replaced with lysine introducing positive charges, (2) for TMV-Cys the cysteine functionality was introduced, (3) E50Q has the same surface charge as wtTMV, but lacks RNA, leading to a higher flexibility, (4) by a mixed assembly process the 30%TMV-His<sub>6</sub> was obtained. Both the histidine and the cysteine functionality are known to strongly interact with zinc ions or even ZnO surfaces.

A simple evaporative assembly approach, the so-called convective assembly (CA), was chosen to produce the virus monolayers. By variation of the concentration of the virus solution and the withdrawal velocity, the assembly behavior of wtTMV and its mutants (TMV-Lys, TMV-Cys, E50Q, and 30%TMV-His<sub>6</sub>) was analyzed. The genetic modification strongly influenced the assembly behavior, which can be seen exemplarily in Figure 5-1.

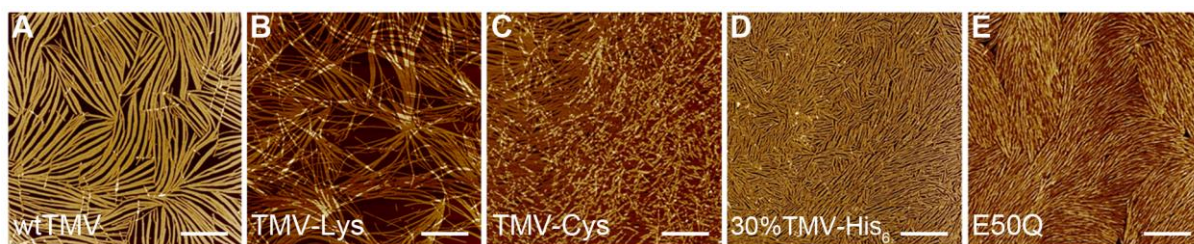


**Figure 5-1:** AFM height images of wtTMV (A), TMV-Lys (B), TMV-Cys (C), 30%TMV-His<sub>6</sub> (D), and E50Q (E) monolayers obtained via CA ( $c = 1.9 \text{ mg mL}^{-1}$ ,  $v_w = 0.6 \text{ mm min}^{-1}$ , humidity: 35% r.H.) without buffer. The withdrawal direction is from right to left. All scale bars represent  $2 \mu\text{m}$  [1].

For each mutant, except 30%TMV-His<sub>6</sub>, CA conditions leading to dense monolayers were determined. Subsequent mineralization of the monolayers in Figure 5-1 clearly proved that the ZnO deposition follows the template monolayer. Thus, the genetically controlled monolayer morphology directly influences the homogeneity of the ZnO layer. The roughness of the deposited ZnO film dropped from  $11.0 \pm 1.5 \text{ nm}$  in the case of wtTMV to  $4.8 \pm 0.3 \text{ nm}$  for E50Q.

In a next step, the CA process was adapted to prestructured field-effect transistor (FET) substrates to implement both wtTMV and E50Q in virus-based ZnO FETs. The results showed that the improved homogeneity of the template monolayer due to genetic modification (E50Q), and thus also the improved quality of the ZnO layer, lead to a superior FET performance. These E50Q-based FETs showed a higher mobility  $\mu$ , a higher on/off ratio  $I_{on/off}$  and a lower threshold voltage  $V_{Th}$  indicating faster and earlier switching compared to wtTMV-based FETs [1].

### MINERALIZATION WITH WATER-CONTAINING REACTION SOLUTION

Mineralization of single virus particles immobilized on a silicon substrate revealed a highly selective ZnO deposition, as well as a variation of the ZnO morphology upon addition of water due to increased particle size. From AFM measurements after each deposition cycle, the ZnO growth per cycle was determined for varying water contents.

The next step was to use the convective assembly condition for dense and homogeneous virus monolayers to synthesize virus-based ZnO thin films in dependency on the water content. Various measurement methods, such as SEM, XRD, and PL confirmed the linear dependency of crystallite/particle size with increasing water contents.



XRD investigations provided further insights into texture changes with varying water contents. Films with 3 and 5 vol% H<sub>2</sub>O showed a 100 texture, whereas 1 and 2 vol% H<sub>2</sub>O lead to a 002 texture of the films. The texture was more pronounced with increasing thickness. However, pronounced differences in the degree of texture were observed on different templates. Whereas films deposited onto NH<sub>2</sub>-SAMs and COOH-SAMs led to texture coefficients of 9 and 5.9, respectively, wtTMV-based films showed a strongly increased texture with a value of 12.7.

Zeta potential measurements at different pH levels revealed that the differing degrees of texture could not be explained by electrostatic interactions. Especially, since deposition takes place in methanolic environments, which leads to low dissociation of surface groups and consequently rather low charges for interaction. Thus, it is concluded for the herein used system that neither the template nor the ZnO crystallites in solution are substantially charged and that electrostatic interactions play a minor part during deposition.

Instead, the higher degree of texture for wtTMV-based samples is attributed to its intrinsic piezoelectricity. Virus particles are strongly deformed due to adhesion to the silicon substrate, as well as immersion in methanol at 60°C. Since the virus structure consists of a helical array of intrinsic dipoles (coat protein), the deformation leads to a more parallel alignment of these dipoles allowing enhanced dipole/dipole interactions between the template and the polar ZnO nanocrystallites leading to an enhanced texture [2].

### **PIEZOELECTRIC THIN FILMS**

The possibility, found in this work, to tune the texture of the deposited ZnO film by adding water to the reaction solution paved the way for synthesizing piezoelectric thin films. As a first step, 100 and 002 textured films were synthesized on NH<sub>2</sub>-SAMs revealing no piezoelectric properties for 100 textured films, as expected. PFM measurements of the 002 textured NH<sub>2</sub>-based ZnO film revealed a small piezoelectric response. The next step was to synthesize 002 textured films on TMV template, since it was proven in this work that the piezoelectric template strongly enhances the texture [2]. The enhanced texture led to an increase of the piezoelectric response of  $\approx 58\%$  by using a piezoelectric template instead of NH<sub>2</sub>-SAMs.

## ZNO-BASED FIELD-EFFECT TRANSISTORS

The FET performance is influenced by numerous parameters, such as crystallite size, interface roughness, active layer thickness, and crystallite orientation. All of these parameters are dependent on the water content in the reaction solution in this work. Thus, the optimum water content and film thickness for best and reproducible FET performances was determined in preliminary experiments on NH<sub>2</sub>-SAMs as template layer. A larger crystallite size leads, on the one hand, to less grain boundaries, but, on the other hand, to a higher interface roughness. Thus, the best and reproducible performance was achieved with the intermediate crystallite size obtained with 2 vol% H<sub>2</sub>O in the reaction solution and a ZnO thickness of 170 – 200 nm.

These findings were transferred to produce wtTMV- and E50Q-based FETs with these optimized conditions. The obtained results were compared to (1) the NH<sub>2</sub>-SAM ZnO FETs and (2) the virus-based FETs prepared without water. Switching from SAMs as templates for ZnO mineralization to viruses led to a strongly reduced threshold voltage  $V_{Th}$  ( $8.9 \pm 0.6$  V for E50Q). Mobility  $\mu$  and on/off ratio  $I_{on/off}$  were not influenced as strongly. The results again confirmed the influence of the quality of the template layer on the FET performance. The dense and homogeneous E50Q monolayer results in a ZnO layer with better surface morphology leading to better FET performance, as already shown without addition of water. The increased crystallite size led to a significant improvement of the FETs. The threshold voltage was reduced by  $\approx 37\%$  for E50Q-based FETs and by  $\approx 33\%$  for wtTMV-based FETs.

## MONOLITHIC ZNO FILMS AND MULTILAYERED FILMS OF TMV AND ZNO

The evaluation of the monolithic references in dependency on the water content revealed a good correlation of the data with the 'inverse Hall-Petch relation', i.e. at a certain grain size the hardness no longer increases with further reductions of the grain size. Thus, the highest hardness and Young's modulus were achieved with 3 vol% H<sub>2</sub>O in the reaction solution leading to values of  $H = 3.6 \pm 0.2$  GPa and  $E = 53 \pm 3$  GPa.

Subsequently, multilayered TMV/ZnO samples were synthesized with wtTMV, E50Q, and TMV-Cys by repeated CA and mineralization in order to improve the toughness of the samples with the aim to maintain their stiffness and hardness. For both wtTMV and E50Q, the multilayered samples showed decreased values of hardness and Young's modulus compared to the monolithic references, which is usually the case when combining stiff and soft materials.

However, for TMV-Cys the multilayered sample did not only maintain hardness and Young's modulus compared to the reference, but the mechanical performance was even higher.

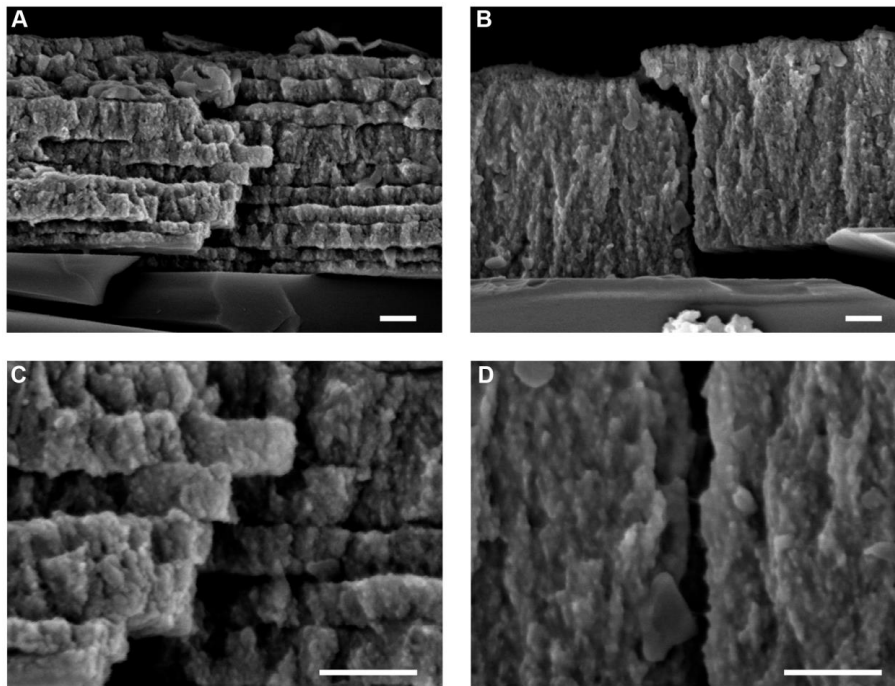


**Figure 5-2:** SEM cross-section images of wtTMV-based MLS (A, B) and monolithic reference (C, D) revealing crack propagation through the films. All scale bars are 200 nm. Samples were sputtered with 0.5 nm Pt:Pd (80:20).

Multi-layered samples have improved toughness e.g. due to deflection of cracks in the soft, organic interlayers, which was also found in the herein prepared samples (Figure 5-2). The multilayered samples all showed crack deflection (Figure 5-2 A, C), whereas the references showed brittle failure (Figure 5-2 B, D).

The fracture toughness was also evaluated quantitatively. The references were more brittle than the silicon substrate, therefore it can only be said that the fracture toughness is lower than that of silicon ( $K_c < 0.83 \text{ MPa m}^{1/2}$  [153]). For wtTMV-based multi-layered samples, the fracture toughness is as high as  $1.8 \pm 0.4 \text{ MPa m}^{1/2}$ , which means an increase by at least  $\approx 54\%$ , whereas the hardness is decreased by  $\approx 40\%$  compared to the reference. The strong interaction of TMV-Cys and ZnO leads to a fracture toughness of  $1.3 \pm 0.4 \text{ MPa m}^{1/2}$ , which means an increase by at least 36%. However, for TMV-Cys the hardness is also increased by  $\approx 27\%$  resulting in a genetically engineered material that is both stiff and tough.



## 6 ZUSAMMENFASSUNG

### REAKTIONSLÖSUNG FÜR DIE ZnO MINERALISIERUNG

Eine methanolische Reaktionslösung, die ein strukturdirigierendes Polymer enthielt, wurde zur Herstellung nanokristallinen ZnO verwendet. Dem System wurden kleine Mengen Wasser zugeführt, um die Kristallitgröße zu steuern, indem die Hydrolyserate beeinflusst wurde. Der Wassergehalt wurde zwischen 0 und 5 vol% variiert und die Reaktionslösung mittels dynamischer Lichtstreuung *in-situ* untersucht. Die Messungen zeigten, dass die Größe der gebildeten Partikel über 100 Minuten konstant blieb ( $\approx 16$  nm). Anschließend erfolgte ein starker Anstieg der Partikelgröße bei längeren Reaktionszeiten (auf  $\approx 55$  nm). Deshalb wurde die Länge der Mineralisierungszyklen für die spätere ZnO-Abscheidung auf 90 Minuten festgelegt. Die Wasserzugabe zum methanolischen Reaktionssystem führte zu einem linearen Anstieg des ermittelten hydrodynamischen Durchmessers von  $11 \pm 3$  nm ohne die Zugabe von Wasser, über  $15 \pm 2$  nm bei 2 vol% H<sub>2</sub>O zu  $23 \pm 1$  nm bei 5 vol% H<sub>2</sub>O.

### HERSTELLUNG VON VIRUS-MONOLAGEN

Zur Synthese funktionaler Dünnschichten auf Viren, wie z.B. TMV und den genetisch modifizierten Mutanten, sind homogene und reproduzierbare Templatmonolagen erforderlich. Ansonsten macht es die Inhomogenität der Templatsschicht unmöglich, veränderte Eigenschaften der genetischen Modifikation zuzuordnen. Die Mutanten wurden so ausgewählt, dass sie ein breites Spektrum verschiedener Oberflächenfunktionalitäten abdecken: (1) Bei TMV-Lys wurde die neutrale Aminosäure Threonin durch Lysin ersetzt, um positive Ladungen einzubringen, (2) bei TMV-Cys wurde eine Cystein-Funktionalität eingebracht, (3) E50Q hat dieselbe Oberflächenladung wie wtTMV, aber keine RNA, was zu höherer Flexibilität führt, (4) wurde durch einen ‚mixed-assembly‘ Prozess die 30%TMV-His<sub>6</sub> Mutante erhalten. Sowohl die Histidin-, also auch die Cystein-Funktionalität haben erwiesenermaßen eine starke Wechselwirkung mit Zinkionen oder auch ZnO-Oberflächen.

Es wurde ein einfacher, verdunstungsbasierter Herstellungsansatz zur Synthese von Virusmonolagen gewählt, die sogenannte ‚convective assembly‘ (CA). Durch Variation der Konzentration der Virenlösung ( $c$ ) und der Rückzugsgeschwindigkeit ( $v_w$ ) wurde das

Anordnungsverhalten von wtTMV und seiner Mutanten (TMV-Lys, TMV-Cys, E50Q und 30%TMV-His<sub>6</sub>) analysiert. Die genetische Modifikation hat das Anordnungsverhalten stark beeinflusst, wie man beispielhaft in Abbildung 5-1 sehen kann.

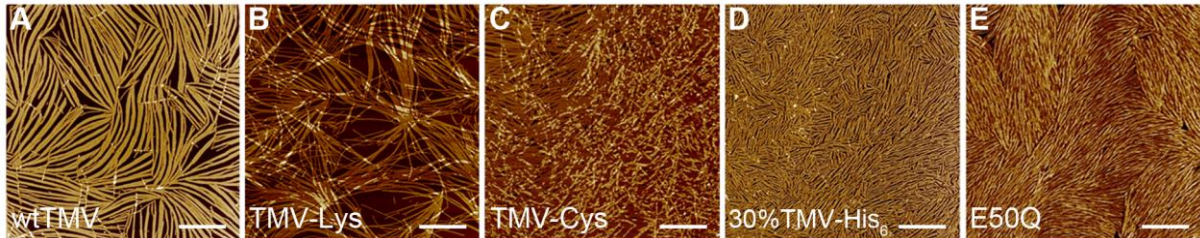


**Abbildung 5-1:** AFM Höhenbilder von wtTMV (A), TMV-Lys (B), TMV-Cys (C), 30%TMV-His<sub>6</sub> (D) und E50Q (E). Die Monolagen wurden mittels CA hergestellt ( $c = 1,9 \text{ mg mL}^{-1}$ ,  $v_w = 0,6 \text{ mm min}^{-1}$ , Luftfeuchtigkeit: 35% r.F.) ohne Puffer in der Virenlösung. Die Rückzugsrichtung ist von rechts nach links. Alle Maßstäbe repräsentieren  $2 \mu\text{m}$  [1].

Für jeden Mutanten, außer 30%TMV-His<sub>6</sub>, wurden die CA-Bedingungen bestimmt, die zu dichten Monolagen führen. Anschließende Mineralisierung der Monolagen, die in Abbildung 5-1 zu sehen sind, bestätigte, dass die ZnO-Abscheidung der Templatmonolage folgt. Damit beeinflusst die genetisch kontrollierte Monolagenmorphologie direkt die Homogenität der ZnO-Schicht. Die Rauigkeit der abgeschiedenen ZnO-Schichten reduzierte sich von  $11,0 \pm 1,5 \text{ nm}$  für wtTMV auf  $4,8 \pm 0,3 \text{ nm}$  für E50Q.

Als nächster Schritt wurde der CA-Prozess für die Verwendung von vorstrukturierten Feldeffekttransistor (FET)-Substraten angepasst, um sowohl wtTMV als auch E50Q in virusbasierten ZnO-FETs einzuführen. Die Ergebnisse zeigten, dass die verbesserte Homogenität der Templatmonolage durch die genetische Modifikation (E50Q) und damit auch die verbesserte ZnO-Homogenität zu einer besseren FET-Performance führten. Diese E50Q-basierten FETs zeigten eine höhere Mobilität  $\mu$ , ein höheres an/aus Verhältnis  $I_{on/off}$  und eine geringere Schwellenspannung  $V_{Th}$ , die ein schnelleres und früheres Schalten im Vergleich zum wtTMV-basierten FET anzeigt.

### MINERALISIERUNG MIT EINER REAKTIONSLÖSUNG, DIE WASSER ENTHÄLT

Die Mineralisierung von einzelnen Viruspartikeln, die auf einem Siliziumsubstrat immobilisiert wurden, führte zu zwei Erkenntnissen: (1) dass die ZnO-Abscheidung hoch selektiv ist und (2), dass es durch die Zugabe von Wasser zu einer veränderten Morphologie des abgeschiedenen ZnO durch die veränderte Partikelgröße kam. Durch AFM-Untersuchungen nach jedem

Mineralisierungszyklus wurde der Zuwachs pro Zyklus für variierenden Wassergehalt bestimmt.

Als Nächstes wurden die CA-Bedingungen für dichte und homogene Virusmonolagen verwendet, um virus-basierte ZnO-Dünnschichten in Abhängigkeit des Wassergehalts herzustellen. Zahlreiche Messmethoden, wie REM, XRD und PL bestätigten die lineare Abhängigkeit der Kristallit- bzw. Partikelgröße vom steigenden Wassergehalt.

Zusätzlich gaben XRD-Untersuchungen einen Einblick auf die Änderung der Textur mit variierendem Wassergehalt. Schichten mit 3 und 5 vol% H<sub>2</sub>O zeigten eine 100 Textur, wohingegen 1 und 2 vol% H<sub>2</sub>O zu einer 002 Textur der Schichten führten. Die Textur war mit zunehmender Schichtdicke ausgeprägter. Jedoch zeigten sich charakteristische Unterschiede im Grad der Texturierung auf verschiedenen Templaten. Während Schichten, die auf NH<sub>2</sub>-SAMs und COOH-SAMs abgeschieden wurden, zu Texturkoeffizienten von 9 bzw. 5,9 führten, zeigte die wtTMV-basierte Schicht eine stark erhöhte Textur mit einem Wert von 12,7.

Messungen des Zetapotentials bei verschiedenen pH-Werten machten deutlich, dass die verschiedenen Grade der Texturierung nicht durch elektrostatische Wechselwirkungen erklärt werden konnten. Insbesondere da sich die Reaktion in methanolischer Umgebung abspielt, was zu einer geringen Dissoziation der Oberflächengruppen führt und damit auch in eher geringen Ladungen zur Wechselwirkung mündet. Daher wurde gefolgert, dass im hier genutzten System weder das Templat noch die ZnO-Partikel wesentlich geladen sind und elektrostatische Wechselwirkungen nur eine untergeordnete Rolle in der Abscheidung spielen.

Stattdessen wird der höhere Grad an Texturierung der wtTMV-basierten Proben auf die intrinsische Piezoelektrizität von wtTMV zurückgeführt. Die Viruspartikel werden während der Adhäsion auf dem Siliziumsubstrat stark verformt. Zusätzlich führt das Eintauchen in Methanol bei 60°C zu einer zusätzlichen Verformung. Da die Virusstruktur aus einer helikalen Anordnung von intrinsischen Dipolen (Hüllprotein) besteht, führt die Deformation der Struktur zu einer paralleleren Ausrichtung dieser Dipole. Dies erlaubt verstärkte Dipol-Dipol-Wechselwirkungen zwischen dem Templat und den dipolaren ZnO Nanokristalliten, die zu einer verbesserten Textur führen [2].

### PIEZOELEKTRISCHE DÜNNE SCHICHTEN

Die in dieser Arbeit gefundene Möglichkeit, die Textur einer abgeschiedenen ZnO-Schicht durch die Zugabe von Wasser zur Reaktionslösung zu tunen, ebnete den Weg zur Synthese von piezoelektrischen Dünnschichten. Als Erstes wurden 100 und 002 texturierte Schichten auf NH<sub>2</sub>-SAMs synthetisiert. Wie erwartet zeigten sich keine piezoelektrischen Eigenschaften der 100 texturierten Schichten. PFM-Messungen der 002 texturierten NH<sub>2</sub>-basierten ZnO-Schichten zeigten eine geringe piezoelektrische Antwort. Der nächste Schritt war 002 texturierte Schichten auf TMV-Templaten zu synthetisieren, da in dieser Arbeit gezeigt wurde, dass das piezoelektrische Templat die Textur stark erhöht [2]. Die verbesserte Textur führte zu einem Anstieg der piezoelektrischen Antwort um  $\approx 58\%$  durch die Verwendung eines piezoelektrischen Templats anstatt der NH<sub>2</sub>-SAMs.

### ZNO-BASIERTE FELDEFFEKTTTRANSISTOREN

Die FET-Performance wird von zahlreichen Parametern, wie Kristallitgröße, Grenzflächenrauigkeit, Dicke der aktiven Schicht und Kristallorientierung beeinflusst. All diese Parameter sind in dieser Arbeit abhängig vom Wassergehalt der Reaktionslösung. Deshalb wurden in einem Vorversuch zunächst der optimale Wassergehalt und die optimale Schichtdicke für die beste und reproduzierbarste FET-Performance auf NH<sub>2</sub>-SAMs als Templat bestimmt. Größere Kristallite führen einerseits zu einer reduzierten Anzahl an Korngrenzen, aber andererseits zu einer erhöhten Grenzflächenrauigkeit. Daher wurde die beste und reproduzierbarste FET-Performance mit einer mittleren Kristallitgröße, die mit 2 vol% H<sub>2</sub>O erhalten wird, und einer Schichtdicke zwischen 170 und 200 nm erreicht.

Diese Erkenntnisse wurden übertragen, um mit diesen optimierten Bedingungen wtTMV- und E50Q-basierte FETs herzustellen. Die so erhaltenen Ergebnisse wurden einerseits mit den NH<sub>2</sub>-SAM-basierten ZnO-FETs und andererseits mit den virus-basierten FETs, die ohne Wasser hergestellt worden waren, verglichen. Der Templatwechsel von NH<sub>2</sub>-SAMs zu Viren für die ZnO-Mineralisierung führte zu einer starken Reduktion der Schwellenspannung  $V_{Th}$  ( $8,9 \pm 0,6$  V bei E50Q). Die Mobilität  $\mu$  und das an/aus Verhältnis  $I_{on/off}$  wurden nicht so stark beeinflusst. Diese Ergebnisse bestätigten ein weiteres Mal, dass die Qualität der Templatschicht einen großen Einfluss auf die FET-Performance hat. Die dichte und homogene E50Q-Monolage bedingt eine ZnO-Schicht mit besserer Oberflächenmorphologie, die zu einer verbesserten FET-Performance führt, wie es auch schon bei den FETs, die ohne Wasser



hergestellt wurden, gezeigt wurde. Die gesteigerte Kristallitgröße durch die Zugabe von Wasser führten zu einer signifikanten Verbesserung der FETs. Die Schwellenspannung  $V_{Th}$  reduzierte sich im Fall der E50Q-basierten FETs um  $\approx 37\%$  und um  $\approx 33\%$  im Fall der wtTMV-basierten FETs.

### MONOLITHISCHE ZNO SCHICHTEN UND MULTILAGENSCHICHTEN AUS TMV UND ZNO

Die Auswertung der monolithischen Referenzen in Abhängigkeit des Wassergehalts gab eine gute Korrelation der Daten mit der ‚inversen Hall-Petch Beziehung‘ zu erkennen. Das heißt, dass ab einer gewissen Korngröße die Härte nicht weiter ansteigt, wenn die Korngröße weiter reduziert wird. Daher wurden die höchste Härte und der höchste E-Modul mit 3 vol% H<sub>2</sub>O in der Reaktionslösung erreicht mit Werten für die Härte von  $H = 3,6 \pm 0,2$  GPa und den E-Modul von  $E = 53 \pm 3$  GPa.

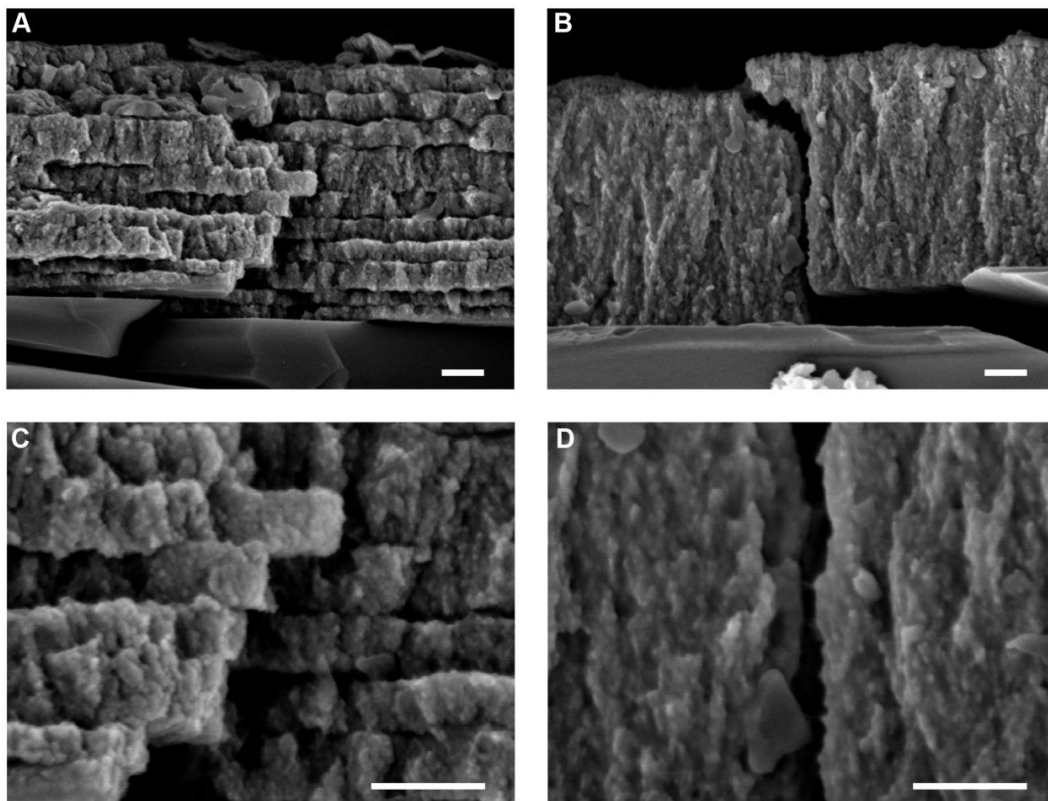


**Abbildung 5-2:** REM Querschnittsbilder von wtTMV-basierten Multilagen (A, B) und den monolithischen Referenz (C, D), die die Rissausbreitung durch die Schichten eröffnet. Alle Maßstäbe repräsentieren 200 nm. Die Proben wurden mit 0,5 nm Pt:Pd (80:20) gesputtert.

Anschließend wurden Multilagen aus abwechselnden TMV- und ZnO-Schichten mit wtTMV, E50Q und TMV-Cys hergestellt, indem abwechselnd Virusmonolagen mittels CA hergestellt wurden und danach ZnO abgeschieden wurde. Das Ziel war so die Zähigkeit der Proben bei

gleichzeitigem Beibehalten der Steifigkeit und Härte zu erhöhen. Sowohl bei wtTMV als auch bei E50Q zeigten die Multilagen reduzierte Werte für Härte und E-Modul im Vergleich zu den monolithischen Referenzen. Diese Reduzierung ist das normale Verhalten bei der Kombination von steifen und weichen Materialien. Jedoch behielt die TMV-Cys-basierte Multilage nicht nur ihre Härte und ihren E-Modul im Vergleich zur Referenz, die Werte waren sogar größer.

Multilagen haben eine erhöhte Zähigkeit, da beispielsweise Risse in die weichen, organischen Zwischenschichten abgelenkt werden, was auch in den hier hergestellten Proben gefunden wurde (Abbildung 5-2). Die Multilagen zeigen Rissablenkung (Abbildung 5-2 A, C), wohingegen die Referenzen einen Sprödbruch zeigen (Abbildung 5-2 B, D).

Die Bruchzähigkeit wurde quantitativ ausgewertet. Die Referenzen sind spröder als das Siliziumsubstrat, daher kann nur gesagt werden, dass die Bruchzähigkeit der Referenzen kleiner ist als die von Silizium ( $K_{c,Ref} = 0.83 \text{ MPa m}^{1/2}$  [153]). Für wtTMV-Multilagen ist die Bruchzähigkeit  $1,8 \pm 0,4 \text{ MPa m}^{1/2}$ , was einen Anstieg um mindestens  $\approx 54\%$  gegenüber der Referenz bedeutet, wohingegen die Härte um  $\approx 40\%$  gegenüber der Referenz reduziert ist. Die starke Wechselwirkung zwischen TMV-Cys und ZnO mündet in einer Bruchzähigkeit von  $1,3 \pm 0,4 \text{ MPa m}^{1/2}$ , was einen Anstieg um mindestens  $36\%$  bedeutet. Jedoch ist bei den TMV-Cys-Multilagen die Härte ebenfalls um  $\approx 27\%$  gegenüber der Referenz gesteigert, was zu einem genetisch veränderten Material führt, das sowohl steif als auch zäh ist.

## 7 PUBLICATION BIBLIOGRAPHY

- [1] Atanasova, P. Stitz, N., Sanctis, S. *et al.* **2015**. *Langmuir* 31, 3897–3903.
- [2] Stitz, N. Eiben, S., Atanasova, P. *et al.* **2016**. *Scientific reports* 6, 26518.
- [3] Ellmer, K., Klein, A. & Rech, B. **2007** *Transparent conductive zinc oxide: basics and applications in thin film solar cells* vol 104: Springer Science & Business Media.
- [4] Brown, H. E. **1976** *Zinc Oxide: Properties and Applications*. New York: International Lead Zinc Research Organization.
- [5] Klingshirn, C. F., Waag, A., Hoffmann, A. & Geurts, J. **2010** *Zinc oxide: From fundamental properties towards novel applications* vol 120: Springer Science & Business Media.
- [6] Takahashi, T. Ebina, A., Kamiyama, A. **1966**. *Jpn. J. Appl. Phys.* 5, 560–561.
- [7] Mofor, A. C. Bakin, A. S., Postels, B. *et al.* **2008**. *Thin Solid Films* 516, 1401–1404.
- [8] Huang, M. H. Wu, Y., Feick, H. *et al.* **2001**. *Adv. Mater.* 13, 113–116.
- [9] Ehrentraut, D. Sato, H., Kagamitani, Y. *et al.* **2006**. *Prog. Cryst. Growth Charact. Mater.* 52, 280–335.
- [10] Li, C. P., Yang, B. H. **2011**. *J. Electron. Mater.* 40, 253–258.
- [11] Bdikin, I. K. Gracio, J., Ayouchi, R. *et al.* **2010**. *Nanotechnology* 21, 235703.
- [12] Shelton, C. T. Sachet, E., Paisley, E. A. *et al.* **2014**. *J. Appl. Phys.* 115, 044912.
- [13] Momeni, K. Odegard, G. M., Yassar, R. S. **2012**. *Acta Mater.* 60, 5117–5124.
- [14] Zhang, K.-M. Zhao, Y.-P., He, F.-Q. *et al.* **2007**. *Chin. J. Chem. Phys.* 20, 721–726.
- [15] Fujimura, N. Nishihara, T., Goto, S. *et al.* **1993**. *J. Cryst. Growth* 130, 269–279.
- [16] Wang, Z. L. **2004**. *J. Phys.: Condens. Matter* 16, R829.
- [17] Wang, Z. L., Song, J. **2006**. *Science* 312, 242–246.
- [18] Saeed, T., O'Brien, P. **1995**. *Thin Solid Films* 271, 35–38.
- [19] Bill, J. Hoffmann, R. C., Fuchs, T. M. *et al.* **2002**. *MEKU* 93, 478–489.
- [20] Hoffmann, R. C. Jia, S., Bill, J. *et al.* **2004**. *J. Ceram. Soc. JPN* 112, S1089-S1092.
- [21] Verges, M. A. Mifsud, A., Serna, C. J. **1990**. *J. Chem. Soc., Faraday Trans.* 86, 959.
- [22] Hoffmann, R. C. Jia, S., Bartolomé, J. C. *et al.* **2003**. *J. Eur. Cera. Soc.* 23, 2119–2123.
- [23] Hoffmann, R. C. Jia, S., Jeurgens, L. P. *et al.* **2006**. *Mater. Sci. and Eng. C* 26, 41–45.
- [24] Gerstel, P. Lipowsky, P., Durupthy, O. *et al.* **2006**. *J. Cera. Soc. JPN* 114, 911–917.
- [25] Lipowsky, P. Hoffmann, R. C., Welzel, U. *et al.* **2007**. *Adv. Funct. Mater.* 17, 2151–2159.

- [26] Lipowsky, P. Hedin, N., Bill, J. *et al.* **2008.** *J. Phys. Chem. C* 112, 5373–5383.
- [27] Karzel, H. Potzel, W., Köfferlein, M. *et al.* **1996.** *Phys. Rev. B* 53, 11425–11438.
- [28] Özgür, Ü. Alivov, Y. I., Liu, C. *et al.* **2005.** *J. Appl. Phys.* 98, 041301.
- [29] Rössler, U. & Blachnik, R. **1999** *Numerical Data and Functional Relationships in Science and Technology.* Berlin: Springer.
- [30] Minami, T. Sato, H., Nanto, H. *et al.* **1985.** *Jpn. J. Appl. Phys.* 24, L781.
- [31] Wagner, P., Helbig, R. **1974.** *J. Phys. Chem. Solids* 35, 327–335.
- [32] Cheng, H.-C. Chen, C.-F., Lee, C.-C. **2006.** *Thin Solid Films* 498, 142–145.
- [33] Li, C. Li, Y., Wu, Y. *et al.* **2007.** *J. Appl. Phys.* 102, 76101.
- [34] Barquinha, P. Pimentel, A., Marques, A. *et al.* **2006.** *J. Non-Cryst. Solids* 352, 1749–1752.
- [35] Okamura, K. Mechau, N., Nikolova, D. *et al.* **2008.** *Appl. Phys. Lett.* 93, 83105.
- [36] Provided by Dr. Rudolf Hoffmann, Technical University of Darmstadt.
- [37] Gray, P. R., Hurst, Paul J., Lewis, S. H. & Meyer, R. G. **2001** *Analysis and Design of Analog Integrated Circuits.* New York: John Wiley & Sons.
- [38] Dal Corso, A. Posternak, M., Resta, R. *et al.* **1994.** *Phys. Rev. B* 50, 10715–10721.
- [39] Willander, M. Nur, O., Zhao, Q. X. *et al.* **2009.** *Nanotechnology* 20, 332001.
- [40] Bahnemann, D. W. Kormann, C., Hoffmann, M. R. **1987.** *J. Phys. Chem.* 91, 3789–3798.
- [41] Vanheusden, K. Seager, C. H., Warren, W. L. *et al.* **1996.** *Appl. Phys. Lett.* 68, 403.
- [42] Vanheusden, K. Warren, W. L., Seager, C. H. *et al.* **1996.** *J. Appl. Phys.* 79, 7983.
- [43] Brus, L. **1986.** *J. Phys. Chem.* 90, 2555–2560.
- [44] Kucheyev, S. O. Bradby, J. E., Williams, J. S. *et al.* **2002.** *Appl. Phys. Lett.* 80, 956.
- [45] Coleman, V. A. Bradby, J. E., Jagadish, C. *et al.* **2005.** *Appl. Phys. Lett.* 86, 203105.
- [46] Basu, S., Barsoum, M. W. **2007.** *J. Mater. Res.* 22, 2470–2477.
- [47] Addadi, L., Weiner, S. **1992.** *Angew. Chem. Int. Ed. Engl.* 31, 153–169.
- [48] Mann, S., Webb, J. M. & Williams, Robert Joseph Paton. **1989** *Biomineralization: Chemical and Biochemical Perspectives:* John Wiley & Sons.
- [49] Bäuerlein, E. **2007** *Handbook of biomineralization; 1.* Handbook of biomineralization. Weinheim: Wiley-VCH-Verl.
- [50] Burghard, Z. Zini, L., Srot, V. *et al.* **2009.** *Nano Lett.* 9, 4103–4108.
- [51] Lin, A. Y.-M., Meyers, M. A. **2009.** *Biological Materials Science* 2, 607–612.
- [52] Behrens, P. **2007** *Handbook of biomineralization; 2.* Handbook of biomineralization. Weinheim: Wiley-VCH-Verl.

- [53] Sarikaya, M. **1994**. *Microsc. Res. Tech.* 27, 360–375.
- [54] Mayer, G. **2005**. *Science* 310, 1144–1147.
- [55] Brinker, C. J. Sellinger, A., Weiss, P. M. *et al.* **1998**. *Nature* 394, 256–260.
- [56] Tang, Z. Kotov, N. A., Magonov, S. *et al.* **2003**. *Nat. Mater.* 2, 413–418.
- [57] Liu, T. Chen, B., Evans, J. R. G. **2008**. *Bioinspir Biomim* 3, 16005.
- [58] Volkmer, D. Harms, M., Gower, L. *et al.* **2005**. *Angew. Chem. Int. Ed. Engl.* 44, 639–644.
- [59] Wei, H. Ma, N., Shi, F. *et al.* **2007**. *Chem. Mater.* 19, 1974–1978.
- [60] Finnemore, A. Cunha, P., Shean, T. *et al.* **2012**. *Nat. Commun.* 3, 966.
- [61] Yeom, B. Kim, S., Cho, J. *et al.* **2006**. *J. Adhes.* 82, 447–468.
- [62] Burghard, Z. Tucic, A., Jeurgens, L. P. H. *et al.* **2007**. *Adv. Mater.* 19, 970–974.
- [63] Lipowsky, P. Burghard, Ž., Jeurgens, L. P. H. *et al.* **2007**. *Nanotechnology* 18, 345707.
- [64] Xu, H. Xie, L., Chen, J.-B. *et al.* **2014**. *Mater. Horiz.* 1, 546.
- [65] Munch, E. Launey, M. E., Alsem, D. H. *et al.* **2008**. *Science* 322, 1516–1520.
- [66] Zlotnikov, I. Gotman, I., Burghard, Z. *et al.* **2010**. *Colloids Surf., A* 361, 138–142.
- [67] Tritschler, U. Zlotnikov, I., Zaslansky, P. *et al.* **2014**. *ACS Nano* 8, 5089–5104.
- [68] Siglreitmeier, M. Wu, B., Kollmann, T. *et al.* **2015**. *Beilstein J Nanotechnol* 6, 134–148.
- [69] Bassett, C. A. L., Becker, R. O. **1962**. *Science* 137, 1063–1064.
- [70] Bassett, C. A. L. Pawluk, R. J., Becker, R. O. **1964**. *Nature* 204, 652–654.
- [71] Becker, R. O. Bassett, C. A. L., Bachman, C. H. **1964**. *H. Frost. New York: Little Brown.*
- [72] Ahn, A. C., Grodzinsky, A. J. **2009**. *Med. Eng. Phys.* 31, 733–741.
- [73] Noris-Suárez, K. Lira-Olivares, J., Ferreira, A. M. *et al.* **2007**. *Biomacromolecules* 8, 941–948.
- [74] Jolivet, J.-P., Henry, M., Livage, J. & Bescher, E. **2000** *Metal Oxide Chemistry and Synthesis - from Solution to Solid State: John Wiley New York.*
- [75] Geissler, M., Xia, Y. **2004**. *Adv. Mater.* 16, 1249–1269.
- [76] Pitta Bauermann, L. Bill, J., Aldinger, F. **2007**. *IJMR* 98, 879–883.
- [77] Baier, J. Strumberger, R., Berger, F. *et al.* **2012**. *Biointerface Res. Appl. Chem.* 2, 339–349.
- [78] Atanasova, P. Weitz, R. T., Gerstel, P. *et al.* **2009**. *Nanotechnology* 20, 365302.
- [79] Mayer, A. **1886**. *Landw. Vers. Sta* 32, 451–467.
- [80] Beijerinck, M. W. **1898**. *Verhandelingen der Koninklijke Akademie.*
- [81] Holmes, F. O. **1929**. *Botanical Gazette* 87, 39–55.
- [82] Klug, A. **1999**. *Philos. Trans. R. Soc. Lond., B, Biol. Sci.* 354, 531–535.

- [83] Bawden, F. C. Pirie, N., W., Bernal, J., D. *et al.* **1936.** *Nature* 8, 1051.
- [84] Butler, P. J. G. **1984.** *J. Gen. Virol.* 65, 253–279.
- [85] Knez, M. **2003** *The Tobacco Mosaic Virus (TMV) as Biological Template for Nanostructuring.* Ulm.
- [86] Provided by Dr. Sabine Eiben, University of Stuttgart.
- [87] Fraenkel-Conrat, H., Narita, K. **1958.** *A. Neuberger, ed*, 249.
- [88] Zaitlin, M. **2000.** *ASM NEWS* 66, 59.
- [89] Bendahmane, M. Koo, M., Karrer, E. *et al.* **1999.** *J. Mol. Biol.* 290, 9–20.
- [90] Schumacher, G. A., van de Ven, Theo G. M. **1991.** *J. Chem. Soc., Faraday Trans.* 87, 971.
- [91] He, J. Niu, Z., Tangirala, R. *et al.* **2009.** *Langmuir* 25, 4979–4987.
- [92] Khan, A. A. Fox, E. K., Górzny, M. ł. *et al.* **2013.** *Langmuir* 29, 2094–2098.
- [93] Alonso, J. M. Górzny, M., Bittner, A. M. **2013.** *Trends Biotechnol.* 31, 530–538.
- [94] Kegel, W. K., van der Schoot, Paul. **2006.** *Biophys. J.* 91, 1501–1512.
- [95] Knez, M. Sumser, M. P., Bittner, A. M. *et al.* **2004.** *Langmuir* 20, 441–447.
- [96] Lee, B. Lo, C.-T., Thiyagarajan, P. *et al.* **2007.** *Langmuir* 23, 11157–11163.
- [97] Zaitlin, M., Palukaitis, P. **2000.** *Annu. Rev. Phytopathol.* 38, 117–143.
- [98] Tsugita, A. Gish, D. T., Young, J. *et al.* **1960.** *PNAS* 46, 1463–1469.
- [99] Bruckman, M. A. Kaur, G., Lee, L. A. *et al.* **2008.** *ChemBioChem* 9, 519–523.
- [100] Smith, M. L. Lindbo, J. A., Dillard-Telm, S. *et al.* **2006.** *Virology* 348, 475–488.
- [101] Turpen, T. H. Reinl, S. J., Charoenvit, Y. *et al.* **1995.** *Nat. Biotechnol.* 13, 53–57.
- [102] Lee, M. H. Brass, D. A., Morris, R. *et al.* **2005.** *Biomaterials* 26, 1721–1730.
- [103] Manocchi, A. K. Horelik, N. E., Lee, B. *et al.* **2010.** *Langmuir* 26, 3670–3677.
- [104] Geiger, F. C. Eber, F. J., Eiben, S. *et al.* **2013.** *Nanoscale* 5, 3808–3816.
- [105] Miller, R. A. Stephanopoulos, N., McFarland, J. M. *et al.* **2010.** *J. Am. Chem. Soc.* 132, 6068–6074.
- [106] Eiben, S. Stitz, N., Eber, F. *et al.* **2014.** *Virus Res.* 180, 92–96.
- [107] Culver, J. N. Dawson, W. O., Plonk, K. *et al.* **1995.** *Virology* 206, 724–730.
- [108] Kadri, A. Maiss, E., Amsharov, N. *et al.* **2011.** *Virus Res.* 157, 35–46.
- [109] Shenton, W. Douglas, T., Young, M. *et al.* **1999.** *Adv. Mater.* 11, 253–256.
- [110] Dujardin, E. Peet, C., Stubbs, G. *et al.* **2003.** *Nano Lett.* 3, 413–417.
- [111] Zhou, K. Zhang, J., Wang, Q. **2015.** *Small* 11, 2505–2509.
- [112] Knez, M. Bittner, A. M., Boes, F. *et al.* **2003.** *Nano Lett.* 3, 1079–1082.

- [113] Balci, S. Bittner, A. M., Hahn, K. *et al.* **2006.** *Electrochim. Acta* 51, 6251–6257.
- [114] Knez, M. Sumser, M., Bittner, A. M. *et al.* **2004.** *Adv. Funct. Mater.* 14, 116–124.
- [115] Chen, X. Gerasopoulos, K., Guo, J. *et al.* **2010.** *ACS nano* 4, 5366–5372.
- [116] Górzny, M. Ł. Walton, A. S., Evans, S. D. **2010.** *Adv. Funct. Mater.* 20, 1295–1300.
- [117] Li, S. Dharmawardana, M., Welch, R. P. *et al.* **2016.** *Angew. Chem.* 128, 10849–10854.
- [118] Knez, M. Kadri, A., Wege, C. *et al.* **2006.** *Nano Lett.* 6, 1172–1177.
- [119] Balci, S. Bittner, A. M., Schirra, M. *et al.* **2009.** *Electrochim. Acta* 54, 5149–5154.
- [120] Atanasova, P. Rothenstein, D., Schneider, J. J. *et al.* **2011.** *Adv. Mater.* 23, 4918–4922.
- [121] Fukada, E. **1995.** *Biorheology* 32, 593–609.
- [122] Tagantsev, A. **1986.** *Phys. Rev. B* 34, 5883–5889.
- [123] Kalinin, S. V. Jesse, S., Liu, W. *et al.* **2006.** *Appl. Phys. Lett.* 88, 153902.
- [124] Torah, R. N. Beeby, S. P., White, N. M. **2004.** *J. Phys. D: Appl. Phys.* 37, 1074–1078.
- [125] Kim, D. M. Eom, C. B., Nagarajan, V. *et al.* **2006.** *Appl. Phys. Lett.* 88, 142904.
- [126] Lee, B. Y. Zhang, J., Zueger, C. *et al.* **2012.** *Nat. Nanotechnol.* 7, 351–356.
- [127] Lu, B. Stubbs, G., Culver, J. N. **1996.** *Virology* 225, 11–20.
- [128] Santos, Jose L R Bispo, Jose A C, Landini, G. F. *et al.* **2004.** *Biophys. Chem.* 111, 53–61.
- [129] Niu, Z. Bruckman, M. A., Li, S. *et al.* **2007.** *Langmuir* 23, 6719–6724.
- [130] Pickering, S. U. **1907.** *J. Chem. Soc., Trans.* 91, 2001.
- [131] Dimitrov, A. S., Nagayama, K. **1996.** *Langmuir* 12, 1303–1311.
- [132] Niwa, D. Fujie, T., Lang, T. *et al.* **2012.** *J. Biomater. Appl.* 27, 131–141.
- [133] Lin, Z. **2012** *Evaporative Self-Assembly of Ordered Complex Structures*: World Scientific.
- [134] Kuncicky, D. M. Naik, R. R., Velev, O. D. **2006.** *Small* 2, 1462–1466.
- [135] Wargacki, S. P. Pate, B., Vaia, R. A. **2008.** *Langmuir* 24, 5439–5444.
- [136] Denkov, N. Velev, O., Kralchevski, P. *et al.* **1992.** *Langmuir* 8, 3183–3190.
- [137] Denkov, N. D. Velev, O. D., Kralchevsky, P. A. *et al.* **1993.** *Nature* 361, 26.
- [138] Prevo, B. G., Velev, O. D. **2004.** *Langmuir* 20, 2099–2107.
- [139] Shimoda, H. Oh, Su, J., Geng, Huai, Zhi *et al.* **2002** 14, 899–901.
- [140] Tang, J. Gao, B., Geng, H. *et al.* **2003.** *Adv. Mater.* 15, 1352–1355.
- [141] Sharma, V. Park, K., Srinivasarao, M. **2009.** *Mater. Sci. Eng., R* 65, 1–38.
- [142] Fraden, S. Maret, G., Caspar, D. *et al.* **1989.** *Phys. Rev. Lett.* 63, 2068–2071.
- [143] Janssen, D. Palma, R. de, Verlaak, S. *et al.* **2006.** *Thin Solid Films* 515, 1433–1438.

- [144] Stitz, N. **2011** *Modified Tobacco Mosaic Viruses as Templates for Synthesis of ZnO Nanowires*. Diplomarbeit. Stuttgart.
- [145] Greß, A. **2014** *Untersuchung der wasserinduzierten Partikelgrößenänderung von ZnO Nanokristalliten in einer methanolischen Reaktionslösung mittels dynamischer Lichtstreuung*. Bachelorarbeit. Stuttgart.
- [146] Fairbrother, F., Mastin, H. **1924**. *J. Chem. Soc., Trans.* 125, 2319–2330.
- [147] Jazbinšek, M., Zgonik, M. **2002**. *Applied Physics B: Lasers and Optics* 74, 407–414.
- [148] Jungk, T. Hoffmann, Á., Soergel, E. **2006**. *Appl. Phys. Lett.* 89, 163507.
- [149] Christman, J. A. Woolcott, R. R., Kingon, A. I. *et al.* **1998**. *Appl. Phys. Lett.* 73, 3851.
- [150] Kalinin, S. V., Bonnell, D. A. **2002**. *Phys. Rev. B* 65.
- [151] Wang, J. Li, W.-Z., Li, H.-D. *et al.* **2000**. *Thin Solid Films* 366, 117–120.
- [152] Oliver, W. C., Pharr, G. M. **1992**. *J. Mater. Res.* 7, 1564–1583.
- [153] Xia, Z. Curtin, W., Sheldon, B. **2004**. *Acta Mater.* 52, 3507–3517.
- [154] Lipowsky, P. **2007** *Deposition of Metal Oxide Thin Films from Solutions Containing Organic Additives*. Stuttgart: Max-Planck-Inst. für Metallforschung.
- [155] Berne, B. J. & Pecora, R. **1976**. *Dynamic Light Scattering*. New York: John Wiley & Sons.
- [156] Mortimer, C. E. & Müller, U. **2003** *Chemie. Das Basiswissen der Chemie ; 125 Tabellen*, 8.th edn. Stuttgart: Thieme.
- [157] Römpp online. **2001-**. *Der effizientere Zugriff auf das Wissen der Chemie*. <http://roempp.thieme.de>. Accessed 2 April 2015.
- [158] Lin, Y. Su, Z., Xiao, G. *et al.* **2011**. *Langmuir* 27, 1398–1402.
- [159] Hunter, R. J. **1981**. *Colloid Science*, 308.
- [160] Meyer, B. K. Stehr, J., Hofstaetter, A. *et al.* **2007**. *Appl. Phys. A* 88, 119–123.
- [161] Atanasova, P. **2007** *A Molecular Approach to Tethered Bilayer Lipid Membranes. Synthesis and Characterization of Novel Anchor Lipids*. Mainz.
- [162] Passerini, A. Punta, M., Ceroni, A. *et al.* **2006**. *Proteins* 65, 305–316.
- [163] Rothenstein, D. Claasen, B., Omiecinski, B. *et al.* **2012**. *J. Am. Chem. Soc.* 134, 12547–12556.
- [164] Altintoprak, K. Seidenstücker, A., Welle, A. *et al.* **2015**. *Beilstein J. Nanotechnol.* 6, 1399–1412.
- [165] Hong, J. H. Duncan, S. E., Dietrich, A. M. **2010**. *Food Qual. Prefer.* 21, 132–139.
- [166] Russell, J. M. Oh, S., LaRue, I. *et al.* **2006**. *Thin Solid Films* 509, 53–57.



- [167] Vonna, L. Limozin, L., Roth, A. *et al.* **2005.** *Langmuir* 21, 9635–9643.
- [168] Zhou, K. Li, F., Dai, G. *et al.* **2013.** *Biomacromolecules* 14, 2593–2600.
- [169] Betz, S. F. **1993.** *Protein Sci.* 2, 1551–1558.
- [170] Hogg, P. J. **2003.** *Trends Biochem. Sci.* 28, 210–214.
- [171] Rong, J. Niu, Z., Lee, L. A. *et al.* **2011.** *COCIS* 16, 441–450.
- [172] Meulenkamp, E. A. **1999.** *J. Phys. Chem. B* 103, 7831–7838.
- [173] Faber, H. Burkhardt, M., Jedaa, A. *et al.* **2009.** *Adv. Mater.* 21, 3099–3104.
- [174] Fujihara, S. Sasaki, C., Kimura, T. **2001.** *Appl. Surf. Sci.* 180, 341–350.
- [175] Kahraman, S. Bayansal, F., Çetinkara, H. A. *et al.* **2012.** *Mater. Chem. Phys.* 134, 1036–1041.
- [176] Wenas, W. W. Yamada, A., Konagai, M. *et al.* **1991.** *Jpn. J. Appl. Phys.* 30, L441.
- [177] Nicolay, S. Faÿ, S., Ballif, C. **2009.** *Cryst. Growth Des.* 9, 4957–4962.
- [178] Nicolay, S. Benkhaira, M., Ding, L. *et al.* **2012.** *Sol. Energy Mater. Sol. Cells* 105, 46–52.
- [179] Fanni, L. Aebersold, B. A., Alexander, D. *et al.* **2014.** *Thin Solid Films* 565, 1–6.
- [180] Kajikawa, Y. **2006.** *J. Cryst. Growth* 289, 387–394.
- [181] Jia, S. **2005** *Polyelectrolyte Assisted Preparation and Characterization of Nanostructured ZnO Thin Films.* Stuttgart.
- [182] Tian, Z. R. Voigt, J. A., Liu, J. *et al.* **2003.** *Nat. Mater.* 2, 821–826.
- [183] Bauermann, L. P. del Campo, A., Bill, J. *et al.* **2006.** *Chem. Mater.* 18, 2016–2020.
- [184] Wang, H. Xie, C., Zeng, D. **2005.** *J. Cryst. Growth* 277, 372–377.
- [185] Delhez, R. de Keijser, Th. H., Mittemeijer, E. J. **1987.** *Surf. Eng.* 3, 331–342.
- [186] Schwer, C., Kenndler, E. **1991.** *Anal. Chem.* 63, 1801–1807.
- [187] Rived, F. Rosés, M., Bosch, E. **1998.** *Anal. Chim. Acta* 374, 309–324.
- [188] Kosmulski, M., Matijević, E. **1992.** *Colloids Surf., A* 64, 57–65.
- [189] Wright, P. B. Lister, A. S., Dorsey, J. G. **1997.** *Anal. Chem.* 69, 3251–3259.
- [190] Diress, A. G., Lucy, C. A. **2004.** *J. Chromatogr. A* 1027, 185–191.
- [191] Geiser, L. Mirgaldi, M., Veuthey, J.-L. **2005.** *J. Chromatogr. A* 1068, 75–81.
- [192] Woan, K. V., Sigmund, W. M. **2011.** *Langmuir* 27, 5377–5385.
- [193] Durkan, C. Welland, M. E., Chu, D. P. *et al.* **1999.** *Phys. Rev. B* 60, 16198–16204.
- [194] Oh, B.-Y. Jeong, M.-C., Ham, M.-H. *et al.* **2007.** *Semicond. Sci. Technol.* 22, 608–612.
- [195] Chung, J. H. Lee, J. Y., Kim, H. S. *et al.* **2008.** *Thin Solid Films* 516, 5597–5601.
- [196] **2008.** *IEEE Std 1620-2008 (Revision of IEEE Std 1620-2004) - Redline*, 1–27.

- [197] Morfa, A. J. Beane, G., Mashford, B. *et al.* **2010.** *J. Phys. Chem. C* 114, 19815–19821.
- [198] Nix, W. D. **1997.** *Mater. Sci. Eng., A* 234-236, 37–44.
- [199] Chokshi, A. H. Rosen, A., Karch, J. *et al.* **1989.** *Scr. Mater.* 23, 1679–1683.
- [200] Nieman, G. W. Weertman, J. R., Siegel, R. W. **1989.** *Scr. Mater.* 23, 2013–2018.
- [201] Lu, K. Wei, W. D., Wang, J. T. **1990.** *Scr. Mater.* 24, 2319–2323.
- [202] Fougere, G. E. Weertman, J. R., Siegel, R. W. *et al.* **1992.** *Scr. Mater.* 26, 1879–1883.
- [203] Jian, S.-R. Chen, G.-J., Wang, S.-K. *et al.* **2013.** *Surf. Coat. Technol.* 231, 176–179.
- [204] Raghavan, R. Bechelany, M., Parlinska, M. *et al.* **2012.** *Appl. Phys. Lett.* 100, 191912.
- [205] Carlton, C. E., Ferreira, P. J. **2007.** *Acta Mater.* 55, 3749–3756.
- [206] Ma, E. **2004.** *Science* 305, 623–624.
- [207] Martin, L. P. Dadon, D., Rosen, M. **1996.** *J. Am. Ceram. Soc.* 79, 1281–1289.
- [208] Gottstein, G. **2001** *Physikalische Grundlagen der Materialkunde. Mit 26 Tabellen.*  
Springer-Lehrbuch, 2. Aufl. Berlin [u.a.]: Springer.
- [209] Braem, M. Van Doren, V. E., Lambrechts, P. *et al.* **1987.** *J. Mater. Sci.* 22, 2037–2042.
- [210] Zhao, Y. Ge, Z., Fang, J. **2008.** *Phys. Rev. E* 78.
- [211] Jackson, A. P. Vincent, J. F. V., Turner, R. M. **1990.** *J. Mater. Sci.* 25, 3173–3178.
- [212] Lasko, G. Burghard, Z., Bill, J. *et al.* **2013.** *Adv. Eng. Mater.*
- [213] Koehler, J. S. **1970.** *Phys. Rev. B* 2, 547–551.
- [214] Fratzl, P. Gupta, H. S., Fischer, F. D. *et al.* **2007.** *Adv. Mater.* 19, 2657–2661.

## 8 DANKSAGUNG

Das Gelingen dieser Arbeit wäre ohne die vielseitige Unterstützung, die mir zu Teil wurde, nicht möglich gewesen. Deshalb möchte ich mich bei zahlreichen Menschen bedanken.

Prof. Dr. Joachim Bill für die Möglichkeit, die Arbeit an seinem Lehrstuhl durchzuführen. Die Freiheiten, die mir nicht nur beim Thema, sondern auch bei der Durchführung der Arbeit gegeben wurde sowie die zahlreichen intensiven Diskussionen.

Prof. Dr. Bernhard Hauer für die Übernahme des Mitberichts.

Prof. Dr. Thomas Schleid nicht nur für die Übernahme des Prüfungsvorsitz, aber auch die ein oder andere sehr kurzweilige Unterhaltung bei Doktorfeiern.

Dr. Petia Atanasova für die tolle und intensive Unterstützung und Betreuung während der Arbeit.

Dr. Zaklina Burghard für die zahlreichen Diskussionen zu Piezoelektrizität und mechanischen Eigenschaften, endlose Geduld, einer Dauerversorgung mit Teebeutel und Obst, sowie immer einem offenen Ohr bei allen Belangen.

Dr. Dirk Rothenstein für Unterstützung im Labor, wenn ich mal wieder eine „kurze“ Frage hatte, intensives Korrekturlesen, anregende Diskussionen und kurzweilige Unterhaltungen bei Konferenzen und Reisen.

Bei meinen zahlreichen Kooperationspartnern im Laufe der Arbeit: Dr. Sabine Eiben und Angela Schneider vom Institut für Biomaterialien und biomolekulare Systeme der Universität Stuttgart für die stete Versorgung mit Viren, Unterstützung bei verschiedenen Messungen und angeregten Diskussionen. Prof. Dr. Jörg Schneider, Dr. Rudolph Hofmann und Shawn Sanctis von der TU Darmstadt für die Zusammenarbeit bei den Feldeffekttransistoren und die vielen Diskussionen im Rahmen dieser. Dr. Neus Domingo für die Hilfe beim PFM sowie den Diskussionen für das Paper. Prof. Dr. Andreas Leineweber für die Diskussionen der XRD Ergebnisse, der Textur und alle Berechnungen, die dafür gemacht wurden.

Für Unterstützung bzw. Durchführung von Messungen Maritta Dudek, Marion Hagel, Nina Blumenstein, Angela Schneider, Sabine Eiben, Shawn Sanctis und Alexander Gress.

Prof. Dr. van Aken und Felicitas Predel vom StEM für die Nutzung sowie das eigenständige Arbeiten am REM.

Der gesamten Gruppe am ‚PML‘ für die angenehme und hilfsbereite Atmosphäre. Insbesondere Juliane Kränzl und Martin Schweizer für viel Hilfe bei administrativen Dingen und IT Notfällen.

Der DFG für die finanzielle Förderung durch die Auszeichnung mit der Anschubfinanzierung für junge Wissenschaftler.

Dr. Hans-Georg Libuda und der IMPRS-CMS, nicht nur für die finanzielle Unterstützung, sondern auch für die Möglichkeit zahlreiche summer und winter schools zu besuchen. Die Zeit in Boston, Freudenstadt und Günzburg bleibt unvergessen. Wichtige Freundschaften sind entstanden und wurden bei unseren Thirsty Thursdays gepflegt. Danke an Tomce, Benni, Matej, Toby, Werner und Susan.

Katha für einfach alles! Tolle Trips, Aufmunterung, Diskussionen und Schörlchen in guten wie in schlechten Zeiten.

Meiner Familie und Yannick, die mich auf diesem Weg mit sehr viel Geduld die gesamte Zeit unterstützt haben. Ihr habt mir die Kraft und das Durchhaltevermögen gegeben, um diese Arbeit erfolgreich zu Ende zu bringen. Ein besonderer Dank an Pascal für das mühsame Korrekturlesen. Ohne Euch hätte ich es nicht geschafft.

## 9 CURRICULUM VITAE

### PERSONAL DATA

---

Name Nina Stitz  
Geburtstag 06.06.1986  
Geburtsort Stuttgart  
Nationalität German

### STUDIUM UND ARBEIT

---

Seit 09/15 **Zuverlässigkeitsingenieurin** bei der Robert Bosch GmbH

Seit 09/2011 **Doktorarbeit** an der Universität Stuttgart am Institut für Materialwissenschaft

10/2005 – 03/2011 **Diplomstudiengang Werkstoffwissenschaft**, Universität Stuttgart  
▪ Diplomarbeit

### AUSBILDUNG

---

09/1996 – 06/2005 **Allgemeines Abitur** am Geschwister-Scholl-Gymnasium Stuttgart

### AUSZEICHNUNGEN

---

09/2014 – 08/15 **Deutsche Forschungsgemeinschaft**  
▪ Ansubfinanzierung (start-up grant) für junge Wissenschaftlerinnerhalb des Schwerpunktprogramms SPP 1569 „Generation of multifunctional inorganic materials by molecular bionics“

Seit 09/2011 **Max Planck Gesellschaft**  
▪ Mitglied der International Max Planck Research School for Condensed Matter Science (davor: for Advanced Materials)